USGS
science for a changing world

The Effect of Selected Cleaning Techniques on Berkshire Lee Marble: A Scientific Study at Philadelphia City Hall

U.S. Geological Survey Professional Paper 1635

U.S. Department of the Interior
U.S. Geological Survey

U.S. Department of the Interior
U.S. Geological Survey

The Effect of Selected Cleaning Techniques on Berkshire Lee Marble: A Scientific Study at Philadelphia City Hall

By

Victor G. Mossotti, A. Raouf Eldeeb, Terry L. Fries, *and* Mary Jane Coombs,
U.S. Geological Survey;

Virginia N. Naudé,
Norton Art Conservation, Inc.;

Lisa Soderberg,
Vitetta Group; *and*

George S. Wheeler,
Metropolitan Museum of Art, New York

Professional Paper 1635

U.S. Department of the Interior
Gale A. Norton, Secretary

U.S. Geological Survey
Charles G. Groat, Director

U.S. Geological Survey, Reston, Virginia: 2002

For additional copies please contact:

USGS Information Services
Box 25286
Denver, CO 80225

This report and any updates to it are available on line at
http://geopubs.wr.usgs.gov/prof-paper/pp1635/

Additional USGS publications can be found on line at
http://geology.usgs.gov/products.html

For more information about the USGS and its products:

Telephone: 1–888–ASK–USGS
World Wide Web: http://www.usgs.gov/

Published in the Western Region, Menlo Park, California
Manuscript approved for publication, April 26, 2000
Edited by George Havach
Layout and design by Sara Boore and Michael Diggles

COVER
East façade of Philadelphia City Hall.

Contents

Contents

Contents

Figures

Contents

Tables

The Effect of Selected Cleaning Techniques on Berkshire Lee Marble: A Scientific Study at Philadelphia City Hall

By Victor G. Mossotti, A. Raouf Eldeeb, Terry L. Fries, Mary Jane Coombs, Virginia N. Naudé,[1] Lisa Soderberg,[2] and George S. Wheeler[3]

Abstract

This report describes a scientific investigation of the effects of eight different cleaning techniques on the Berkshire Lee marble component of the façade of the East Center Pavilion at Philadelphia City Hall; the study was commissioned by the city of Philadelphia. The eight cleaning techniques evaluated in this study were power wash (proprietary gel detergent followed by water rinse under pressure), misting (treatment with potable, nebulized water for 24–36 hours), gommage (proprietary Thomann-Hanry low-pressure, air-driven, small-particle, dry abrasion), combination (gommage followed by misting), Armax (sodium bicarbonate delivered under pressure in a water wash), JOS (dolomite powder delivered in a low-pressure rotary-vortex water wash), laser (thermal ablation), and dry ice (powdered-dry-ice abrasion delivered under pressure).

In the quasi-experimental design, a control sample, taken from an area of stone protected by epoxy adjoining an unprotected test area, was simultaneously cored with the test sample. In our study, approximately 160 cores were removed from the building for laboratory analysis. As a basis for differentiating the various cleaning techniques, we measured the changes in the structural properties of the stone on the microscale (0.1–100 μm), and in the esthetic features of the stone on the mesoscale (0.1–5 mm) and macroscale (≥0.5 cm), caused by each of the cleaning techniques.

The spatially averaged distribution of particulate matter and salts on the control and test surfaces side by side was measured by electron microscopy on the microscale and by optical reflectance on the mesoscale to macroscale (0.1–20 mm). We developed a computer program to analyze scanning-electron-micrograph (SEM) images for the fractal dimension and other morphologic parameters of the stone surface on the microscale; the fractal dimension is a factor in the surface-roughness test. The program also computed the near-surface fracture density of the stone.

An analysis of more than 1,100 samples cut from the cores provided a statistical basis for crafting the essential elements of a reduced-form, mixed-kinetics conceptual model that represents the deterioration of calcareous stone in terms of self-organized soiling and erosion patterns. This model, in turn, provided a basis for identifying the variables that are affected by the cleaning techniques and for evaluating the extent to which such variables influence the stability of the stone. The model integrates the mutual dependence of processes controlling the primary deposition of soiling agents, the secondary mobilization of transportable materials, and the permanent alteration of the stone through critical feedback paths in the model system.

The model recognizes three classes of variables that may influence the soiling load on the stone, including such exogenous environmental variables as airborne moisture, pollutant concentrations, local aerodynamics, and so on, and such endogenous stone variables as surface chemistry and microstructure (fracturing, roughness, and so on). Our study showed that morphologic variables on the mesoscale to macroscale are not generally affected by the choice of a cleaning technique. For example, surface-recession tests indicate that differences in mass loss from technique to technique are virtually inconsequential over the long term. The model also explains the spatial distribution of particulate matter and salts over the building by the action of water on the stone surface. According to this mechanism, the soiling pattern on the building is controlled mainly by the macromorphology and orientation of the stone. Thus, the long-term soiling pattern on the building is independent of the cleaning technique applied.

This study also showed that micromorphologic variables are differentially affected by the various cleaning techniques. Although the extent to which surface microstructure and microchemistry influence the soiling load requires further study, we assumed in our evaluation that the long-term esthetic and structural properties of the stone are closely related to the lateral and vertical distribution of particulate matter and salts and to the mechanical bonding between calcite, phlogopite, and dolomite grains in the matrix. Contrary to our original conjecture, we found no evidence that soluble salts play a significant role in the deterioration of Berkshire Lee marble. Although salts were evident in cracks and fissures of the heavily soiled stone, such salts did not penetrate the surface to a depth of more than a few hundred micrometers.

Interestingly, we noted that the strength of the relation between the fracture density and the surface roughness was distinctly sensitive to the cleaning technique used, and so we used this relation as a measure of the marginal ability of each technique to clean the stone without causing collateral damage to the surface. Thus, the criteria used to differentiate the cleaning techniques were ultimately based on the ability of each technique to remove soiling without altering the texture of the stone surface. This study identified both the gommage and JOS techniques as appropriate for cleaning ashlar surfaces and the combination technique as appropriate for cleaning highly carved surfaces at the entablatures, cornices, and column capitals.

[1]Norton Art Conservation, Inc.
[2]Vitetta Group.
[3]Metropolitan Museum of Art, New York.

Introduction

Background

One of the finest American examples of the Second Empire Style of picturesque eclectic architecture, Philadelphia City Hall, dedicated in 1901, is a bold and massive marble and granite edifice that occupies the city's central square. Each of the building's exterior walls consists of a granite base topped with marble that extends almost 500 ft in length, together representing one of the largest load-bearing masonry structures in the United States. The masonry structure, designed by John McArthur, Jr., is distinguished by a rich and vast sculptural program: all the major architectural elements are adorned with marble carvings by Alexander Milne Calder. The unusual historic and architectural significance of the building, as well as the magnitude and importance of the sculptural program, provided both the impetus and rationale for initiating an extensive testing program for masonry cleaning and preservation techniques.

In 1991, the city of Philadelphia contracted the Vitetta Group, in association with Kelly/Maiello, to complete the building's restoration, modernization, and rehabilitation and to provide a framework for the restoration of the entire exterior of the building. A multidisciplinary project team of preservation architects, conservators, and scientists helped formulate a conservative and comprehensive masonry-cleaning program as a critical part of the exterior restoration and long-term preservation of the building. The project team for the work—completed during winter-spring 1995—included preservation architects from the Vitetta Group; the conservator Virginia Naudé of Norton Art Conservation, Inc.; and the chemist George S. Wheeler. In addition, a group of scientists at the U.S. Geological Survey (USGS) in Menlo Park, Calif., who developed a process to analyze and measure the characteristics and alteration patterns of the stone, were selected to collaborate with the project team. This group of scientists, consisting of Victor Mossotti, Raouf Eldeeb, and Terry L. Fries, had recently completed an investigation of cleaning techniques on the limestone façade of the Chicago *Tribune* tower that compared the effects on the underlying substrate of the Thomann-Hanry dry process with those of water-based techniques. As participants in the U.S. National Acid Precipitation Assessment Program since its inception in 1983, these scientists developed software to investigate the fractal structure of stone surfaces as viewed in SEM images, as well as a wet-deposition model. This software and model facilitated the quantitative study of the complex stone structure at a level well beyond the reach of classical models. The scientists proposed to apply their recent research on the Chicago *Tribune* tower in order to evaluate the characteristics and alteration patterns of the marble at Philadelphia City Hall after cleaning and artificial weathering of the masonry. Toward this goal, they conducted preliminary tests as part of the design phase of the building's restoration. These tests were planned as a demonstration project to serve as a model for the restoration of the entire exterior of the building.

Goals of the Masonry-Cleaning Process

The institution of a testing program was essential to identify the type of stone deterioration at Philadelphia City Hall and to determine how the stone would be affected by selected cleaning techniques. Unlike metals, which can be preserved by maintenance programs and by the application of surface coatings, no coatings have been developed to ensure the preservation of stone. In fact, on many buildings, the application of coatings can contribute to stone deterioration. The most effective strategy for preservation of the dolomitic marble and granite at Philadelphia City Hall includes the selection of cleaning techniques to provide a stone surface that is minimally reactive and maximally durable against the inevitable attack of weather and airborne pollutants within an urban environment. This strategy necessitates the selection of a cleaning technique that will achieve an appropriate balance between what is removed from and what is allowed to remain on the surface. The efficacy and impact of a given cleaning technique depend on the petrologic and surficial features of the dolomite and granite, properties determined by the source of the stone, the method of quarrying, and surface dressing; the exposure to the environment; the soiling patterns; and any previous cleanings.

The project team identified these goals of the masonry-cleaning program: to replicate as closely as possible the building's original appearance, with a minimal impact on the integrity of the underlying substrate; and to apply a cleaning technique that promotes the health and well-being of people, extends the longevity of the building, and protects the surrounding environment. The masonry-cleaning program, which removes destructive pollutant crusts and arrests established cycles of stone deterioration, is integral to the long-term preservation of the building. All the cleaning treatments tested on the century-old stone remove grime and gypsum with a minute loss of the original substrate. The project team acknowledged that some people would advocate no cleaning at all as the safest option because of potential damage to the underlying substrate. However, the city did not consider "no cleaning" as a viable option. If the city was to commit funds for the restoration of the exterior masonry, an appropriate public image had to be maintained, and the building's original clean appearance had to be replicated as closely as possible. Also, cleaning was essential to gain a complete understanding of the structural condition of the building and to ensure that adequate masonry-stabilization measures were instituted. Layers of soiling and guano on large sections of the building, particularly at the locations of carvings and former repairs, prevented any determination of the stability of the underlying marble before cleaning. The project team was committed to cleaning with the assurance that any alteration of the stone surface would be minimal, predictable, and acceptable. An overriding consideration was to determine the degree of loss that is acceptable in order to achieve an appropriate esthetic solution, while ensuring the long-term preservation of the stone.

Preliminary Testing Program

The first tests of cleaning techniques at Philadelphia City Hall were conducted during March and April 1994 as part of the design phase for restoration of the East Center Pavilion. These tests, which addressed the preservation of the exterior marble walls, were designed to determine:

- The least destructive cleaning techniques for the building
- The locations on the building where each cleaning technique, within the selected set, would best be used
- The development of a restoration program and contract documents for preservation of the building
- The cost implications of these decisions

Water-Based Cleaning Techniques

Initially, the project team tested several water-based cleaning techniques. In the United States, such techniques, both with and without detergent, have traditionally been the least expensive and safest available—safer than both chemical and abrasive techniques. However, the harmful effects of water infiltration on the building, as well as the volume of water required to clean large stone structures, have led preservationists to seek alternative cleaning techniques.

Dry Cleaning Techniques

The impact of water-based cleaning techniques have been recognized in Europe, where the dry cleaning of stone with very small particles delivered at low air pressure has played an important role in conservative stone cleaning for decades. Because open joints are typical throughout large areas of Philadelphia City Hall, the preliminary testing program addressed alternatives to the traditional water-based cleaning techniques. A low-pressure, small-particle, air-abrasive cleaning technique—one that uses no water, chemicals, or detergents and eliminates the potential for water infiltration—was identified for testing during this preliminary testing program. Because the city determined that specifications would be developed for all cleaning techniques tested, the project team requested demonstrations from vendors with long performance records of cleaning buildings with low-pressure, small-particle, air-abrasive techniques. One vendor, Thomann-Hanry, Inc., had developed a proprietary cleaning technique in France in 1965. The project team themselves tested all the chemical and water-based cleaning techniques. The various cleaning techniques tested were described and briefly analyzed by Naudé (1994).

Conclusions

On the basis of a qualitative assessment, both visual and under low-power, hand-held magnification, the project team rejected chemical cleaning as too harsh but concluded that the stone could be cleaned by either power-wash and detergent techniques or a low-pressure, small-particle, air-abrasive technique. The effects of the various cleaning techniques on different conditions of the marble surfaces indicated the desirability of cleaning the stone with a combination of wet and dry techniques. However, the optimal combination of such techniques was unclear after the preliminary testing program, particularly in regard to the removal of salts, which, if present, may contribute to continued deterioration of the stone. Onsite observations during the preliminary testing program raised additional questions about surface alterations that the project team concluded could be answered only with quantitative scientific data. Among the questions to be addressed by these data were (1) the quantity and location of soluble salts; (2) the effectiveness of the removal of soluble salts, if present, by water-based and abrasive techniques; and (3) the degree of damage to the stone surface by abrasive techniques.

Expansion of the Masonry-Cleaning Program

After the preliminary testing program was completed, the project team recommended that testing be continued in a second phase to provide additional scientific data to measure the impact of any masonry-cleaning program on the long-term preservation of the building. The primary goal of the second phase, which took place during winter-spring 1995, was to characterize and quantify alterations to the surface after cleaning and, in some areas, artificial weathering of the stone. Eight cleaning techniques were evaluated in this phase of our study:

- **Power wash**: proprietary gel detergent application, followed by a water rinse under pressure
- **Misting**: potable, nebulized water applied at low pressure for 24 to 36 hours
- **Gommage**: proprietary Thomann-Hanry, Inc., low-pressure, air-driven, small-particle, dry abrasion
- **Combination**: gommage followed by misting
- **Armax**: sodium bicarbonate delivered under pressure in a water wash
- **JOS**: dolomite powder delivered in a low-pressure rotary vortex water wash
- **Laser**: thermal ablation
- **Dry ice**: powdered-dry-ice abrasion delivered under pressure

A description of each cleaning technique, including the rationale of its selection for testing and information on how each technique is currently used in architectural conservation, is presented in appendix 1. The specific purpose of this study was to establish a set of criteria by which the various cleaning techniques could be evaluated. This evaluation involved scoring each technique against a reference level of cleanliness for the various masonry components of the building and against specifications that define an acceptable level of physical and chemical stability of the cleaned stone.

Condition of the Building Stone

Petrology of Unweathered Building Stone

The composition of the building stone was determined by petrographic analysis of thin sections prepared from the center

of two core samples taken from representative areas of the building. The core samples were also studied by qualitative energy-dispersive X-ray-fluorescence and backscattered-electron imaging in an electron microprobe. The two core samples studied for baseline petrology showed no significant differences.

The marble is composed of more than 95 volume percent dolomite. Grain size ranges from 0.13 to 0.66 mm in a granoblastic texture, with the essential mineral constituents approximately equal in size. The grain boundaries are generally smooth and curved. Some calcite occurs as small (less than 0.1 mm) grains at grain boundaries between larger dolomite crystals. Somewhat more abundant than calcite is phlogopite, a magnesium-rich mineral of the mica group: $K(Mg,Fe)_3AlSi_3O_{10}(OH,F)_2$. Phlogopite, which is yellowish brown to brownish red or copper colored, commonly occurs in limestone as a result of dedolomitization. Phlogopite is near biotite in composition but contains little iron. A few scattered thick, platelike, honey-colored crystals of this mineral are visible in the core samples under low magnification. In thin sections, phlogopite is colorless and occurs in thin, elongate prismatic grains, as much as 1 mm long, that appear to have some preferred orientation. Also observed in the marble were a few grains of apatite: $Ca_5(PO_4,CO_3)_3(F,OH,Cl)$. Altogether, these minor minerals do not appear to make up more than 2 to 3 volume percent of the marble.

Condition of Weathered Building Stone

The richly articulated sculptural program of the building provides a wide variety of surface-soiling conditions from which to sample. However, visual inspection of the façade from the street and at close range suggests that most of the surface can be characterized as one of four conditions: lightly soiled, smooth (LSS, fig. 1*A*); lightly soiled, rough (LSR, fig. 1*B*); gypsum crusted, smooth (GCS, fig. 1*C*); or gypsum crusted, rough (GCR, fig. 1*D*).

Lightly Soiled, Smooth

LSS-condition stone, which comprises approximately 8 percent of the building's façade, is observed mainly on ashlars. These areas are lightly washed during periods of rain and are protected from extreme weather by cornices and columns. A few pits or ridges are visible in the surface. The colors of LSS areas are various shades of light gray.

Lightly Soiled, Rough

LSR-condition stone, which comprises approximately 85 percent of the building's façade, includes both ashlars and sculptural ornaments, which generally are directly exposed to weather. To the naked eye, the surface is pitted and commonly exhibits ridges that reflect subtle patterns of rain runoff. Surface erosion is clearly apparent where cracks or natural fissures are present. The colors of LSR areas are various shades of dark gray.

Gypsum Crusted, Smooth

GCS-condition stone, which comprises approximately 4 percent of the building's façade, is recognizable by smooth black soiling that cannot be brushed away. Such soiling is conspicuous in protected areas and in pockets on exposed sculptural ornament. Gypsum crusted, smooth stone was later found to be consistently carbon-soiled.

Gypsum Crusted, Rough

GCR-condition stone, which comprises approximately 1 percent of the building's façade, is easily distinguishable by blotches of thick black crust with a granular texture. Virtually all of these areas were identified in deeply carved stone that is protected from rain runoff. Laboratory tests show that the dark crust which forms the exterior veneer on both GCS and GCR surfaces is composed largely of gypsum impregnated with partially soluble particulate matter.

In addition to these four surface conditions, about 2 percent of the building's façade is severely deteriorated. Such stone, which generally has a sugary texture, is commonly found in sculptural projections with maximum exposure and on stone located in the path of rain runoff. Such severely deteriorated stone, which has vastly different requirements for cleaning and preservation, was considered atypical of the marble that requires cleaning and so was omitted from our study.

Methods and Procedures

Framework for Study

The central focus of this study was on the capability of a given cleaning technique to remove soiling from the exterior stone on the building and on the effect, if any, of each technique on the stone itself. The many issues related to this problem can be viewed in terms of a model in which the thermodynamic state of the stone is represented by a set of state variables.[1] For example, several variables that reflect the state of the stone include the chemical composition of the surface, surface roughness, and surface fracturing. Consider the four surface-soiling conditions (LSS, LSR, GCS, GCR), as represented in the state diagram in figure 2. We can view stone erosion and surface soiling in terms of the set of processes that act to transform the surface from one state to another. In this view, we regard cleaning as an effort to reverse some of the effects of erosion and soiling, as represented in figure 3,

although, in general, a complete reversibility of weathering is impossible.

To define the specifications against which the various cleaning techniques can be scored, we first need to identify the variables that are affected by the cleaning techniques and to evaluate the extent to which such variables influence the stability of the stone. The basic elements of a model that expands on the notion introduced in figure 2 are illustrated in figure 4. These elements include the processes that determine the future state of the stone (center panel), and the variables that influence such processes and that reflect the state of the stone at a given point in time (boxes A–C). Three general classes of variables are illustrated in figure 4: those that characterize the ambient conditions to which the building is subjected (box A), those that quantify the physical condition of the stone (morphology, orientation of surface, subsurface fracturing, degree of grain consolidation, and so on; box B), and those that determine the chemical state of the stone (elemental composition, crystalline structure, and so on; box C). In general, such variables are both spatially and temporally dependent. The schematic segregation of these three classes of variables in figure 4 acknowledges their mutual dependence with regard to a set of complex linked processes that themselves are controlled by the ambient environment and by the state of the stone. Two main classes of linked processes are diagrammed in figure 4: those driving the delivery and removal of weathering agents to and from the stone (transport), and those affecting the chemistry and structure of the stone (alteration).

We found it useful to consider material-transport processes exclusively in terms of primary or secondary mechanisms that deliver materials to or remove materials from a particular location on the surface, as illustrated in figure 5. Primary deposition is the mode by which weathering agents that soil or deteriorate the stone are introduced from outside the surface area, including the gravity-independent attack of such gases as SO_2 and the gravity-dependent deposition of particulate matter and water. The critical distinction between primary and secondary deposition is that in primary deposition, the weathering agent of interest first interacts with the stone at the point of delivery.[2] This interaction governs the local flux of the weathering agent to the stone. In contrast, secondary transport takes place when the weathering agents, or their reaction products, are mobilized after primary deposition and redeposited elsewhere within the catchment.[3] Such mobilization is commonly driven by the action of water. Both primary and secondary deposition commonly occur on rain-washed buildings and monuments.

Measurement Tools

Many physicochemical factors influence actual stone erosion and its measurement. We assumed that the physical microstructure of the stone is a key factor governing the stone's reactivity in both primary and secondary deposition processes. In particular, we hypothesized that the fractal morphology of the stone over a range of scale from perhaps a few nanometers to tens of micrometers[4] critically influences the reactivity of the surface in primary deposition processes; controlled atmospheric-chamber experiments to evaluate this hypothesis were conducted at the U.S. National Center for Preservation Technology and Training in Natchitoches, La., and are discussed in Bede (2001). We also suspect that the stone porosity over the nanoscale and microscale regulates the transport of salts below the stone surface and that microscale grain consolidation and pore-space morphology govern the friability of the stone surface.

For the purposes of this study, we used microscale fracturing and surface-roughness measurements and nanoscale surface-reactivity measurements to infer the relative stability of test surfaces for each cleaning technique. The surface-roughness measurements, which are based on a mathematical analysis of digitized electron micrographs, utilize the fractal properties of the stone surface to characterize morphologic features of the stone on the microscale. The near-surface fracture density was also assessed by computer analysis of microscale electron micrographs. The surface-reactivity measurements, which are based on the release rate of Ca^{2+} from the stone surface into water, reflect the fractal structure of the stone surface on the nanoscale. The degree of cleanliness is determined on the microscale by scanning-electron microscopy (SEM) and X-ray microanalysis,[5] and on the macroscale by systematic optical examination of both uncleaned and cleaned surfaces. Most of these measurements provide ratio-type data; the details of laboratory operations are discussed in appendixes 2 through 8.

Experimental Design

Many extraneous variables could influence the score assigned to a given cleaning technique. In addition to the degree of surface soiling before the stone is cleaned, such variables might include the surface morphology, friability, and porosity over a wide range of scale, as well as the mechanical stress between mineral grains at the stone surface (surface free energy introduced by carving, erosion, and so on). Although the influence of such variables can be minimized by testing the cleaning technique on stone surfaces of only one type (for example, ashlar), such optimization of internal validity would sacrifice the generalizability of the results and otherwise limit their value to preservation architects and conservators. As an alternative approach, we undertook an experimental design that partly controlled for extraneous variables by including a control group of test surfaces in the study. However, in view of the surface transformation caused by the cleaning technique, the exact same surface could not be examined before and after a given cleaning technique was applied. We developed a strategy by which a control surface adjacent to a given test surface was sampled simultaneously with the test surface. The actual coring procedure required protection of the soiled control surface such that both the control and cleaned surfaces were represented in each core, as illustrated in figure 6. As part of the setup pro-

cedure for each core, the soiled control surface was protected from cleaning with a layer of epoxy resin in advance of application of the cleaning technique. Specifically, about 150 cm^2 of the soiled stone surface was coated with epoxy resin to provide an approximately 15-cm-long boundary between the adjacent control and test surfaces. The cleaning technique was then applied to the test surface over an area that included the line of demarcation between the control and test surfaces. After application of the cleaning technique, the cleaned area was treated with an extremely low viscosity acrylic resin (L.R. white), followed by a layer of epoxy resin, to stabilize the stone before coring. The core was then taken from the cleaned area in such a way to include the line of demarcation between the control and test surfaces. Once in the laboratory, the cores were studied in cross section such that both the control and test surfaces could be examined in the same SEM image.

To represent as many extraneous variables as possible, a total of 160 1-in.-diameter cores were taken from pseudorandomly selected sites representing each surface condition. The choice of core location was generally biased toward extreme examples of a given surface-soiling condition. An overview of the sample-coring methods and information on the sample inventory selected for this study are presented in appendix 1; the procedures used for measuring these properties are detailed in appendixes 2 through 9. The exposed surfaces of the cores were tested for cleanliness and surface reactivity.

Cleaning Efficacy

The central question in this study concerns the ability of a given cleaning technique to remove a given type of surface soiling from the façade of the building with minimal impact on the integrity of the substrate and without compromising the surrounding environment. Three measurements on the cleaned stone were used to determine the efficacy of each cleaning technique (see fig. 35): (1) the surface distribution of particulate matter, (2) the structural penetration of salts, and (3) the surface reflectivity (grayness).

Particulate Matter

The ability of the cleaning techniques to remove soiling from the stone was first evaluated with optical techniques. To study the surface distribution of particulate matter on the microscale, we prepared optical photomicrographs, mostly at the relatively low magnification of 67×, for most of the uncleaned and cleaned surfaces used in this study.[6] The closeup surface views provided by the optical microscope supplemented the SEM and X-ray images[7] used to investigate the penetration of salts into the stone.

The photomicrographs in figure 7 show a qualitative difference between the soiling on LSS- and LSR-condition stone and on GCS- and GCR-condition stone. Although the soiling increases on uncleaned surfaces along the series LSS-LSR-GCS-GCR, in LSS- and LSR-condition stone particulate matter appeared to be widely disseminated among dolomite crystals that are relatively pristine, whereas in GCS- and GCR-condition stone, aggregations of dark particles and white deposits appear to virtually cover the dolomite substrate and to be deeply encrusted in nooks and crannies of the surface. It is precisely the distribution of such particulate matter on the microscale that determines general surface reflectivity on the macroscale.

Salts

At the outset of this study, one of our chief concerns was the distribution of various salts in pores and cracks of the stone. In addition to causing unsightly blemishes on the stone, such salts as $CaSO_4 \cdot 2H_2O$ (gypsum) may participate in processes that eventually can result in catastrophic mechanical failure of the stone.

Primary X-ray analysis with an electron microscope was used to depth-profile the core cross sections. The spatial resolution of the analytical method was ≈5 μm, and the chemical detection limit and sensitivity were ≈0.25 and 0.50 atomic percent, respectively. The lateral distribution of salts was measured in uncleaned and cleaned areas of cores with all four surface conditions (LSS, LSR, GCS, GCR).

Typical cross-sectional SEM images of uncleaned core samples in the LSS, LSR, GCS, and GCR series are shown in figure 8. Among LSS, LSR, and GCS cores, the stone substrate supporting the layer of soiling seems to be relatively undamaged by the overlayer of soiling, whereas GCR cores presented a broad and continuous distribution in the extent of surface fracturing and the degree of surface roughness. Six GCR cores with extensive fracturing and surface roughness were particularly conspicuous by their apparent mechanical instability. These cores appeared in two forms—either sugary textured or highly fractured. In both forms, the surfaces below the crusts were noticeably more friable when examined with a mechanical probe than were the other GCR cores with smoother surfaces. The sugary-textured stone was distinguished by large, uniform, unconsolidated grains throughout the matrix. SEM images of samples GCRD–1A and GCRC–1, the only two examples of sugary-textured stone identified in the data set, are shown in figures 9*A* and 9*B*, respectively.

Except in cores of the sugary-textured stone, we discovered no relation between near-surface and subsurface fracturing. Apart from these cores, the extent of subsurface fracturing consistently ranged from 0 to 4 percent. The main connection between the sugary-textured and highly fractured GCR cores is that cores representing both surface-soiling conditions invariably were retrieved from carved stone (see figs. 50–52 for locations). Carved stone is generally positioned on the building in locations directly exposed to weathering and is commonly in the path of water streaming from adjacent carved elements. Because we are observing this material in its uncleaned weathered state, we have no information on the state of the freshly carved virgin stone. However, we speculate that the virgin

stone may have been inordinately stressed during carving and, accordingly, was predisposed to extreme weathering.

We assume that salt deposits, which may be present at concentrations of less than ≈1 weight percent of the stone matrix, play no significant role in the degradation of the stone by mechanisms involving salt crystallization. Evidently, the Berkshire Lee marble on the building is not deteriorating in a manner that enables salts to penetrate and collect in significant concentrations.

As expected, various mineral inclusions were discovered within several hundred micrometers of the exposed surfaces in all of the cores. Such mineral inclusions are easily differentiated from salt deposits and from particulate matter by their distinctive chemical profiles and morphology. Bremsstrahlung X-radiation was used to qualitatively identify organic particulate matter. Significant observations relating to the distribution and penetration of salts include the following:

- No salts were detected on either uncleaned or cleaned LSS, LSR, and GCS surfaces.
- Gypsum generally was found to be irregularly distributed throughout the crust on the uncleaned surfaces of GCR cores. The gypsum did not appear to penetrate cracks and fissures of the surface to a depth more than a few micrometers.
- Only three of the eight cleaning techniques tested were successful in completely removing gypsum from GCR surfaces: combination, Armax, and JOS.

For future research, we suggest an investigation of the dissemination of salts into pores with more sensitive techniques, such as electron microprobe or secondary-ion mass spectroscopy. Although the results of such proposed work probably will not affect the conclusions of the current study, such information could significantly further our understanding of the fundamental mechanisms of salt transport into and out of porous stone.

Soiling

The procedures that we developed for measuring the surface reflectivity of core samples were based on the method of Reimann (1994). Surface reflectivity governs the general appearance of the stone as viewed from a distance of several meters or more. Two methods were used to estimate the surface reflectivity of the core surfaces: a quantity ß in gray-scale (gs) units, and a quantity complementary to the surface reflectivity. For both methods, ß was calibrated on a scale of 0 to 10 gs units, where 0 indicates the shade of a freshly fractured white marble surface and 10 indicates 100-percent soiling of the surface (for example, sample GCRV–4). In the first method, the automatic shutter on the optical-microscope camera provided a means for electronically measuring the surface reflectivity of core samples in a highly localized area (≈3.4 mm^2). In this method, the exposure time was used as a measure of the surface reflectivity of the core surface: The longer the shutter time required for a preset exposure, the darker the surface. We used the electronic reflectance measurements to explore the lateral distribution of soiling, on the microscale, across core surfaces. Not surprisingly, the lateral cluster density of particulate matter strongly correlates with the appearance of the surfaces, as shown in figure 7.

The second method was based on a systematic ordinal ranking of core surfaces by visual inspection. The reproducibility of this method, at ±0.2 gs units, was about 10 times better than that of the first method. Because this second method measures the average surface reflectivity of the entire core surface, we decided to rely on it for making ratio-data grayness assignments for evaluating the cleaning techniques. Details relating to the production of the optical photomicrographs and to the measurement of surface reflectivity are given in appendix 3. Grayness values for the various soiling-surface conditions and cleaning techniques are summarized in table 5 (see app. 3) for core series 3 through 6 (see app. 1), and are graphed in figure 10.

LSS and LSR Surfaces

Most LSS and LSR cores studied were distinguished by relatively light surface fracturing and well-consolidated grains. The surface reflectivity of LSS and LSR cores is due to superficially distributed particulate matter, as shown in figure 7. This interpretation was verified by SEM energy-dispersive X-ray analysis, which failed to detect any salts on or below the protected (uncleaned) surfaces of LSS or LSR cores. Because the surface reflectivity of these cores was about 2.0 and 4.0 gs units, respectively, the demands on the cleaning techniques are relatively low when applied to LSS- and LSR-condition stone. Although figure 10 shows that the gommage and combination techniques produce slightly cleaner surfaces than do the Armax and JOS techniques, the various cleaning techniques are nonetheless relatively undifferentiated when applied to LSS- and LSR-condition stone.

GCS and GCR Surfaces

The cleaning of GCS and GCR surfaces without concomitant damage to the stone is especially important because such surfaces are generally found on the carved stone that gives the building much of its esthetic appeal and historic character. Many GCS and GCR cores had well-consolidated grains near the surface and throughout the matrix. Five of the eight cleaning techniques successfully reduced the surface reflectivity of GCS cores to 2 gs units or less (fig. 10*C*: gommage, combination, Armax, JOS, and dry ice; the laser technique was not tested on GCR cores for surface reflectivity due to off-schedule completion of laser field work). The gommage and combination techniques produced slightly cleaner surfaces than those produced by the Armax, JOS, and dry-ice techniques, especially on GCR cores.

The blotches of black crusts that distinguish uncleaned GCS and GCR surfaces provide a suitable challenge for differentiation of the cleaning techniques. The gommage, combination, Armax, JOS, and laser techniques are superior in removing surface soiling that imparts a dark color to GCR-condition stone (fig. 10*D*). In this test, these five cleaning techniques produced a consistently uniform stone color. Although the laser technique removed most dark material, the resulting stone had splotches of bleached, yellow deposits that appeared to be fused into the surface. Also, similar to the dry-ice tech-

nique, the laser technique was less reproducible from point to point on the surface.

The dry-ice technique was virtually eliminated from contention by the test on GCR-condition stone. The test area was originally dark and somewhat yellow. The core provided for testing was sugary-textured and friable, and no protected control area was available against which to reference the results. We recommend that the dry-ice technique not be used without additional testing.

The gommage, combination, Armax, and JOS techniques produce cleaned stone with a surface reflectivity in the range 1.5–3 gray-scale units; the combination technique produced the cleanest surfaces of these four cleaning techniques. The photomicrographs shown in figure 7 are qualitatively consistent with the grayness values of cleaned GSR surfaces. They show that the Armax technique removes slightly more particulate material than does the JOS technique. With the possible exception of the gommage technique,[8] SEM images show that virtually all of the gypsum and particulate matter was removed from cracks and crevices in the stone by all four cleaning techniques. To further differentiate them, a quantitative definition of the reference level of cleanliness, C^*, and an established limit on the acceptable level of damage to the stone would be needed (see section below entitled "Synthesis and Interpretation of Results").

Surface Structure Before and After Cleaning

In this section, we focus on those properties of the stone which influence its susceptibility to processes which alter its structural integrity. Our operating assumption here is that the soiling load on the surface and the actual friability of the stone are related to the surface roughness and the near-surface fracture density. Possibly the most critical property controlling the microstructure of the stone is the degree and type of the contact among calcite, phlogopite, and dolomite grains in the matrix. As these grains are eroded, the stone develops a discernible sugary texture, and the near-surface fracture density increases. As a means of monitoring the influence of the various cleaning techniques on stone microstructure, we measured the near-surface and subsurface fracture density and the surface roughness before and after cleaning. These measurements were made by computer analysis of 100× SEM images of core cross sections; both binary-image files and photomicrographs were generated to document the profiles. Details of the surface-roughness and fracture-density tests are given in appendixes 6 and 7, respectively, and the software for SEM image analysis is outlined in appendix 2. The fracture density is reported as a volume percentage of the matrix occupied by fractures, crevices, and pore space. Although the measurement, which is limited by the operator's ability to duplicate the calibration of the SEM image, is reproducible to within about ±0.25 percent, natural variations in the near-surface and subsurface fracture density are generally about ±4 and ±0.4 percent, respectively.[9]

The mathematical tool (Mossotti and others, 2001) used to monitor surface roughness (see app. 7) takes into account the fractal properties of the surface morphology over the range of observation. The surface roughness is reported in terms of a shape factor, Γ, whose units, in μm^{D-2}, depend on the surface fractal dimension D. For the core samples tested in this study, the shape factor ranges from 0 to about 10, where 0 indicates a perfectly smooth plane and 10 corresponds to an irregular surface over the range 10–10^4 μm (0.0001–1 cm). The absolute reproducibility of the measured shape factor, as estimated by an analysis of replicate samples and of replicate views of a given surface-soiling condition, was calculated to be 0.41 cm^{D-2}.

Friability of the Stone Before Cleaning

Before we consider the effect of various cleaning techniques on the structure of the stone, we must understand the structural state of the various surface conditions before any cleaning. If the stone has substantially deteriorated, our ability to replicate the building's original appearance would be limited, and it would be unrealistic to establish specifications that are impossible to achieve.

In this analysis, we used the near-surface fracture density and the surface roughness to infer the friability of the stone on the microscale. In figure 11*A*, the near-surface fracture density is plotted against the shape factor for uncleaned stone (protected side of core below soiling) and for all surface-soiling conditions. As we might have expected, from the general distribution of data points, the fracture density and surface roughness appear to be directly related. Although all but one of the data points in figure 11*A* are widely scattered, the distribution of data points along the surface-roughness axis does not extend below a shape factor of 2.0. As discussed below in "Synthesis and Interpretation of Results," this observation provides a basis for establishing a target surface roughness against which we can evaluate the various cleaning techniques.

Under our operating assumption, the farther a data point falls from the origin in the plot, the more friable will be the stone. To facilitate a statistical analysis of these plots, we used the fracture density (FD) and the shape factor (Γ) to define a parameter that we call the friability index (FI), which is a measure of the distance from the origin to a given data point in the plot. To uniformly weigh the fracture density and the shape factor in the definition of the friability index, the shape factor is scaled, Γ_R, as a percentage of an arbitrary full-scale value of 10 cm^{D-2}; thus, Γ_R is unitless. The friability index is given by

$$FI = \sqrt{(FD)^2 + (\Gamma_R)^2}. \quad (1)$$

The mean FI values and standard deviations for each surface-soiling condition before and after cleaning are plotted in figure 11*C*. The friability index was found to be gamma-distributed for all of these plots. Among the uncleaned cores, the statistical patterns in figure 11*C* reveal two distinct data sets with a significant statistical disparity, one containing cores visually classified as smooth (LSS, GCS), and the other containing cores visually classified as rough (LSR, GCR).[10] In particular, most cores in the first data set exhibit FI values in the range 31–51 percent, with an average of 40 percent; the

cores in this data set show no discernible relation between the fracture density and the shape factor. In contrast, most cores in the second data set have FI values in the range 20–80 percent, with an average of 51 percent.

The data plotted in figure 11*C* provide information on the relevance of the friability index in the formation of the soiling pattern on the building. Because both lightly and heavily soiled surfaces share the same friability index, the local soiling must be independent of the local microstructure of the stone. The data plotted in figure 11*C* also indicate that the formation of the soiling pattern on the building must be dominated by variables other than fracture density or surface roughness. We speculate that the soiling pattern is predominately controlled by secondary mobilization processes acting over a wide range of scale. This model, which precludes a strong influence of microstructure of the substrate on the local surface chemistry of the stone, is modeled in figure 12. Note that the model does not preclude the possibility of a significant influence of the fracture density and the surface roughness on the primary deposition of SO_2 and particulate matter.

The data points in figures 11*A* and 11*B* are resolved in plots of fracture density versus shape factor for all four surface-soiling conditions before and after cleaning (fig. 13). As the stone becomes more heavily soiled in the series LSS→LSR→GCS→GCR, the relation between the fracture density and the shape factor becomes closer. The fraction of the variation in the fracture density that is associated with the variation in the shape factor is measured by the R^2 value (square of the correlation coefficient) indicated on each plot. In the LSS and LSR group shown in figures 13*A* through 13*D*, the distribution of data points is nearly random; in the GCS group shown in figures 13*E* and 13*F*, a very weak correlation is evident; and in the GCR group shown in figures 13*G* and 13*H*, a definitive correlation is apparent.

Surface Fracturing and Roughness After Cleaning

A plot of fracture density versus shape factor for cleaned cores is shown in figure 11*B*, similar to that for uncleaned cores in figure 11*A*. As in figure 11*A*, nearly all data points in figure 11*B* fall above a surface-roughness value of 2.0. Also similar to figure 11*A*, a conspicuous, though somewhat veiled, correlation between fracture density and the shape factor is evident in figure 11*B*; this correlation augments our understanding of the causality between the soiling load on the stone and the microstructure of the substrate. On resolution of figure 11*B* into component sets for each surface-soiling condition in figures 13*B*, 13*D*, 13*F*, and 13*H*, the correlation evident in figure 11*B* is blurred by the random distribution of data points. The relation between the fracture density and the surface roughness is shown in sharper relief in figures 13*F* and 13*H*.

The R^2 values of the plots for uncleaned and cleaned stone in figure 13 are summarized in figure 14, where the surface-soiling conditions can be partitioned into the LSS and LSR group, characterized by random plots, and the GCS and GCR group, which features a strong relation between the fracture density and the shape factor.[11] From this definitive partitioning, we conclude that the marked dependence of the friability index on the shape factor emerges as a result of applying the cleaning techniques to the heavily soiled stone. However, the fact that the correlation between the fracture density and the shape factor does not appear in the microstructure of either uncleaned or cleaned surfaces of LSS or LSR stone is strong evidence that the cleaning techniques do not generally cause such damage to the stone surfaces but simply expose the close relation between fracture density and the surface roughness (see section below entitled "Synthesis and Interpretation of Results"). The data in figure 14 also support the conclusion that GCS and GCR surfaces have been marginally damaged by surface alteration mechanisms concurrently affecting the fracture density and the surface roughness, and that such mechanisms are driven by the soiling load on the stone, as modeled in figure 15.

The ensemble mean friability indices and standard deviations for all of the cleaned cores are summarized in figure 11*B*. Although we could not statistically differentiate the various surface-soiling conditions on the basis of friability index after cleaning, we could sharply partition the cores into two groups on the basis of the statistical disparity between cleaning techniques. The cleaning techniques producing the lowest friability indices and, presumably, the most stable stone surfaces are gommage, combination, Armax, and JOS; with few exceptions, these techniques result in surfaces with FI values of 30±5 percent. In contrast, the cleaning techniques with the most erratic friability indices and the least stable stone surfaces are dry ice, laser, misting, and power wash; these techniques result in surfaces with FI values of 48±8 percent. The interpretation of these results is clarified by the surface-recession tests discussed in the next section, and is examined in detail in the section below entitled "Synthesis and Interpretation of Results."

How well do the above observations support our operating assumption relating the fracture density and the roughness to the actual friability of the stone? Under our operating assumption, we expect that surfaces with different friability indices would exhibit corresponding differences in mass loss when cleaned by a particular technique, provided the technique is sufficiently destructive to breach the threshold for disintegration of the stone. Even disregarding statistical considerations, we believe that the relation between the friability index and the actual friability of the stone is radically nonlinear, as well as dependent on the specific process acting to alter the stone. In the next section, we use surface-recession measurements (actually, an estimate of the friability of the stone during cleaning) to statistically analyze the relation between the friability index and the actual friability of the stone. Once we have demonstrated this relation, we use the friability index of cleaned surfaces to differentiate the various cleaning techniques.

Accelerated Weathering of Cleaned Surfaces

A critical factor in the design of strategies for the maintenance of stone buildings is an understanding of how the envi-

ronment at a given site affects the utility[12] of the building stone. Because the marginal effects of weathering on stone appear only after an extended period of time, researchers in preservation technology have been motivated to design techniques that allow such research to be conducted over a relatively brief period, and that accelerate our understanding of the effects of the environment on stone. In the approach most commonly used to accelerate the study of weathering effects, the test surface is exposed to controlled chemical and (or) physical stress by systematic manipulation of the chemical and (or) physical environmental variables. To expedite the appearance of weathering effects, one or more of these environmental variables are raised to levels far exceeding those that occur naturally. For example, the test surface might be subjected to extreme concentrations of SO_2 at an elevated temperature, with the intention of causing discernible chemical alteration in the shortest possible time. In contrast to this approach, the project team designed a program to study weathering effects without resorting to artificial manipulation of the environmental variables to their extreme limits. Instead, we developed techniques that closely replicate the effects of the actual ambient environment on the building stone. Accordingly, we designed our physicochemical measurement and data-analysis techniques to emphasize the differential sensitivity of cleaned surfaces to specific processes that are known to degrade the utility of the stone. Requisite to this strategy is the use of the most exacting, state-of-the-art analytical-chemical methodology. To the extent that the tests conducted by the project team produced results within a relatively brief period, these techniques also accelerated the study of weathering effects. We believe that this strategy provides a more effective evaluation of the impact of environmental conditions on the building stone than would previously published accelerated-weathering tests.

Stone deterioration is driven by complexly interacting physical and chemical mechanisms. The three most important chemical agents acting to diminish the utility of calcareous stone are water, SO_2 gas, and particulate matter. In both primary and secondary deposition, water weakens the stone and alters its morphology over a wide range of scale by dissolving dolomite grains. The rate of mass loss by dissolution in water is directly proportional to the fractal area exposed to flowing water, a complex quantity related to the microscale morphology of the stone surface. SO_2 gas can be an important factor in stone deterioration within an urban environment because of its alteration effect on calcareous stone. A complex set of mechanisms involving oxidation of SO_2, neutralization of H_2SO_4, and secondary deposition of gypsum into poorly washed areas of the building surface can set the stage for discoloration of the stone and for surface spallation. Similarly, particulate material degrades the stone over a wide range of scale by serving as a nutrient base for biological organisms (mold, lichen, moss) and through mechanisms involving the entrapment of fly ash in gypsum deposits.

Physical mechanisms generally dominate the transport of chemical reactants and reaction products. The physical aspects of primary and secondary deposition, mainly hydrodynamic-flow patterns, are governed by the macroscale properties of the building itself (morphology and orientation of the stone structures) and do not fall under the purview of accelerated-weathering testing. The deterioration processes controlled by the microscale physical properties of the stone that critically influence building-maintenance decisions include (1) the loss of structural integrity of the stone on the macroscale due to fractures in the stone, (2) the loss of surface mass on the microscale due to wind- and water-driven abrasion, and (3) the affinity of the surface for particulate matter. All three of these processes are governed to some degree by the near-surface fracture density and the surface roughness.

Our strategy for accelerating the study of weathering effects makes use of physical and chemical stressing of core samples to differentiate the relative stabilities of cleaned stone. Three tests were designed for this purpose; the results from two of these tests are included in this report. (1) The surface-recession test, described below, measures the mass loss from the surface due to the various cleaning techniques. The results from this test clarify the interpretation of the friability index and provide insight into the affinity of cleaned surfaces for primary deposition of particulate matter. (2) The controlled-atmosphere test (Bede, 2000, 2001), which permits close control over such experimental conditions as SO_2 concentration, windspeed, temperature, and relative humidity, measured the deposition velocity of SO_2 onto cleaned core surfaces. (3) The surface-reactivity test, also described below, which exploits the clean-rain effect to measure the fractal area of the stone over the nanoscale to microscale range, was used here to assess the susceptibility of the cleaned stone to dissolution by water.

Surface Recession and Friability of the Stone

The surface-recession test (actually, an indirect measurement of mass loss from the stone during cleaning) was designed to determine the mass loss associated with each cleaning technique, and to explore the relation between the friability index and the actual friability of the stone. By exploiting the destructiveness of the various cleaning techniques, this test provides information with which we can infer the friability of cleaned stone without having to subject the cleaned stone to any mechanical stress.

The mass loss from the surface during cleaning depends on at least four factors. We hypothesize that the first factor, the actual friability of stone, depends on the near-surface fracture density and the surface roughness. As mentioned in the preceding section, we believe that the relation between the friability index and the actual friability of the stone is radically nonlinear; this relation is determined by the surface-recession test. The second factor is the specific cleaning technique used. Although experience teaches us that the more destructive the cleaning technique, the greater will be the mass loss, we also suspect a power threshold below which the mass loss from the surface will be minimal. The third factor is the thickness and composition of the overlayer of soiling on the stone. A heavy soiling overlayer generally will require the extended

application of a given cleaning technique or the use of a more destructive cleaning technique on the stone. The fourth factor is the marginal friability of the cleaned stone. Once the soiling has been removed from the substrate, the cleaned surface is exposed to the treatment for a finite period, during which the mass loss from the surface may marginally increase.

Given the complexity of the issues relating to mass loss, how can we obtain useful weathering information with the surface-recession test? Because our purpose is to rank the cleaning techniques in terms of the expected friabilities of the cleaned stone, the issue of nonlinearity is inconsequential. Therefore, we simply need to establish the relation between the friability index and the actual friability of the stone. Then, we can use the FI values of cleaned surfaces to rank the various cleaning techniques.

The surface-recession test is based on a measurement of the change in microscale relief of the stone substrate during cleaning. These measurements were made by computer-assisted analysis of 10× SEM images of polished cross sections of core samples in which the lateral field of view included both the protected and cleaned area of the core. Two methods were used to measure the change in relief, one based on direct observation of the distance between the average elevation of the cleaned surface and the average elevation of the substrate on the protected side of the core, and the other based on the amount of surface smoothing resulting from the cleaning technique. Because the second method contains a systematic offset error, this method estimates only the minimal surface recession (fig. 16). The first method is fundamentally limited by natural irregularities in the stone surface over the lateral range of observation. The standard deviation of the natural morphology of the surface over 1 cm ranged from 35 to 150 μm, depending on the particular location on the building from which the core was taken. These measurements are discussed in more detail in appendix 5.

The observed surface-recession values for all of the cores for which such tests were possible are listed in table 8 (see app. 5). The most favorable values, with uncertainties of ±33 μm, apply when the measured surface recession was largely due to changes in morphologic relief from the protected side of the core to the cleaned side rather than from laterally uniform mass loss across the sample surface. The uncertainties in such values were estimated from the statistical reproducibility of the morphologic variations across the lateral range of observation.

Under our operating assumption, we expect that surfaces cleaned by a given technique would undergo a mass loss in direct relation to the magnitude of the friability index. A plot of surface recession versus friability index for uncleaned cores (fig. 17) generally validates this operating assumption by differentiating the cores that were visually classified as rough from those classified as smooth. For FI values greater than ≈35 percent and surface-recession values greater than ≈75 μm, a distinct correlation exists between the friability index and the measured surface recession: the R^2 value for the regression line through the points falling above (30,75) is 0.60. For FI values and surface-recession values excluding the point (30,75), the correlation, if any, is much less definitive. This result is understandable if we recall that the uncertainty in the measured surface recession ranges from 33 to 90 μm, an interval that virtually guarantees poor analytical precision for the points below an FI value of 30 percent and a surface-recession value of 75 μm. This interpretation is supported by an analysis of the residuals from the regression line which indicates that the conditional probability distributions of the measured surface recession for a given friability index do not have the same variance, and that the relation between friability index and surface recession is not significantly nonlinear over the range of observation. Although the cleaning techniques are not statistically differentiated by the surface-recession test, the results plotted in figure 17 validate the use of the friability index as an appropriate tool for ranking the various cleaning techniques on the basis of the inferred friability of the cleaned stone. The fact that the cleaning techniques are statistically differentiated by the friability indices of the uncleaned stone but not by the surface-recession tests, as shown in figure 11*C*, indicates that the mass loss due to cleaning depends more on the microstructure of the soiled stone than on the cleaning technique used.

The results plotted in figure 18*E* show that the dry-ice, misting, and laser techniques are less reproducible and result in potentially more friable surfaces than do the JOS, gommage, combination, and Armax techniques. Interestingly, this grouping is consistent with the statistical partitioning of cleaning techniques shown in figure 11*B* that was based on the friability index of uncleaned stone.

For future work, we recommend that all cleaning techniques be tested on the same soiling condition of ashlar so that they can be compared under similar limitations. Because of statistical problems related to undersampling, the relative contributions of the various factors contributing to surface recession could not be determined by multivariate analysis.

Surface Reactivity to Water

The surface-reactivity test was designed as a simple indirect method for measuring the reactivity of the stone over the nanoscale to microscale. Central to this test is a reduced-form model which finds that the rate of release of Ca^{2+} ions into flowing water is directly proportional to the effective reactive area of the stone. The surface-reactivity test, which is based on the clean-rain effect (Mossotti and others, 2001), measures the susceptibility of the cleaned stone to dissolution by flowing water.

Theoretical Summary

The dissolution of calcite is described by the reaction (Plummer and others, 1978)

$$CaCO_3 + H_2O \leftrightarrow Ca^{2+} + HCO_3^- + OH^- \quad (k_3=10^{-6.92}\ \text{cm/s}), \quad (2)$$

where k_3 is the rate constant for the reaction. In this formulation, we explicitly ignore the reverse reaction, $Ca^{2+}+CO_3^{2-}\rightarrow$

$CaCO_3$, and regard the test solution as undersaturated in Ca^{2+} with respect to calcite. Given the sensitivity of analytical methods for calcium, this condition is easy to satisfy. If the stone surface is Euclidean, the rate of mass loss due to reaction (2) (in millimoles per second), M_t, is given by

$$M_t = k_3 A, \tag{3}$$

where A (in square centimeters) represents the Euclidean area. If the stone surface exhibits fractal properties, the mass of Ca^{2+} lost over time t (in seconds), M_t (in millimoles), is given by an integral of the form

$$M_t = k_3 \int_0^t \int_{\text{surface}} k_H \, dH dt, \tag{4}$$

where dH represents the two-dimensional Hausdorf measure[13] of a cleaned stone surface of fractal dimension D and k_H, a constant equal to 1 cm^2–D, reconciles noninteger units of the Hausdorf measure. For the conditions under which the rate of stone dissolution is controlled by reaction 2, we define the surface reactivity, $\hat{A}$ (in square centimeters), by the surface integral embedded in equation 4 as follows:

$$\hat{A} = k_H \int_{\text{surface}} dH. \tag{5}$$

Thus, the mass loss of Ca^{2+} (in millimoles) is given by

$$M_t = k_3 \hat{A} t. \tag{6}$$

Equation 6, which encapsulates the central principle of the surface-reactivity test, shows that the total amount of Ca^{2+} lost depends only on the product of the surface reactivity and the time of wetness. This result is subject to two caveats: (1) the flow rate of water over the stone must be sufficiently fast to sweep the surface of reaction products that may accumulate and participate in the reverse reaction, and (2) steady-state conditions must be maintained at the molecular scale. Phenomenologically, the surface-reactivity test, which is outlined in detail in appendix 8, is designed to measure the area covered by H_2O molecules on the stone surface. The surface reactivity,[14] which is a property of the stone, is an intricate function of the stone morphology at the nanoscale.

In principle, the laboratory implementation of the surface-reactivity test is quite simple because the rate of release of Ca^{2+} ions is independent of the local hydrodynamics of the test solution once a critical threshold surface flow rate has been exceeded.[15] As modeled in figure 19, any apparatus that provides for continuous recycling of a fixed volume of water over a selected area of stone surface will meet the basic conditions required for the surface-reactivity test. Continuous recycling can be implemented with an infusion pump with a feedback loop or, possibly, by swirling the test solution over the sample surface in a beaker. After a measured period, the Ca^{2+} concentration in the test solution is determined, and the release rate is computed. Depending on the sensitivity of the analytical method of choice for Ca^{2+} determination, the test can be completed in less than 3 or as long as 45 minutes.

Results

The absolute rate of release of Ca^{2+} ions, sorted in descending order for all cores tested, is plotted in figure 20. The reproducibility of the surface-reactivity test on a given sample on a given day is generally better than ±1 percent; the reproducibility on the same sample from month to month is approximately ±7 percent. Because the variation in relative surface activity of different cores in a given series (for example, samples GCS–3, GCS–4) ranged from about ±8 to 11 percent, the natural variation in relative surface activity from point to point on the building appears to dominate sample-to-sample excursions in the test results. The absolute rate of release of Ca^{2+} ions versus shape factor for all cleaned (unprotected side) cores for all surface-soiling conditions (fig. 21) shows that at least 17 percent of the relative surface activity can be accounted for by the surface roughness of the stone on the microscale.

The average relative surface activities for each surface-soiling condition and each cleaning technique in core series 3 and 4 are plotted in figure 22. Without the use of a sulfate correction on the Ca^{2+} concentration in the test solution, the possible interference from gypsum in the surface-reactivity test precluded any measurement of the surface reactivity on uncleaned surfaces. This interference, however, was not a problem for any of the cleaned surfaces, for two reasons. First, all of the cores were extensively washed with deionized water before being tested. Second, gypsum was detected by X-ray analysis only on core series GCRM, which, interestingly, exhibited the lowest surface reactivity in the entire data set.

The relative surface activities plotted in figures 22*A* and 22*B* show similar patterns for the four cleaning techniques (power wash, gommage, JOS, dry ice) that were used on both LSS and LSR surfaces. For these surfaces, those cleaned by the gommage technique generally exhibit the highest rate of stone dissolution, whereas those cleaned by the JOS technique exhibit the lowest. Note that the relative surface activity of surfaces cleaned by the gommage technique is statistically the same as that expected from a Euclidean calcite surface. Similarly, the range in relative surface activity observed for GCR surfaces (fig. 22*A*) is consistent with those observed for LSS and LSR surfaces. On the basis of the natural variation in relative surface activity between samples, the probability of a chance occurrence of the patterns observed in figures 22*A* and 22*B* is vanishingly low. Thus, the relative surface activity is a surface property that is remarkably sensitive to the state of the stone.

The relative surface activities associated with GCS surface provide insight into the mechanisms of stone erosion by water. Most notable are the high relative surface activities for cores cleaned by the Armax and dry-ice techniques. Apparently, the surface-reactivity test is hypersensitive to small differences in the state variables associated with LSS, LSR, GCS, and GCR surfaces; conceivably, such differences may be amplified when the surfaces are cleaned by either the gommage, Armax, or dry-ice technique. Because the same

cleaning technique applied to various surface-soiling conditions gives drastically different relative surface activities, the surface reactivity appears to depend on a complex set of variables that are unique to the state of the surface over a highly localized area. The data plotted in figure 22*C* suggest that cleaned areas of the stone are statistically undersampled in the surface-reactivity test when a projected surface area of only ≈3 cm^2 is probed. Such erratic relative surface activities could account for the highly localized pockets of acute erosion that are commonly observed on carved stone.

The results for the gommage and combination cleaning techniques plotted in figure 22*C* are particularly puzzling. Because these two techniques are virtually identical once the cores have been subjected to the surface-reactivity test, we would expect to observe the same relative surface activities for both techniques. The measured difference in relative surface activities indicates that the misting applied immediately after gommage deactivates the surface before the cores cleaned by the gommage technique are taken for laboratory testing. In particular, such deactivation can occur by dissolution of mechanically stressed microstructures on the surface. Presumably, such deactivation would occur naturally when the stone is washed during the first rain event after the building has been cleaned. Thus, from figure 22, we infer that the absolute surface reactivity depends more on the petrologic structure and composition of the stone than on the cleaning technique used. The relation between a marginal change in the rate of release of Ca^{2+} ions and marginal increases in the level of stone cleanliness for all surface conditions is plotted in figure 23*A*; the surface reflectivity, given by 1–ß (grayness value, in gray-scale units), was used as a measure of the cleanliness of the stone. Plots for cleaned LSS, LSR, GCS, and GCR cores (figs. 22*B* through 23*E*, respectively) suggest that marginal application of the various cleaning techniques to surfaces carrying different soiling loads does not systematically change the surface reactivity.

Effect of Surface Reactivity to Water on Global Variables

In general, water erosion can alter the morphology of the stone over a wide range of scale. On the nanoscale to microscale, water can differentially alter the microstructure of the stone by preferential dissolution of the more reactive surface areas. On the building, for example, such hyperreactive stone might include dolomite crystals with a high surface free energy in areas of highly carved stone, or, possibly, the less consolidated calcite and phlogopite grains in the stone. Given enough time, the action of water erosion can alter the morphology of the stone in highly carved areas over an intermediate range of scale (millimeters to centimeters) and can even change the local orientation of the surface. A general model of the relation between water-driven physicochemical-alteration processes and the physical surface structure of the stone is shown in figure 24. As discussed earlier, the surface chemistry, with regard to the local soiling load, can also accelerate changes in the surface microstructure (see fig. 15).

Surface Sensitivity to SO_2 and Particulate Matter

It is well known that SO_2 can be an important factor in stone deterioration because of its alteration effect on calcareous stone. Equally damaging, primarily to the esthetic utility of a building in an urban environment, are such agents as airborne particulate matter. The first stage in the sequence of processes leading to SO_2-driven damage to the stone is gravity-independent primary deposition of SO_2 onto the stone surface. Similarly, the total load of particulate matter on the building surface is governed by the efficiency of primary deposition processes. The influence of surface microstructure on the efficiency of primary deposition processes is still under active investigation. The U.S. National Park Service and the University of Delaware conducted collaborative research on primary-deposition effects at the National Center for Preservation Technology and Training in Natchitoches, La. (Bede, 2001). The primary-deposition experiments included measurement of the deposition velocity of SO_2 onto model surfaces; materials studied in the controlled-atmosphere chamber included the Salem limestone, quarried in Bloomington, Indiana; the Cordova Cream limestone, quarried in Cedar Park, Texas; the Cottonwood Top Ledge limestone, quarried in Council Grove, Kansas; and the Monks Park limestone, quarried in Wiltshire, England. This collaborative research extends the earlier dry-deposition studies by Spiker and others (1992) and Wu and others (1990). The twofold purpose of this research was to increase our understanding of the role and importance of surface microstructure on (1) the deposition velocity of SO_2 under meteorologic conditions similar to those on Philadelphia City Hall, and (2) the deposition efficiency of particulate matter, as illustrated in figure 25.

Synthesis and Interpretation of Results

Stone Stability

A central issue in the evaluation of cleaning techniques is the long-term utility of the cleaned stone. Implicit in the operational concept of long-term utility are considerations of esthetic value and stone stability. In the parlance of the conservation community, the esthetic value is reflected by the "presentation appearance" of the stone; and in the idiom of mathematics, stone stability has meaning only when considered in terms of a set of specific degradation processes on a well-defined planning horizon.

The concept of stone stability is simple in principle but somewhat complex in practice. All deterioration processes manifest as changes in the physicochemical properties of the stone that affect its general utility. Changes in such properties, including color, structural integrity, and morphology, are driven by both physical and chemical mechanisms. During erosion, the state of the stone is slightly altered immediately on the first contact with soiling agents. The time required for the stone surface to change from its initial state to some reference state

depends on the states traced by the stone. Because deterioration processes are iterative, the traditional use of a statistical half-life to represent the stability of a section of a building is inappropriate. However, models of the relation between the variables defining the present state of a stone surface and its state at some point in the future are of only limited external validity and are generally restricted to application over a range of scale of 0.1 to 10 cm and within a relatively short period.

For the purposes of this study, we developed a semiquantitative framework within which we can infer the relative stone stability of test surfaces without explicitly specifying a planning horizon. Our intention in this analysis is to rank the expected stabilities of the cleaned surfaces produced by the various cleaning techniques. This framework rests on the assumption that the state trajectories followed by dissimilar surfaces may converge but may never cross if the surfaces weather within the same environment. Consider the following example. If the stone morphology on the microscale is regarded as a state variable, we assume that a given surface which is originally rougher than a reference surface will never spontaneously become smoother than the reference surface as long as both surfaces weather within the same environment. Under this assumption, it follows that if the stone stability depends on the surface state, then the ranking of a set of stone surfaces on the basis of stability will never change if the test surfaces weather under identical conditions. Our goal in this evaluation then reduces to that of identifying a suitable set of parameters from which we can rank the stabilities of stone surfaces. Central to this model are a set of assumptions about how each particular parameter relates to the stone stability.

Data-Synthesis Model

An important goal of the experimental work described in the preceding paragraphs, and a task prerequisite to defining the specifications against which the various cleaning techniques can be evaluated, was to (1) identify the variables that are affected by the cleaning techniques, and (2) evaluate the extent to which such variables influence the stability and utility of the stone. Toward this goal, we found it useful to consolidate the relation represented in figures 5 (primary deposition and secondary mobilization), 12 (soiling-pattern development), 15 (alteration by soiling load), 24 (alteration by water), and 25 (factors controlling primary deposition) into a composite model of the soiling-agent-delivery and stone-alteration processes, as illustrated in figure 26.

A critical factor controlling the operation of the overall system represented in figure 26 is the multiplicity of feedback loops. The importance of this feature to the operation of the system cannot be overestimated. If the feedback loops are negative, the state of the system tends to adapt to changes in the input variables and to maintain a stable output. If the feedback loops are positive, the state of the system tends to move toward a particular extreme limit imposed by a set of physical constants; an extreme example of such a limit would be mechanical failure of the stone. In figure 26, only the main feedback paths are shown.

Two additional properties of the overall system are not apparent in figure 26: (1) the system dynamics are iterative, and (2) the system has a long memory. In iterative systems with long-term memory, the inputs at any given time are influenced by the cumulative outputs over an extended period in the past. Such systems, which run continuously, are exceedingly sensitive to initial conditions and tend to be attracted to extreme limit states. The four surface-soiling conditions identified on the building in this study, LSS, LSR, GCS, and GCR, represent possible examples of such limit states.[16] From the perspective of figure 26, we now consider the variables that are affected by the cleaning techniques, and evaluate the extent to which such variables influence the utility and stability of the stone.

Soiling Load

The most obvious effect of the soiling load is on the esthetic utility of the stone (box E, fig. 26). Clearly, the variable over which the cleaning techniques have the greatest control is the grayness value of the stone.

In accordance with the model shown in figure 26, we believe that processes on the macroscale are regulated by the waterflow, which itself is controlled by the gross morphology and orientation of the stone. Thus, the model incorporates the expectation that secondary mobilization processes play a predominant role in determining the soiling pattern. Because the cleaning techniques being evaluated can affect the physicochemical properties of the stone only at the nanoscale and microscale, the influence of the cleaning techniques on the stone stability will be evident only in the total soiling load on the building surface. Although the soiling load has been shown to influence the microstructure of the stone, we did not consider the effect of residual soiling on the stone stability as a means to differentiate the cleaning techniques, because all the techniques will have to first pass the esthetic specification in order to be considered. To pass this specification, the cleaning technique will have to remove virtually all the soiling load from the surface. However, because this removal is a primary function of the building-cleaning program, the level of residual surface soiling will constitute a key element in the specifications for cleaning techniques.

Surface Microstructure

The three variables related to surface microstructure that are significantly influenced by the choice of cleaning techniques are the fracture density, the surface roughness, and the correlation coefficient reflecting the relation between the fracture density and the surface roughness. How significant are these variables with regard to the long-term stability of the stone, and should we use them to establish cleaning criteria for the various techniques?

Three links connect the stone morphology to the dominant processes in the model shown in figure 26, all three of which are significantly controlled by the microstructure of the

stone. The first influence of the stone microstructure on the stone stability is shown by the connection between panel B and box G in figure 26, which is part of a positive feedback loop with panels B, C, and D, and box G. If the fracture density or surface roughness increases, the number of active sites for dry deposition of SO_2 and particulate matter likewise increases. In addition, the ability of the surface to attract and retain moisture increases; the additional moisture on the surface accelerates the rate of dry deposition on the stone surface and enhances its affinity for airborne particulate matter. Thus, the greater the fracture density and the surface roughness, the more efficient will be the primary deposition processes that feed the mechanisms controlling the evolution of the soiling load. Over the long term, the increased soiling load drives irreversible damage to the stone substrate, as suggested by the connections between panels D and E and box G in figure 26. Such damage is commonly evident as an increase in the fracture density and the surface roughness.

The second influence of the stone microstructure on the stone stability is suggested by the connection between panel C and box G in figure 26. This connection acknowledges the effect of the stone microstructure on the waterflow pattern over the surface. Because water is the dominant environmental agent mobilizing salts and particulate matter in secondary deposition processes, the stone microstructure is clearly a critical determinant of the long-term stability of the stone.

The third influence of the stone microstructure on the stone stability is through its regulation of physicochemical alteration processes, as shown by the connection between panel D and box G in figure 26. The monomolecular dissolution of dolomite by water is one of many examples of physicochemical alteration processes that are surface controlled on the nanoscale and microscale. In view of the significant influence of the stone microstructure on the long-term stability of the stone, we used the microstructure-variables (fracture density, shape factor, R^2 value) to evaluate the cleaning techniques.

Surface Recession

Two aspects of the surface-recession test are of interest in this discussion, both relating to the significance of the mass loss to the state variables represented in box F in figure 26. The first aspect concerns the influence of a single episodic mass loss on secondary mobilization processes (panel C, fig. 26), and the second aspect pertains to the effect of a single episodic mass loss on the esthetic value of highly carved stone. From a strictly mechanistic viewpoint, the pattern of waterflow on the surface that drives secondary deposition processes is mainly governed by the morphologic relief and orientation of the surface on the macroscale. Because the worst-case surface recession is measured on the microscale, the effect of surface recession is relatively insignificant. From an esthetic point of view, it is inconceivable that the utility of the stone could be affected by a single episodic recession event measured in microns. Finally, because we can account for 60 percent of the variation in the measured surface recession greater than 75 μm by the friability index of the uncleaned surface (see subsection above entitled "Surface Recession and Friability of the Stone"), we believe that the observed surface recession primarily reflects the initial state of the surface rather than the various cleaning techniques or the initial state of soiling. Accordingly, we disregarded the surface recession as a factor for evaluating the cleaning techniques.

Surface Reactivity

Water is probably the most important environmental agent in the degradation of building stone. Water is included in box A in figure 26 as an environmental agent that is delivered to the building surface by primary deposition, and water constitutes the carrier agent in box C. In figure 22, the rate of stone dissolution by pure water is drastically affected by the choice of cleaning technique. Nonetheless, because our understanding of the absolute rate of release of Ca^{2+} ions is incomplete, we used the surface-reactivity test only as a supplementary factor for evaluating the cleaning techniques. Because figure 21 shows that the surface reactivity is linearly related to the surface roughness, we used the surface-reactivity test only in conjunction with the surface-roughness test for evaluating the cleaning techniques.

Cleaning Criteria and Selection of Cleaning Techniques

In the above discussion, we argued that measurements which reflect the soiling load and the surface microstructure could be used to evaluate the cleaning techniques. In this section, we consider how to define the reference (target) values for the measurements to be used for evaluation, and we develop a scoring technique for discovering which of the cleaning techniques come closest to concurrently matching more than a single reference value. This scoring technique, which assumes the format of the common dartboard, provides a basis for estimating the expected relative reproducibility of the various cleaning techniques.

Capacity, Accuracy, and Finesse

The capacity, accuracy, and finesse of a cleaning technique are all closely related concepts. The *capacity* of the technique measures its ability to alter a particular state variable; the difference between the final value and the initial value of the variable is a measure of the capacity. The *accuracy* of the technique measures its ability to produce the target value of a given state variable; the systematic deviation between the final value and the target value of the state variable is a measure of the accuracy.[17] Finally, the *finesse* of the technique measures its marginal effect on the variable of interest relative to the reference state. Depending on how the reference state is defined, the finesse can measure the ability of the technique to produce the desired result without causing collateral damage to the stone surface.

In figure 3, we defined a general measurement variable X that provides a signature of an underlying state variable. In figure 3, the initial surface is schematically represented by the variable $X°$, the final surface by the variable X, and the reference or target surface by the variable X^*. For the purposes of this study, we can uniquely specify the reference surface for any particular cleaning problem. For example, if we specify a target value of the variable, X^*, for the cleaned stone, we can compute a score for each of the cleaning techniques that gauges how closely the actual cleaned surface matches the reference surface. For a given variable X, we define the capacity and accuracy of the cleaning technique in terms of the difference variables ΔX and $\Delta X°$, respectively, where

$$\Delta X = X - X° \quad \text{(final – initial)} \tag{7}$$

and

$$\Delta X° = X - X^* \quad \text{(final – target).} \tag{8}$$

That is, the difference variable ΔX measures the ability of the technique to change the variable X, and the difference variable ΔX^* measures the ability of the technique to restore the variable X to its target value. If the final condition of the cleaned surface as measured by the variable X exactly matches the reference condition, then $\Delta X^*=0$. In such a situation, we would regard the particular cleaning technique as ideal as measured by the variable X.

We can further classify the cleaning techniques on the basis of the finesse of each technique. If a given technique undershoots the target value as measured by the variable X, we classify the technique as soft (S). If the cleaning technique overshoots the target value as measured by the variable X, we classify the technique as hard (H). Although the difference variables ΔX and ΔX^* are analog-ratio variables, we can downgrade them to nominal Boolean variables for the purpose of defining the attributes H and S as Boolean classifications. Thus

$$\begin{aligned} S &= \Delta X \, \overline{\Delta X^*} + \overline{\Delta X} \, \Delta X^* \\ &= \Delta X \, (+) \, \Delta X^*, \end{aligned} \tag{9}$$

and

$$\begin{aligned} H &= \overline{\Delta X} \, \overline{\Delta X^*} + \Delta X \, \Delta X^* \\ &= \overline{S}, \end{aligned} \tag{10}$$

where ΔX^* and ΔX are logically true if the measurement variables are equal to or greater than zero, and logically false if the measurement variables are less than zero. In equations 9 and 10, the symbols "+" and "(+)" denote the Boolean OR and exclusive-OR functions, respectively. Equations 9 and 10 are consistent with the definitions of the attributes H and S. To illustrate, because class H techniques overshoot the target value, both the capacity and the accuracy will have the same sign under any circumstances. In contrast, because class S techniques undershoot the target value, the signs of the capacity and accuracy will always be opposite.

The definitions provided by equations 9 and 10 enable us to exclusively categorize the cleaning techniques as either class S or class H. Incremental application of class S techniques drives the measurement variable toward the target value, X^*, regardless of the initial state of the stone. In contrast, incremental application of class H techniques drives the measurement variable away from the target value. Equations 9 and 10 show that the actual classification of a given cleaning technique depends on the variable selected to measure the state of the system, as well as on the definition of the reference, or target, state.

Criteria for Removal of Soiling Load

Although the reflectivity of the stone surface is generally controlled by microscale variables, a sidewalk view of the building may not necessarily reveal the presence of isolated pockets of particulate matter and salts, which may play an active role in deterioration of the stone. Therefore, we used three variables to score the cleaning efficacy of each technique, two on the microscale and one on the macroscale. On the microscale, we determined the amount and distribution of particulate matter over the surface, and we estimated the amount and composition of salts in the cracks and crevices before and after cleaning. On the macroscale, we measured the general surface reflectivity.

Removal of Salts

Energy-dispersive X-ray-fluorescence microanalysis was used to vertically explore the test cores for all common salts, including gypsum. The spatial resolution was less than ≈5 μm, and the chemical detection limit and sensitivity were ≈0.25 and 0.50 atomic percent, respectively. As implied in our earlier discussion in the subsection above entitled "Particulate Matter," our objective was to remove all adventitious salts from the building. The ability of the various cleaning techniques to remove salts from the building, along with the results of other tests applied to GCS- and GCR-condition stone, is summarized in the section below entitled "Conclusions and Preservation Strategy" (see fig. 35). In particular, only three of the eight techniques successfully reduced the gypsum concentration to a level below the detection limit of the analysis technique: combination, Armax, and JOS.

Removal of Soiling

The removal of soiling, which is largely in the form of particulate matter, from the building was the chief motivation for this work. If the stone does not appear to be clean on the basis of esthetic criteria, any question relating to the distribution and chemistry of salts and particulate matter is inconsequential. Our observations on the building show that the lateral cluster density of particulate matter on the microscale (see fig. 7) strongly correlates with the visual appearance of the stone on the macroscale. The cluster density of particulate matter and the surface reflectivity of the stone are integrated into a single filter for evaluating the ability of the various cleaning techniques to remove soiling from the building. This filter, which we call the esthetic utility, is discussed in the following paragraphs.

We will now consider the ability of the cleaning techniques to affect the appearance of the stone from a sidewalk point of view. We need to address three questions as we consider the cleanliness of the stone: (1) When is the stone sufficiently clean? (2) When is the stone overcleaned? and (3) When is the cleaning method sufficiently reproducible?

The answer to the first question depends on the scale at which we probe the surface. On the microscale, the issue could be fundamentally framed in terms of the number of dirt particles per unit area. Ultimately, however, the criteria have to be anchored in subjective considerations of how the stone appears on the macroscale—that is, the esthetic utility of the stone. An approximate esthetic-utility curve for the building is plotted in figure 27. The profile of this curve was determined subjectively by a visual evaluation of the cleaned stone against reference color standards in the building's setting. The most important feature of the curve is its shape. If the stone initially is heavily soiled but is not structurally deteriorated, marginal changes in the esthetic utility will be conspicuous when the stone is cleaned initially. As the cleanliness of the stone improves, it is reasonable to assume that incremental application of the cleaning technique will diminish the esthetic utility of the stone. On the basis of our subjective interpretations of the data in figures 7 and 10 and on our visual inspection of the stone in the field, we suggest that the maximally acceptable cleanliness of the cleaned stone should be 3.0 gray-scale (gs) units.

How, then, can we can we determine when the stone is overcleaned, and how can we discover the optimal target cleanliness? If we were to base our reply on figure 27 alone, we would conclude that the stone is never overcleaned because the slope of the esthetic-utility curve is positive everywhere. In principle, the stone is overcleaned when one or more of the critical state variables have been adjusted beyond the range of acceptable values corresponding to the optimal general utility. Because our goal is to restore the building's original appearance with a minimal impact on the underlying substrate, the general utility will be optimized when each of the state variables is corrected to a value that defines the slightly weathered stone appearing on the building shortly after its original construction. These reference values for the state variables, once established, will provide a basis for defining the cleaning criteria for the building. Before we can identify the range of acceptable values for the cleanliness of the stone, we need to consider issues related to the reproducibility of the cleaning techniques, as well as how the microstructure variables impact the shape of the general-utility curve.

By what criteria should we judge the reproducibility of the cleaning techniques? There are two issues of concern here, the first linked to the ability of the technique to replicate a preset level of cleanliness, and the second associated with the intrinsic application intensity of the method. The importance of the first issue depends on the shape of the esthetic-utility curve (fig. 27). Because of the diminishing marginal esthetic utility, the importance of the reproducibility of the cleaning techniques decreases as the minimally acceptable cleanliness is set at increasingly higher values. If surface grayness were our only consideration, the maximum target cleanliness would have to be set to allow for a standard deviation of at least 1.5σ in the grayness value associated with a given cleaning technique. For example, if our maximally acceptable cleanliness is 3.0 gs units, the target cleanliness would have to be set at 1.5–3.0σ to accommodate variations in the application of the technique. The reproducibility of a given cleaning technique would be inadequate if the variation in surface grayness of the cleaned stone exceeded the range of acceptability as determined by the shape of the esthetic-utility curve.

To determine the reproducibility of the cleaning techniques, we need to couple the criterion based on the esthetic-utility curve (fig. 27) with the criterion based on the intrinsic application intensity of each technique. We noticed that, for each cleaning technique, there is an intrinsic application intensity used by the operator to remove the soiling. We argue that each cleaning technique is most reproducible when it is applied without any constraints imposed on the operator. With the use of the finesse classification defined in equations 9 and 10, we can determine the intrinsic application intensity of the techniques in conjunction with the esthetic-utility criterion. Finesse-classification diagrams based on a target cleanliness (C^*) within the range 1.5–3.0 gs units for all surface-soiling and cleaning techniques are shown in figure 28. Our objective in using these diagrams is to discover the target cleanliness, within the range 0–3.0 gs units, that will maximize the number of cleaning techniques with an optimal reproducibility of C^*.

Two elements of information are contained in the finesse-classification diagrams (fig. 28). First, because the radius vector to any point in the diagram represents the accuracy of the cleaning technique, ΔC^*, the circles represent how far the techniques miss the target cleanliness; the central value, 0.2 gs units, is the reproducibility of the measurement. Second, the plotting algorithm for each finesse-classification diagram prescribes a grouping of cleaning techniques such that all points falling below the horizontal dashed line correspond to techniques which underclean the surface relative to the target cleanliness (soft methods), and all points falling above the horizontal dashed line correspond to techniques which overclean the surface relative to the target brightness (hard methods). These finesse-classification diagrams are best viewed in rapid sequence from figures 28*A* through 28*E*. Note the natural convergence of data points as C^* is systematically varied from 3.0 to 1.5 gs units. Clearly, all of the techniques overclean LSS, LSR, and GCS surfaces when C^*=3.0 gs units. Because most techniques come close to producing a grayness value in the range 1.5–2.0 gs units, we selected this range for the grayness criterion.

We can now determine which cleaning techniques produce the best scores on GCR surfaces relative to a range in target cleanliness of $1.5 \leq C \leq 3.0$ gs units. Finesse-classification diagrams based on a target cleanliness in the range 1.5–3.0 gs units for GCR-condition stone are shown in figure 29. For the selected grayness values C^*=1.5 gs units (fig. 29*C*) and C^*=2.0 (fig. 29*D*), the combination, Armax, and JOS techniques all produce excellent results.

Criteria for Alteration of Microstructure

The statistical disparity between cleaned and uncleaned LSR and GCR cores in figure 11*B* indicates that the surface

roughness is especially affected when the stone is cleaned. Moreover, figure 21 shows that the surface reactivity is closely related to the surface roughness. Therefore, the cleaning criteria should be based on a general-utility curve that simultaneously incorporates the effect of the cleaning techniques on the surface roughness and grayness value of the stone.

Surface Roughness

The selection of a target roughness, R^*, is based on the idea of an optimal surface roughness that would maximize the stability of the stone under ambient conditions of the building. Experience, as well as thermodynamics, tells us that a perfectly smooth stone surface will eventually become rougher from exposure to the elements. Likewise, an exceedingly jagged stone surface may well lose a certain amount of morphologic relief from exposure to wind and rain. This experience suggests that every type of stone will change to its most stable condition in a given environment and that the intrinsic surface roughness for each particular type of stone, in general, will be finite.

Figure 21 indicates that the smoother the stone surface, the stabler will be the stone with respect to erosion by pure water. In contrast, the regression (dashed) line plotted in figure 11*B* suggests that the intrinsic surface roughness in the environment of the building ranges from 1.75 to 2.0 (in shape-factor units). Finesse-classification diagrams based on target-surface-roughness (R^*) values over the range 1.6–3.5 shape-factor units for all surface-soiling conditions and cleaning techniques are shown in figure 30. Evidently, the surface roughness converges toward a target value R^* in the range $1.8 \le R^* \le 2.5$ shape-factor units.

In the preceding paragraphs, we established the reference ranges over which the surface grayness and surface roughness of the cleaned stone will optimize the reproducibility of most cleaning techniques on most surface-soiling conditions. However, we still have not determined the reproducibility criteria. To address this question, we need to know the shape of the utility curve that incorporates the effect of all critical variables on both the long-term stability and the esthetic utility of the stone. This general-utility curve has a more complex shape than the curve shown in figure 27.[18] By considering the problem within a general-utility framework, we can deal directly with the mutual dependence between state variables. For example, any adjustment in the degree of cleanliness of the stone will simultaneously affect other state variables, including the surface roughness. Because the general-utility curve captures the mutual dependence of the state variables, we simultaneously identify the reference cleanliness and the reference surface roughness by finding the optimal utility from the general-utility curve. Thus, the general-utility curve provides a means for us to specify both the acceptable range of surface grayness and the acceptable surface roughness, at least in principle. Once these criteria have been established jointly, we can then specify the acceptable reproducibility.

On the basis of our interpretation of figures 7, 10, and 28 through 30, we selected a range in target cleanliness of $1.5 \le C^* \le 2.0$ gs units and a range in target surface roughness of $1.8 \le R^* \le 2.5$ shape-factor units for the cleaned stone. The approximate shape of projections of the general-utility curve onto the utility/roughness plane for various grayness values based on the above ranges is shown in figure 31. The utility response to both cleanliness and surface roughness represented in figure 31 delimits the reproducibility of the cleaning techniques.

We can now use the joint criteria $1.5 \le C^* \le 2.0$ gs units and $1.8 \le R^* \le 2.5$ shape-factor units for cleanliness and surface roughness, respectively, to concurrently select the optimal cleaning techniques for GCR-condition stone. A finesse-classification diagram based on the grayness value and surface roughness of cleaned GCR-condition stone for the reference pair $C^*=1.5$ gs units and $R^*=2.5$ shape-factor units is shown in figure 32. The combination, Armax, and JOS cleaning techniques all simultaneously satisfy the joint criteria.

Friability Index

The correlation between the friability index of uncleaned surfaces and the surface recession (fig. 17) validates the use of the FI value as a surrogate variable for the friability of the cleaned stone. The target FI value is based on the definition of FI given in the subsection above entitled "Friability of the Stone Before Cleaning" and on the reference fracture density and surface roughness. Because it is reasonable to set the reference fracture density to zero, the range in target FI value (FI^*) follows directly as a rescaled range in target surface: $15 \le FI^* \le 25$. The summary of average FI values for cleaned GCR-condition stone plotted in figure 18*E* indicates that the JOS, gommage, combination, and Armax cleaning techniques not only are the most reproducible, as measured by the FI value, but also produce surfaces with FI values in the target range, as diagrammed in figure 35 below.

Statistical Link Between Fracture Density and Surface Roughness

In this section, we consider the extent to which the various cleaning techniques affect the apparent correlation between the fracture density and the shape factor. By way of review, plots of fracture density versus shape factor for both uncleaned and cleaned stone (figs. 11*A* and 11*B*, respectively) show that the cleaning techniques generally change the strength of the relation between the fracture density and the shape factor of the cleaned stone. The R^2 values for all surface conditions are summarized in figure 14. Our analysis is based on the implied assumption that for certain surfaces, notably those most heavily soiled, the fracture density and the shape factor are inherently associated. Figure 33 resolves figures 11*A* and 11*B* into component sets for each cleaning technique.

As a point of clarification, it would be unrealistic to expect a functional, much less linear, relation between the fracture density and the surface roughness. It is entirely reasonable, however, that the fracture density might statistically vary with the extent of surface roughness. Although we cannot predict the exact fracture density of an individual sample from the surface

roughness, we might expect to be able to estimate the average fracture density of all samples with the same shape factor in a given set. If the errors in the fracture density and the shape factor are small relative to the inherent variation among randomly selected samples, and if the variables are unrestricted, the sample correlation coefficient can be used to estimate the parent-population correlation coefficient (ρ, fig. 33), which we assume to be greater than zero.

In this analysis, we distinguish the cleaning techniques on the basis of their capacity to alter the apparent microstructure of the stone (see eqs. 11, 12). We adopt the parent-population correlation coefficient (ρ, fig. 33) as a measure of the relation between the fracture density and the shape factor. Accordingly, the capacity of the technique to alter the microstructure is measured by the difference variable $\Delta r = r - r^{\circ}$, and the accuracy of the technique to produce a target microstructure is measured by the difference variable $\Delta r^{*} = r - r^{*}$, where r° is the initial value, r is the final value, and r^{*} is the target value of the correlation coefficient.

Because we are interested in measuring changes in the strength of the relation between the fracture density and the shape factor on cleaning, we define $r^{*} \equiv r^{\circ}$. Therefore, $\Delta r \equiv \Delta r^{*}$, and so a high-capacity method will have a low accuracy with respect to changes in the microstructure of the stone. Under the convention that $r^{*} = r^{\circ}$, any cleaning technique that modifies the microstructure would be classified as hard because the marginal effect of the technique would cause the surface microstructure to diverge from its original state. Our interest is in the capacity of the technique, Δr. If the initial value of the correlation coefficient is positive, a positive capacity indicates that the technique tends to strengthen the relation between the fracture density and the shape factor, and a negative capacity indicates that the technique tends to eradicate the original microstructure. If the initial value of the correlation coefficient is negative, these relations are reversed.

The statistics given in figure 33 are summarized in figure 34. Interpretation of figures 33 and 34 depends on a strict application of the confidence intervals, which are expected to include the true fracture density for any shape factor 95 percent of the time.[19] For example, although the confidence intervals in figure 33*K* allow considerable latitude for the location of the negatively sloped least-squares regression line, the exclusion of zero from the confidence intervals of laser-cleaned cores for the parent-population correlation coefficient in figure 34 is convincing evidence that the slope of the least-squares regression line in figure 33*K* is truly negative. The capacity (horizontal bar, fig. 34) is greater than 1 because of the drastic change from a negative to a positive correlation coefficient after laser cleaning. The confidence interval for the parent-population correlation coefficient of laser-cleaned stone indicates that the true value of this correlation coefficient may be as low as –0.54, as high as 0.90, or anywhere in between these two limits. Because zero falls nearly in the center of this confidence interval, we conclude that the fracture density and the surface roughness are essentially unrelated for laser-cleaned stone. The uncertainty in the confidence interval for the parent-population correlation coefficient is reflected by the divergent confidence intervals toward the ends of the least-squares regression line in figure 33*L*. Furthermore, the R^2 value for this regression line indicates that only 25 percent of the variance in the fracture density is accounted for by the least-squares regression line. Therefore, the slightly positive slope of the least-squares regression line should not be overinterpreted. Because the sign of the initial value of the correlation coefficient is negative, the positive capacity suggests that laser cleaning eradicates the initial microstructure rather than exposing it by delicately removing the soiling. Thus, we classify the laser technique as hard (H).

Likewise, for the JOS cleaning technique, we observe that the R^2 value and the confidence interval for the parent-population correlation coefficient of soiled stone indicate that the measured variables are initially uncorrelated. However, after JOS cleaning, the confidence interval is sufficiently shifted in a positive direction so as to exclude zero, indicating a high probability of a strengthened relation between the fracture density and the surface roughness. Although the JOS technique does not appear to damage the stone surface, it does seem to remove soiling that obscures the intrinsic relation between the measured variables. Thus, we classify the JOS technique as soft (S).

We note that the power-wash and combination cleaning techniques show statistically similar patterns. Although both of these techniques show positive capacities of about the same magnitude, the confidence intervals for the parent-population correlation coefficients of both soiled and cleaned stone are broad and include zero. We find little evidence of a statistically significant relation between the measured variables on either soiled or cleaned stone for these two techniques. Although the finesse score for these two techniques indicates that they are soft (S), the sample population (degrees of freedom) in the measurement is insufficient to validate such a classification. Similarly, although the capacity of the dry-ice cleaning technique is nearly zero, the statistics of this technique are similar to those of the power-wash and combination techniques. Because all three cleaning techniques are statistically undetermined, we do not filter them specifically from consideration in the summary diagram in figure 35, where they are indicated by a question mark where appropriate.

In contrast to the five cleaning techniques already discussed, the Armax and the gommage techniques appear to virtually obliterate the microstructure of the soiled stone, as illustrated in figures 33*C*, 33*D*, 33*G*, and 33*H*. Thus, we classify the Armax and gommage techniques as hard (H).

From the results summarized in figure 34, we might argue that the preferred cleaning technique should remove the soiling without altering the microstructure of the stone. The problem with this approach is that the stone surface may be inconsistent from point to point and the operator would lose some control over the final condition of the stone. Alternatively, we might argue that the preferred cleaning technique should remove the microstructure below the soiling to a depth of perhaps 75 μm and impose a consistent, possibly more stable, microstructure over all the cleaned areas. We reason that any cleaning technique would be most reproducible when applied without any constraints imposed on the operator. In particular, if the operator either has to hold back in applying the technique or push it beyond its limitations to reach a given target grayness value, then the reproducibility of the technique

will be compromised. The summary diagram in figure 35 shows our selection of the gommage, Armax, and JOS techniques for the cleaning of lightly soiled, smooth and rough stone, and the gommage, combination, and Armax cleaning techniques for the cleaning of gypsum crusted, smooth and rough stone on the basis of this reasoning. We retained the combination method for final consideration because of its superior ability to remove salts and because it extends the gommage technique.

Conclusions and Preservation Strategy

In the preceding sections of this report, we established a set of criteria for judging the effectiveness of eight cleaning techniques on the marble façade of the building. The data we collected narrowed the options regarding appropriate cleaning techniques for the building. The architects and conservators overlaid the scientific analysis with additional filters or criteria to establish their final recommendations, delineated below.

Selection of Cleaning Techniques

Summary of Testing and Analysis

Our testing of eight different cleaning techniques on four surface conditions of soiling of the Berkshire Lee marble at Philadelphia City Hall was done onsite under varying field conditions by technicians skilled in applying the specific techniques. We assumed that each technique would be applied with some variation from area to area. A total of 160 cores, randomly selected from several possible 1-in.-round sites, represent a limited statistical sampling of the surface-soiling conditions of the stone.

Scientific Cleaning Criteria

Of the specific criteria identified during this study for differentiating the various cleaning techniques, several proved to be ineffective in our evaluation.

Cleaning Techniques Not Differentiated by Surface Recession

The surface-recession measurements (see app. 5) indicate that differences in mass loss from cleaning technique to cleaning technique and from surface-soiling condition to surface-soiling condition are virtually inconsequential over the long term. Some differences in surface recession between techniques were noted, but they were insignificant. With only a few exceptions, the surface recession produced by all the cleaning techniques tested was less than 175 μm, which is less than the maximum surface-recession criterion established by this study. In comparison with the rate of natural weathering, the minute measurable surface recession associated with any of the cleaning techniques, applied as a one-time event every quarter-century, including the familiar methods of power washing and misting, is irrelevant to the long-term stability or utility of the stone.

The Role of Soluble Salts in Marble Deterioration

Contrary to our original conjecture, we found no evidence that soluble salts play a significant role in the deterioration of Berkshire Lee marble. Although salts were evident in the cracks and fissures of GCR cores, they did not penetrate the surface to a depth of more than a few micrometers.

Surface Reactivity

The project team initially considered that cleaning may create a more reactive surface and therefore accelerate deterioration on the basis of preliminary, though statistically compromised, surface-reactivity measurements on phase I cores (see app. 8). The results of a larger statistical sampling of cores indicated that cleaning the stone does not marginally activate its surface for dissolution.

Selection Criteria: Cleanliness and Friability

The project team concluded that the cleaning standards which would satisfy the needs of the client and fulfill the goals of this study include a target grayness value, C^*, in the range $1.5 \leq C^* \leq 2.0$ gs units, a target surface roughness, R^*, in the range 1.8 R^* 2.5 shape-scale units, and a minimal level of surface fracturing, a criterion corresponding to a target friability index, FI^*, in the range 15 FI * 25 percent. The recommended cleaning techniques produce a presentation surface that closely approximates the original appearance of the historic stone, while also leaving a surface that is stable and minimally reactive to future cycles of weathering.

Cleaning Techniques That Satisfy the Selection Criteria

As shown in figure 35, four cleaning techniques did not meet all the selection criteria. Cores taken from future test sites where these techniques might be performed, with modifications, may yield more successful scores for these techniques. Four techniques emerge from this study as satisfactory to meet the goals of esthetic presentation and long-term utility: gommage and Armax, which are classified as hard (H); JOS, which is classified as soft (S); and combination, which has a statistically undetermined finesse factor. The "soft" classification designates a technique that cleaned the stone to the

target level but did not alter its characteristics as described by the friability index, and the "hard" classification designates a technique that cleaned the stone to the target level but imposed a new microstructure on the surface.

Alteration of Microstructure: Hard Versus Soft Cleaning Techniques

At this time, the project team cannot provide an argument that supports the selection of a hard over a soft technique on the basis of this classification alone. One remaining question is whether Berkshire Lee marble is more stable and less reactive to alteration by soiling and chemical processes if a hard or soft technique is used. It remains to be determined whether a stone substrate that retains the microcracking and surface-roughness patterns formed over many years is more stable than a freshly cut substrate obtained through application of a hard technique. The choice between soft and hard cannot be resolved practically because all the techniques are operator dependent. It is reasonable to assume that, over the cleaned area of an entire building, any technique may be marginally more destructive in some places than in others, owing to variations in its application. Unless a given cleaning technique is applied with nearly perfect reproducibility, a marble façade that is cleaned by even a single technique may represent a mixture of both hard and soft finishes.

Cleaning Criteria Established by Preservation Architects and Conservators

This study recommended four cleaning techniques that were noninvasive, as determined by reproducible laboratory measurements, of the stable marble substrate. However, these scientific criteria must be overlaid with practical considerations to produce an effective result. The foremost variables that need to be evaluated to ensure that a selected cleaning technique is in keeping with our preservation strategy for the building are as follows:

- The ease of applying the technique
- The skill required by operators to ensure a safe and effective result
- The capacity of the technique to provide a uniformly clean surface
- Environmental and health factors; for example, the effective, controlled, and safe disposal of the cleaning media
- The risk of damage from cleaning with large volumes of water, particularly on a building with numerous open joints
- The cost of the technique

Apparently, it will always be cheaper to clean a building with chemicals and water than by using gentle air abrasion. Although the gommage and JOS techniques are more expensive than traditional water-wash techniques, the results of this study emphasize that the Armax, JOS, gommage, and combination techniques significantly increase the utility of the building, ensuring the long-term preservation of this important marble edifice.

The following brief comments summarize the criteria that the client's agents, including future preservation architects and conservators, are encouraged to consider. The project team concluded that three of the four recommended cleaning techniques are equally satisfactory in meeting these criteria.

Gommage Technique

The gommage technique, tested in 1994, was chosen for cleaning of the building. The other three techniques were not tested until 1995, too late for the execution of construction documents for the building's restoration. The work was carried out satisfactorily by Thomann-Hanry, Inc.; operators were able to control the cleaning by using small nozzles and by minimizing the abrasive impact on the more fragile carved areas. The project team had two chief concerns about the gommage technique: (1) the difficulty of safe collection of spent cleaning media in a situation where a pressure cabin cannot be used, and (2) the skill required of operators in carrying out the technique. The quality assurance from future contractors who may compete with Thomann-Hanry may be difficult to validate until after injury to the stone has occurred.

Combination Technique

The combination technique—gommage followed by misting—was used on carved areas to remove grime and pollutants from crevices that could not be reached by the cleaning gun; this technique is the most thoroughly cleaning of all the techniques evaluated. Though more expensive initially, the combination technique provides the most complete preservation over the long term and is the most likely technique to remove potentially destructive salts from GCR-condition stone. The above comments about the gommage technique apply here as well.

Armax Technique

The advantage of the Armax technique is its relatively low cost. Quality is assured to the extent that the media manufacturer requires that the media and equipment be sold only to official agents who employ trained personnel. The project team had some concern that residual sodium bicarbonate would convert to sodium bisulfate and that subsurface crystallization would lead to spalling. Although no salt residues were found on the core samples of Berkshire Lee marble used in this study, no cores were taken at sites where a visible accumulation of residual sodium bicarbonate became apparent after the stone dried. Protection of deep cracks and crevices, good control of overspray from powerful delivery of the cleaning media, and adequate rinsing of cleaned and oversprayed areas are critical; proper attention to these details may affect cost. We do not recommend the Armax technique for the building at this time because of the observed inability of operators to control overspray and runoff and to remove residual cleaning media from the masonry surfaces.

JOS Technique

The JOS technique is carried out exclusively by trained operators; however, it is potentially more applicable than the gommage technique because it can be used by all contractors who purchase the required equipment and media and who are trained and certified by the equipment manufacturer. In this study, the JOS technique seemed to allow more control in delivery of the cleaning media. The presence of a small volume of water in the delivery system resulted in cleaner air in the work area than was observed in applying a dry technique. The slurry runoff could be controlled for collection.

Recommendations

For future cleaning of the building, the project team recommends the gommage, combination, and JOS techniques. Both the JOS and combination techniques use an extremely small volume of water. As a result, they do not introduce the problems associated with traditional water-wash methods such as (1) infiltration of water into the building through holes, fissures, and open joints in the stone; (2) slow drying of the stone and associated potential promotion of salt efflorescence and staining, including iron staining; and (3) control of a large volume of water runoff. To ensure that all salts are removed, the project team recommends that:

- the gommage or JOS technique be used on ashlar surfaces,
- the combination technique be used on highly carved surfaces at the entablatures, cornices, and column capitals, and
- the combination technique, with especially delicate application, be used on fragile GCR-surface stone.

The recommended cleaning techniques for the building are in keeping with a current trend in the United States toward masonry-cleaning treatments that are more environmentally friendly and have minimal disposal issues. Our study is a major contribution to the importance of this trend in that it provides scientific data which demonstrate that the risk for stone damage by some of these newer techniques is equal to or, in many places, less than that of traditional water-wash methods.

Specification and Monitoring of Cleaning Techniques

The specifications for selection of a cleaning technique should be written so that only qualified bidders with experienced operators undertake the cleaning of the building. A safe and effective cleaning technique can be monitored in the field by a trained preservation architect or conservator. Judgments can easily be made by visual comparison of the color and texture of the cleaned stone against a set of reference standards.

Impact of Cleaning Techniques on the Long-Term Condition of the Stone

One of the important findings of this study is that most of the cleaning techniques evaluated did not significantly affect the long-term condition of the stone in regard to its projected utility. The study identified variables and processes that affect all buildings constructed of calcareous stone. According to figure 26, the processes controlling the primary deposition of soiling agents, the secondary mobilization of transportable materials, and the permanent alteration of the stone are all mutually dependent. Although the long-term condition of the stone is governed by the collective action of these interdependent processes, the distribution of soiling agents over the building is chiefly controlled by the action of water on the stone surface. Accordingly, the soiling pattern on the building is mainly controlled by the large-scale morphology and orientation of the stone; these macroscopic variables are not affected by the choice of cleaning technique. Moreover, the total soiling load is largely influenced by environmental variables (airborne moisture, local aerodynamics, concentrations of such pollutants as SO_2 and airborne particulate matter, and so on) and by certain microscale variables (for example, the chemical composition of the stone) that also are unaffected by cleaning. To a lesser degree, certain microscale variables that are affected by cleaning (for example, surface roughness) may influence the total soiling load on the building. Thus, after the stone is cleaned, both the pattern and amount of soiling appearing on the building over a period of decades should be independent of cleaning technique because the variables controlling these phenomena were found to be unaffected by any of the cleaning techniques evaluated. This conclusion has yet to be experimentally tested.

Significance of This Study as a Model

This study appears to be unique in its design of controlled field tests for eight cleaning techniques, especially with respect to the use of scientific analysis for formulating a conservation strategy for a particular type of stone on a particular building. Accordingly, the study can be used as a model for other buildings constructed of Berkshire Lee marble or of marble with a similar petrology located in a temperate urban environment. Although the study was stone specific, our questions about the characteristics of surface alteration due to a given cleaning technique are universally applicable. The study should also serve as a starting point for preservation architects and conservators in collecting data about other building stones.

Significance of This Study to Preservation Strategies

The construction of Philadelphia City Hall spanned more than 30 years (1870–1901), a period of vast technologi-

cal change. It is somehow fitting that the decade in which the building is being restored is witnessing technological advances that increase our understanding of the application of cleaning techniques and that will ensure the long-term preservation of this historic edifice. As the masonry-cleaning program progresses around the perimeter and courtyard façades, other cleaning techniques may be developed that prove safer to the environment. These new techniques will have to ensure the long-term preservation of the stone as did the earlier-selected techniques. As these techniques are developed and become economically feasible, the city of Philadelphia will need sophisticated methods to evaluate their effectiveness. This study has established baseline data that will enable preservation architects and conservators to evaluate new cleaning techniques in the future.

Ideally, cleaning techniques should be evaluated during the design phase of any masonry-cleaning project. Such evaluation is critical to understand the construction of a building and the condition of its stone, and to formulate an appropriate and effective preservation strategy for the building. The completion of this study underscores the importance of scientific testing in formulating such a strategy for any building.

Acknowledgments

This research was supported by the U.S. National Park Service (NPS)'s National Center for Preservation Technology and Training, the Philadelphia Historical Commission, and the city of Philadelphia; development of the SEM image-analysis software (MORPH–I and MORPH–II) was specifically supported by the NPS. Susan Sherwood assisted in organizing the multidisciplinary project team of preservation architects, conservators, and scientists. We also thank Chandra Reedy, ElizaBeth Bede, Susan I. Sherwood, and Richard Tosdal for their reviews of the manuscript.

References Cited

Bede, E.A., 2000, Characterization of surface morphology of carbonate stone and its effect on surface uptake of SO_2 in International Conference on the Deterioration and Conservation of Stone, 9th, Venice, Italy, 2000 [Proceedings], v. 1, p. 303–311.

Bede, E.A., 2001, The surface morphology of limestone and its effect on SO2 deposition: Newark, University of Delaware, Ph.D. thesis, 298 p.

Mossotti, V.G. and Eldeeb, A.R., 2000, MORPH–II, a software package for the analysis of scanning-electron-micrograph images for the assessment of the fractal dimension of exposed stone surfaces: U.S. Geological Survey Open-File Report 00–013 (URL http://geopubs.wr.usgs.gov/open-file/of00-013).

Mossotti, V.G., Eldeeb, A.R., and Oscarson, Robert, 1998, MORPH–I (Ver. 1.0), a software package for the analysis of scanning electron micrograph (binary formatted) images for the assessment of the fractal dimension of enclosed pore surfaces: U.S. Geological Survey Open-File Report 98–248 (URL http://geopubs.wr.usgs.gov/open-file/of98-248)

Mossotti, V.G., Eldeeb, A.R., Reddy, M.M., Fries, T.L., Coombs, Mary Jane, Schmiermund, R.L., and Sherwood, S.I., 2001, Statistical compilation of NAPAP chemical erosion observations on limestone and marble: U.S. Geological Survey Open-File Report 98–755 (URL http://geopubs.wr.usgs.gov/open-file/of98-755).

Murray, J.D., and vanRyper, William, 1996, Encyclopedia of graphics file formats (2d ed.): Sebastopol, Calif., O'Reilly & Associates, 1,154 p.

Naudé, V.N., 1994, Report on stone cleaning tests March–April 1994—to support a masonry preservation strategy for the restoration of the east center pavilion of the Philadelphia City Hall, sec. 8 *in* app. 1 *of* Proposal for masonry testing; development of cleaning treatments and preservation strategies: Philadelphia, Vitetta Group, p. 8.1–8.20.

Peitgen, H.O., Jürgens, Hartmut, and Saupe, Dietmar, 1992, Chaos and fractals—new frontiers of science: New York, Springer-Verlag, 953 p.

Plummer, L.N., Wigley, T.M.L., and Parkhurst, D.L., 1978, The kinetics of calcite dissolution in CO_2-water systems at 5 to 60°C and 0.0 to 1.0 atm CO_2: American Journal of Science, v. 278, p. 179–216.

Reimann, K.J., 1994, Chemical alteration of limestone and marble samples exposed to acid rain and weathering in the eastern United States: Argonne National Laboratory Report ANL–89/34, 104 p.

Spiker, F.C., Comer, V.J., Hosker, R.P., and Sherwood, S.I., 1992, Dry deposition of SO_2 on limestone and marble—role of humidity in International Conference on Deterioration and Conservation of Stone, 7th, Lisbon, 1992 [Proceedings], p. 397–406.

Vitetta Group, 1994, Proposal for masonry testing; development of cleaning treatments and preservation strategies: Philadelphia, Vitetta Group [variously paged].

Wu, V.L., Davidson, C.I., Dolske, D.A., and Sherwood, S.I, 1990, Dry deposition of atmospheric contaminants at Gettysburg, Penn.: Air and Waste Management Association Annual Meeting, 83d, Pittsburgh, Preprints, paper 90–110.5.

Appendix 1. Cleaning Techniques and Core Inventory

Surface-Soiling Conditions

The richly articulated sculptural program of Philadelphia City Hall provides a wide variety of surface-soiling conditions to sample. However, visual inspection of the façade both from street level and at close range suggests that most of the stone surface may be characterized as being in one of four conditions: (1) lightly soiled, smooth (LSS); (2) lightly soiled, rough (LSR); (3) gypsum crusted, smooth (GCS); and (4) gypsum crusted, rough (GCR). About 2 percent of the sur-

face is severely deteriorated, sugary stone, found in sculptural projections with maximum exposure and on stone located in the path of rain runoff. These areas were not considered typical of the masonry that requires cleaning.

Lightly Soiled, Smooth

LSS areas, which are largely ashlar, constitute about 8 percent of the surface. Such areas are generally protected from extreme weather by cornices and columns, but become wet during periods of rain. A few pits or ridges are visible. The color of LSS areas is various shades of gray.

Lightly Soiled, Rough

LSR areas, which are commonly found on both ashlar and sculptural stone, constitute about 85 percent of the surface. Such areas generally are directly exposed to weather. LSR areas are visibly pitted and commonly exhibit surface ridges that subtly reflect the rain-runoff flow pattern. Where cracks or natural fissures are present, excessive erosion is apparent. The color of LSR areas is various shades of dark gray.

Gypsum Crusted, Smooth

GCS areas, which have a smooth black surface that cannot be brushed away, constitute about 4 percent of the surface. Such areas were found in places protected from rain runoff by projecting architectural elements and in pockets of carving on exposed sculptural ornament.

Gypsum Crusted, Rough

GCR areas constitute about 1 percent of the surface. Such areas generally are identified on carved stone—that is, areas that are critical in providing the building with its esthetic value. Thick black crusts, with a granular texture, characterize GCR areas protected from rain runoff.

Choice and Description of Cleaning Techniques

Cleaning Techniques Selected for the First Phase of This Study

The selection of water-based cleaning techniques for the first phase of the study was based on tests carried out in March 1994 as a part of research for the building restoration project. Power wash without detergent, power wash with various chemical cleaning agents, and steam cleaning with and without detergent were all tested on the building's façade. The power-wash and misting techniques were judged to be the most effective without deleterious effects on the stone. Technical details of the four cleaning techniques selected in the first phase of this study are summarized in table 1. The Vitetta Group (1994) reported on these tests and presented a rationale and design for further testing with scientific support that led to the 1995 masonry-cleaning program which is the subject of the present report.

Power Wash

Tests were conducted using a Simpson Powerwasher operating at 3 gal per minute and capable of delivering 1,500 lb/in^2 measured at the unit. Operations were carried out with a 12-in. hose using a 25° tip and a working distance of 10 to 12 in. from the surface of the stone. We calculated a cleaning force of about 900 to 1,000 lb/in^2. A proprietary detergent was selected: ProSoCo 1026 Liquid Marble Cleaner, a high-alkali cleaning compound in gel form, widely used in the industry. Brushed on wet stone directly from the container, the blue gel was allowed to sit for 10 to 15 minutes, after which it was rinsed with the Powerwasher. Repeated applications of the detergent did not appear to significantly change the color of the cleaned stone. Areas sampled for this study were all at sites that had been cleaned with only one treatment.

Misting

The stone was washed for 8 hours on each of two consecutive days with a water mist, which served to keep the surface wet but had no other impact. The spray was delivered from small nozzles (Spraying Systems nozzles LN 1.5) mounted on a plastic (polyvinyl chloride) pipe with flexible adapters leading to the nozzle tips. The system was designed to position nozzles at 10-in. intervals 10 in. from the wall, but the direction of the nozzles was adjusted onsite to best clean sculptural detail. The direction of the nozzles was readjusted, and loosened grime was brushed away with a bristle brush twice each day or about every 2 to 3 hours.

Gommage

The Thomann-Hanry, or gommage, dry cleaning technique uses what is essentially a low-pressure, small-particle air abrasive system familiar to museum conservators that was developed by a French company for large-scale use. Delivered at pressures of 35 to 50 lb/in^2, the particles range in size from 15 to 90 μm. Published information states that the mix contains SiO_2 (49.65 weight percent), Al_2O_3 (27.64 weight percent), Fe_2O_3 (8.49 weight percent), K_2O (4.11 weight percent), CaO (3.64 weight percent), and MgO (2.41 weight percent).

The operator held the nozzles at eye level, perpendicular to and about 10 in. from the surface. Test sampling was conducted to determine the number of passes needed to slowly diminish the soiling layer. During testing, it was noted that two passes produced a good cleaning and a third pass made the stone whiter; the level of cleaning could be

monitored visually. The nozzle and media mix are proprietary, as is the light-weight vacuum cabin that can be installed against a building on a boom truck or suspended from outriggers. Airborne particles were captured in a vacuum unit, moistened with a water spray, and flushed through a hose to a ground-level containment system. The nontoxic powders are safe for normal landfill disposal. The benefits of the vacuum cabin, a device requiring a fairly flat façade, are unavailable for buildings like Philadelphia City Hall. Work was accomplished from scaffolding, and vacuums were used to clear waste.

Cleaning Techniques Selected for the Second Phase of This Study

Combination

The combination cleaning technique was specified for testing during phase 2 because the project team was concerned that a dry cleaning technique, such as gommage, would fail to remove water-soluble salts from the marble.

Armax

The blast medium for the popular, inexpensive Armax cleaning technique is sodium bicarbonate. This technique was developed by the Church and Dwight Co., which sells Arm and Hammer products. The medium is delivered by proprietary equipment that is sold to local companies whose employees receive training and are then authorized to use the system. The equipment they proposed for the January 18, 1995, demonstration at Philadelphia City Hall was the Accustrip System model 12X, blast nozzle Hypro No. 6. The particle size was 180 μm, provided as Armax Blast Media Maintenance Formula with SupraKleen Rinse Accelerator.

The stone surface was prewetted and then cleaned with a stream of medium and water mixed for delivery at 40- to 50-lb/in^2 pressure at a standoff distance of 12 in. The blast angle was 60°, at a water flow rate of 2 gal per minute.

JOS

Named for the developer of the technique by a German materials-cleaning company, the JOS cleaning technique operates by delivering pressurized air, water, and particles from the same nozzle. This nozzle is designed so that the cleaning media travel forward in a vortex and provide a circular scrubbing action on the stone surface. For demonstration on our samples, JOS Quintek Corp. used the largest nozzle they had at the time with No. 2 dolomite grade, particles 60 to 600 μm in size, with 75 percent of the particles in the size range 70 to 270 μm. They worked at 28 lb/in^2 pressure approximately 12 in. from the surface. The waterflow rate can be adjusted within the range 1.5 to 12 gal per hour. Waste, in the form of a wet slurry on the ground, can be channeled for runoff. Operators are trained to work with three nozzles and with several grades of cleaning granules. During tests at the building, the smallest (piccolo) nozzle was used with the same No. 2 medium to clean the more intricate parts of carvings.

Laser

Tests of the laser cleaning technique were made on the building by Atlas Laser Systems, Inc., of Sainte-Foy, Quebec, Canada. Their technique uses an intense beam of light in the near-infrared or deep-ultraviolet range to clean the stone. As the energy of the photon stream is absorbed by the target surface, bonds are broken between the substrate and surface soiling. The equipment provided was an infrared Q-switched Nd-YAG-type laser developed by the Quantel Group of France.

A 23-Hz portable (25 lb) machine, 2 by 2 by 1 ft in dimensions, was brought to the 6th-floor level of City Hall and lifted out the window onto the wide ledge outside Room 622, where it was plugged into a 110-V outlet just inside the window. Outside, light was carried to the test areas by a 25-ft fiber-optic cable so that cleaning could be carried not only on ashlar near the machine but also on column capitals that the specialist conservator reached by ladder. The machine provided energy of 230 mJ per pulse and ran at a rate of 25 pulses per second, with a pulse duration of 20 ns; the wavelength was 1.064 μm. During the test, approximately 1 in^2 was cleaned in half a minute.

Precautions were taken that the light beam was shielded, at all times, by dense black cloth because it can damage the eye. Operators and people near the light source wore goggles. Observers who could not see the cleaning process directly followed its sound.

The rapid ejection of material from the surface causes a shock pulse audible as a snapping sound. When the light does not find any more dark material to vaporize, it causes no cleaning action, and the shock pulses cease. Residues, in the form of a dust spray, are typically removed by a vacuum unit at the work area.

Dry Ice

The dry-ice cleaning technique uses equipment that converts liquid CO_2 into dense dry-ice pellets that are air driven to the cleaning surface; the impact removes superficial contaminants, which form a powdery residue. The cleaning medium reverts to CO_2 gas, and waste is removed by a vacuum unit. The project team investigated this technique because of its obvious health and environmental advantages and future potential. Onsite tests were not requested because of high costs to the vendor; the dry-ice technique was not expected to be selected in 1995.

Stone fragments found loose on the building's façade were prepared in the same way as the test areas and sent to

Marlimar Enterprises, Inc., near Buffalo, N.Y., which was concurrently working on tests to clean limestone, granite, and bronze with the graduate program in art conservation at the State University of New York, Buffalo. We were told that the samples were cleaned with pellets driven at 30-lb/in^2 pressure at a velocity of 60 to 80 mi per hour. We noted that the areas appeared especially clean, possibly even more than we would have requested. The process can be controlled to vary the size and density of pellets, rate of delivery, air pressure, velocity, standoff distance, and dwell time.

Operational features of four of the eight cleaning techniques evaluated in this study, as well as chemical techniques studied in 1994 (Naudé, 1994), are summarized in table 2.

Coring Methods

Site Selection and Equipment

The areas on the building from which cores were selected were those that were considered typical of a particular surface-soiling condition and that presented the most continuous surface without pitting, cracking, stains, or inclusions. Closeups of the areas that were cored are shown in figures 36 through 63. The actual sites selected for coring were marked in pencil on the stone and located on a diagram where they were numbered according to the inventory system described in the next section.[20]

A series of 1-in.-outside-diameter cores were taken with a RemGrit tungsten carbide hole saw; cores were drilled 1 in. deep. As each core was taken, it was bagged along with a numbered label; the outside of the bag was also numbered. Later, in the conservation studio, the cores were inspected one at a time, and a number was written on the side of the core in pencil before it was returned to its bag for shipment to the USGS.

Use of Epoxy to Preserve Surface Soiling

Thick epoxy resin that would protect the surface from cleaning procedures was placed on the uncleaned stone in strips approximately ¾ in. wide by 3 in. long. After cleaning, ¾-in.-inside-diameter core samples were taken with a presentation surface 50 percent cleaned and 50 percent protected by epoxy resin. The strips of epoxy resin were laid on the uncleaned stone over an area larger than required to provide several choices for the core locations. Devcon 5-minute epoxy resin was chosen because of its ready availability, ease of working with in the field, and rapid curing time.

A second type of protectant, an acrylic resin from Ernest F. Fullam, Inc., was chosen to seal the cleaned surface so as to prevent alteration during coring. This low-viscosity resin was applied adjacent to the Devcon epoxy strip in the areas that appeared to provide the least pitted study surface. The curing time for this resin is about half an hour in moderate weather conditions. During much of the fieldwork in January and February 1995, the resin was heated and cured in about 1 hour. The acrylic resin is designated L.R. white, medium grade, catalog No. 51002, with catalyst and L.R. white accelerator, catalog No. 51000.

Core Inventory

Seven series of cores were taken for each surface-soiling condition, and numbered 1 through 7. Core series 1 and 2 were prepared with the two types of epoxy resin, as described above; these cores were used to prepare cross sections, as described in appendix 2. Core series 3 and 4 were taken for accelerated-weathering tests; no epoxy resins were applied to the surfaces of these samples. Core series 5 and 6 were taken for deposition-velocity tests; likewise, no epoxy resins were applied to the surfaces of these samples. Core series 7 was taken for archival purposes and as backup for the laboratory tests.

A complete inventory of all cores taken from the building is listed in table 3. Note that certain cores are missing from this inventory because, during the course of the project, considerations for the cost of replacing the cores with dutchmen led to the intentional omission of certain cores from the set that was originally planned. Thus, core series 1 and 2 are complete, but the cores in series 3 through 6 were not always replicated. Several additional cores indicated in the inventory were taken after onsite modification of the cleaning techniques upon request of the USGS.

At the end of the project, marble dutchmen prepared from a similar (but not Berkshire Lee) marble were used to replace the core samples removed from the building. The dutchmen were set slightly proud, using Hilti C–100 epoxy resin tinted off-white with titanium white dry pigment. The surfaces of the dutchmen were dressed with chisels to resemble the texture of the adjacent stone.

Appendix 2. Sample Preparation, Image Indexing, and SEM-Image Analysis

Core samples from series 1 and 2 (see app. 1) were selected for SEM-image analysis of their physical and chemical properties. This appendix provides detailed information on SEM-image indexing and collection, computer analysis, and procedural details related to the preparation of samples for SEM-image analysis.

Sample Preparation

The core samples from series 1 and 2 were prepared for SEM-image analysis according to the protocol outlined in figure 64.

After general shaping of the potted samples with a belt sander, the exposed faces of the samples were polished in the

following sequence: (1) 200-grit wheel, (2) 600-grit wheel, (3) 5-μm Al_2O_3 on Texmet polishing cloth, (4) 0.3-μm Al_2O_3 on Texmet polishing cloth, and (5) 0.05-μm Al_2O_3 on Texmet polishing cloth. After the samples were polished to a mirror finish, they were ultrasonically cleaned, washed with deionized water, dried at 105 °C for 2 hours, and gold-coated for SEM-image analysis.

Image Generation

The basic premise of SEM-image analysis is that the physical properties of interest can be measured by computer analysis of SEM images. The images were collected by raster-scanning the SEM beam over selected areas of the sample; the magnification was controlled by varying the size of the scanned area. All of the images used for computer analysis were electron-backscatter images made with the primary-beam illumination angle set at 20° from normal. The electron-beam current, nominally 350 μA, was focused into a spot approximately 0.05 μm in diameter, providing a depth of focus of about 5 μm. Under the instrumental conditions used in this study, the lateral extent represented by the width of a single pixel at the highest resolution is approximately 0.01 μm; because of excitation-volume effects along the edge of the sample, the actual lateral resolution ranges from 0.01 to 0.05 μm. Thus, to make full use of the spatial-resolution capabilities of the instrument, the sample must be polished to a flatness of 0.05 μm. This approach to image generation eliminated any signal distortions associated with stereo shadows and minimized problems related to contrast interpretation.

Image Indexing

The objective of SEM-image analysis was to determine the salt distribution in the samples and to measure such physical properties as mass loss (surface recession), surface roughness, and fracture density.

The main method for measuring the mass loss (surface recession) caused by a given cleaning technique was based on estimating the elevation difference between the protected and cleaned sides of the core surface. For this purpose, a relatively low magnification of 10× was used to obtain a vista view of both the protected and cleaned sides in the same image; vista views show 3 to 4 mm of the protected and cleaned sides in the same exposure. All such low-magnification images were designated "A" in the indexing system used in this study. For several samples, a higher-magnification view of the border between the protected and cleaned sides was needed; such border views were designated "H".

Such physical properties as surface roughness and fracture density were measured from the SEM images at a magnification of 100×. Three images were collected from each sample on both the protected and cleaned sides; these images were designated "B" through "D" (protected) and "E" through "G" (cleaned), respectively. For example, the eight images collected from sample LSRP-2 were indexed as follows:

Sample	*Description*
LSRP–2A	10×, vista view
LSRP–2B	100×, protected or virgin surface
LSRP–2C	100×, protected or virgin surface
LSRP–2D	100×, protected or virgin surface
LSRP–2E	100×, cleaned surface
LSRP–2F	100×, cleaned surface
LSRP–2G	100×, cleaned surface
LSRP–2H	100×, transition region

The inventory of samples for SEM-image analysis is summarized in table 4. Some additional exposures were made below the exposed surface to assess the extent of subsurface fracturing; these exposures were indexed by adding an extension onto the main designation. Thus, the notation "LSRP–2F.1" would denote a second exposure below the exposed surface on the cleaned side of sample LSRP–2 in the region covered by the SEM image of sample LSRP–2F.

SEM images were made of the views, as denoted by the checkmarks in table 4. Both binary-file SEM images and photomicrographs were made for each view. The binary-file SEM images are included with the CD–ROM version of this report; the photomicrographs are available on request.

SEM-Image Analysis

This study exploits the ability of SEM to provide cross-sectional images of samples over a wide range of scales. Details of the computer programs for SEM-image analysis were described by Mossotti and others (1998), and Mossotti and Eldeeb (2000). The technique, which depends on direct observation of edge geometry in cross section, is based on the notion that the observed variegations along the polished cross section of a sample represent irregularities in the stone surface. We assume that the marble microstructure is isotropic. The set of programs used for SEM-image analysis are diagrammed in figure 65. The function and operation of each program are summarized below.

Hardware Requirements

The programs used for SEM-image analysis are executable on personal computers (PC's) running an MS–DOS-compatible operating system with an SVGA display. A 486DX PC is recommended; 640K of RAM is required.

Program SEM2BIN

Program function.—SEM2BIN, version 1.0, is a stand-alone program that converts the special Tracor Northern IMG formatting to a binary format suitable for image processing. The original SEM image consists of 512 rows each containing

512 pixels. The SEM encodes the image data with eight bits of information per pixel representing 256 shades of gray. The original image data can be regarded as a serial stream representing a raster scanned image made up of 262,144 pixels. For local storage, the original SEM data files are passed to a translator program called XI that is supplied by Tracor Northern for the SEM. The translator program generates and downloads the specially formatted files to a block device; in our SEM laboratory, a Macintosh II (40-MB hard disk) was used to log the image files. These files can then be downloaded to a PC over telephone lines, over a LAN, or with a physical diskette. Programs such as MAC2DOS are available for translation of the Macintosh files to a PC-compatible format. For transmission over telephone lines, any set of standard communication packages may be been used; the Kermit protocol is especially useful because of its ability to support batch processing.

Program environment.—SEM2BIN is scheduled from an MS–DOS-compatible command line.

Synopsis of the command line.—SEM2BIN is run from the DOS command line in accordance with the syntax shown in figure 66,[21] where the /h switch cues SEM2BIN to write the header information to the monitor (stdout); version 2.0, Mossotti and Eldeeb (2000) uses the /t switch to prompt the program to write the output file in the standard TIFF format.

Program I/O.—The input file is an image file in the Tracor Northern IMG format; the output file is given the input file name with an SEM extension. SEM2BIN provides no graphics display and requires no user interaction. Details of the program functioning and the source code were presented by Mossotti and others (1998), and Mossotti and Eldeeb (2000). SEM2BIN generates an output file consisting of an array of 262,144 bytes if the header information is discarded. If the /h command-line switch is used, the first line of the IMG file is discarded, and the next 64 lines are converted to their original ASCII characters. Thus, the actual data, which start at the 2,049th byte, will be indexed 2,048 (800 hexidecimal). Each byte represents the intensity of one pixel on a scale of 256 shades of gray. Each row in the 512- by 512-byte image is represented by serially ordered subsets of 512 bytes in the array, associated with the original image as follows:

```
{
pixel at row0, column0 ; pixel at row0, column1 ; …
pixel at row1, column0 ; pixel at row1, column1 ; …
… (no line feeds between rows) …
}
```

The translator program XI, supplied by Tracor Northern, carries out its function without error checking. From time to time, XI fails to accurately transmit part of a line or several complete lines. If the image file is corrupted by an odd number of bytes, the resulting image may appear as a blur of random pixels after a certain point. If an even number of bytes are lost, a shift may appear at some point in the image. When such problems occur, it is possible to repair the image file with a text editor by padding the corrupted line or by inserting additional lines into the file. As a diagnostic for such problems, SEM2BIN reports on all lines that do not contain exactly 64 characters, and on the total number of lines in the file; this information is useful for identifying the corrupted location in the image file. The reader who is interested in converting the image files to a standard format (TIFF, PCX, GIF, Postscript, and so on) is referred to Murray and vanRyper (1996).

Use of the program.—SEM2BIN requires no user interaction.

Program SHOWPIX

Program function.—Three DOS applications, each of which uses different combinations of graphics modes and image manipulations, were written to display the binary image on a PC monitor.

Program environment.—Three versions of SHOWPIX have been developed:

- SHOWPIX version 1.0 uses standard VGA (640 by 480 pixels) and requires the Borland graphics library; standard VGA can display 16 shades of gray.
- SHOWPIX version 1.1 uses standard VGA and near pointers in video memory to create the illusion of SEM operation.
- SHOWPIX version 2.0 uses SVGA mode 103 (800 by 600 pixels) and requires the proprietary Flash Graphics library; SVGA mode 103 can display 256 colors with 64 shades of gray. In addition, the Flash Graphics library produces faster and more efficient code than the Borland graphics library.

Synopsis of the command line.—SHOWPIX is run from the DOS command line in accordance with the syntax shown in figure 67. All versions of SHOWPIX can be invoked with a DOS mask to select a file series. Because DOS cannot recognize its own mask symbols, these programs can display only the first 50 files that match the mask.

Use of the program.—All versions of SHOWPIX display the SEM image on the PC monitor. Version 1.1 accepts input from the arrow keys to translate the displayed part of the image on the monitor, creating the illusion that the user is sweeping the SEM over a magnified surface of the sample.

Program PROFILE

Program function.—Image calibration is the first step in SEM-image analysis. A fundamental technical problem in automated SEM-image analysis concerns the interpretation of contrast. Because the SEM images are optimized for interpretation by the human eye, an intensity-modulated image will show intermediate gray levels monotonically allocated between the extreme light and dark areas of the image. The purpose of image calibration is to identify the threshold gray level that will be used to identify and partition the pixels into the logical sets.

Calcite and Epoxy

Because all of the SEM-image analysis in this study was conducted with epoxy-potted specimens in which the aver-

age atomic number of the epoxy was less than the average atomic number of calcite, and because all the samples were highly polished, we assume that all gray values exceeding a certain threshold value represent the backscatter signal from calcite. This approach allows us to dismiss any requirements for a linear relation between gray level and topologic depth or between gray level and average atomic number. However, because the surface of the sample is not perfectly flat, we can acknowledge any polishing imperfections by identifying a range of gray values to represent the uncertainty in the signal transition between the calcite and the epoxy.

Program environment.—PROFILE is scheduled from an MS–DOS-compatible command line. The program requires SVGA mode 103. The source code for PROFILE was presented by Mossotti and others (1998).

Synopsis of the command line.—PROFILE is run from the DOS command line in accordance with the syntax shown in figure 68. PROFILE accepts binary image files as input. On termination, the program displays the upper and lower values of the threshold pseudocolor.

Program I/O.—PROFILE is a stand-alone program that generates calibration parameters for the input image. PROFILE displays the input binary image on the monitor along with a histogram of the image gray values. The program also shows a menu instructing the user to use the arrow keys to move the upper and lower threshold levels. In response, the program refreshes the tristate image with the new threshold values. On termination, the program outputs the final threshold values to the monitor.

Use of the program.—The selection of a given pseudocolor for partitioning the calcite and epoxy pixels is the first crucial step in SEM-image analysis. Because the selection of a suitable threshold gray level is somewhat subjective, the first program provided in our image-processing package, PROFILE, is interactively designed to assist in this selection. Using PROFILE, the user can partition the full set of image pixels into three sets. The user graphically selects upper and lower threshold values from the histogram of pixel pseudocolors while viewing a dynamically updated tricolor thresholded image. A typical image displayed by PROFILE is shown in figure 69. The bimodal histogram in figure 69 shows a high occurrence frequency of both dark and light pixels. The locations of the bimodal peaks along the gray scale differ from image to image because SEM images do not have the same average brightness. Threshold values can be interactively selected on the histogram such that all pixels falling below the lower threshold value are displayed as black (logical value, EPOXY), all pixels falling above the upper threshold value are displayed as white (logical value, CALCITE), and all pixels falling in between the two threshold levels are displayed as a particular gray-scale pseudocolor (logical value, EDGE, shown in red on the computer screen and in black in fig. 69).

Program EDGE

Program function.—EDGE is used to calibrate and edit SEM images and to calculate surface roughness, fracture density, and surface recession.

Program environment.—EDGE is scheduled from an MS–DOS-compatible command line. The program requires SVGA mode 103. The source code for EDGE was presented by Mossotti and Eldeeb (2000).

Synopsis of the command line.—EDGE is run from the DOS command line in accordance with the syntax in figure 70.

Program I/O.—EDGE requires a binary image file as input. The program displays the image and a menu of operations on the PC monitor; the menu is accessible by the user with either arrow keys or hot keys, as indicated by highlighted colors on the menu. Calibration parameters are displayed and automatically used by the program for various computations, the results of which are also displayed on the PC monitor. At the user's request, the program will write a new edited output image file.

Use of the program. —EDGE displays the following menu below the image on the PC monitor:

Edit **C**lip e**R**ase **S**ave **P**rofile **D**ensity **L**oss e**X**it

The corresponding image operations are:

- Edit: Pixel-by-pixel edit function
- Clip: Clips large sections of image
- Erase: Erases section of image with swath control
- Save: Saves edited image
- Profile: Changes calibration parameters
- Density: Computes fracture density
- Loss: Provides image calipers for measuring recession
- Exit: Exits the program

Appendix 3. Optical Microscopy and Gray-Scale Measurements

To evaluate the efficacy of the cleaning techniques, we developed a quantitative assessment of the extent of superficial soiling on the surfaces of the cores taken from the building. Two methods were used for this purpose: a visual assessment ranking the cores by surface grayness, and an electronic method providing quantitative interval data representing the surface reflectivity of the cores over an area of 23 mm^2. This appendix presents the procedural details and unprocessed laboratory data associated with these measurements.

Visual Assessment of Surface Soiling

A color scale, from 0 to 10, was developed such that the higher the number, the greater the apparent darkness of the core surface, with two significant figures used to represent the degree of soiling. The bottom of the scale, 0.0, was assigned to the inside surface of a fractured core, which we assumed to represent a pristine, unsoiled, unexposed surface. The high end, 10, was assigned to the surface of sample GSRV–4, on which the dark crust covered virtually 100 percent of the exposed surface. To be precise, this gray scale is without explicit

units because each value corresponds to the fractional reflectivity of the stone surface. In the following discussion, the notation "c/" is used with a number to designate a gray-scale value.

Core series 3 through 6 were taken from the building as replicates of the same material (class of soiling, cleaning, coring procedure). These series were compared for consistency in color to determine the variation of the surfaces in a given class and for quality-assurance purposes. Core series 1 and 2 were not examined for color because 50 percent of the core surfaces were covered with epoxy resin and because the cleaned surfaces were treated with L.R. white, which may have altered the surface color. Detailed observations on core comparisons for surface roughness and color are given below. The surface-grayness determinations for the core series 3 through 6 are summarized in table 5. In the following discussion, the notations "S–3", "S–4", and so on designate the core series.

LSSV (lightly soiled, smooth; uncleaned):
S–3R and S–4 match (c/3).
S–5 and S–6 match (c/2).
- S–3R and S–4 are discernibly darker than S–5 and S–6.
- S–3R and S–4 are discernibly rougher than S–5 and S–6.

LSSP (lightly soiled, smooth; power wash):
S–3 and S–4 match (c/1.4).
S–5 and S–6 match (c/1.9).
- S–3 and S–4 are discernibly cleaner than S–5 and S–6.
- S–3 and S–4 have about the same surface roughness as S–5 and S–6.

LSSG (lightly soiled, smooth; gommage):
S–3 and S–4 match (c/1.4).
S–5 (c/1.5).
- S–3, S–4, and S–5 have about the same surface roughness.

Uncleaned surfaces appeared to be rougher than cleaned surfaces. Gommage-cleaned surfaces are generally smoother than power-wash-cleaned surfaces.

LSRV (lightly soiled, rough; uncleaned):
S–3 and S–4 match (c/4.0).
S–5 and S–6 match (c/4.0).
- S–3 and S–4 have about the same surface roughness as S–5 and S–6.

LSRP (lightly soiled, rough; power wash):
S–3 and S–4 match (c/2.0).
S–5 and S–6 match (c/1.8).
- S–3 and S–4 have about the same surface roughness as S–5 and S–6.
- Sample LSRP–6 has a ≈2½-mm-wide brown stain (see fig. 71).
- Sample LSRP–3 has small, diffuse brown stains.

LSRG (lightly soiled, rough; gommage):
S–3 and S–4 match (c/1.4).
S–5 (c/1.4).
- S–3 and S–4 have about the same color as S–5.
- S–3 and S–4 have about the same surface roughness as S–5.

GCSV (gypsum crusted, smooth; uncleaned):
S–3 (c/8.0).
S–5 and S–6 match (c/8.0).
- S–3 has about the same color as S–5 and S–6.
- S–3 has about the same surface roughness as S–5 and S–6.

GCSM (gypsum crusted, smooth, misting):
S–3 (c/4.0).
S–5 and S–6 match (c/4.0).
- S–3 has about the same color as S–5 and S–6.
- S–3 has about the same surface roughness as S–5 and S–6.

GCSG (gypsum crusted, smooth; gommage):
S–3 and S–4 match (c/1.4).
S–5 and S–6 match (c/1.4).
- S–3 and S–4 have about the same color as S–5 and S–6.
- S–5 and S–6 have about the same surface roughness as S–5 and S–6.

GCSC (gypsum crusted, smooth; combination):
S–3 (c/1.4).
S–5 (c/1.3).
S–6 (c/1.4).
- S–3 has about the same surface roughness as S–5 and S–6.

GCRV (gypsum crusted, rough; uncleaned):
S–3R (c/8.0).
S–3 (c/10.0).
S–4 (c/10.0).
S–5 (c/9.0).
S–6 (c/9.0).
- S–3 has an uncertain surface roughness.
- Information on S–5 is unavailable.
- S–4 and S–6 have about the same surface roughness, but greater than S–5.

GCRM (gypsum crusted, rough; misting):
S–3 (c/3.2); sample GCRM–3 has a brown stain (≈2½ by 1½ mm; fig. 72).
S–5 (c/4.0).
S–6 (c/5.0).
- S–3 is rough but has less surface roughness than S–5 and S–6.
- S–5 and S–6 have about the same surface roughness.

GCRG (gypsum crusted, rough; gommage):
S–3 (c/2.5).
S–5 (c/3.0).
S–6 (c/4.0).
- S–3 is highly irregular; its surface roughness cannot be determined.
- S–5 and S–6 have about the same surface roughness.

All three fractured surfaces and core sides are darker (c/3.5) than corresponding surfaces on any of the other cores. S–3 has a discernibly lighter color (c/2.0) zonation visible in cross section, 3 to 4 mm thick, that follows the external surface morphology (fig. 73).

GCRC (gypsum crusted, rough; combination):
S–3 (c/1.5).
S–5 (c/1.5).
S–6 (c/1.5).
- S–3, S–5 and S–6 all have about the same surface roughness.

All GCRC cores have a general blotchy brown stain over the entire surface (fig. 74). In general, the GCRG and GCRC series are smoother than the GCRV and GCRM series.

Electronic Gray-Scale Measurements

The automatic shutter on the optical-microscope camera provided a means for electronically measuring the surface reflectance of core samples in a highly localized area (≈23 mm^2). In this technique, the exposure time was used as a measure of the grayness of the core surface. A two-step procedure was used. First, an image of the cleaned surface was brought into focus with a 67× lens, with the surface obliquely illuminated by a fixed tungsten source. The tilt of the sample was adjusted to maximize the amount of reflected light into the microscope. The method was calibrated on a gray scale of 0 to 10 (gs units). By setting the *f*-stop of the camera lens such that an exposure of the surface of sample GCRV–4 required 10 s, we were able to calibrate the electronic exposure measurement at the high end of the scale. In this technique, we implicitly assumed a linear relation between the electronically measured exposure time and the extent of surface soiling within the surface area intersecting the solid angle subtended by the camera lens.

The observed color values, in descending order from 10 to 0, and as measured by the electronic technique and the visual method, are plotted in figures 75*A* and 75*B*, respectively. The electronic measurements (fig. 75*A*) ranged smoothly from the most heavily soiled to the cleanest surfaces, whereas the visual measurements relegated the cores to a well-defined level across the series. Because of the differences between the average surface reflectivity as perceived by the visual method and the local reflectivity as electronically measured, the samples spanned the full range of the scale.

The relation between the electronic exposure times and the visually assessed gray-level measurements is plotted in figure 76. The reproducibility of the electronic method was about a factor of 10 poorer than the visual method (visual, ±0.2 gray-scale units; electronic, ±2 gray-scale units). Not only does the electronic method survey a much smaller area than does the visual method, but the electronic technique also is more sensitive to the local angle of incidence of the light beam on the sample surface. Also, the intensity of the reflected light as measured electronically is more sensitive to small-scale surface roughness (≈5 mm) than is the intensity of the reflection over the full area of the sample as visually perceived. Thus, the wide variation in the electronic gray-level measurements is largely due to local inhomogeneities in surface color and texture.

Appendix 4. Salt-Penetration Measurements

Numerous reports in the literature have speculated on the influence of such adventitious salts as calcium sulfate dihydrate (gypsum) on the appearance and stability of calcareous building stone. Rain-chemistry data for the Philadelphia area (table 6) show average Ca^{2+} and Mg^{2+} concentrations of 73 and 30 μequiv/L, respectively. This appendix reviews representative laboratory data on the lateral and vertical distribution of gypsum over the stone surface and in pores and cracks of the stone.

Sulfate Analysis

Methods

Two methods, both based on X-ray-fluorescence spectroscopy, were used to measure the sulfur concentration in the stone samples. The first method, which was more convenient, was by energy-dispersive X-ray analysis, while the sample was mounted under vacuum on the SEM. The chemical sensitivity of this method for sulfur in the small area sampled by the primary electron beam was ≈0.25 atomic percent, and the spatial resolution was ≈5 μm. The second method was conducted with a Kevex energy-dispersive spectrometer with the specimens open to air. This method provided trace analysis for sulfur with a sensitivity of ≈200 ppm over a sample area of about 1 cm^2.

Applications

Sulfate Content of the Applied Resins

To assess the contribution of the epoxy and acrylic resins to the sulfur signal, we analyzed the coatings on fractured sections of the marble cores that were previously determined to be sulfur free. Typical X-ray-fluorescence spectra of the epoxy and acrylic resins are shown in figure 77. It is evident from the respective background levels that the exposures were nominally the same for both sample types and that a substantial amount of sulfur is present in the epoxy resin, whereas sulfur is absent in the acrylic resin.

Sulfate Content of Soiling on Sample Surfaces

The uncleaned samples in core series GCS and GCR (1 and 2) were analyzed for sulfur in the open air with the Kevex spectrometer. In figure 78, typical X-ray-fluorescence spectra of uncleaned samples (free of epoxy resin) provide evidence for the presence of gypsum on the stone surface in the GCR core series. The inorganic component of the crust on sample GCRV–2, the most well defined in core series GCR, was found to be mainly calcium and sulfur. No sulfur was detected at the interface between the crust and matrix, in the void areas where the crust had separated from the matrix, or in the calcite matrix.

The surfaces of uncleaned samples in core series GCR appear as much darker (lower average atomic number) areas in most SEM images, partly because of the surface roughness in the direction parallel to the electron beam. The bright spots on the surface were identified as silicate and iron minerals; the very dark regions in the SEM images are holes. Typical X-ray-fluorescence spectra of such silicate and iron minerals are shown in figure 79. A typical semiquantitative analysis of the silicate inclusions is listed in table 7. One grain of a mineral that showed the X-ray-fluorescence profile of apatite was observed directly on the stone surface.

Sulfate Content of Cracks, Fissures, and Matrix

A vertical path from the several hundred micrometers below protected or cleaned surfaces, through debris, into the potting material, was analyzed by X-ray-fluorescence spectroscopy. This procedure was repeated on every sample that we suspected might contain gypsum. No sulfur was detected at any point along such vertical paths in any sample, or anywhere in the cracks and crevices or in the debris that remained in some of the pockets on cleaned surfaces.

Appendix 5. Surface-Recession Test

This appendix details the procedures used for measuring the mass loss associated with each cleaning technique. The amount of surface recession caused by the cleaning was used as a surrogate measure for the mass loss. As detailed in appendix 1, approximately half of each core was protected during cleaning by a thick layer of epoxy resin. This procedure permitted a side-by-side comparison of the uncleaned and cleaned surfaces of the stone by examining polished cross sections taken at a 90° angle across the cleaned and uncleaned zones.

Two methods were used to estimate the surface recession. The first method was based on the change in the level of the cleaning surface relative to that of the original soiled surface. The second method was based on changes in the deviation of the surface profile around the mean level between the cleaned and uncleaned surfaces; this method, a measure of surface smoothing, yields an estimate of the minimum mass loss due to cleaning. These minima were used in the data analysis only when the values obtained by the first method were highly uncertain or below background.

Surface Recession Based on Change in Surface Level

An example of the application of the SEM-image-analysis program EDGE (see app. 2) to estimation of the surface recession on the clean side of sample FCRC–1 is shown in figure 16. The recession calipers shown in figure 16 are used to estimate the average change in relief across uncleaned and cleaned surfaces. The program EDGE displays the calipers in "recession" mode and continuously outputs the separation of the calipers to the left of the image on the computer screen (not shown); precalibration of the calipers is based on the assumption that the image magnification is 10×. The calipers can be rotated to match the slope of the surfaces in accordance with the action of the function keys described in the menu below the image on the computer screen.

This method of surface-recession measurement is fundamentally limited by natural irregularities in the stone surface over the lateral range of observation. The standard deviation of the natural morphology over a 1-cm scale was found to range from 35 to 150 μm, depending on the particular location on the building from which the core was taken. The estimated surface recession for different surface-soiling conditions as measured by the two methods is listed in table 8. The uncertainties listed were estimated from precise measurements of the standard deviations of the surfaces and from the estimated statistical reproducibility of the morphologic variations across the lateral range of observation. With the possible exception of GCR surfaces, the mass loss due to any of the cleaning techniques is insignificant. In four of the seven cases studied, the mass loss is less than the detection limit of the method, which averages about 75 μm. Therefore, we suggest that much of the mass loss on stone surfaces is due to smoothing. Furthermore, the change in the deviation of the surface profile from the mean level should provide an alternative measure of the mass loss. The extent of surface smoothing can be estimated with considerable precision by computer analysis of the SEM images of core cross sections.

Surfaces Recession Based on Surface Smoothing

Use of the program EDGE (see app. 2) in "trace" mode provided a measure of the standard deviation of surface excursions from the mean level. The program is calibrated to output the standard deviation, in micrometer units, on the computer monitor. Although the precision of this method based on surface smoothing (35 μm) is about double that of the first method, the second method is flawed by a systematic offset error that cannot be estimated.[22] Because of this error, the second method provided an estimate of only the minimum mass loss by the cleaning technique. The surface-recession values obtained by the second method were used for data analysis only when those obtained by the first method were highly uncertain (table 8).

Appendix 6. Fracture-Density Measurements and SEM-Image-Analysis Data

The fracture density is a measure of the fraction of the stone volume filled by fractures. The measurement of fracture density is based on SEM-image analysis. The program EDGE (see app. 2) was developed inhouse to analyze the SEM images of samples prepared as described in appendix 2. The results of program computations are displayed on a PC monitor.

The first step in the measurement of fracture density is calibration of the SEM image. The user can control the threshold gray level that delineates a fracture from surrounding unfractured material in the SEM image. As the user adjusts the threshold gray level, the image is refreshed in real time, with all of the pixels to be counted as fractures and edges colored in red. Subjective judgment must be exercised in selection of the threshold gray level, which delineates pixels into three logical classes: fracture, edge, and mass.

The second step in the measurement of fracture density is selection of the size of the spatial window for the measurement. The program EDGE reports the percentage of pixels identified as components of the fractures in the window, which can be moved to any location on the SEM image. We noted that the

natural variation in fracture density was about ±4 percent in most of the SEM images examined: The most homogeneous stone showed a natural variation of about ±0.5 percent, and the most inhomogeneous stone showed a natural variation of about ±15 percent. The results of fracture-density measurements on all the SEM images obtained in this study are listed in table 9.

Appendix 7. Surface-Roughness Test

The surface roughness of core samples was measured by mathematical analysis of their cross-sectional SEM profiles at 100× magnification. The measure of surface roughness derived for this study, the shape factor, is not unlike a "gathering factor" that might be conjured when sewing ruffles in fabric. The shape factor measured on the cores examined in this study ranged from 0 to about 10, where 0 represents a perfectly smooth plane and 10 corresponds to a surface exhibiting an irregular morphology over the range 10 to 10^5 μm.

The shape factor is based on the fractal nature of the exposed surface. The challenge of computing the fractal dimension of a surface from the shape of its cross section is similar in many respects to the classical length-of-shoreline problem. Our method for determining the fractal dimension is based on a Richardson structured walk along the cross-sectional lateral trace of the surface. The Richardson effect, in its elegant simplicity, asserts that the trace of a ragged pattern can be approximated with a broken line made up of N intervals of length ε, where

$$N = \mu_D \varepsilon^{-D}. \tag{11}$$

If the value of the exponent D is constant within a range of ε values, the ragged pattern is said to be fractal, and the exponent D is called the fractal dimension, on which the proportionality constant μ_D depends. In keeping with common analytical practice, our algorithm uses the slope of the curve log N versus log ε to estimate the fractal dimension for a given contour. Since the measurement is made across the trace of the surface cross section, the fractal dimension will range from 1 to 2. If the marble surface is morphologically isotropic, we can calculate its fractal dimension by simply incrementing by the fractal dimension determined for the surface cross section. However, in calculating the shape factor for measuring the surface roughness, the fractional part of the Richardson dimension is used as the scale-independent paramenter.

In general, the length, L, along the trace of the surface cross section is given by

$$\begin{aligned} L &= N\varepsilon \\ &= (\mu_D \varepsilon^{-D})\varepsilon \\ &= \mu_D \varepsilon^{1-D}, \end{aligned} \tag{12}$$

where L has the units μm^{1-D}.

If we measure L relative to a reference state L^*, we can define the shape factor, Γ, by the ratio μ_D/μ_D^* and use the following algorithm for its computation:

$$\Gamma \approx (L/L^*)\varepsilon^{D-D^*}, \tag{13}$$

where Γ has the units μm^*.

In this study, L was taken as the number of pixels in the trace of the exposed surface. L values for all SEM images analyzed are listed in table 9. The reference value L^*, the Euclidean length of the trace of the exposed surface, is reported in the rows labeled "Ecldn Length" in the same table. The ε value used in the SEM images made at 100× magnification is equal to 1.76 μm/pixel. In equation 13, the Euclidean length is converted to pixel units by use of the factor 512/22.5 pixels/cm. The fractal dimension of the trace of the exposed surface, given in the row labeled "FRghness" in table 9, is reported as the fractional part of the Richardson dimension multiplied by 100.

Appendix 8. Surface-Reactivity Test

Theoretical Overview

Equation 6 shows that the total Ca^{2+} released into a flowing solution over calcareous stone by the dissolution action of pure water depends only on the product of the surface reactivity and the time of wetness.[23] Incorporated into equation 6 is the assumption that the flow rate of water over the stone is sufficiently fast to sweep the surface of reaction products which may accumulate and participate in the backreaction. Under such conditions, the monomolecular kinetics (Plummer and others, 1978) of the forward dissolution reaction

$$CaCO_3 + H_2O \rightarrow Ca^{2+} + HCO_3^- + OH^- \quad (k_3 = 10^{-6.92}\ \text{cm/s}) \tag{14}$$

is unchecked by the backreaction in which $CaCO_3$ is precipitated. From equation 6, we can expect that the rate of release of Ca^{2+} ions is independent of the local hydrodynamics of the test solution once a critical threshold surface flow rate has been exceeded. We have empirically established that the flow rate of the test solution must exceed 0.01 cm^3/s per centimeter of contour for the surface-reactivity test to be relatively insensitive to the dynamics of the test solution.

To compare the results of the surface-reactivity test from sample to sample, we normalized the amount of Ca^{2+} released in a given test by the amount of Ca^{2+}, ${}^E M_t$, that theoretically would be released from Euclidean area A in t seconds. The ratio $M_t/{}^E M_t$, here called the relative surface activity, is denoted Ω. From this definition, using equation 6, Ω is given by

$$\begin{aligned} \Omega &= M_t/{}^E M_t \\ &= k_3 \hat{A} t / k_3 A t \\ &= \hat{A} / A. \end{aligned} \tag{15}$$

Thus, equation 6 can be rewritten to include Ω as follows:

$$M_t = k_3 \Omega A t \qquad \text{(in millimoles).} \quad (16)$$

The surface-reactivity test is based on a simple rearrangement of the equation 8 as follows:

$$\Omega = \frac{M_t}{k_3 A t} = \frac{[Ca^{2+}]U}{k_3 A t}, \qquad (17)$$

where $[Ca^{2+}]$ is the Ca^{2+} concentration in U cm^3 of test solution and t (in seconds) is the exposure time.

Laboratory Implementation

Apparatus

The laboratory implementation of the surface-reactivity test is simplicity itself. Two different laboratory setups were used to recycle a given volume (5–10 mL) of deionized water over the top surface of the sample. In each setup, the top surface of the sample was isolated by mounting each sample with silicone rubber adhesive in a Delrin (acetyl) ring, and the flow rate of the test solution over the core surface was controlled by an infusion pump to exceed the requisite threshold flow rate of 0.01 cm^3/s per centimeter of contour.

The two different laboratory setups are diagrammed in figures 80 and 81. In each setup, a measured volume of water was recycled over the core surface. After the water had washed the core surface for a measured period, an aliquot of the homogenized test solution was analyzed for Ca^{2+} by inductively coupled plasma-emission spectrometry.

Equation 17 was then used to compute the Ω value of the core surface. In figure 76, the test solution was recycled through a dripline positioned about 3 cm above the test surface; in figure 77, the test solution was pumped over a vertically mounted core surface. With these simple techniques, we find that the Ω value can vary by as much as 300 percent, depending on the type of calcareous stone and on the surface-soiling condition of the stone.

Test Procedure

The following procedure was followed in the surface-reactivity test. All core surfaces were (1) cleaned with compressed air to remove dust, (2) washed with 50 mL of deionized water, (3) dried at 110°C overnight, (4) mounted for isolation of the top surface, (5) soaked overnight in deionized water, (6) purged of loose droplets by shaking, (7) mounted in a test beaker, (8) conditioned by flowing deionized water over the core surface for 10 minutes, (9) washed with 20 mL of deionized water, (10) treated with 10 mL of deionized water , and (11) exposed to flowing test solution for t seconds.

Results

The Ω values of sample surfaces in core series 3 are plotted in figure 82. An analysis of the average surface-reactivity values from replicate tests on these samples is presented in the section above entitled “Synthesis and Interpretation of Results.”

Footnotes

[1]To define the state of a surface, a complete set of state variables is needed. In particular, a given state variable, such as roughness, does not uniquely define the state of the surface; the same level of roughness can reflect an infinite number of states. Although our present knowledge of a complete set of state variables for weathered stone is incomplete, the thermodynamic model is useful in developing a formalism for data analysis.

[2]Primary deposition of a given weathering agent at a specific location can be represented by a spatially and temporally dependent flux-density function, a vector quantity with units of mass per unit area per unit time.

[3]Secondary mobilization of a given weathering agent to a specific location can be represented by a spatially and temporally dependent surface-flow function, a vector quantity directed across the contour line with units of mass per unit time per unit length along the contour.

[4]The following definitions are used in this report:

nanoscale	0.1 to 100 nm
microscale	0.1 to 100 mm
mesoscale	0.1 to 5 mm
macroscale	0.5 cm.

[5]Because SEM measurements were used, core samples had to be taken from the building.

[6]Although the laser-cleaned surfaces were visually examined by optical microscopy, no photomicrographs were prepared because of offschedule delivery of the cores.

[7]Much of the soiling consists of carbon-based particulate matter that is not effectively imaged by backscatter SEM; only the gypsum in the soiling can be monitored with SEM energy-dispersive X-ray analysis.

[8]We detected a fragment of gypsum in only one SEM image of a GCRG-series sample out of 20 such images examined for gypsum; in this particular SEM image, the gypsum may have been trapped by the L.R. white epoxy because of the location of the crevice near the protected area of the sample.

[9]Most of the cores tested were found to be quite homogeneous below the surface, with a natural variation in fracture density of about ±0.25 percent. At the opposite extreme, we have seen variations of ±15 percent in several cores examined in this study.

[10]χ^2 analysis of a 2-by-2 contingency table of surface roughness (smooth, rough) versus friability index (FI≥57, <57) gave the outcome χ^2=6.8, with p=99 for DF=1. In terms of surface roughness, in figure 11C the shape factor falls mainly in the range 2–4 cm^D for uncleaned smooth cores (LSS, GCS) and in the range 2–8 cm^D for uncleaned rough cores (LSR, GCR).

[11]χ^2 analysis of a 2-by-2 contingency table of soiling (light, heavy) versus relation (yes, no) gave the outcome χ^2=62, with p>99.9 for DF=1.

[12]The utility of a resource, an economic concept, provides a common quantitative unit, the "util," for measuring the satisfaction provided by that resource. For buildings, this concept is useful for aggregating component utilities (shelter, emotional value, and so on) and for comparing the value of resources. For example, Philadelphia City Hall minimally provides structural utility, esthetic utility, and indirect economic utility on the basis of its effect on tourism. The importance of this concept is not so much the absolute number of utility units assigned to each resource component but the relative magnitudes of the utility of each component in the data set under consideration.

[13]For a discussion of the Hausdorf measure, see Peitgen and others, 1992, p. 216–217.

[14]To compare the results of the surface-reactivity test from one sample to the next, we generally normalize the mass of Ca^{2+} released in a given test by the mass of Ca^{2+} that would theoretically appear in a test solution if the fractal dimension of the test sample were equal to 2 (Euclidean area); we refer to this ratio as the relative surface activity.

[15]As discussed in appendix 8, the surface-reactivity test is relatively insensitive to the dynamics of the delivery and collection of the test solution if the surface flow rate of the test solution exceeds ≈0.01 cm^3/s per centimeter of contour.

[16]The notion of a limit state, sometimes called emergent criticality, is codified in the theory of disordered systems, popularly known as chaos theory.

[17]This definition is in keeping with the conventional statistical definition of accuracy as a measure of systematic error. The smaller the error, the higher the accuracy.

[18]In principle, the general-utility curve is actually a hypersurface because the utility space incorporates the effects of a multiplicity of state variables.

[19]Note that the confidence intervals for the curve as a whole, which imply joint statements about any number of data points across the curve, are larger by the ratio $\sqrt{2F/t}$ (where F is the F-distribution and t is the table statistic) than corresponding intervals for any single data point.

[20]The photographic record of core sites has been submitted to the Philadelphia Department of Public Property in fieldnote format. This record documents the sites before they were contaminated by a film crew while making a movie and then, later, after the entire exterior of the building was recleaned by the gommage technique.

[21]When viewing a syntax diagram, read from left to right and from top to bottom. The command name and items required to make the command work appear on the baseline; the items below the baseline are optional. A line ending with an arrowhead means that the diagram is contiued. A line starting with an arrowhead means that the syntax is continued from the previous line. A vertical bar marks the end of the command syntax.

[22]In the data treatment shown in the main document (see fig. 17), the surface-recession values obtained by the second method were used when the surface-recession values obtained by the first method were in the same order of magnitude as the noise level associated with the first method.

[23]The expected time needed to generate about 1 ppm Ca^{2+} in 5 mL of deionized water flowing over the surface of a 0.75-in.-diameter calcite core sample is given by

$$t = [Ca^{2+}]U/k_3A$$

$$= \frac{1_{(\mu g/mL)}5_{(mL)}}{\{40.103_{(\mu g/mmol)}10^{-6.92}{}_{(mmol/cm^2-s)}\pi[(0.75/2)_{(in.)}2.54_{(cm/in.)}]^2\}}$$

$$= 365 \text{ s}$$

$$\approx 6 \text{ minutes.}$$

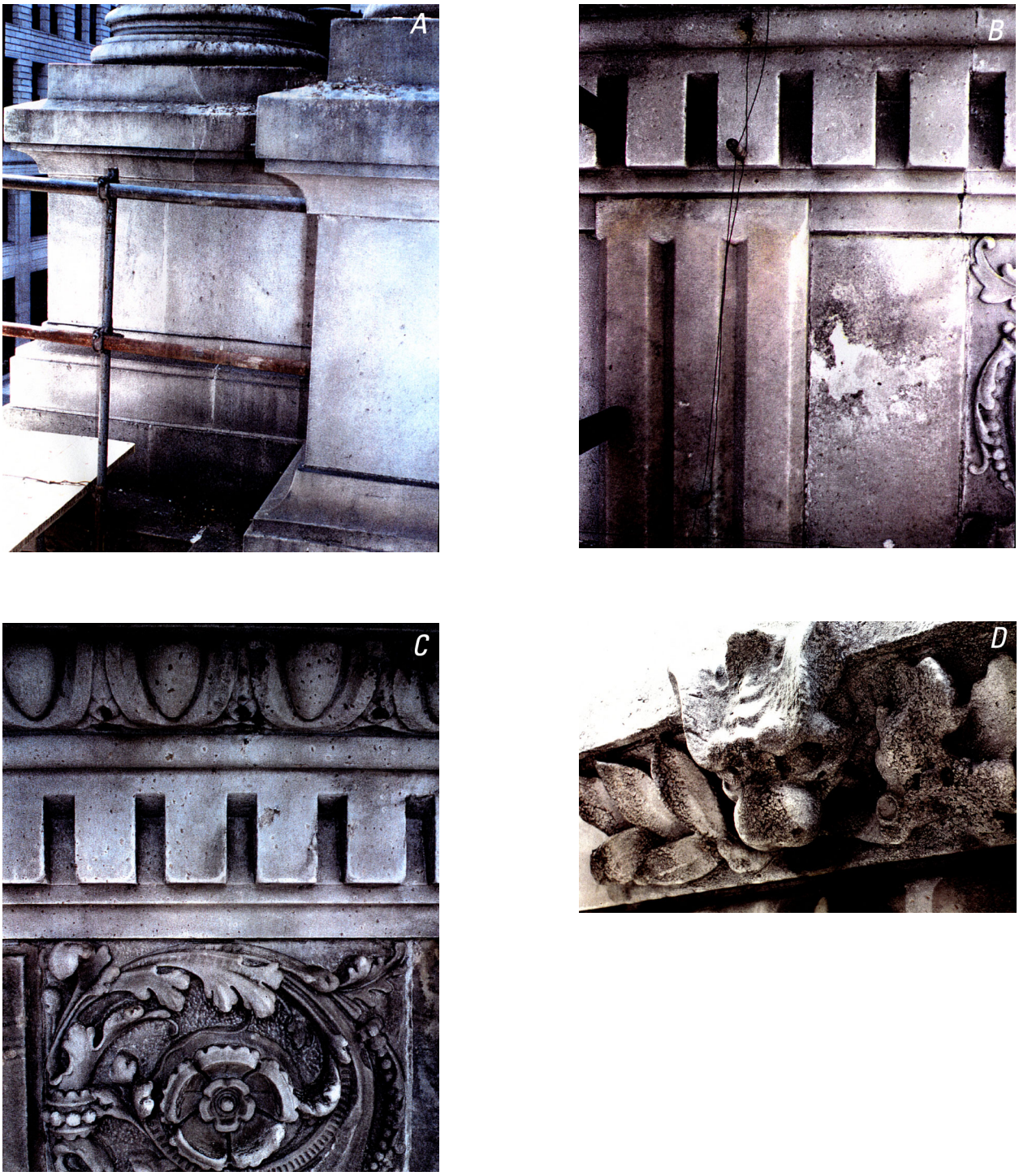

Figure 1.—Typical examples of surface-soiling conditions on Philadelphia City Hall. *A*, Lightly soiled, smooth. *B*, Lightly soiled, rough. *C*, Gypsum crusted, smooth. *D*, Gypsum crusted, rough.

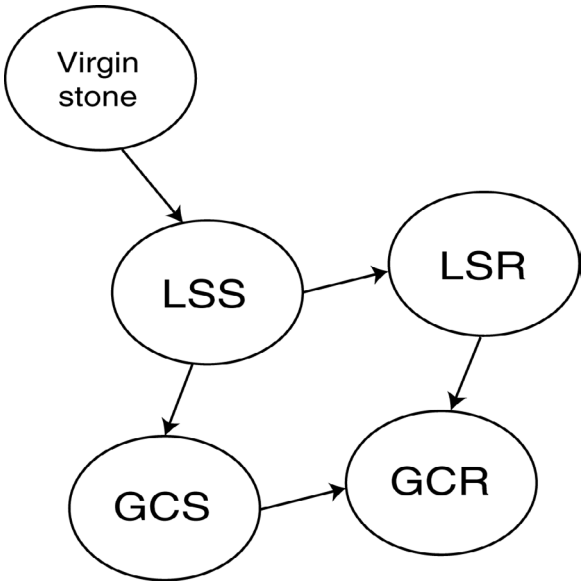

Figure 2.—State diagram of stone surface, in which each surface-soiling condition is viewed as a unique thermodynamic state. Surface-soiling conditions: GCR, gypsum crusted, rough; GCS, gypsum crusted, smooth; LSR, lightly soiled, rough; LSS, lightly soiled, smooth.

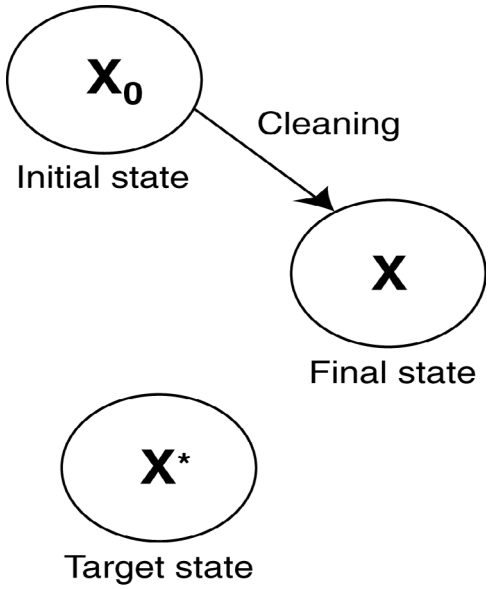

Figure 3.—Generalized cleaning process.

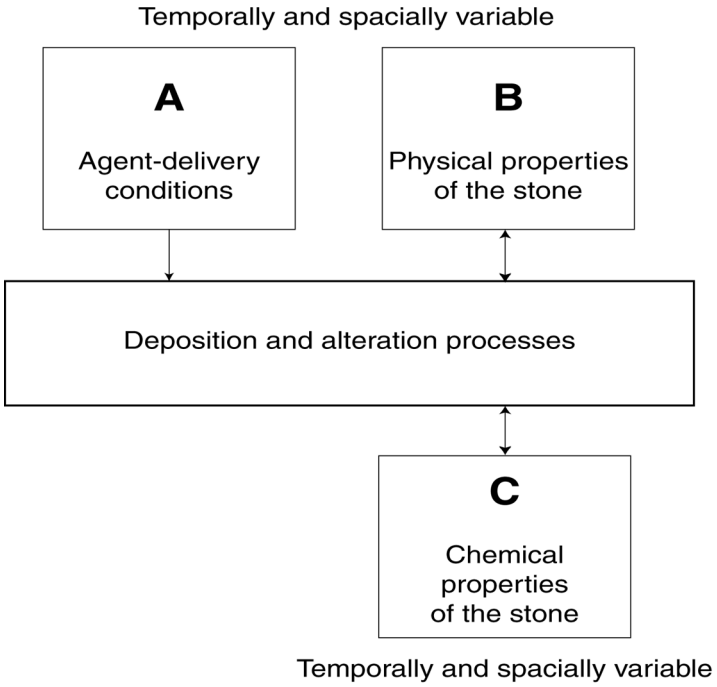

Figure 4.—Basic components of stone-weathering model.

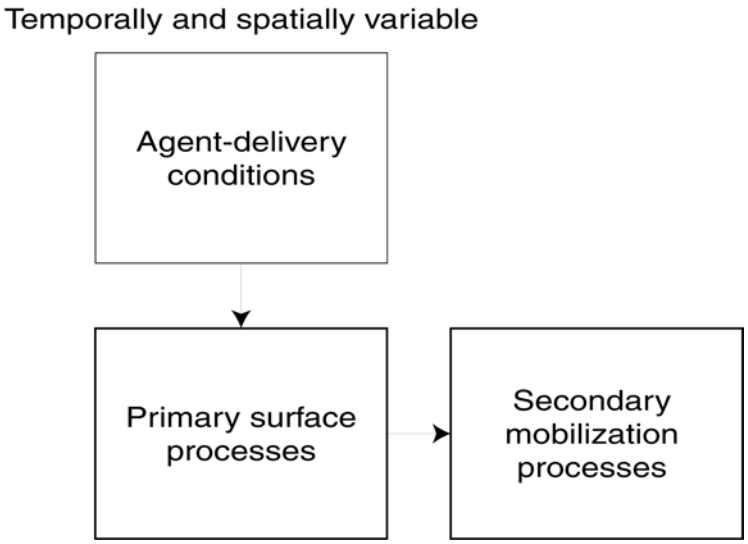

Figure 5.—Primary deposition and secondary mobilization processes in stone-weathering model.

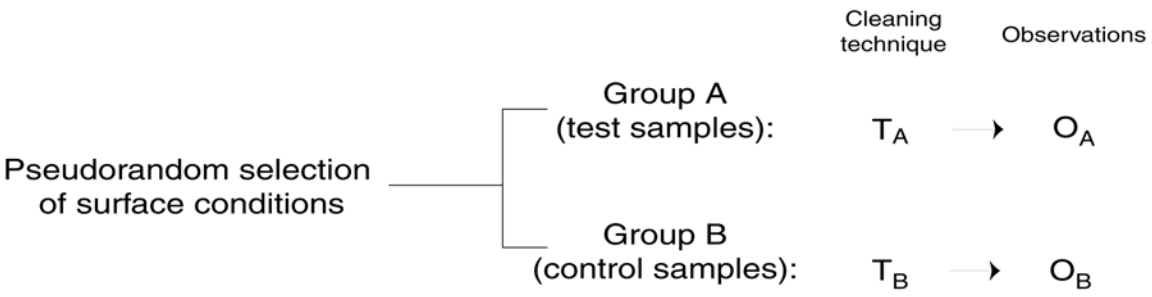

Figure 6.—Experimental design for controlling extraneous variables. T_B, epoxy protection layer applied to control test surfaces; T_A, cleaning treatment followed by the epoxy protection layer; O_A-O_B, effect of interest in all measurements.

	V	P or M	G	C
LSS	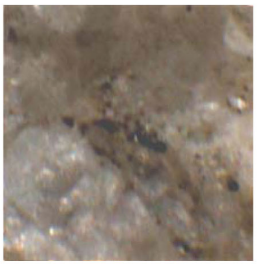	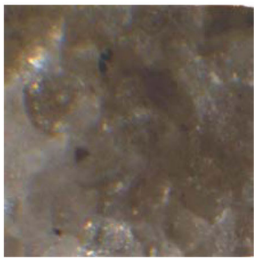	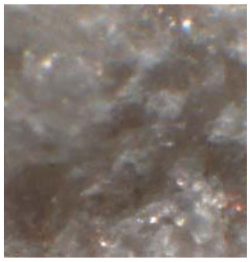	No test
LSR	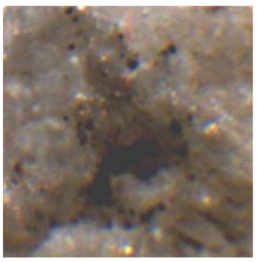	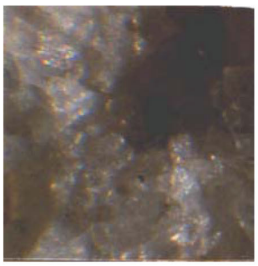	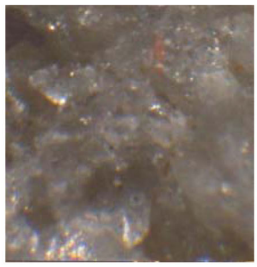	No test
GCS	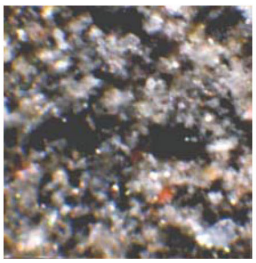	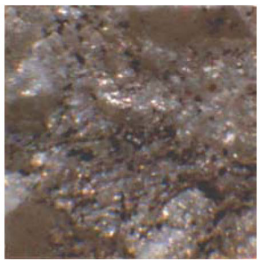	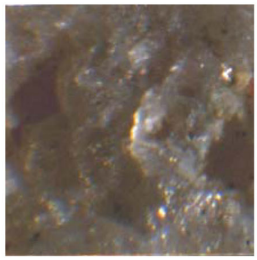	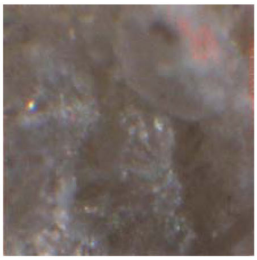
GCR	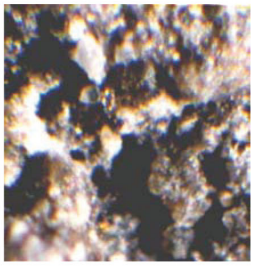	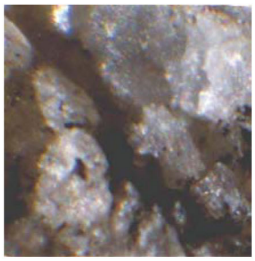	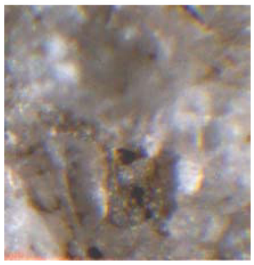	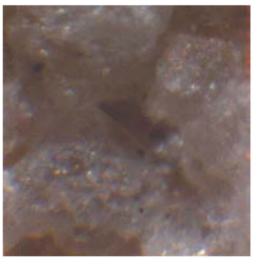

Figure 7.—Photomicrographs of typical soiled surfaces in cores series 3 through 6 before and after application of cleaning techniques, showing morphologic features of surface and dissemination of soiling agents in cracks and crevices of stone surface. Cleaning techniques: A, Armax; C, combination; D, dry ice; G, gommage; J, JOS; L, laser; M, misting; P, power wash; V, virgin. Surface-soiling conditions: GCR, gypsum crusted, rough; GCS, gypsum crusted, smooth; LSR, lightly soiled, rough; LSS, lightly soiled, smooth. Magnification, 67x—Continued.

	A	J	L	D
LSS	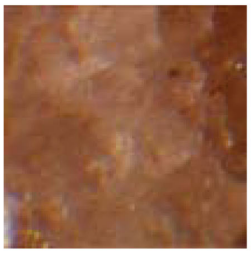	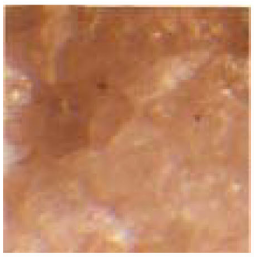	Micrograph not available	Micrograph not available
LSR	Micrograph not available			Micrograph not available
GCS			Micrograph not available	Micrograph not available
GCR	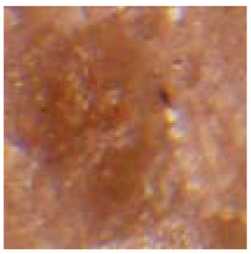	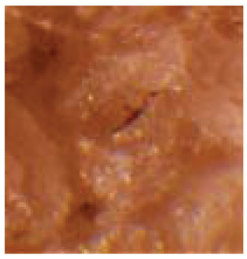	Micrograph not available	Micrograph not available

Figure 7 (Cont.)—Photomicrographs of typical soiled surfaces in cores series 3 through 6 before and after application of cleaning techniques, showing morphologic features of surface and dissemination of soiling agents in cracks and crevices of stone surface. Cleaning techniques: A, Armax; C, combination; D, dry ice; G, gommage; J, JOS; L, laser; M, misting; P, power wash; V, virgin. Surface-soiling conditions: GCR, gypsum crusted, rough; GCS, gypsum crusted, smooth; LSR, lightly soiled, rough; LSS, lightly soiled, smooth. Magnification, 67x.

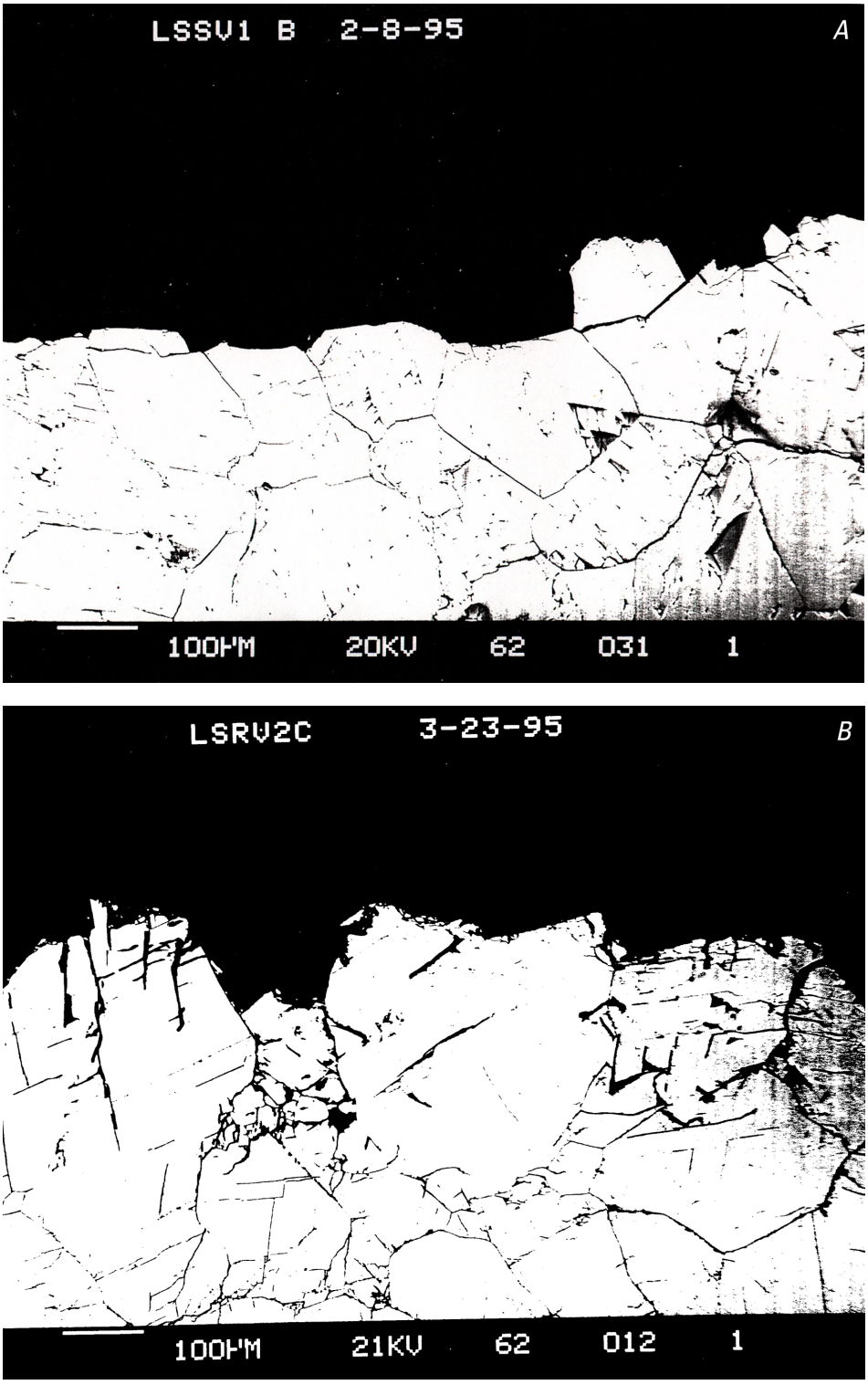

Figure 8.—Typical cross-sectional scanning-electron-microscope images of uncleaned cores, showing substrate of various surface-soiling conditions: lightly soiled, smooth (*A*, sample LSSV–1); lightly soiled, rough (*B*, sample LSRV–2C); gypsum crusted, smooth (*C*, sample GCSV–1); and gypsum crusted, rough (*D*, sample GCRV–2)—Continued.

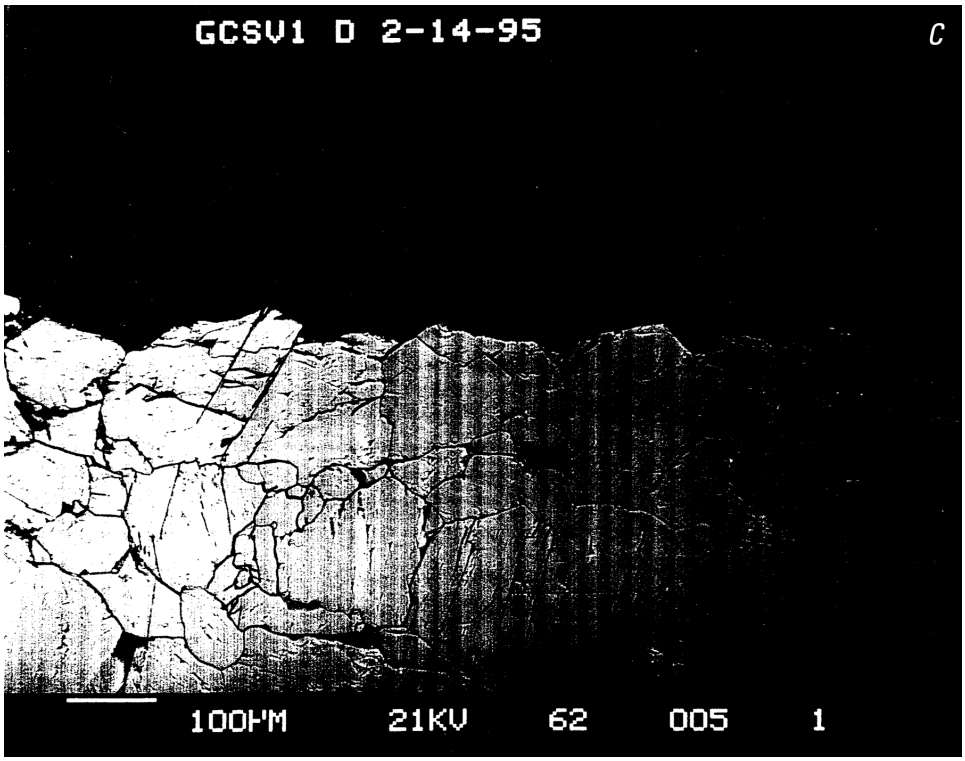

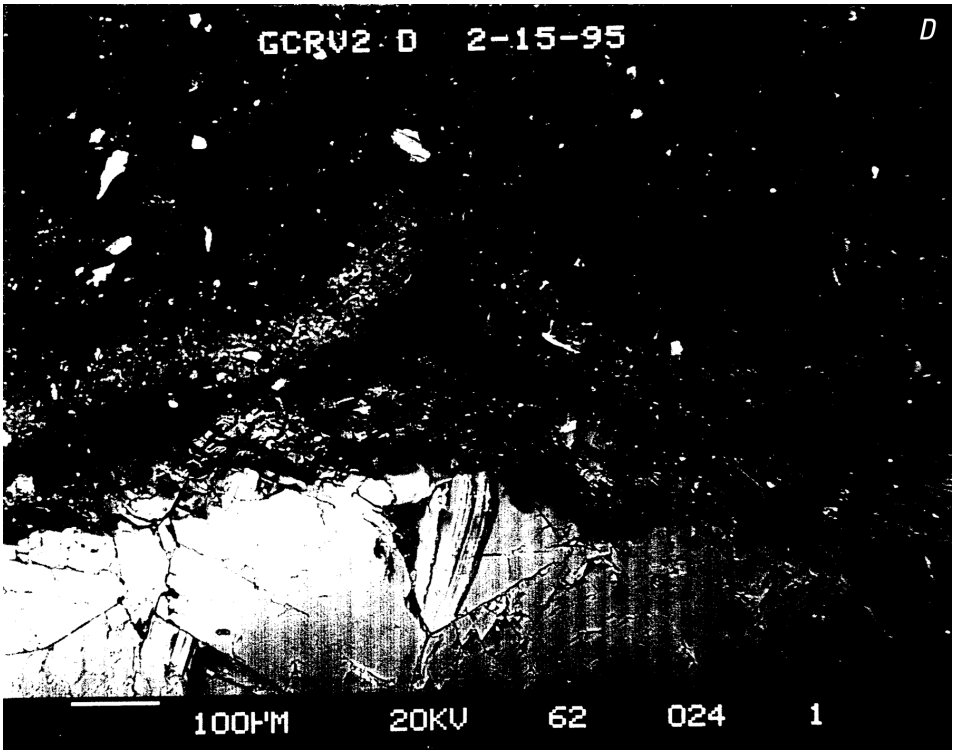

Figure 8 (Cont.)—Typical cross-sectional scanning-electron-microscope images of uncleaned cores, showing substrate of various surface-soiling conditions: lightly soiled, smooth (*A*, sample LSSV–1); lightly soiled, rough (*B*, sample LSRV–2C); gypsum crusted, smooth (*C*, sample GCSV–1); and gypsum crusted, rough (*D*, sample GCRV–2).

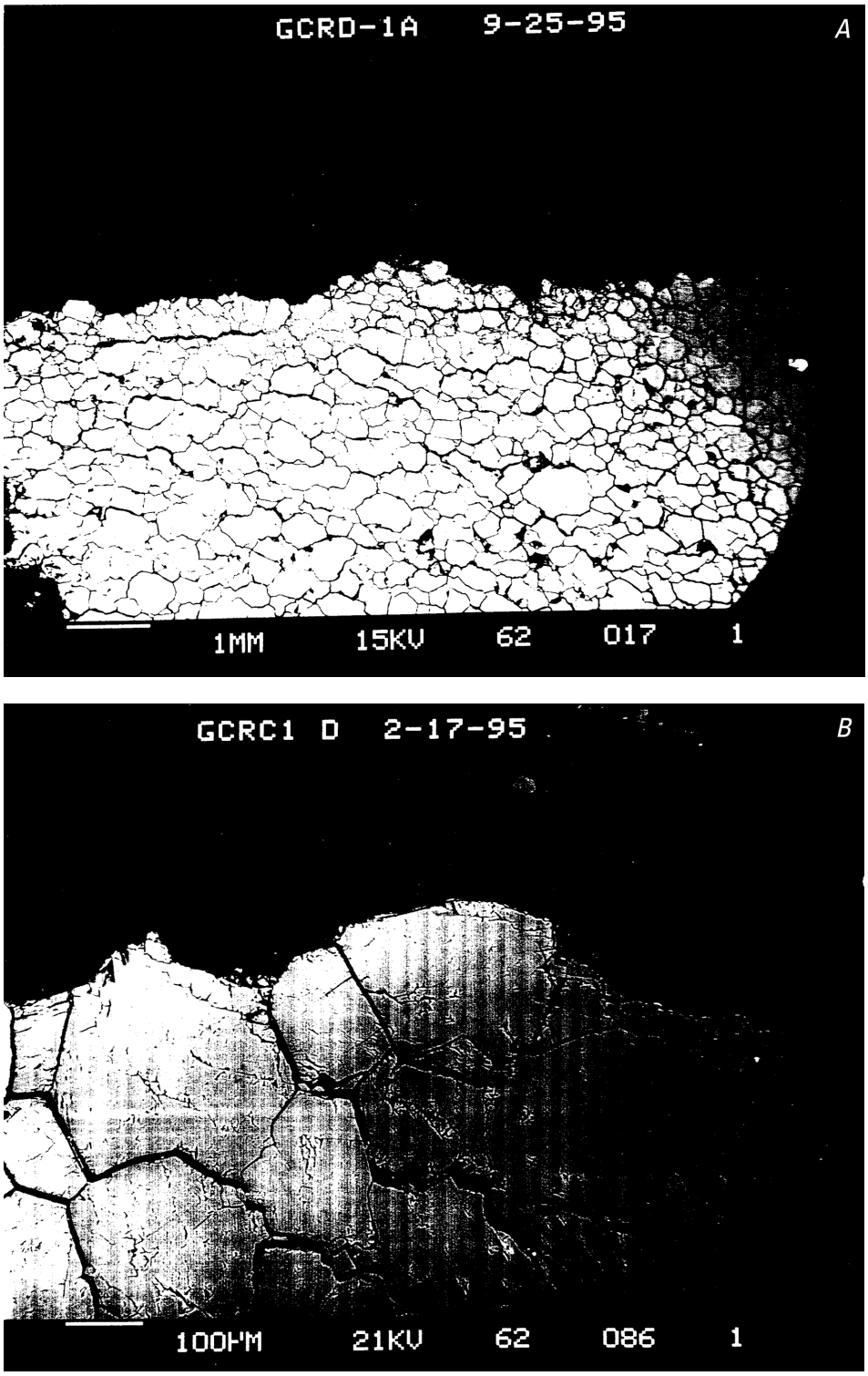

Figure 9.—Scanning-electron-microscope images of core samples with gypsum-crusted, rough surface-soiling condition. *A*, sample GCRD–1A. Note sugary texture of matrix throughout bulk of core. Magnification, 10x. *B*, sample GCRC–1. Note relatively smooth surface. Magnification, 100x. *C*, sample GCRA–1D. Note highly fractured surface. Magnification, 100x. *D*, sample GCRG–1D. Note highly fractured surface. Magnification, 100x. Such GCR cores typically exhibit a complex morphology within ~250 m of surface and well-consolidated grains 200 to 300 µm below surface—Continued.

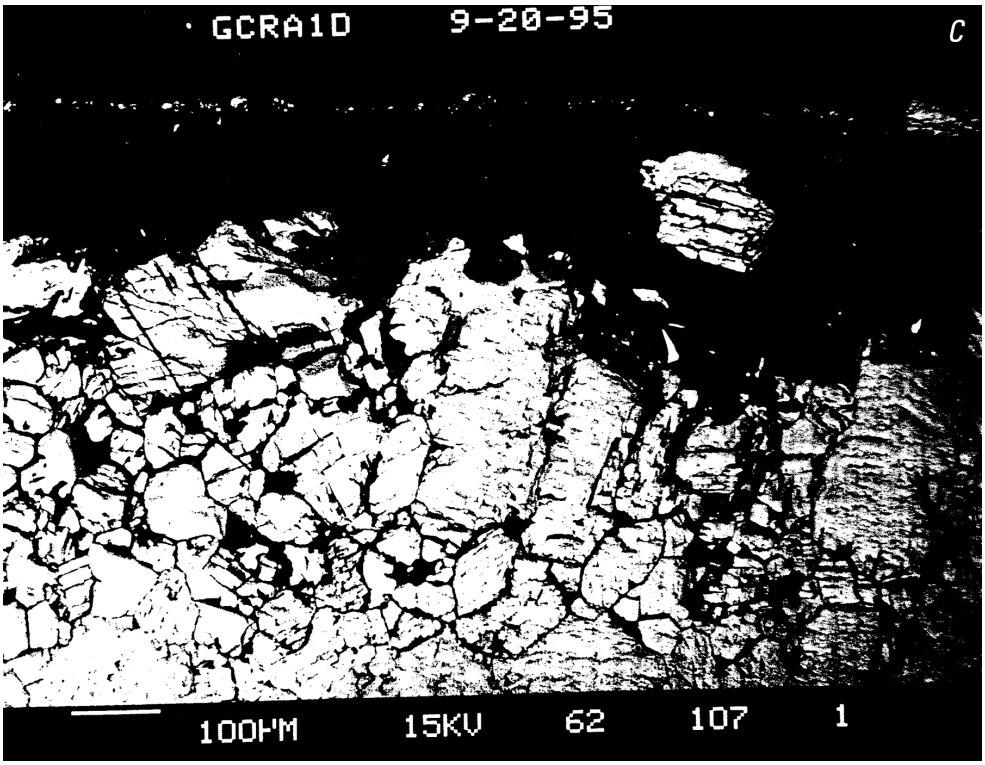

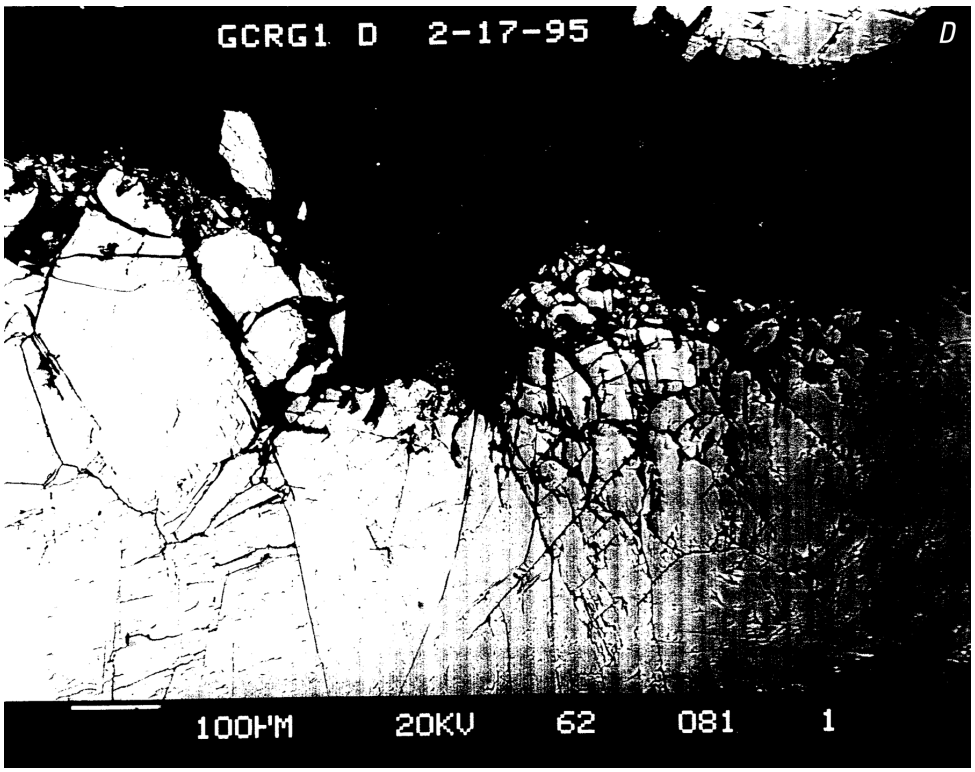

Figure 9 (Cont.)—Scanning-electron-microscope images of core samples with gypsum-crusted, rough surface-soiling condition. *A*, sample GCRD–1A. Note sugary texture of matrix throughout bulk of core. Magnification, 10x. *B*, sample GCRC–1. Note relatively smooth surface. Magnification, 100x. *C*, sample GCRA–1D. Note highly fractured surface. Magnification, 100x. *D*, sample GCRG–1D. Note highly fractured surface. Magnification, 100x. Such GCR cores typically exhibit a complex morphology within ~250 µm of surface and well-consolidated grains 200 to 300 µm below surface.

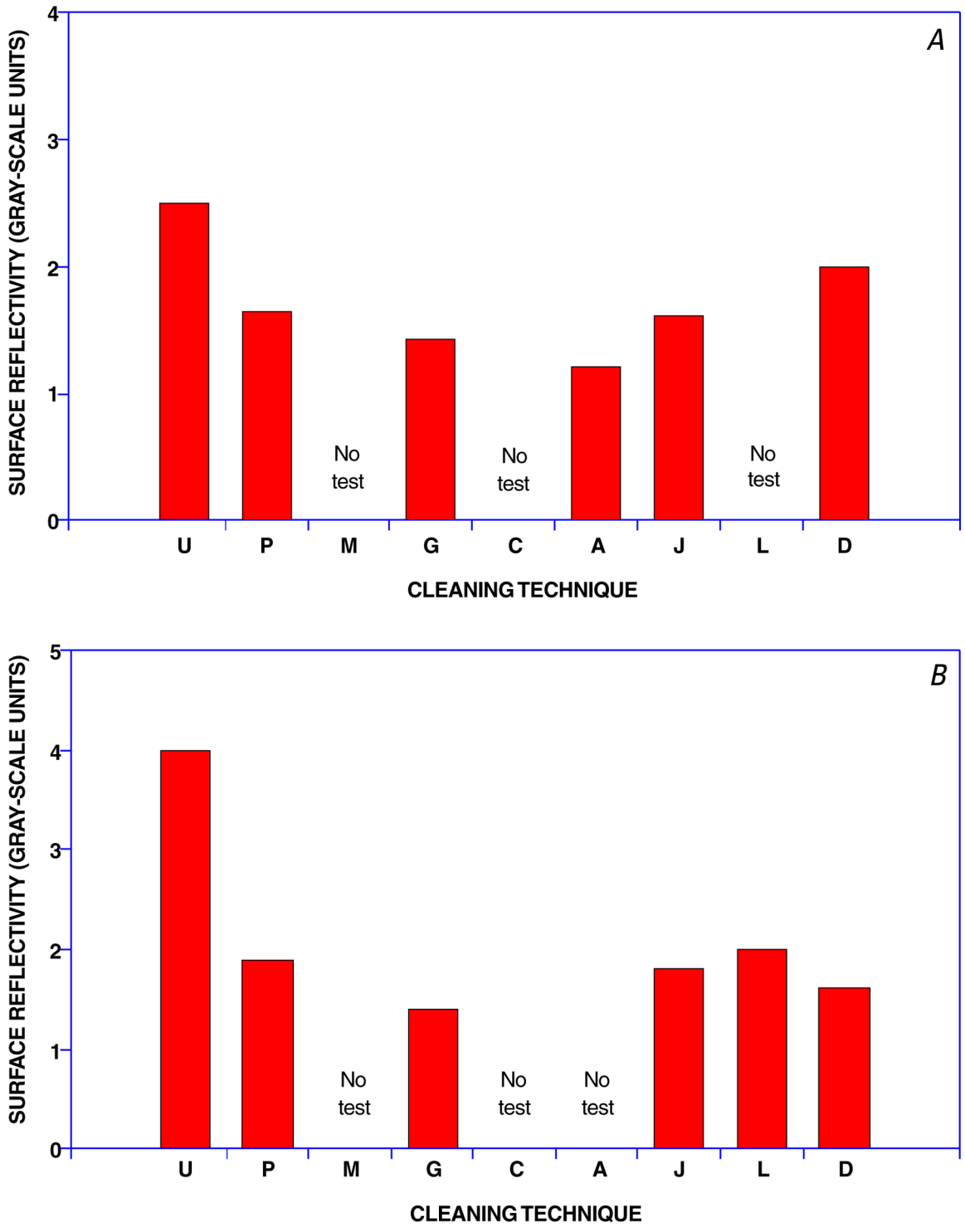

Figure 10.—Surface reflectivity (grayness value) of soiled stone after cleaning. Cleaning techniques: A, Armax; C, combination; D, dry ice; G, gommage; J, JOS; L, laser; M, misting; P, power wash; U, uncleaned. Surface-soiling conditions: lightly soiled, smooth (*A*); lightly soiled, rough (*B*); gypsum crusted, smooth (*C*); gypsum crusted, rough (*D*)—Continued.

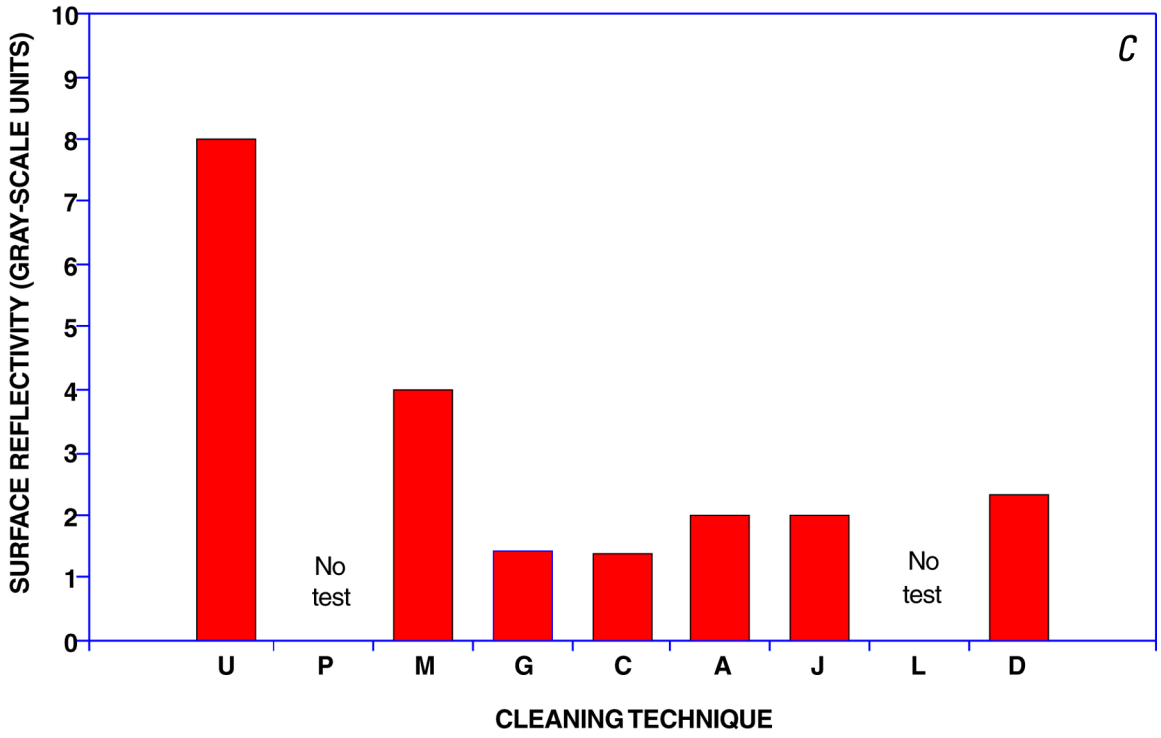

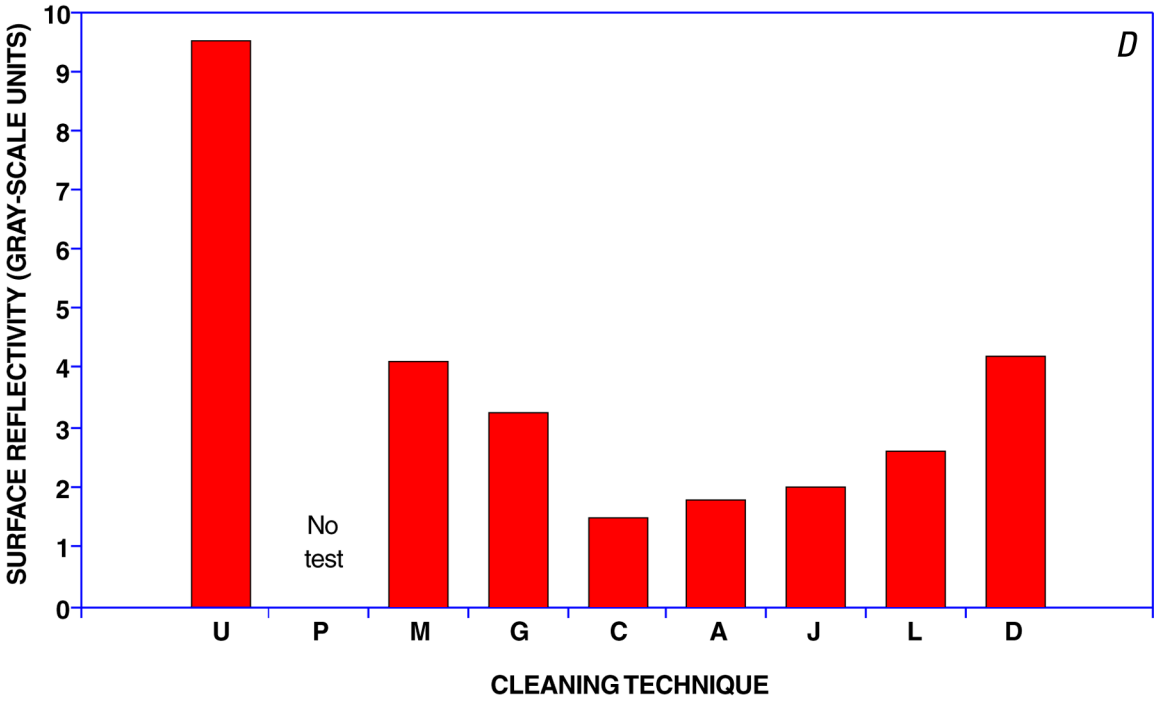

Figure 10 (Cont.)—Surface reflectivity (grayness value) of soiled stone after cleaning. Cleaning techniques: A, Armax; C, combination; D, dry ice; G, gommage; J, JOS; L, laser; M, misting; P, power wash; U, uncleaned. Surface-soiling conditions: lightly soiled, smooth (*A*); lightly soiled, rough (*B*); gypsum crusted, smooth (*C*); gypsum crusted, rough (*D*).

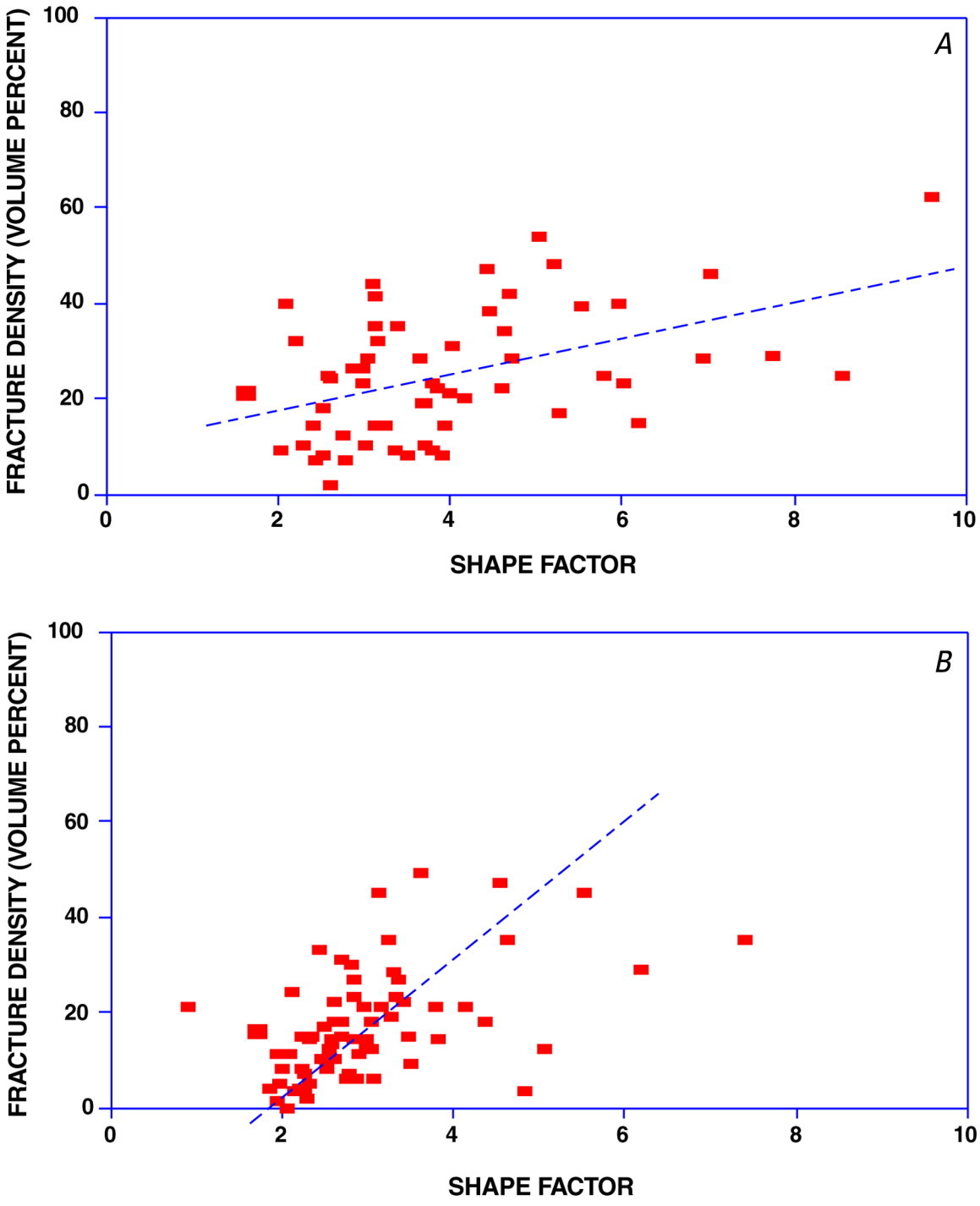

Figure 11.—Friability of stone, showing near-surface fracture density versus shape factor for all cores before (*A*) and after (*B*) cleaning, with friability index ±1σ (error bars) for various surface-soiling conditions and two groups of cleaning techniques (*C*). Straight line is best-fit curve to data points. Surface-soiling conditions: GCR, gypsum crusted, rough; GCS, gypsum crusted, smooth; LSR, lightly soiled, rough; LSS, lightly soiled, smooth. Cleaning techniques: group I, JOS, gommage, combination, and Armax; group II, dry ice, laser, misting, and power wash—Continued.

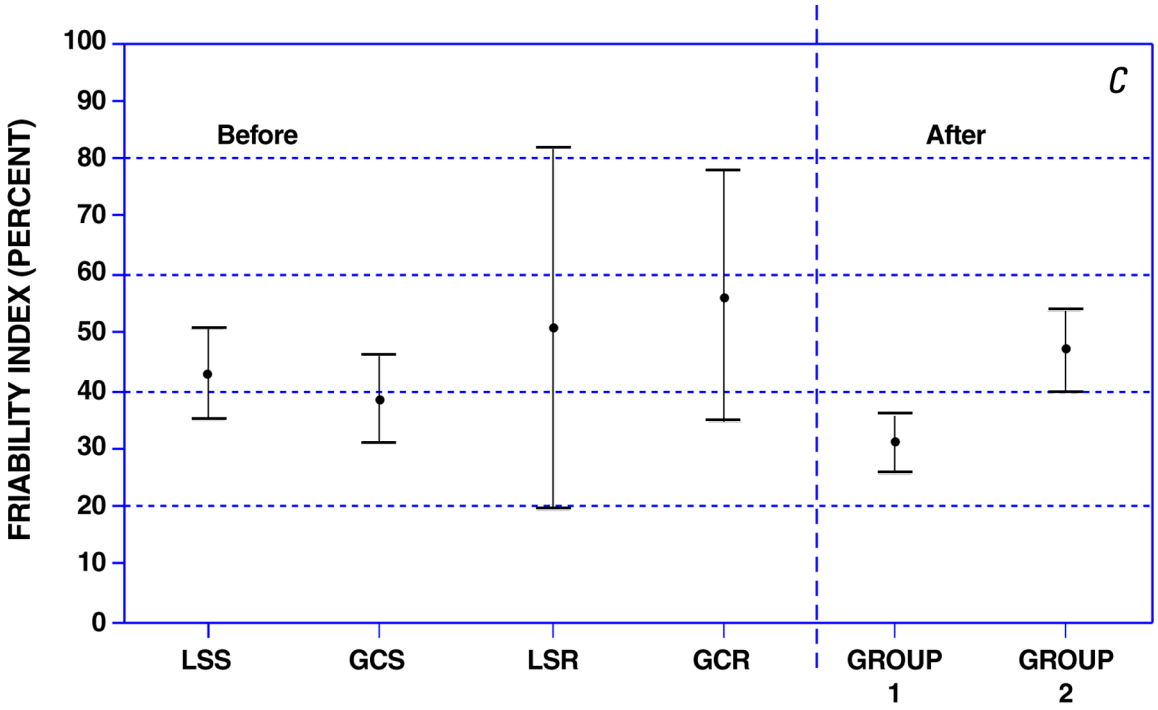

Figure 11 (Cont.)—Friability of stone, showing near-surface fracture density versus shape factor for all cores before (*A*) and after (*B*) cleaning, with friability index ±1σ (error bars) for various surface-soiling conditions and two groups of cleaning techniques (*C*). Straight line is best-fit curve to data points. Surface-soiling conditions: GCR, gypsum crusted, rough; GCS, gypsum crusted, smooth; LSR, lightly soiled, rough; LSS, lightly soiled, smooth. Cleaning techniques: group I, JOS, gommage, combination, and Armax; group II, dry ice, laser, misting, and power wash.

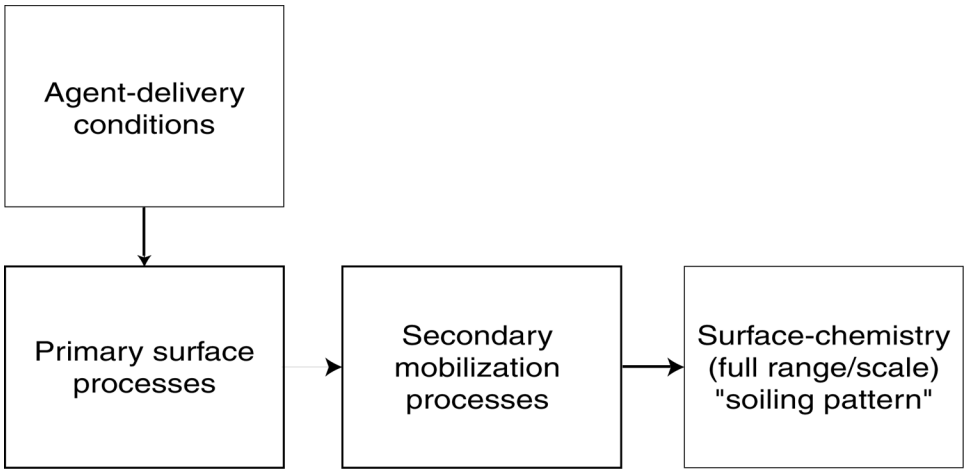

Figure 12.—Model of soiling-pattern development.

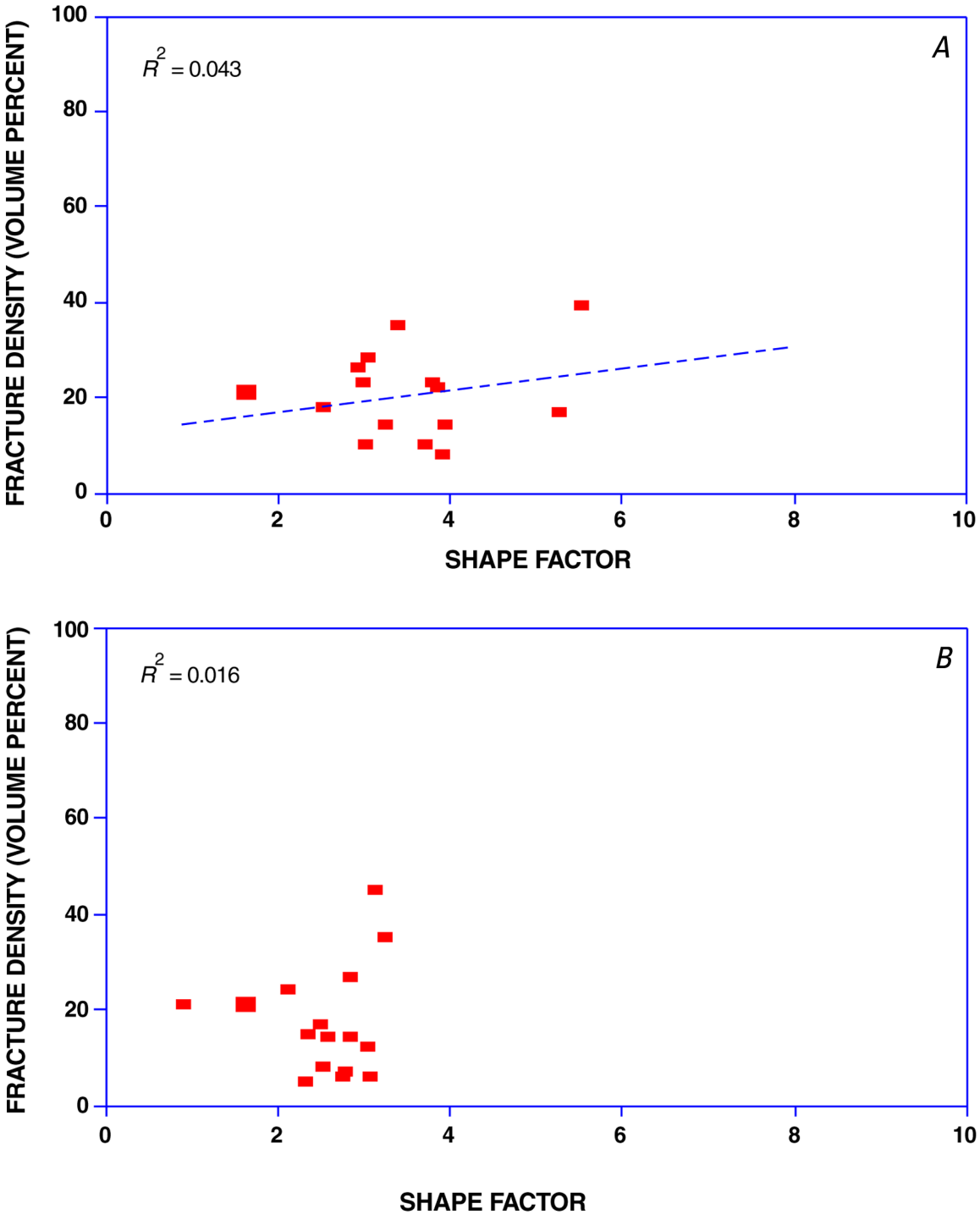

Figure 13.—Fracture density versus shape factor (in units of cm^D, where D is the surface fractal dimension) before (*A*, *C*, *E*, *G*) and after (*B*, *D*, *F*, *H*) cleaning for various surface-soiling conditions: lightly soiled, smooth (*A*, *B*); lightly soiled, rough (*C*, *D*); gypsum crusted, smooth (*E*, *F*); and gypsum crusted, rough (*G*, *H*). Least-squares regression line (dashed) is best-fit curve to data points. R^2 value, square of correlation coefficient. Textures (figs. 13*G*, 13*H*): squares, sugary; crossed squares, fractured; solid squares, all others—Continued.

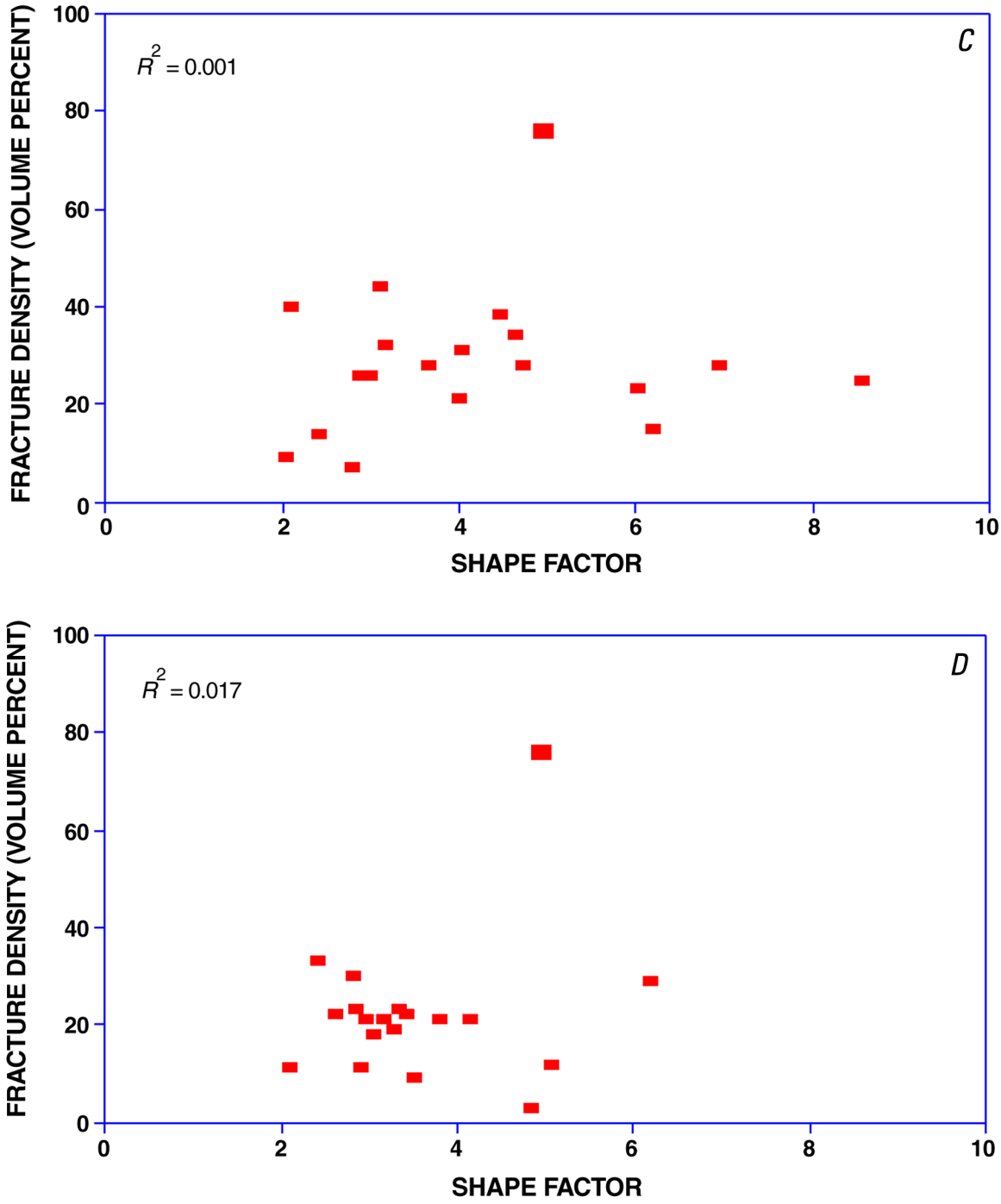

Figure 13 (Cont.)—Fracture density versus shape factor (in units of cm^D, where D is the surface fractal dimension) before (*A*, *C*, *E*, *G*) and after (*B*, *D*, *F*, *H*) cleaning for various surface-soiling conditions: lightly soiled, smooth (*A*, *B*); lightly soiled, rough (*C*, *D*); gypsum crusted, smooth (*E*, *F*); and gypsum crusted, rough (*G*, *H*). Least-squares regression line (dashed) is best-fit curve to data points. R^2 value, square of correlation coefficient. Textures (figs. 13*G*, 13*H*): squares, sugary; crossed squares, fractured; solid squares, all others—Continued.

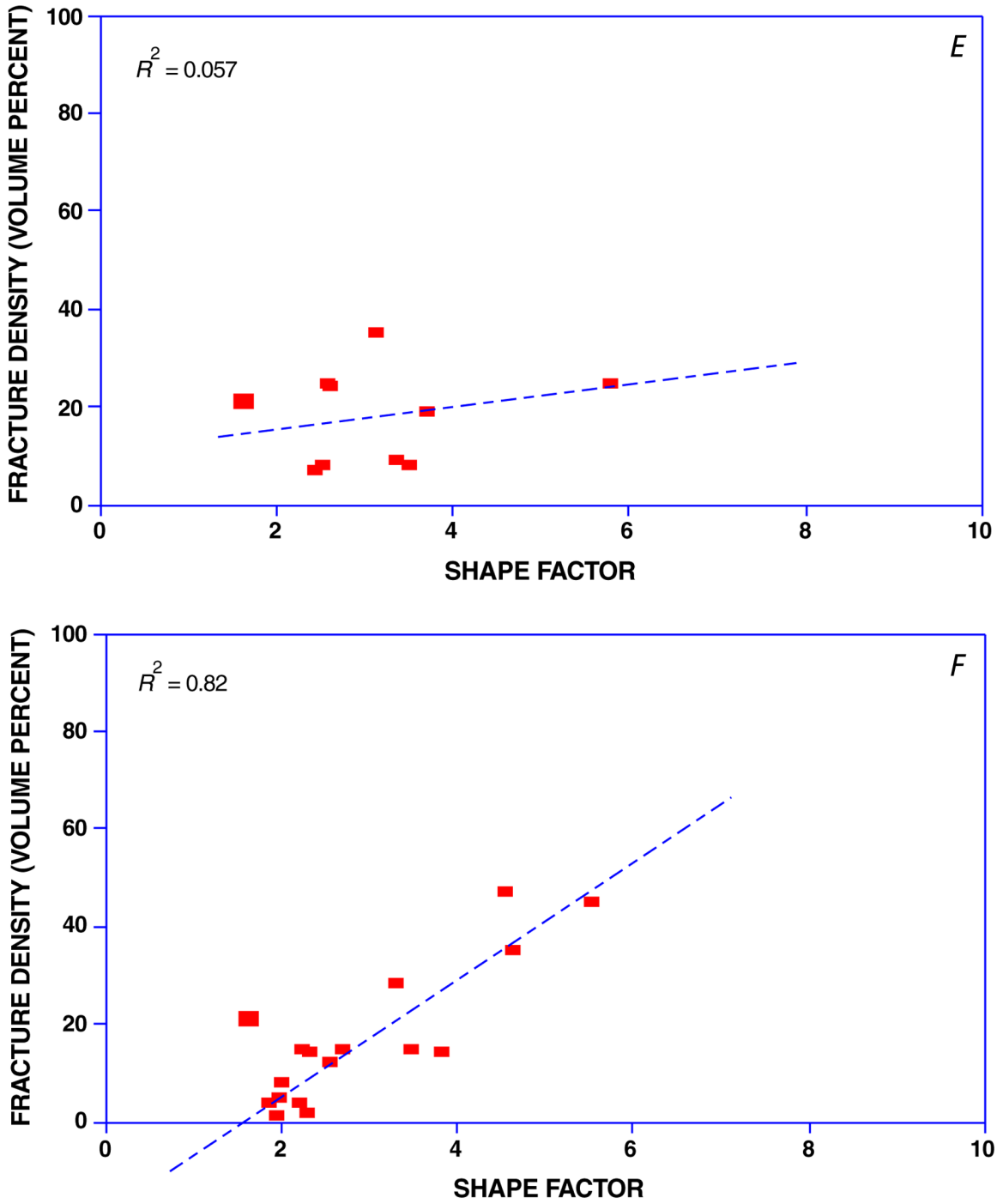

Figure 13 (Cont.)—Fracture density versus shape factor (in units of cm^D, where D is the surface fractal dimension) before (*A*, *C*, *E*, *G*) and after (*B*, *D*, *F*, *H*) cleaning for various surface-soiling conditions: lightly soiled, smooth (*A*, *B*); lightly soiled, rough (*C*, *D*); gypsum crusted, smooth (*E*, *F*); and gypsum crusted, rough (*G*, *H*). Least-squares regression line (dashed) is best-fit curve to data points. R^2 value, square of correlation coefficient. Textures (figs. 13*G*, 13*H*): squares, sugary; crossed squares, fractured; solid squares, all others—Continued.

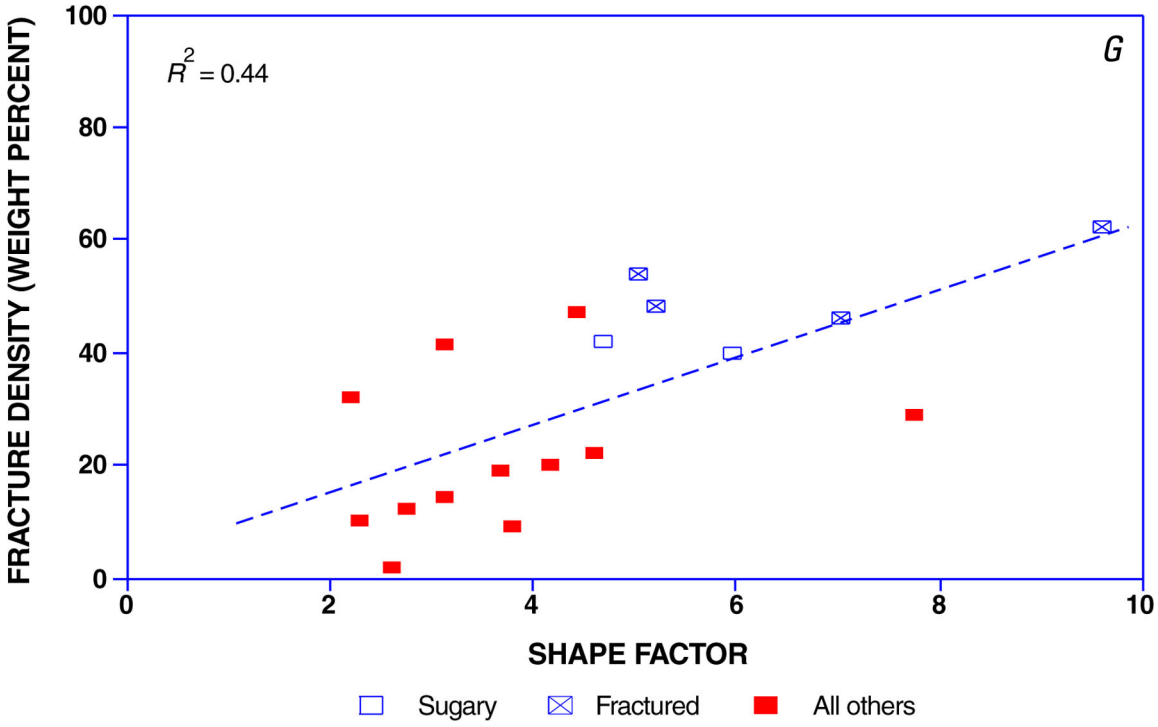

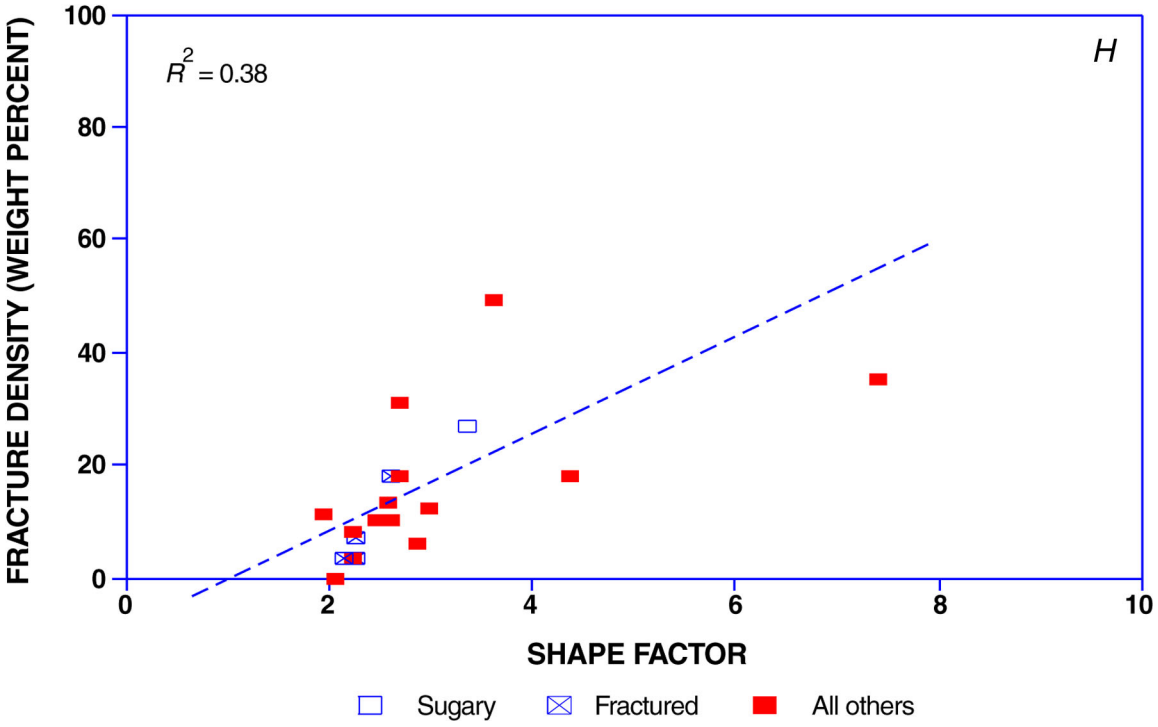

Figure 13 (Cont.)—Fracture density versus shape factor (in units of cm^D, where D is the surface fractal dimension) before (*A*, *C*, *E*, *G*) and after (*B*, *D*, *F*, *H*) cleaning for various surface-soiling conditions: lightly soiled, smooth (*A*, *B*); lightly soiled, rough (*C*, *D*); gypsum crusted, smooth (*E*, *F*); and gypsum crusted, rough (*G*, *H*). Least-squares regression line (dashed) is best-fit curve to data points. R^2 value, square of correlation coefficient. Textures (figs. 13*G*, 13*H*): squares, sugary; crossed squares, fractured; solid squares, all others.

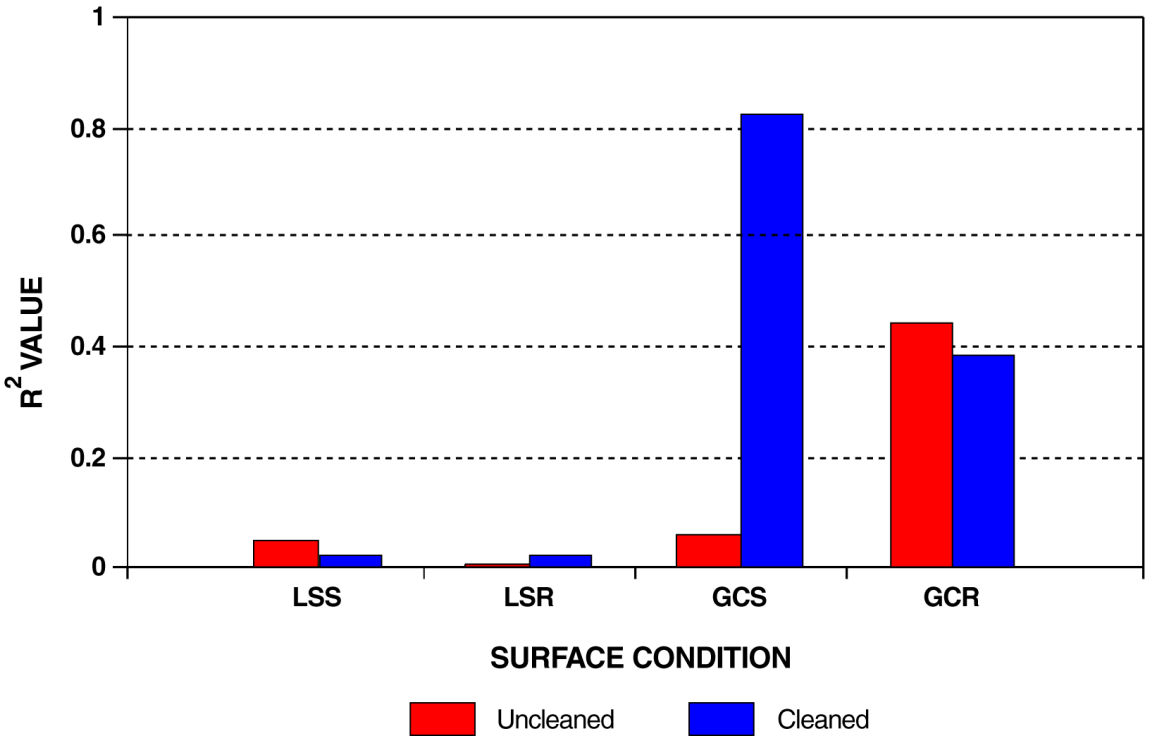

Figure 14.—R^2 value (square of correlation coefficient) versus surface-soiling condition of stone for data plotted in figure 13.

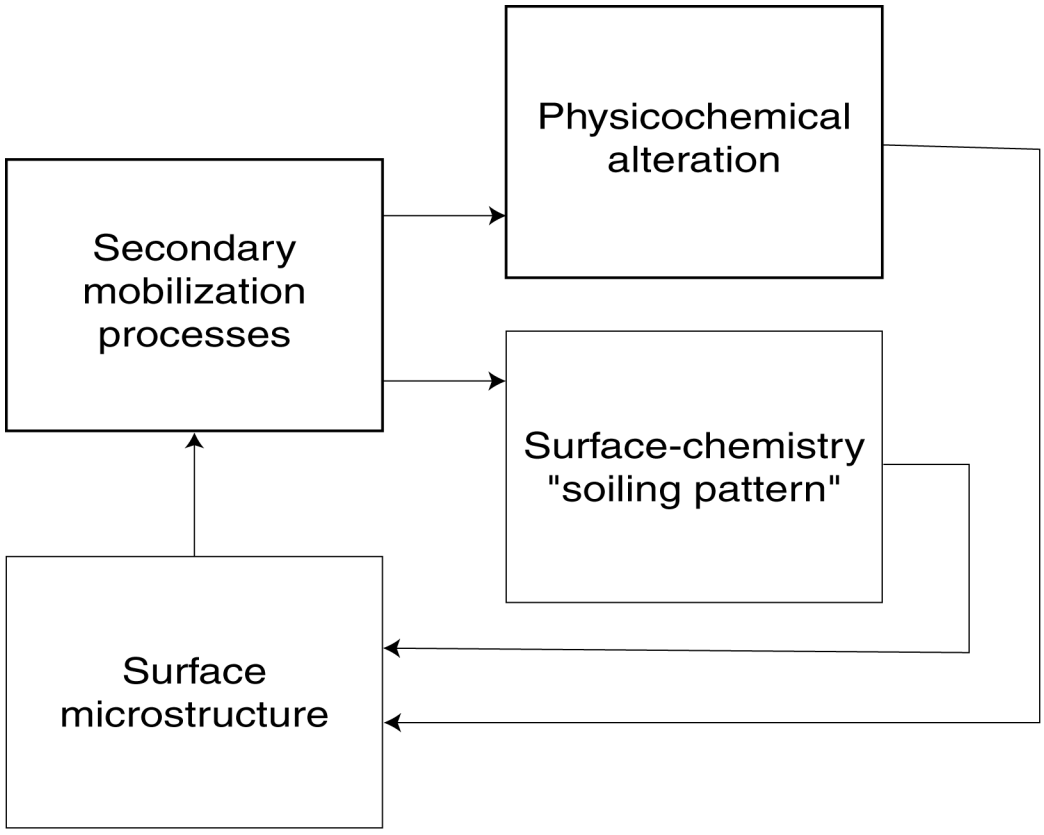

Figure 15.—Model of surface alteration by soiling load.

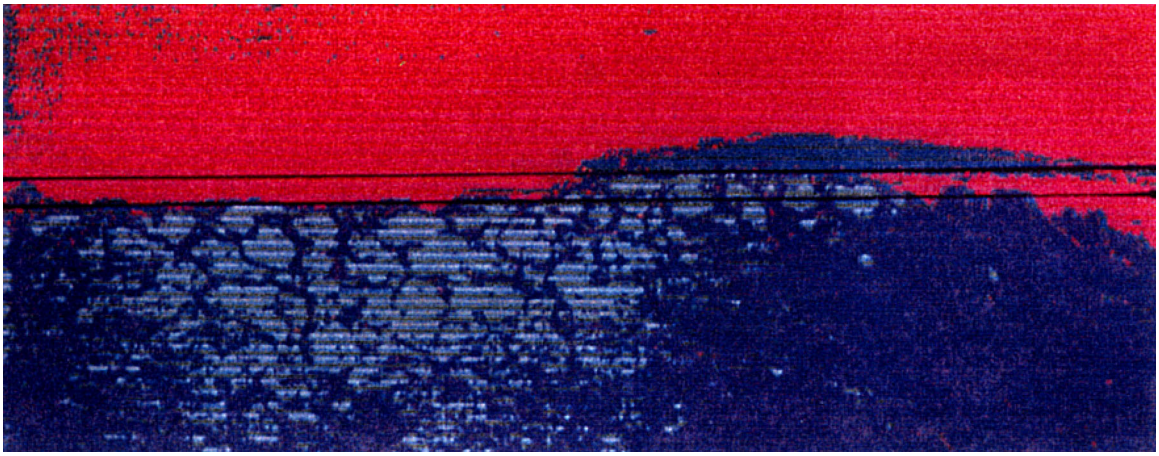

Figure 16.—Output of program EDGE (see app. 2) for cleaned side of sample GCRC–1 (left side of image), showing ~278 µm of surface recession. Red, potting epoxy resin; green, fast-curing epoxy resin; blue and light green, stone matrix. Magnification, 10x.

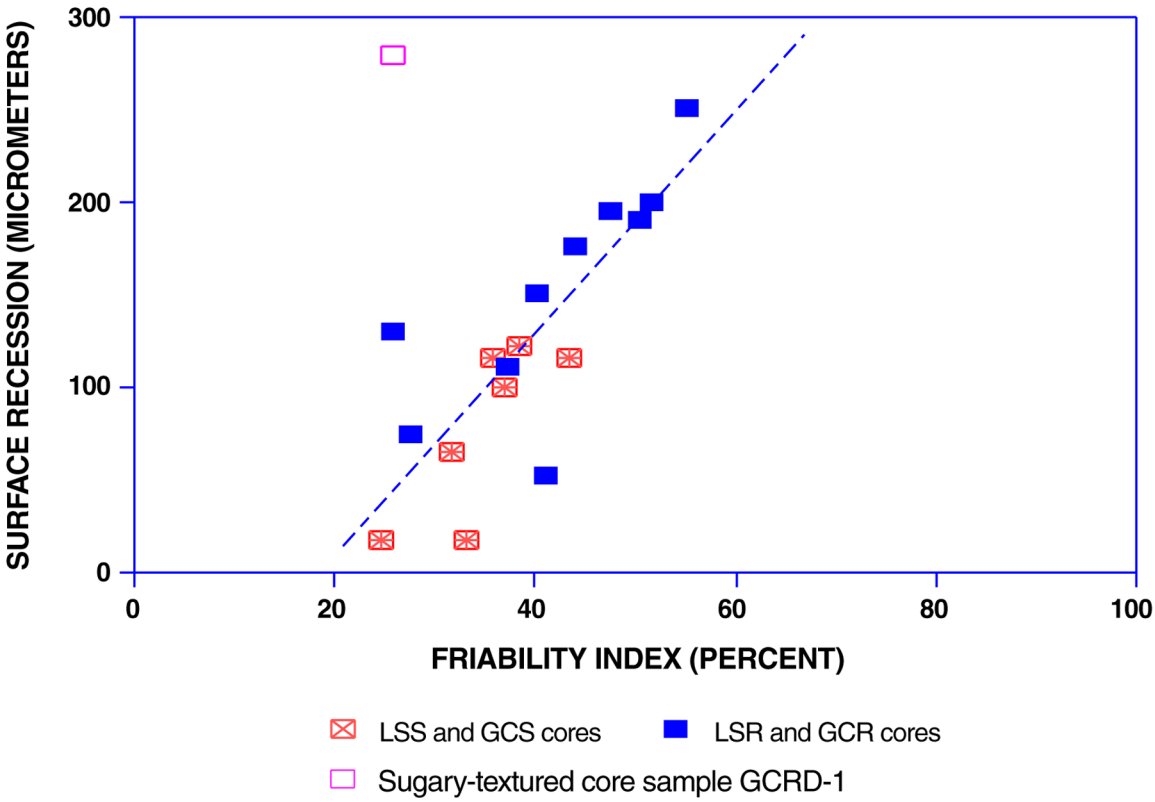

Figure 17.—Surface recession versus friability index for two groups of smooth and rough uncleaned cores. Surface-soiling conditions: GCR, gypsum crusted, rough; GCS, gypsum crusted, smooth; LSR, lightly soiled, rough; LSS, lightly soiled, smooth. Least-squares regression line (dashed) excludes data point for sugary-textured sample GCRD–1.

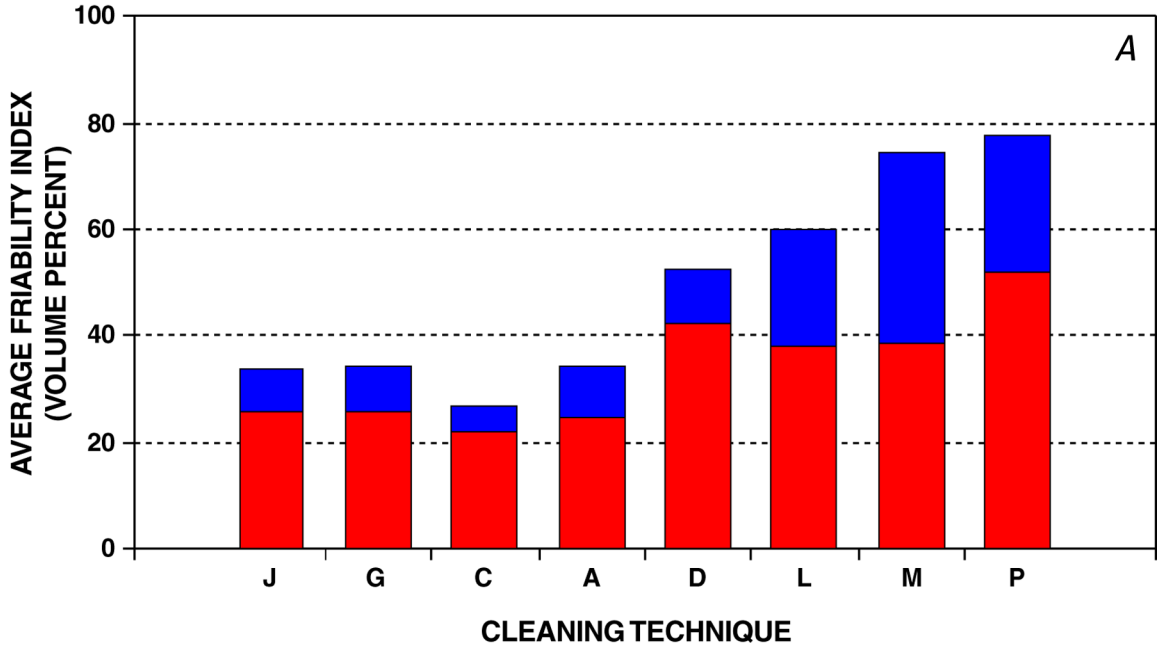

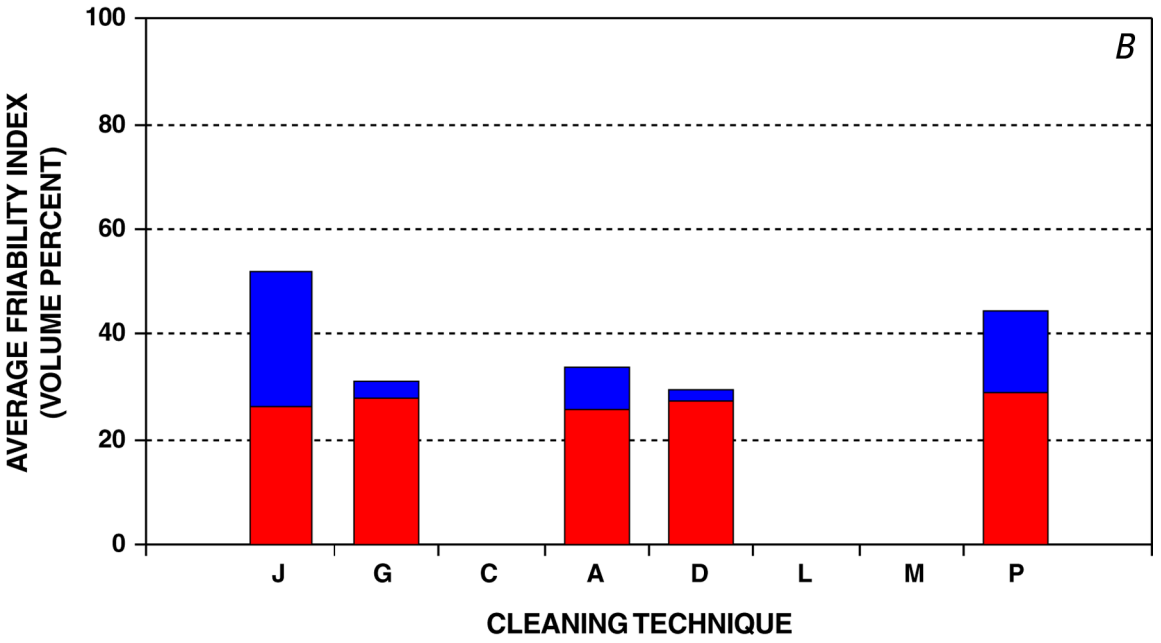

Figure 18.—Average friability index after application of each cleaning technique for all cores tested. Cleaning techniques: A, Armax; C, combination; D, dry ice; G, gommage; J, JOS; L, laser; M, misting; P, power wash. Black bars indicate 2σ. *A*, Cores with all surface-soiling conditions. *B*, All lightly soiled, smooth cores. *C*, All lightly soiled, rough cores. *D*, All gypsum crusted, smooth cores. *E*, All gypsum crusted, rough cores—Continued.

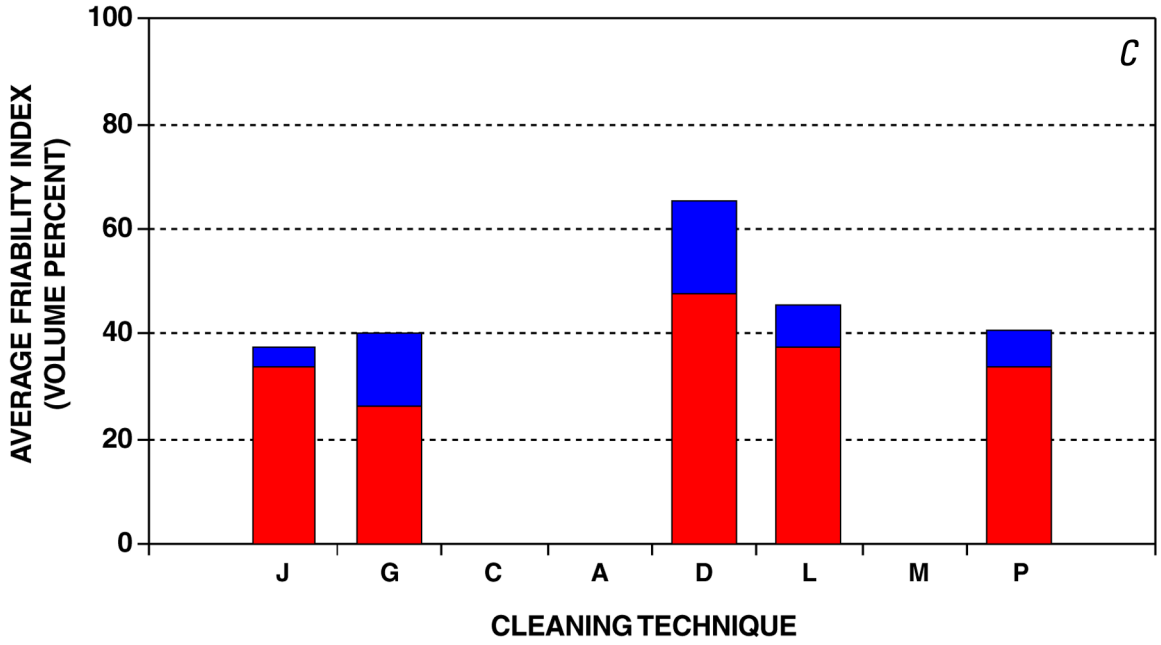

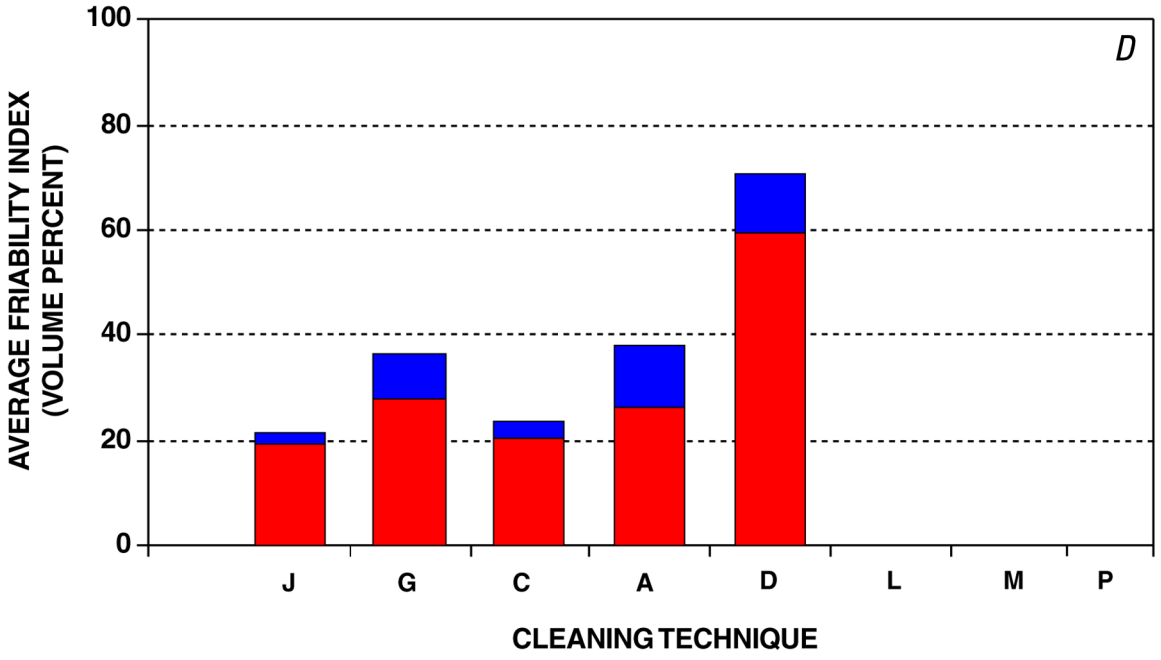

Figure 18 (Cont.)—Average friability index after application of each cleaning technique for all cores tested. Cleaning techniques: A, Armax; C, combination; D, dry ice; G, gommage; J, JOS; L, laser; M, misting; P, power wash. Black bars indicate 2σ. *A*, Cores with all surface-soiling conditions. *B*, All lightly soiled, smooth cores. *C*, All lightly soiled, rough cores. *D*, All gypsum crusted, smooth cores. *E*, All gypsum crusted, rough cores—Continued.

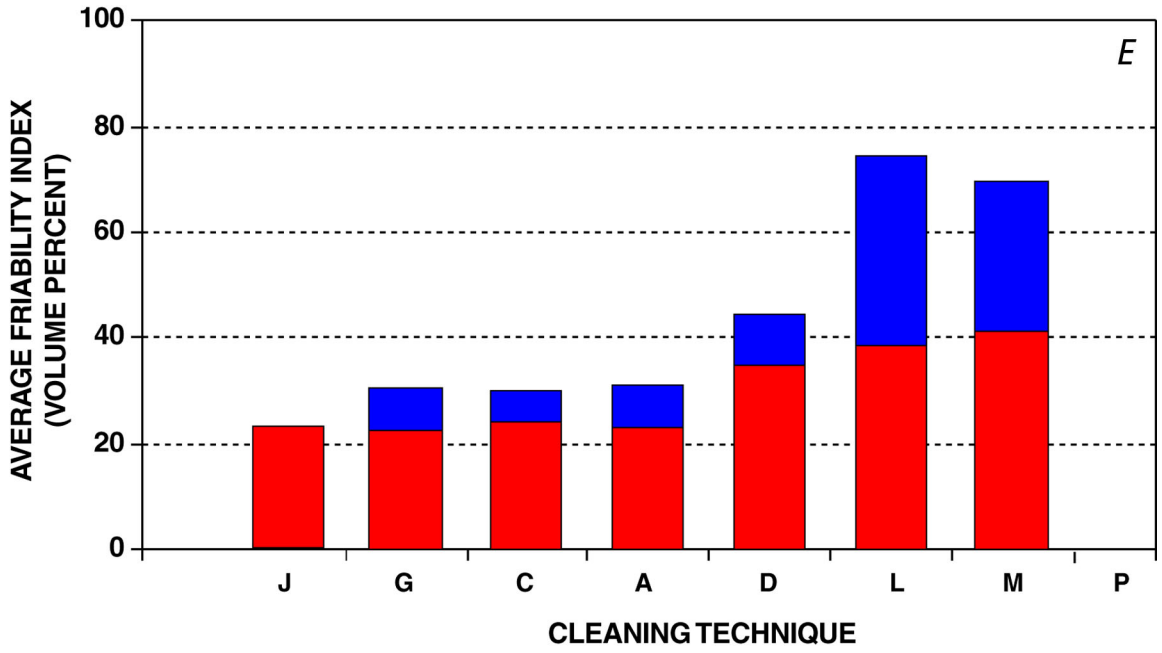

Figure 18 (Cont.)—Average friability index after application of each cleaning technique for all cores tested. Cleaning techniques: A, Armax; C, combination; D, dry ice; G, gommage; J, JOS; L, laser; M, misting; P, power wash. Black bars indicate 2σ. *A*, Cores with all surface-soiling conditions. *B*, All lightly soiled, smooth cores. *C*, All lightly soiled, rough cores. *D*, All gypsum crusted, smooth cores. *E*, All gypsum crusted, rough cores.

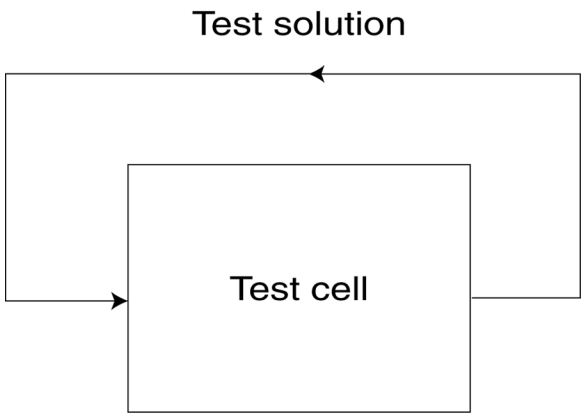

Figure 19.—Model of laboratory configuration used for implementation of surface-reactivity tests. Surface flow rate, ≥0.01 cm^3/s per centimeter of contour.

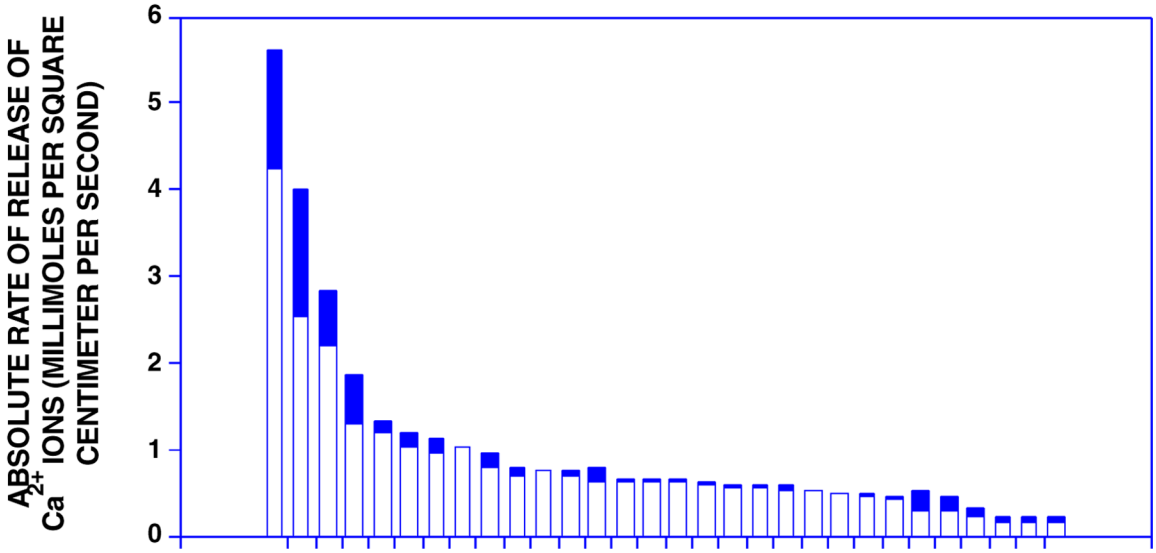

Figure 20.—Absolute rate of release of Ca^{2+} ions for all cores tested, in descending order. Black bars indicate 2σ.

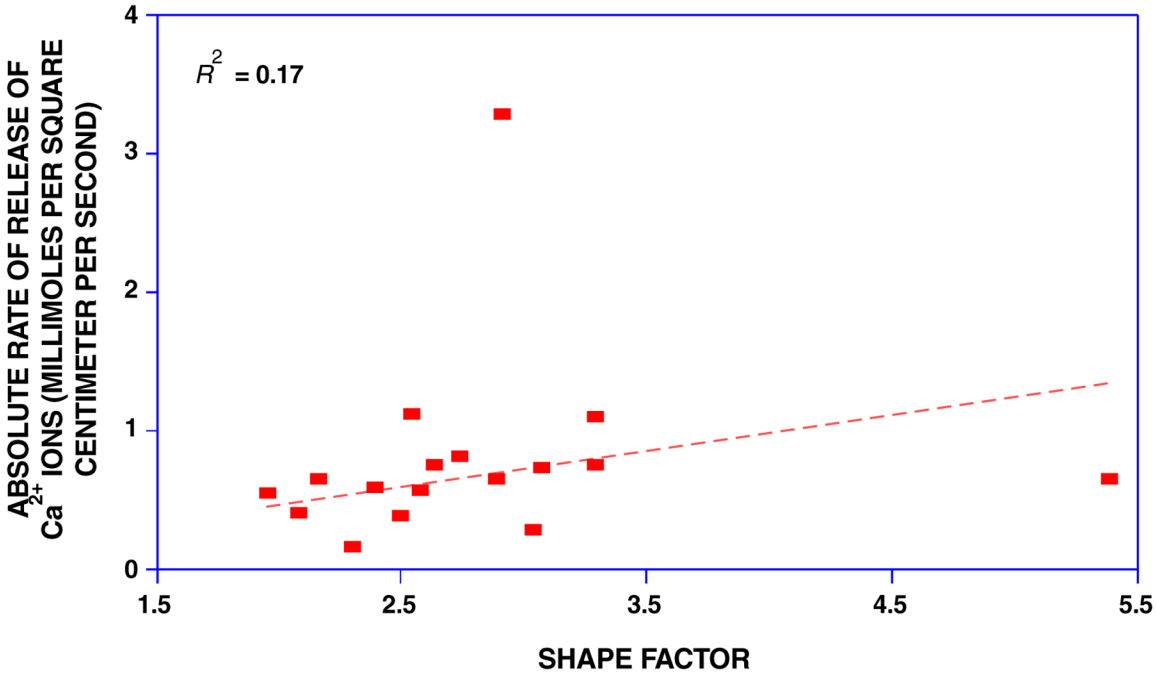

Figure 21.—Absolute rate of release of Ca^{2+} ions versus shape factor for all cleaned cores. R^2 value, square of correlation coefficient. Two most erratic data points have been omitted from least-squares regression line (dashed).

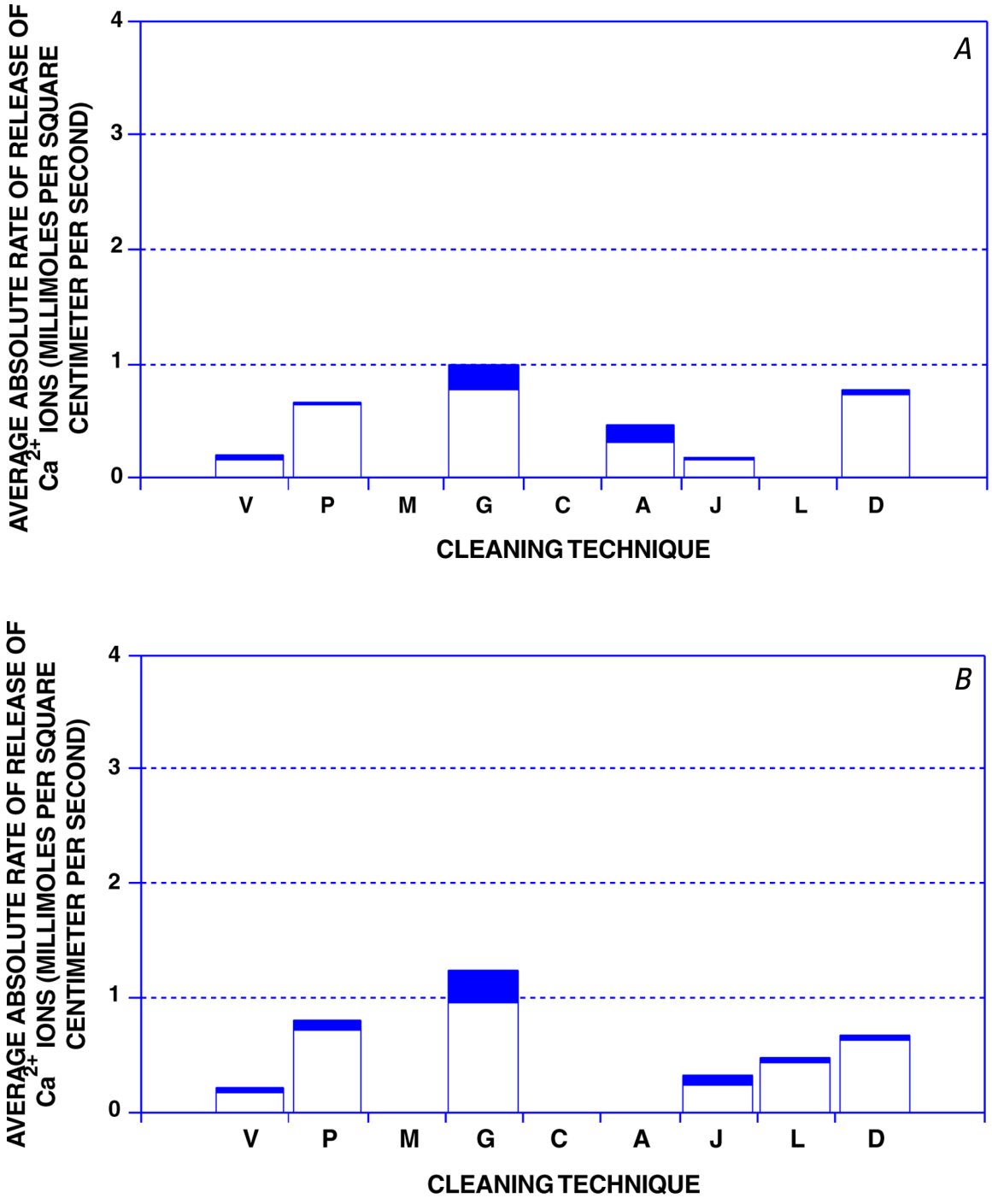

Figure 22.—Average absolute rate of release of Ca^{2+} ions for each cleaning technique for various surface-soiling conditions: lightly soiled, smooth (*A*); lightly soiled, rough (*B*); gypsum crusted, smooth (*C*); and gypsum crusted, rough (*D*). Cleaning techniques: A, Armax; C, combination; D, dry ice; G, gommage; J, JOS; L, laser; M, misting; P, power wash; V, virgin. Black bars indicate 2σ—Continued.

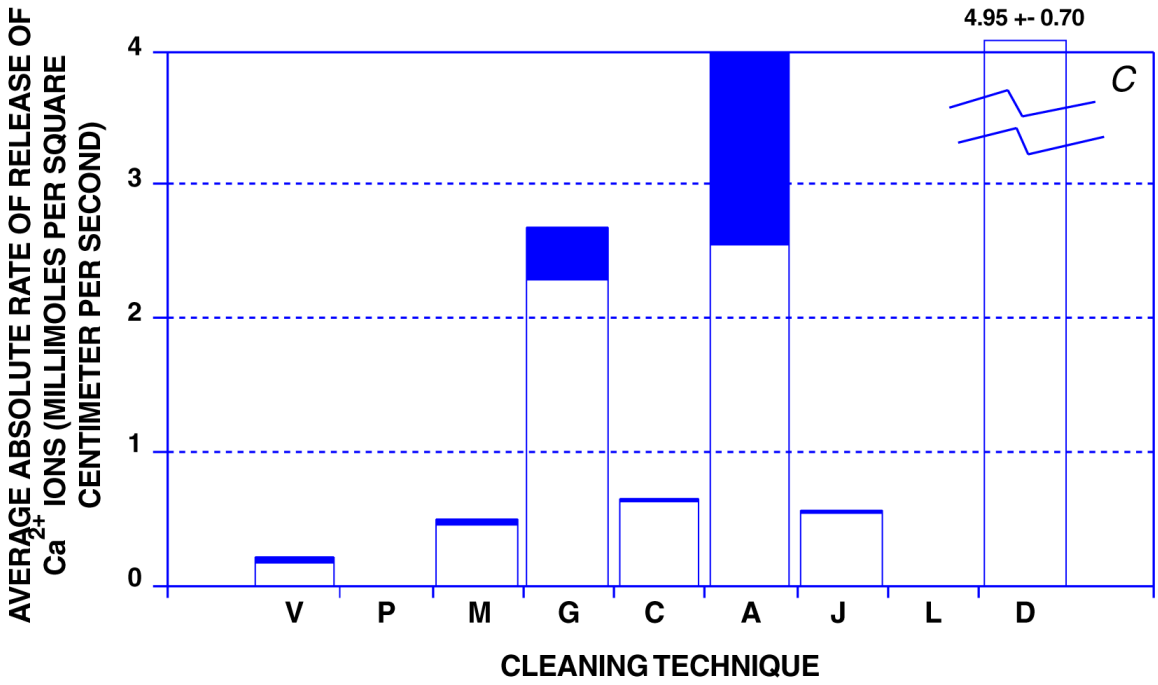

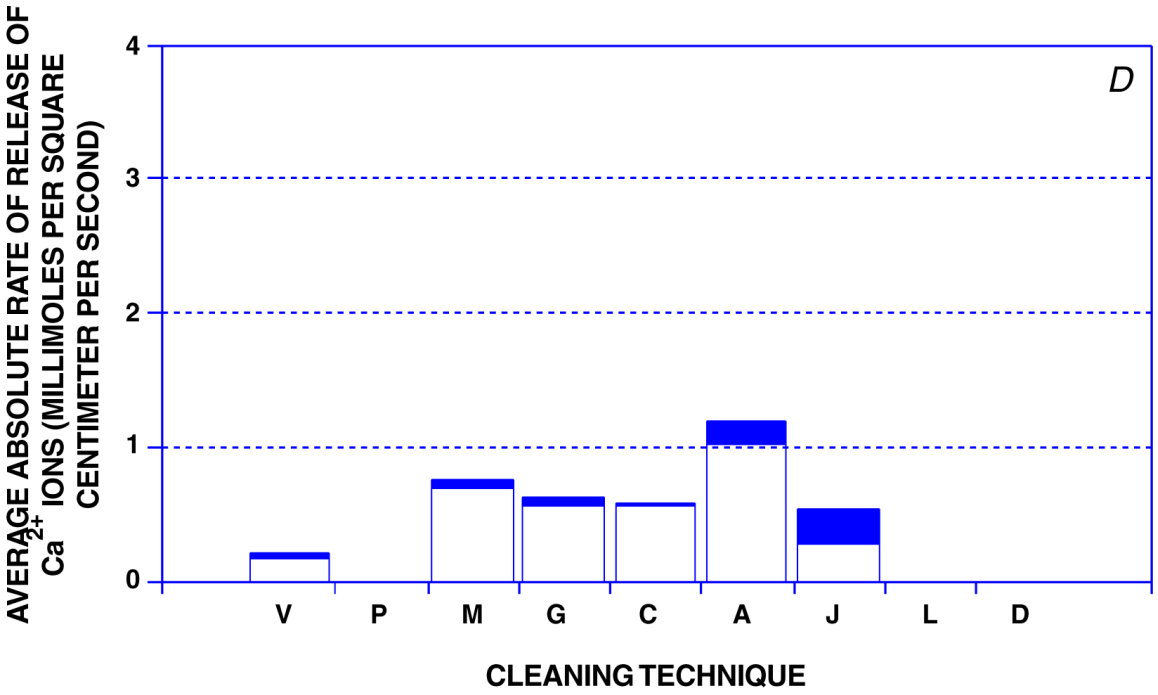

Figure 22 (Cont.)—Average absolute rate of release of Ca^{2+} ions for each cleaning technique for various surface-soiling conditions: lightly soiled, smooth (*A*); lightly soiled, rough (*B*); gypsum crusted, smooth (*C*); and gypsum crusted, rough (*D*). Cleaning techniques: A, Armax; C, combination; D, dry ice; G, gommage; J, JOS; L, laser; M, misting; P, power wash; V, virgin. Black bars indicate 2σ.

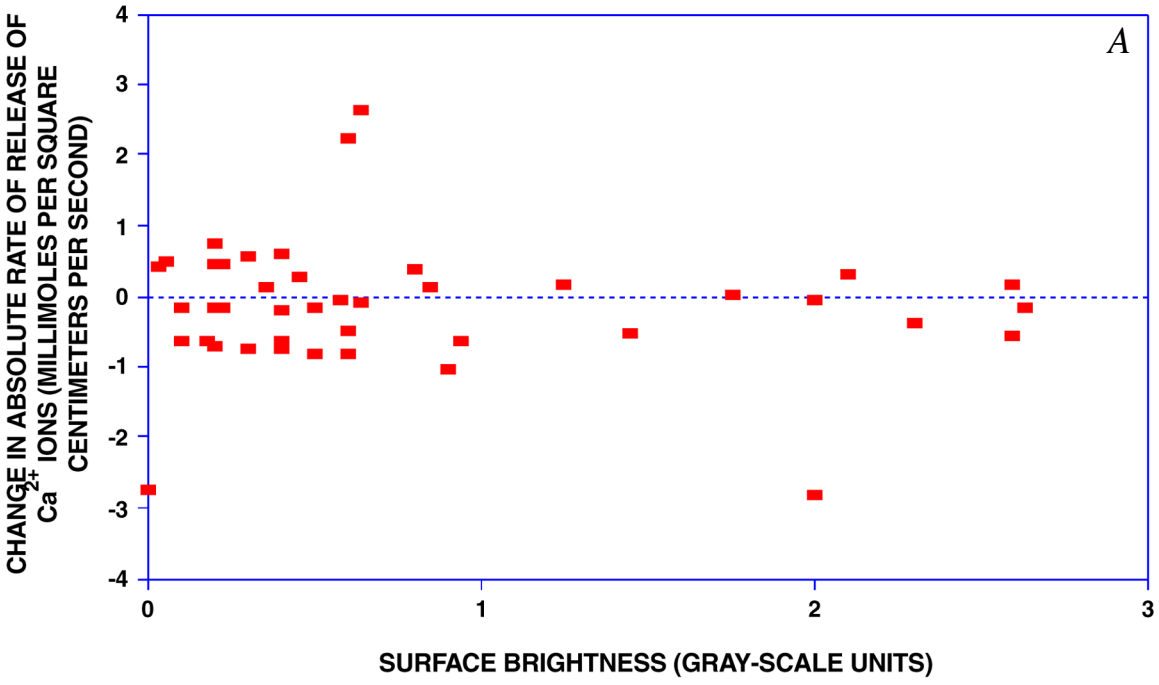

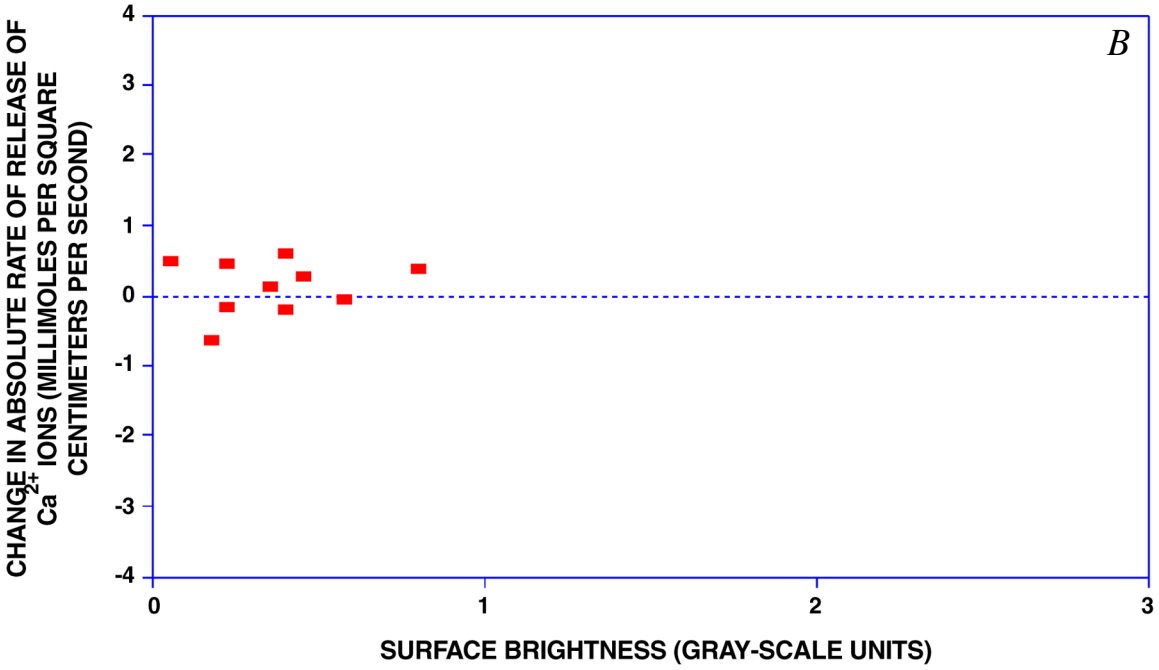

Figure 23.—Change in absolute rate of release of Ca^{2+} ions versus surface color for all cores (*A*) and for various surface-soiling conditions: lightly soiled, smooth (*B*); lightly soiled, rough (*C*); gypsum crusted, smooth (*D*); and gypsum crusted, rough (*E*)—Continued.

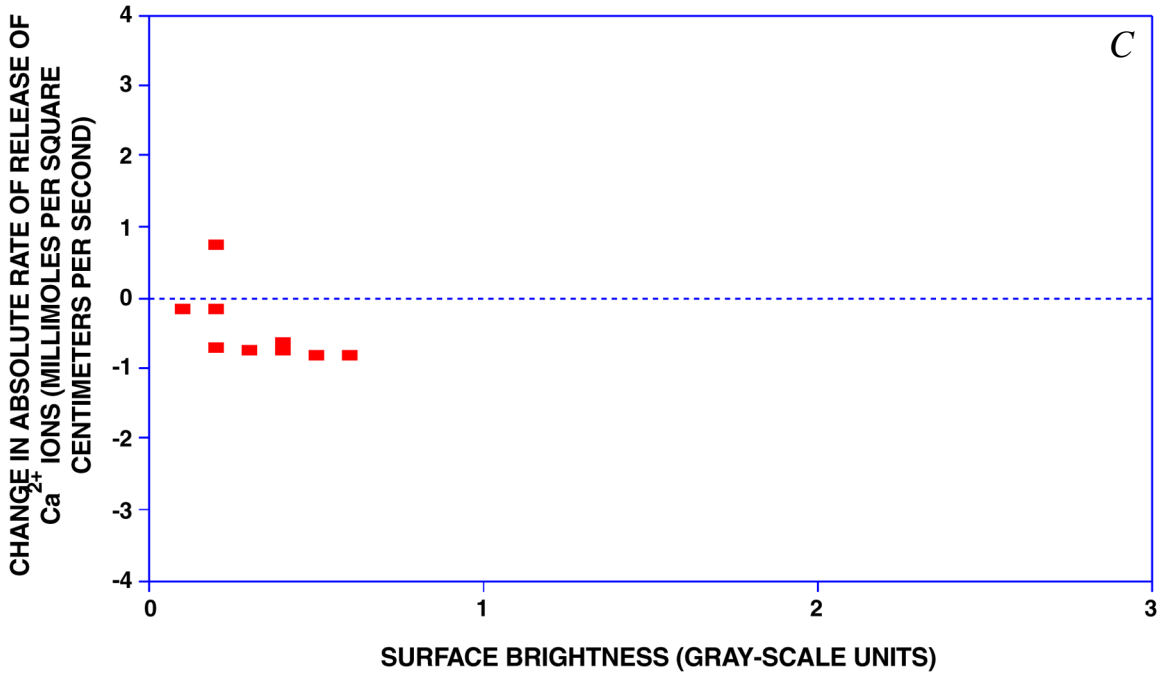

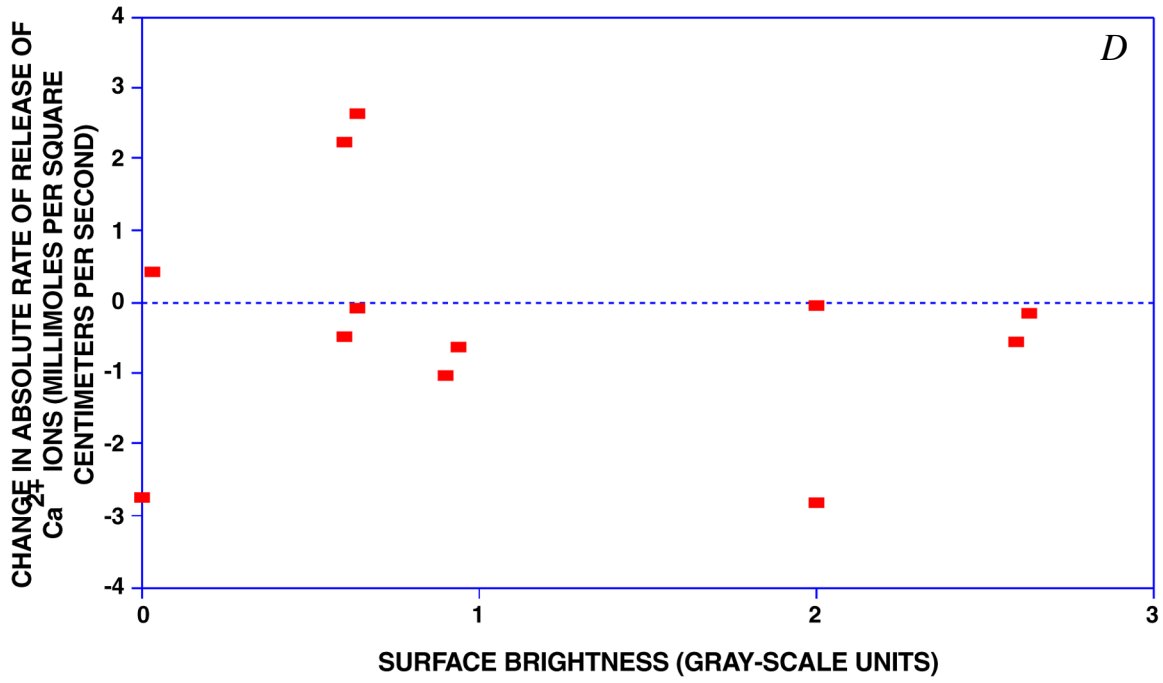

Figure 23 (Cont.)—Change in absolute rate of release of Ca^{2+} ions versus surface color for all cores (*A*) and for various surface-soiling conditions: lightly soiled, smooth (*B*); lightly soiled, rough (*C*); gypsum crusted, smooth (*D*); and gypsum crusted, rough (*E*)—Continued.

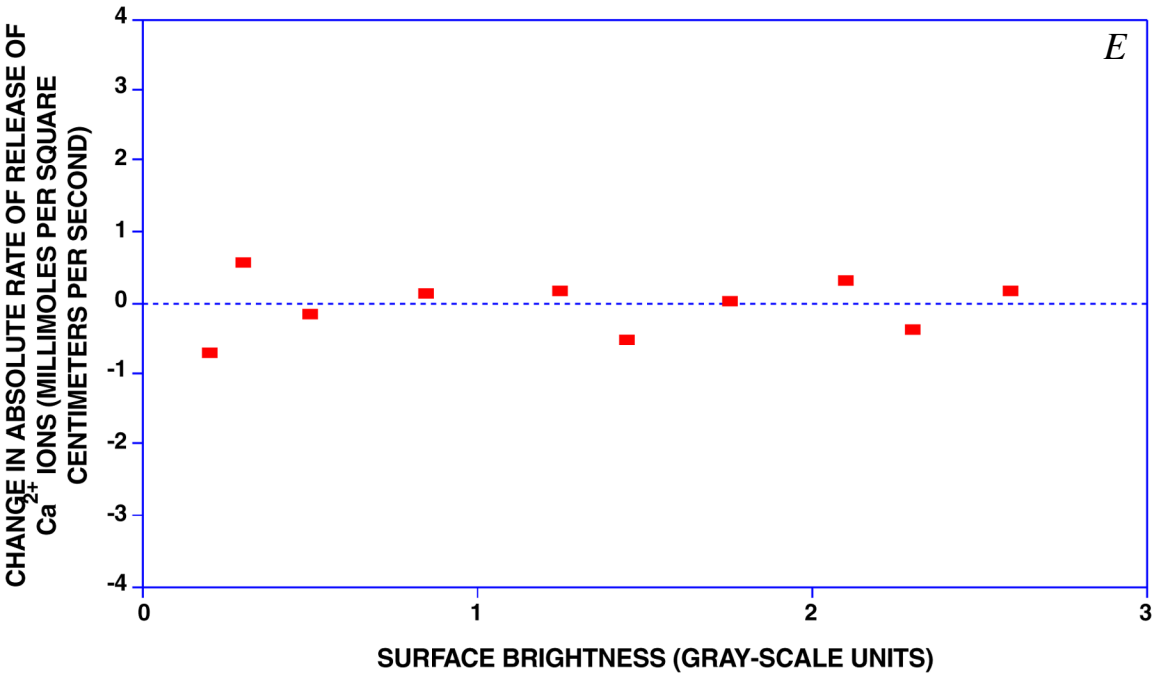

Figure 23 (Cont.)—Change in absolute rate of release of Ca^{2+} ions versus surface color for all cores (*A*) and for various surface-soiling conditions: lightly soiled, smooth (*B*); lightly soiled, rough (*C*); gypsum crusted, smooth (*D*); and gypsum crusted, rough (*E*).

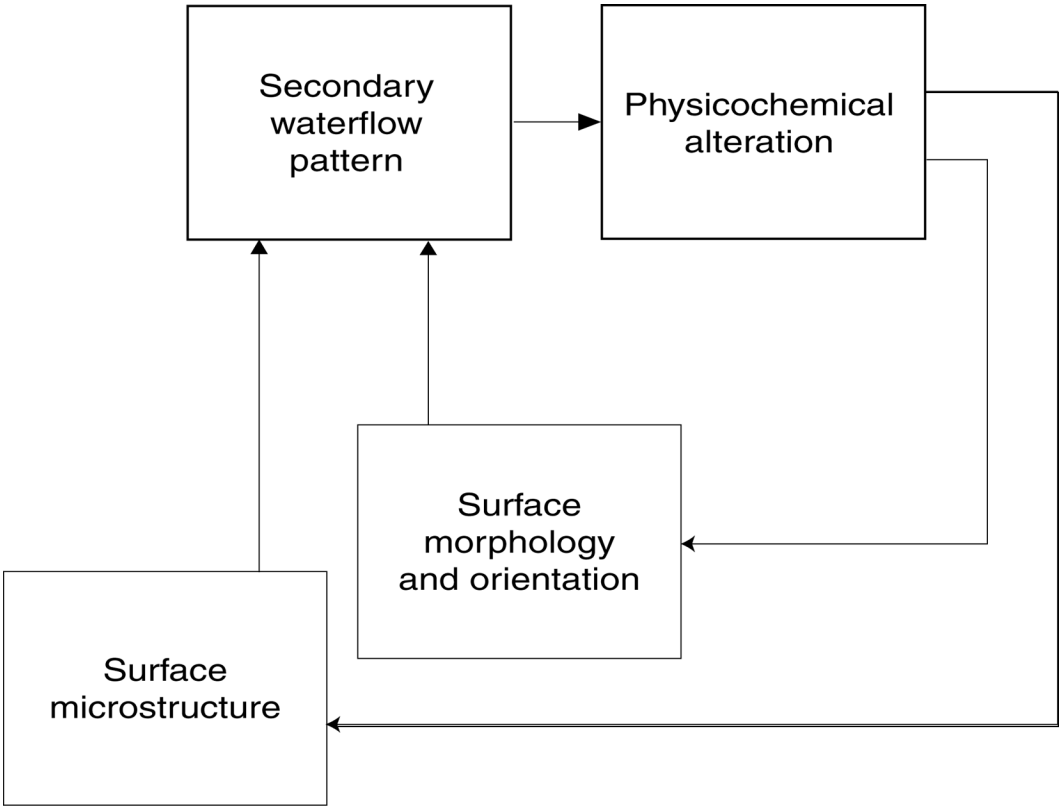

Figure 24.—Model of physical alteration of stone surface by water. Panel labeled "Physicochemical alteration" comprises various physical and chemical processes that can result in changes of surface morphology from nanoscale to macroscale.

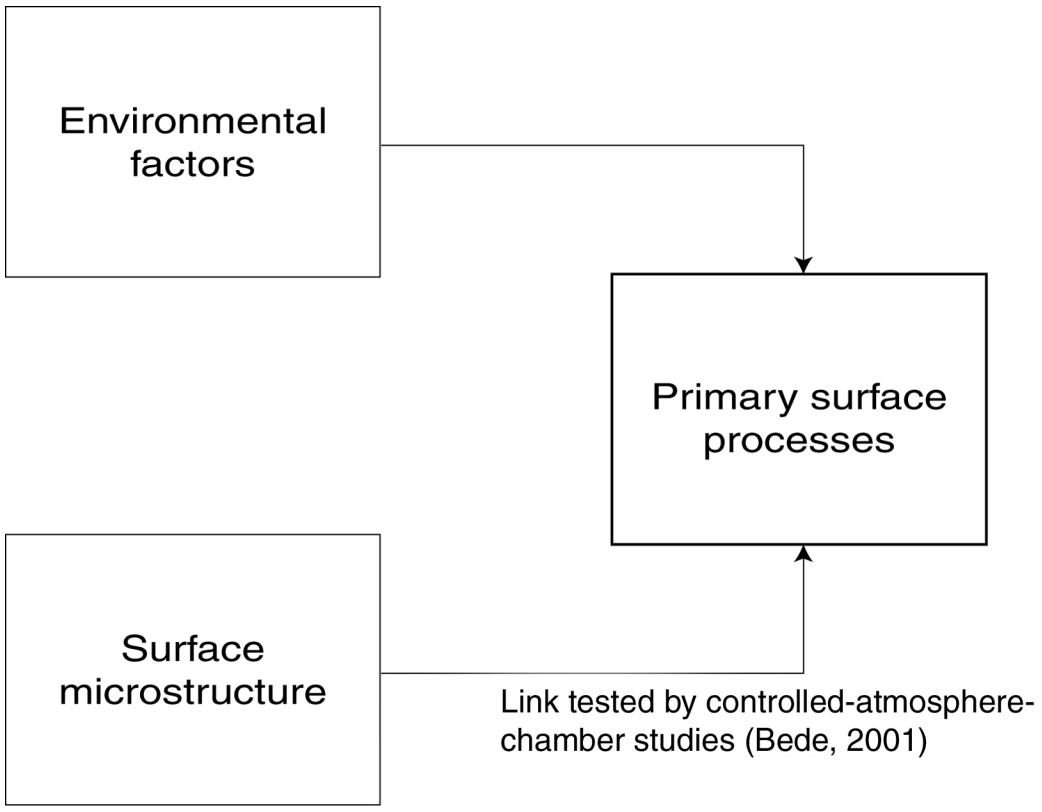

Figure 25.—Model of factors controlling deposition of salts and particulate matter on stone surface.

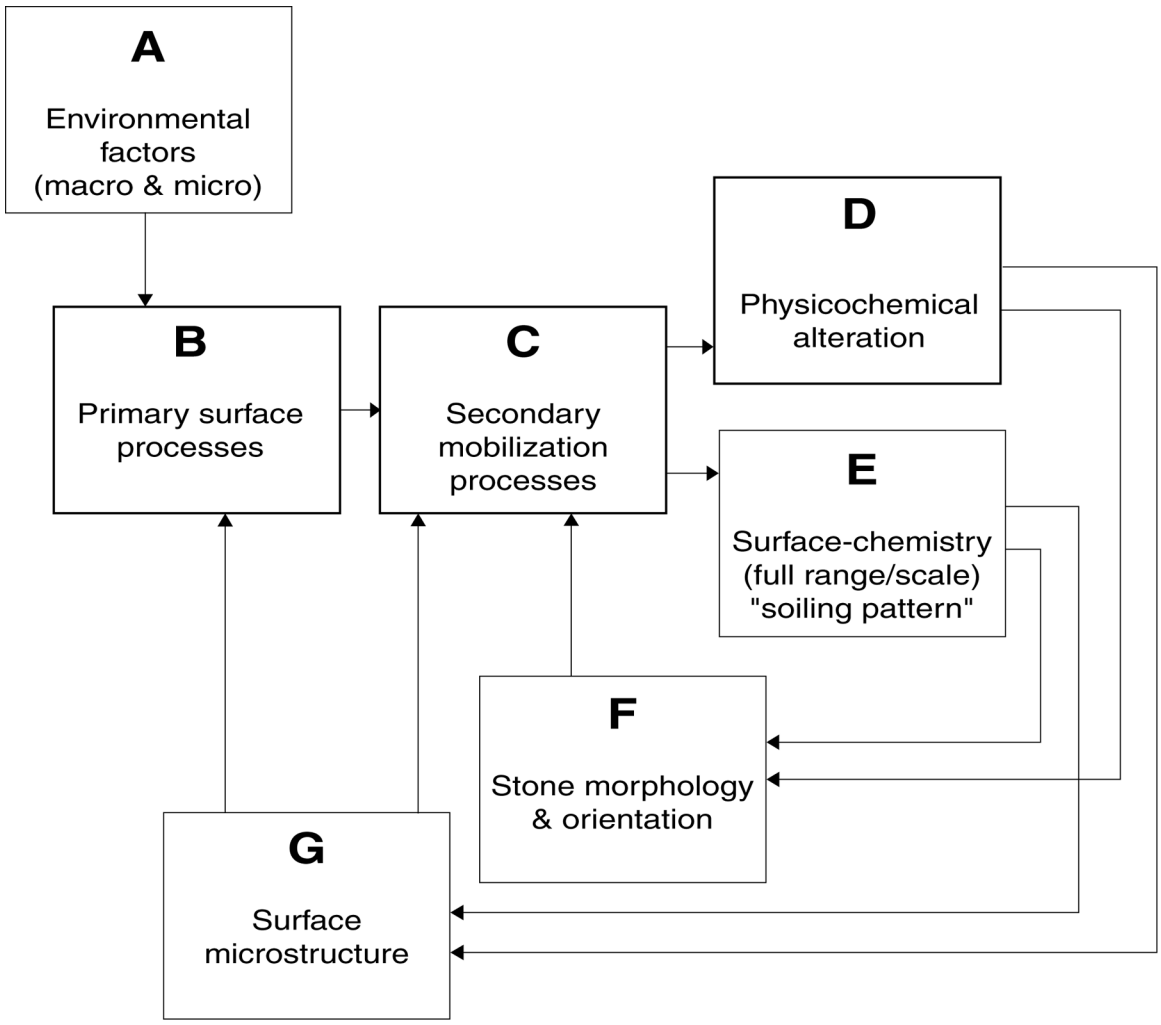

Figure 26.—Integrated model of dominant soiling-agent-delivery and stone-alteration processes. Boxes A, E, F, and G represent collections of variables that drive the processes represented in panels B, C, and D. Box A includes variables controlling extraneous inputs to the system, including ambient SO_2 concentration; meteorologic and geotechnical conditions to which system is subjected: rain, diurnal moisture, and rising damp-delivery patterns; and level of airborne particulate matter. Implicit in connections between panels B and C is the assumption that primary rate of deposition of SO_2 and airborne particulate matter is closely linked to the total amount of soiling agents available for secondary mobilization and deposition on the building. Otherwise stated, primary deposition processes feed secondary mobilization processes. Panel D represents processes related to rate of loss of utility resulting from mass loss, changes in microstructure, and changes in surface morphology. Boxes E, F, and G represent state variables of the system, including a complete set of physicochemical variables required to define the state of the system. For the purposes of this study, box E represents system output. Because delivery and transport processes represented by box A and panels B and C control surface waterflow pattern, these variables define the physical extent of the system and set an upper limit on the range of scale over which processes represented by panels B, C, and D operate.

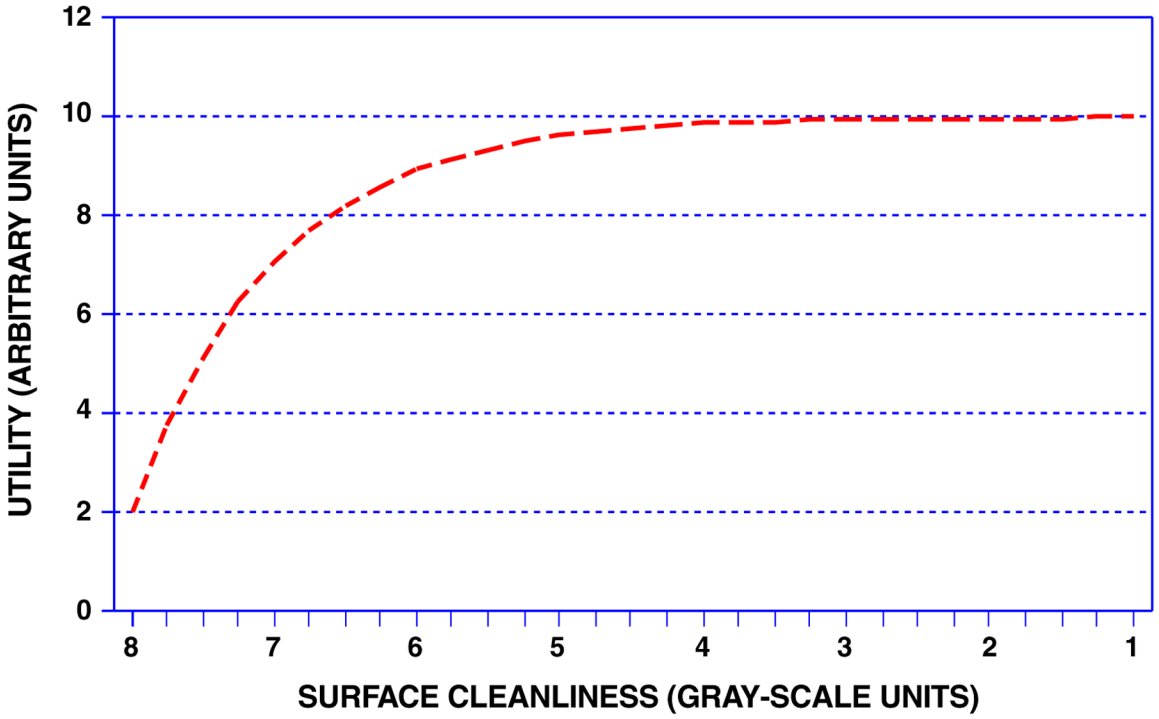

Figure 27.—Utility versus surface cleanliness, showing general shape of esthetic-utility curve for the building.

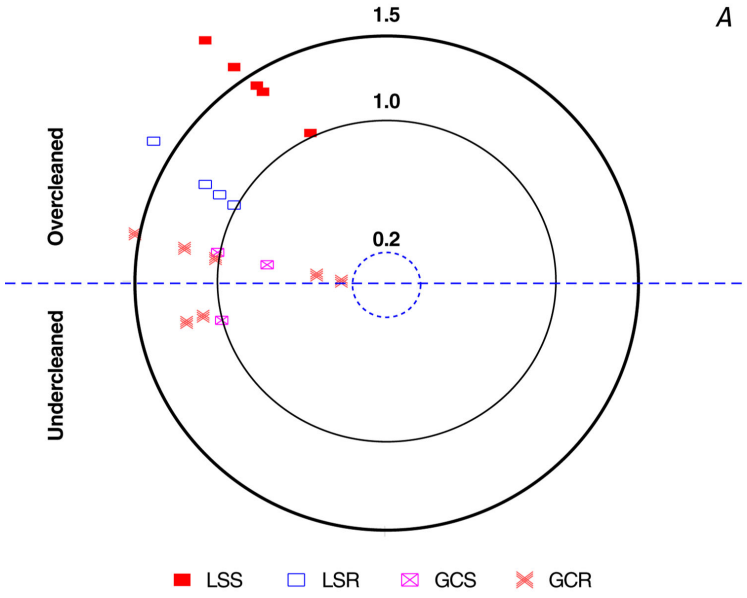

Figure 28.—Finesse-classification diagrams for various surface-soiling conditions, based on a range of target cleanliness (C^*) values (in gray-scale units): 3.0 (*A*), 2.5 (*B*), 2.0 (*C*), 1.6 (*D*), and 1.5 (*E*). Each diagram is plotted in polar coordinate, with grayness value (accuracy), C^*, as radius vector. Polar angle is given by $\tan^{-1}(\Delta C^*/\Delta C)$, if $\Delta C \geq 0$, and by $-\tan^{-1}(\Delta C^*/\Delta C)$ if $\Delta C < 0$, where ΔC^* and ΔC are defined in equations 9 and 10. Surface-soiling conditions: GCR, gypsum crusted, rough; GCS, gypsum crusted, smooth; LSR, lightly soiled, rough; LSS, lightly soiled, smooth—Continued.

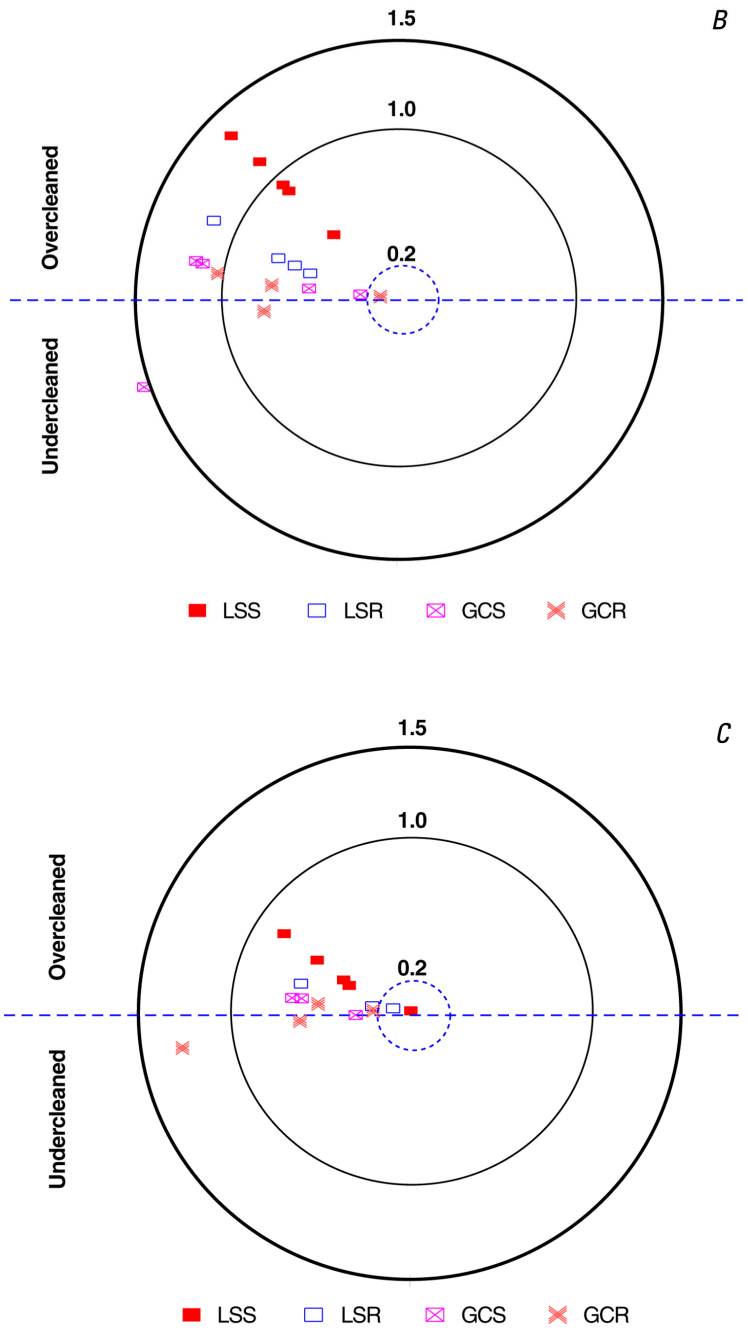

Figure 28 (Cont.)—Finesse-classification diagrams for various surface-soiling conditions, based on a range of target cleanliness (C^*) values (in gray-scale units): 3.0 (*A*), 2.5 (*B*), 2.0 (*C*), 1.6 (*D*), and 1.5 (*E*). Each diagram is plotted in polar coordinate, with grayness value (accuracy), C^*, as radius vector. Polar angle is given by $\tan^{-1}(\Delta C^*/\Delta C)$, if $\Delta C \geq 0$, and by $-\tan^{-1}(\Delta C^*/\Delta C)$ if $\Delta C < 0$, where ΔC^* and ΔC are defined in equations 9 and 10. Surface-soiling conditions: GCR, gypsum crusted, rough; GCS, gypsum crusted, smooth; LSR, lightly soiled, rough; LSS, lightly soiled, smooth—Continued.

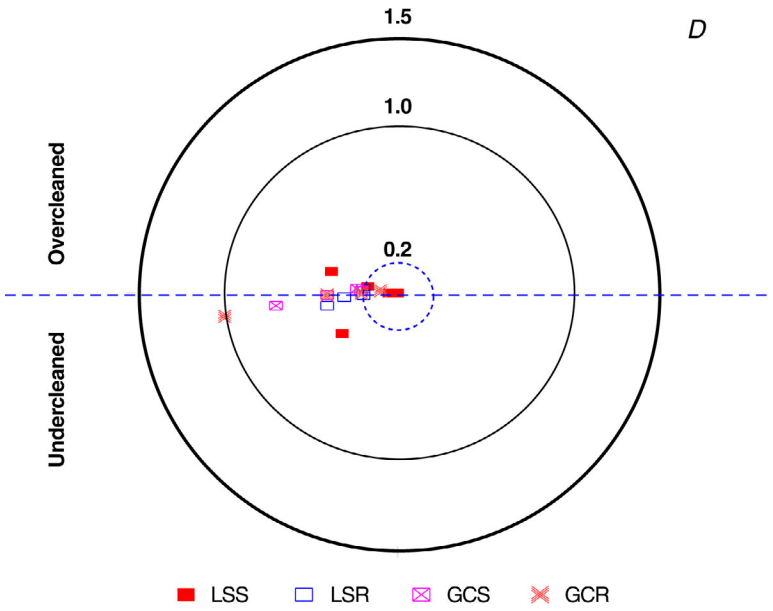

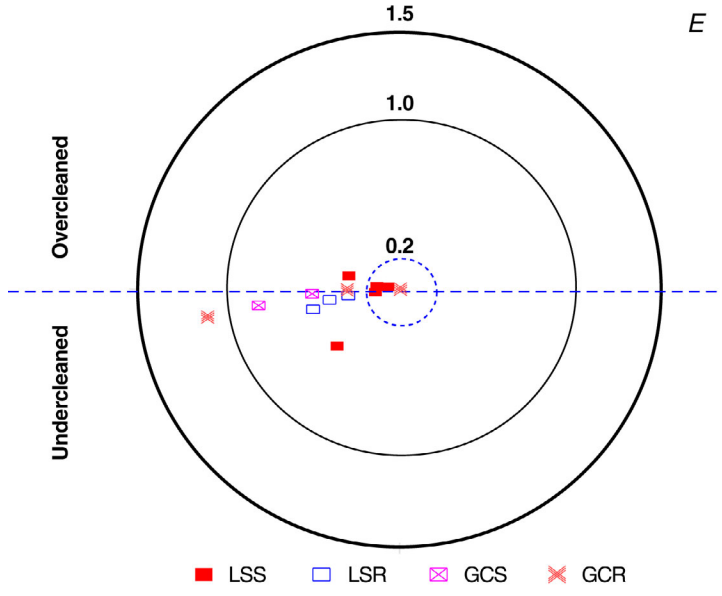

Figure 28 (Cont.)—Finesse-classification diagrams for various surface-soiling conditions, based on a range of target cleanliness (C^*) values (in gray-scale units): 3.0 (*A*), 2.5 (*B*), 2.0 (*C*), 1.6 (*D*), and 1.5 (*E*). Each diagram is plotted in polar coordinate, with grayness value (accuracy), C^*, as radius vector. Polar angle is given by $\tan^{-1}(\Delta C^*/\Delta C)$, if $\Delta C \geq 0$, and by $-\tan^{-1}(\Delta C^*/\Delta C)$ if $\Delta C < 0$, where ΔC^* and ΔC are defined in equations 9 and 10. Surface-soiling conditions: GCR, gypsum crusted, rough; GCS, gypsum crusted, smooth; LSR, lightly soiled, rough; LSS, lightly soiled, smooth.

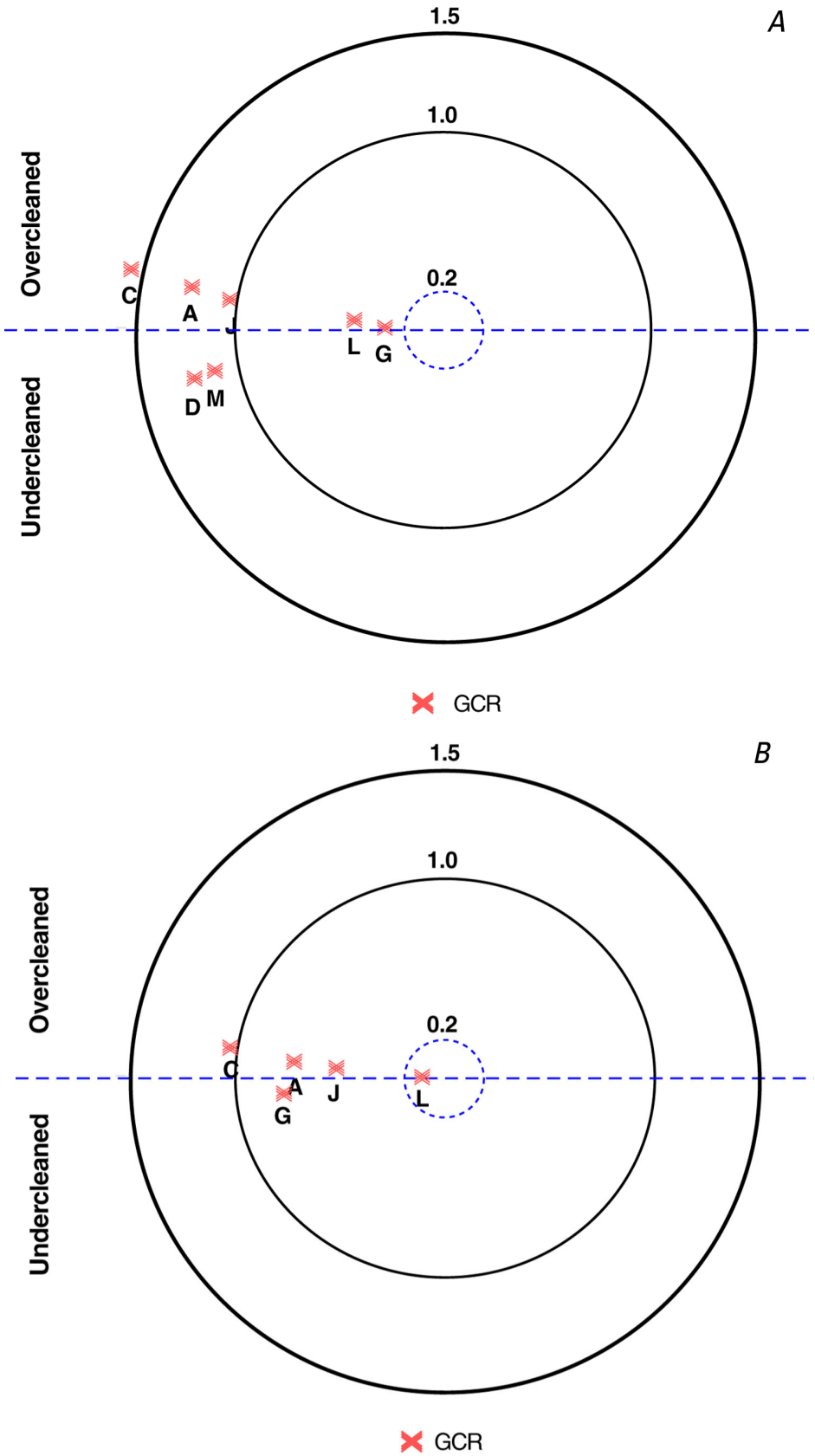

Figure 29.—Finesse-classification diagrams for gypsum-crusted, rough (GCR) stone, based on a range of target-cleanliness (C^*) values (in gray-scale units): 3.0 (*A*), 2.5 (*B*), 2.0 (*C*), and 1.5 (*D*)—Continued.

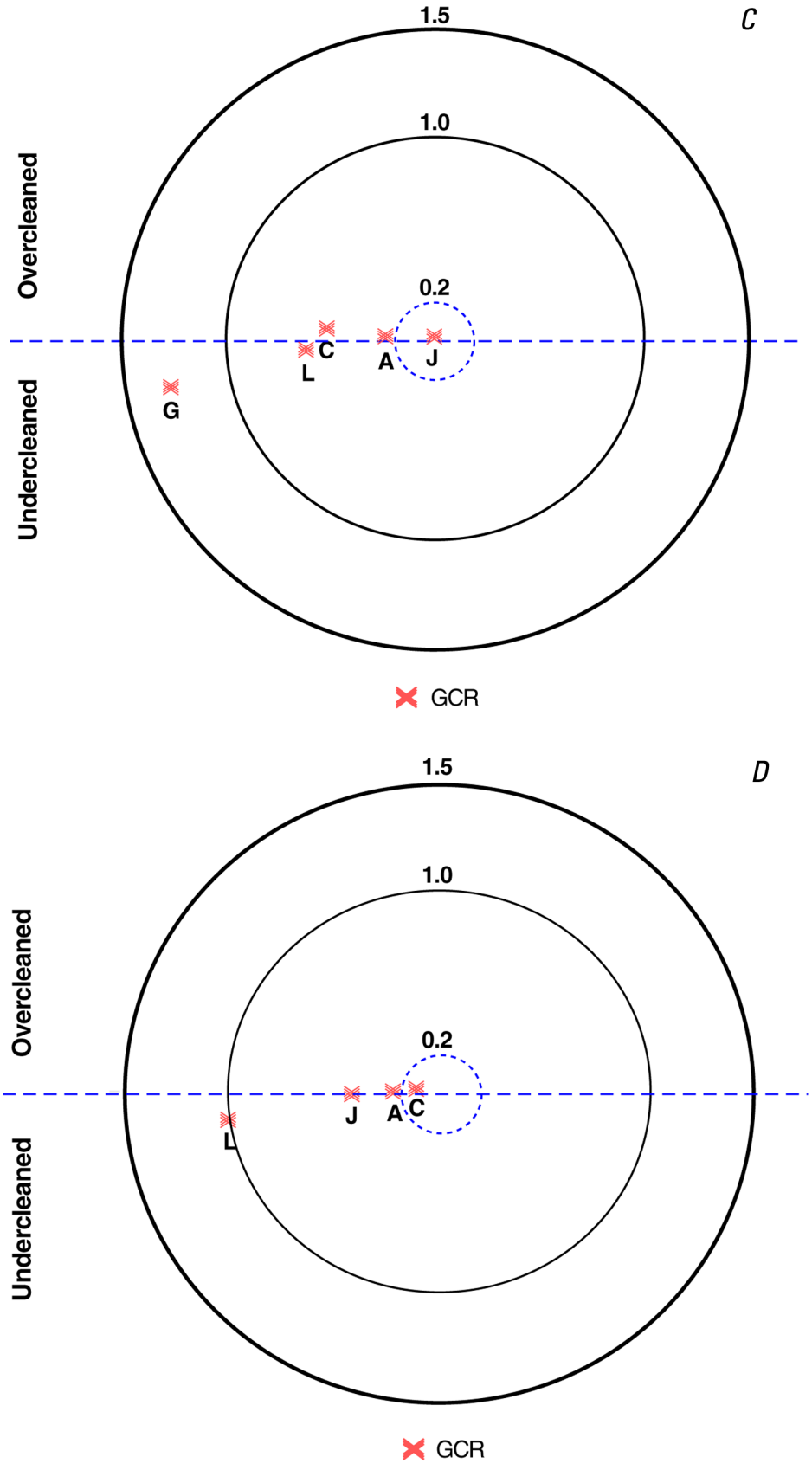

Figure 29 (Cont.)—Finesse-classification diagrams for gypsum-crusted, rough (GCR) stone, based on a range of target-cleanliness (C^*) values (in gray-scale units): 3.0 (*A*), 2.5 (*B*), 2.0 (*C*), and 1.5 (*D*).

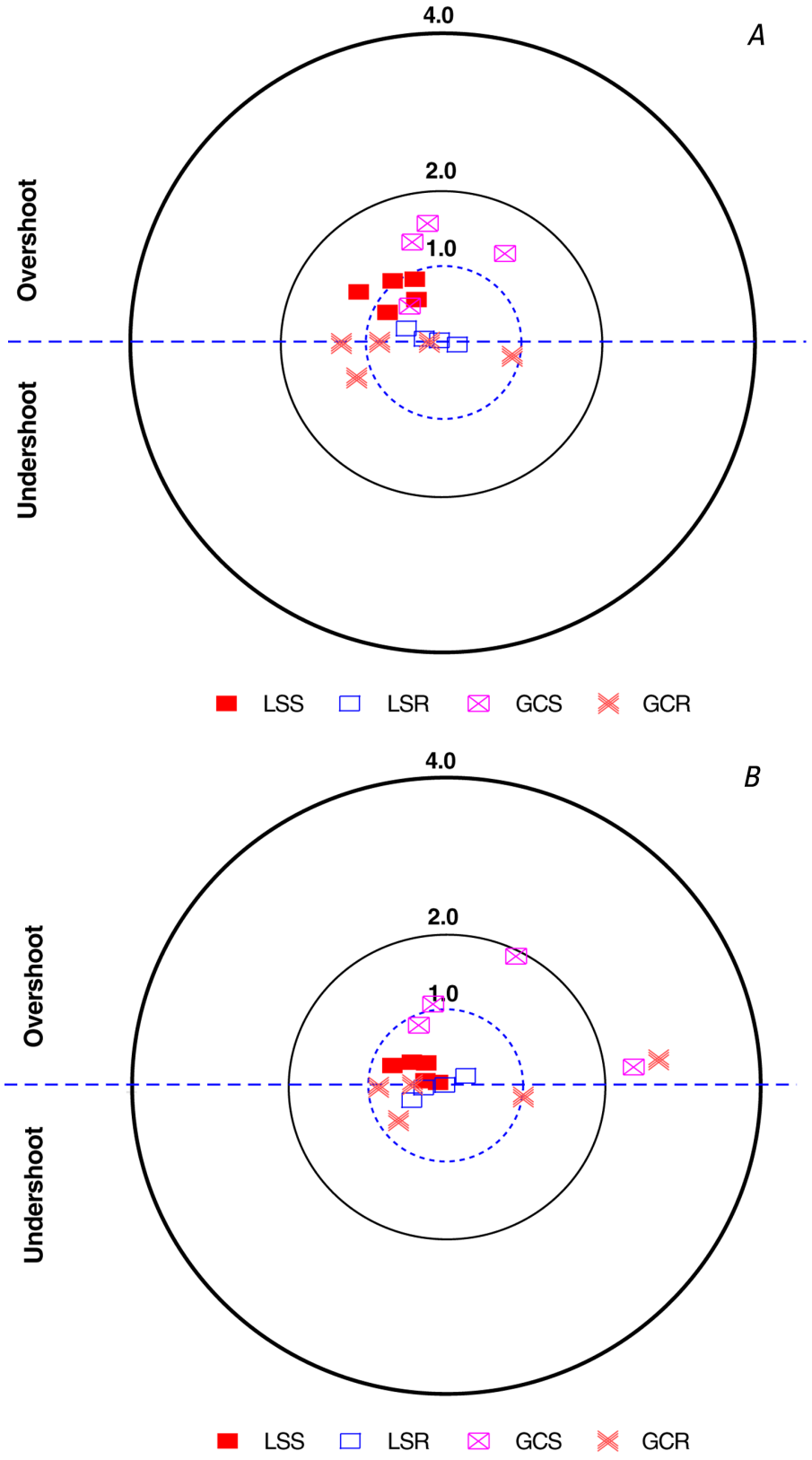

Figure 30.—Finesse-classification diagrams for various surface-soiling conditions, based on a range of target-roughness (R^*) values (in shape-factor units): 3.5 (*A*), 3.0 (*B*), 2.5 (*C*), 2.0 (*D*), and 1.6 (*E*). Surface-soiling conditions: GCR, gypsum crusted, rough; GCS, gypsum crusted, smooth; LSR, lightly soiled, rough; LSS, lightly soiled, smooth—Continued.

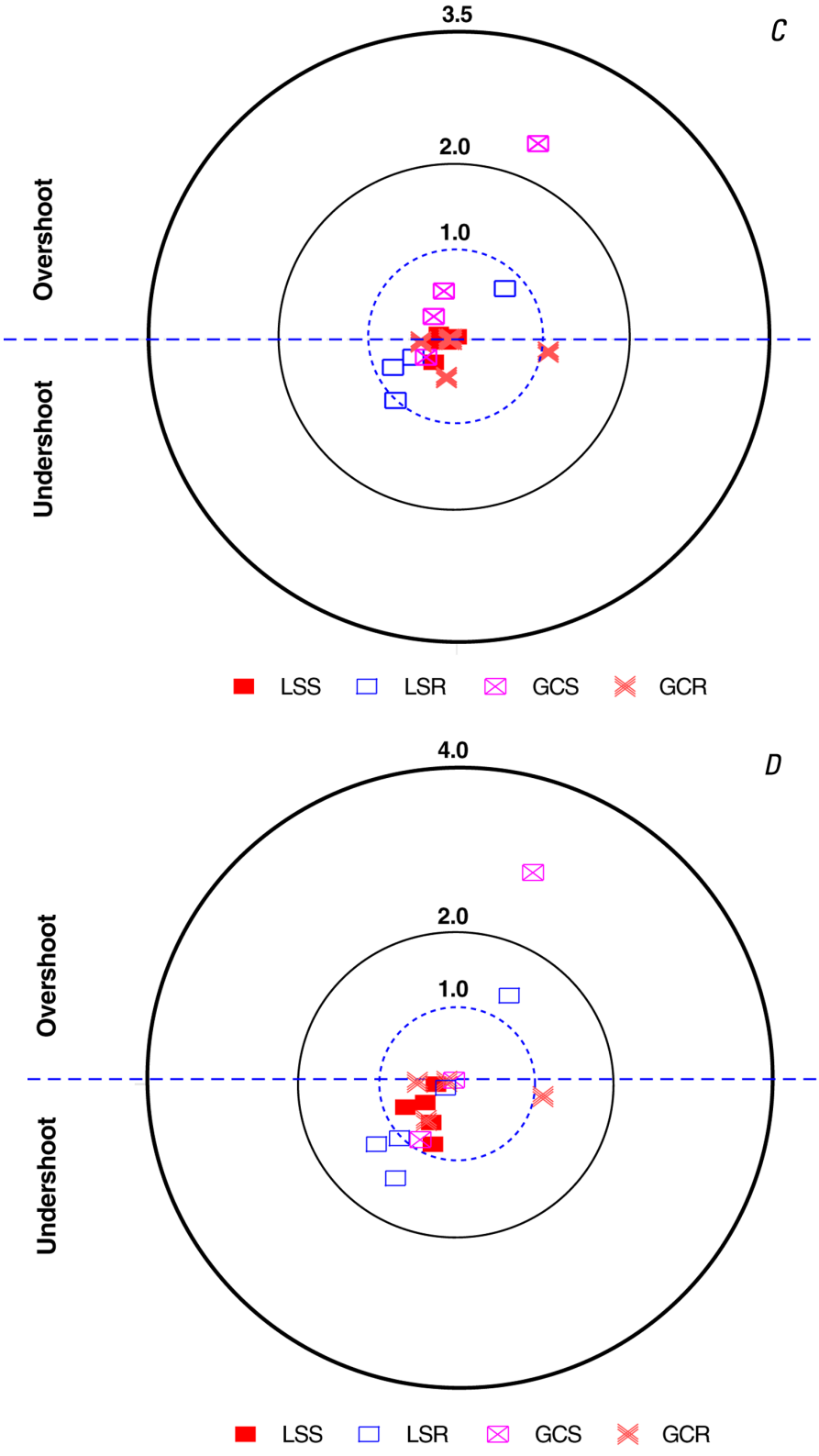

Figure 30 (Cont.)—Finesse-classification diagrams for various surface-soiling conditions, based on a range of target-roughness (R^*) values (in shape-factor units): 3.5 (*A*), 3.0 (*B*), 2.5 (*C*), 2.0 (*D*), and 1.6 (*E*). Surface-soiling conditions: GCR, gypsum crusted, rough; GCS, gypsum crusted, smooth; LSR, lightly soiled, rough; LSS, lightly soiled, smooth—Continued.

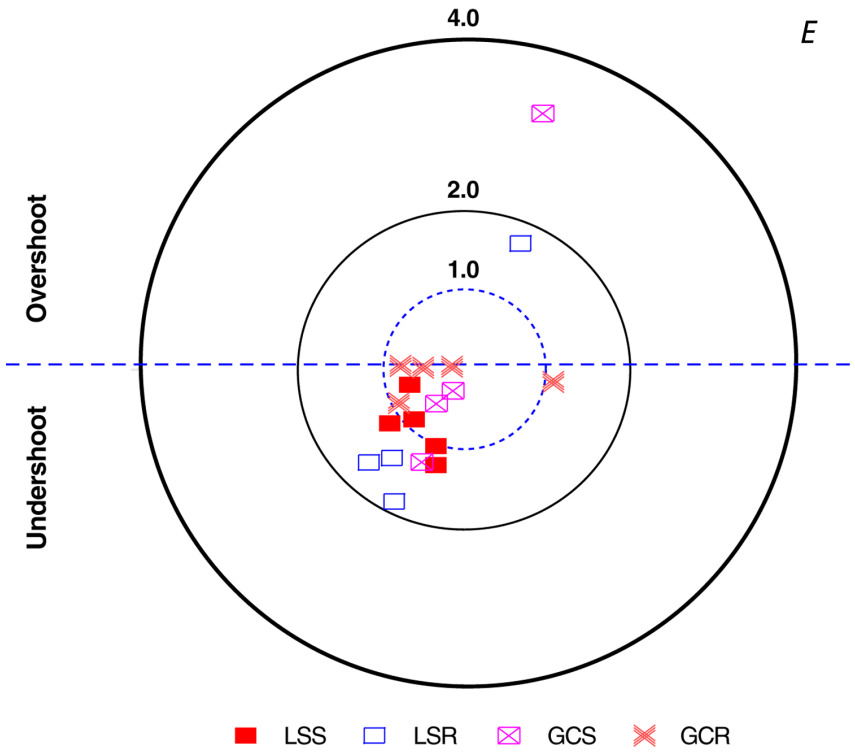

Figure 30 (Cont.)—Finesse-classification diagrams for various surface-soiling conditions, based on a range of target-roughness (R^*) values (in shape-factor units): 3.5 (*A*), 3.0 (*B*), 2.5 (*C*), 2.0 (*D*), and 1.6 (*E*). Surface-soiling conditions: GCR, gypsum crusted, rough; GCS, gypsum crusted, smooth; LSR, lightly soiled, rough; LSS, lightly soiled, smooth.

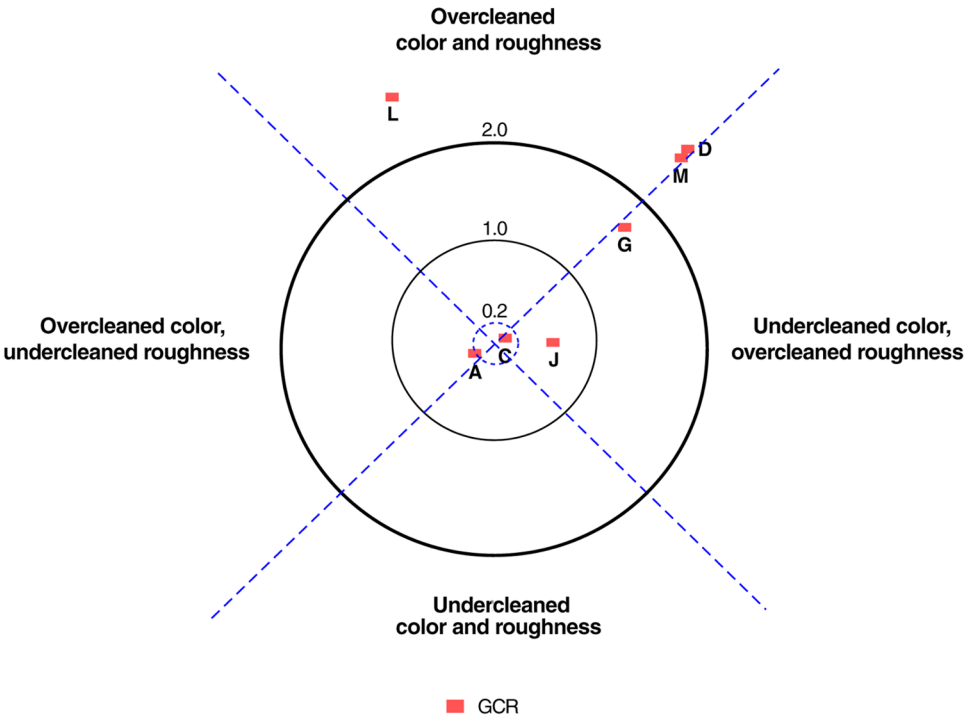

Figure 31.—Approximate shape of projections of general utility curve onto utility/roughness plane for gypsum crusted, rough (GCR) stone, based on various target cleanliness (C^*) values, in gray-scale units.

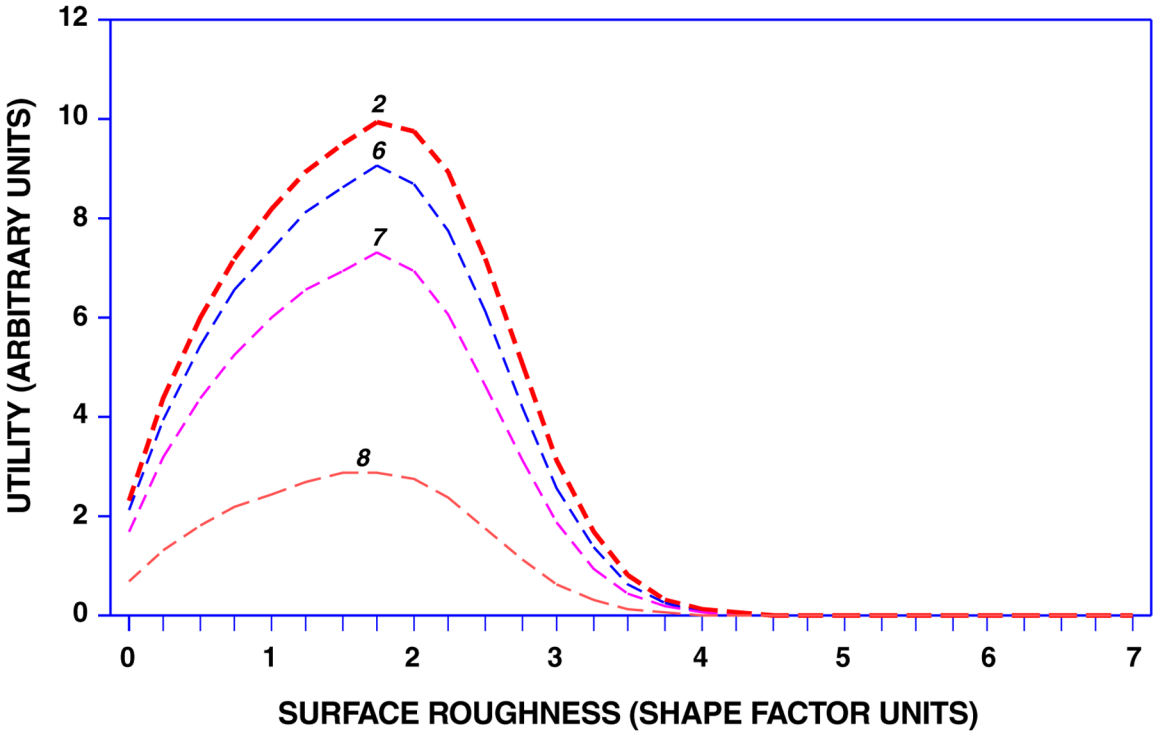

Figure 32.—Utility versus surface roughness for various target-cleanliness (C^*) values for gypsum-crusted, rough stone after cleaning. Numbered curves denote various C^* values, in gray-scale units.

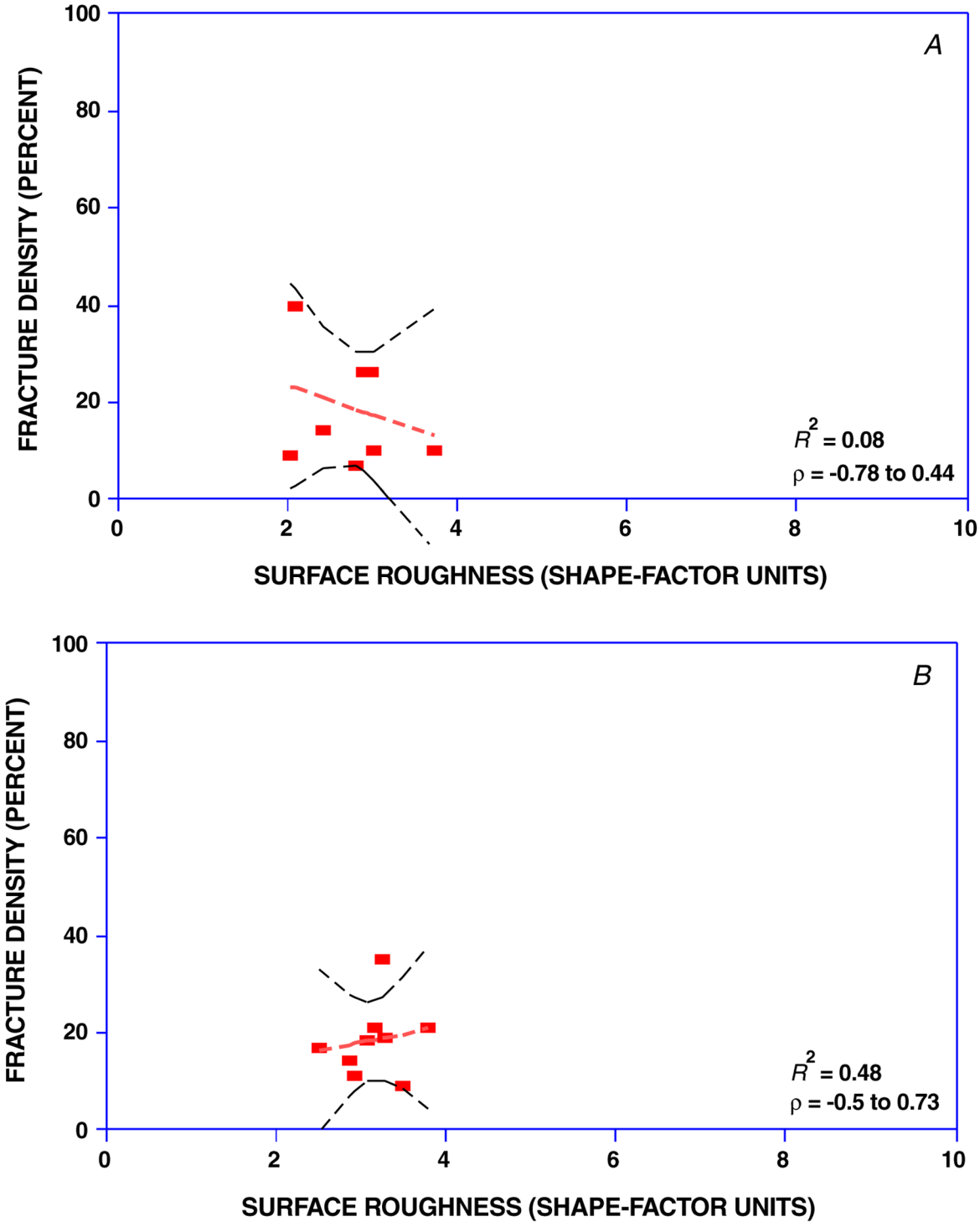

Figure 33.—Fracture density versus surface roughness for uncleaned (*A*, *C*, *E*, *G*, *I*, *K*, *M*) and cleaned (*B*, *D*, *F*, *H*, *J*, *L*, *N*) sides of core samples cleaned by power-wash (*A*, *B*), gommage (*C*, *D*), combination (*E*, *F*), Armax (*G*, *H*), JOS (*I*, *J*), laser (*K*, *L*), and dry-ice (*M*, *N*) techniques. Dashed line, least-squares regression line; opposed dashed curves, confidence intervals for least-squares regression line; R^2 value, square of correlation coefficient; ρ, confidence intervals for parent-population correlation coefficient. All confidence intervals were calculated at 95-percent-confidence level—Continued.

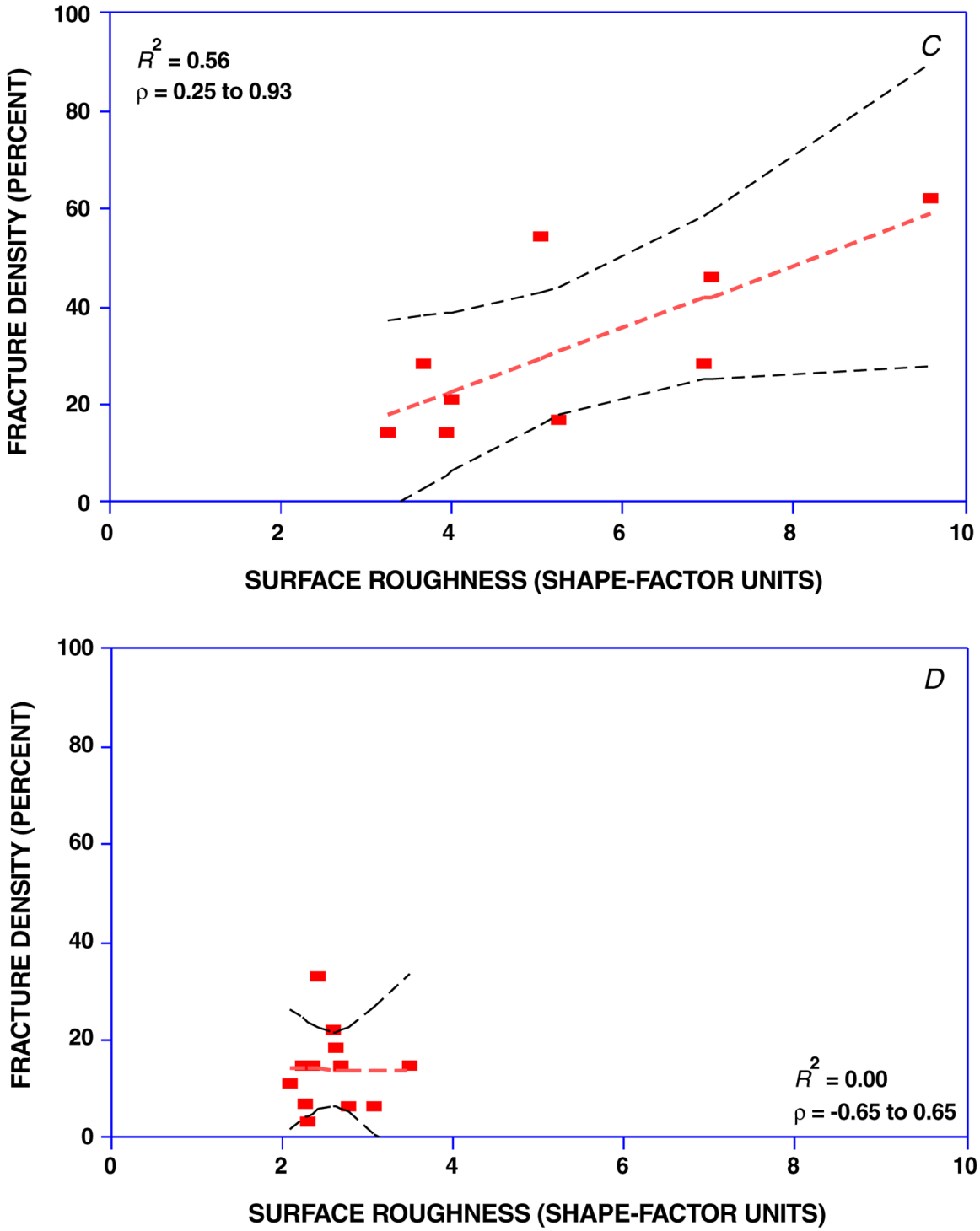

Figure 33 (Cont.)—Fracture density versus surface roughness for uncleaned (*A*, *C*, *E*, *G*, *I*, *K*, *M*) and cleaned (*B*, *D*, *F*, *H*, *J*, *L*, *N*) sides of core samples cleaned by power-wash (*A*, *B*), gommage (*C*, *D*), combination (*E*, *F*), Armax (*G*, *H*), JOS (*I*, *J*), laser (*K*, *L*), and dry-ice (*M*, *N*) techniques. Dashed line, least-squares regression line; opposed dashed curves, confidence intervals for least-squares regression line; R^2 value, square of correlation coefficient; ρ, confidence intervals for parent-population correlation coefficient. All confidence intervals were calculated at 95-percent-confidence level—Continued.

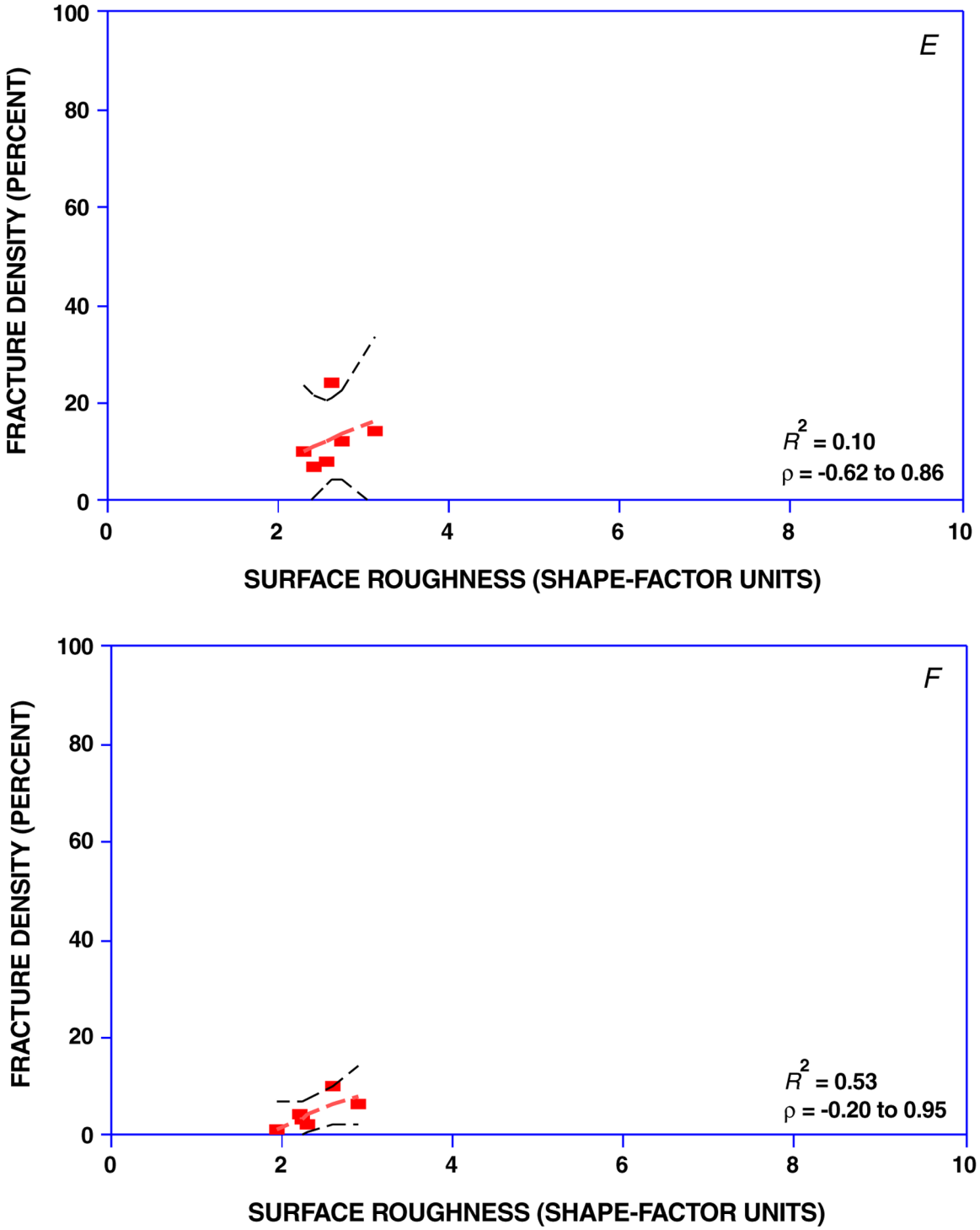

Figure 33 (Cont.)—Fracture density versus surface roughness for uncleaned (*A*, *C*, *E*, *G*, *I*, *K*, *M*) and cleaned (*B*, *D*, *F*, *H*, *J*, *L*, *N*) sides of core samples cleaned by power-wash (*A*, *B*), gommage (*C*, *D*), combination (*E*, *F*), Armax (*G*, *H*), JOS (*I*, *J*), laser (*K*, *L*), and dry-ice (*M*, *N*) techniques. Dashed line, least-squares regression line; opposed dashed curves, confidence intervals for least-squares regression line; R^2 value, square of correlation coefficient; ρ, confidence intervals for parent-population correlation coefficient. All confidence intervals were calculated at 95-percent-confidence level—Continued.

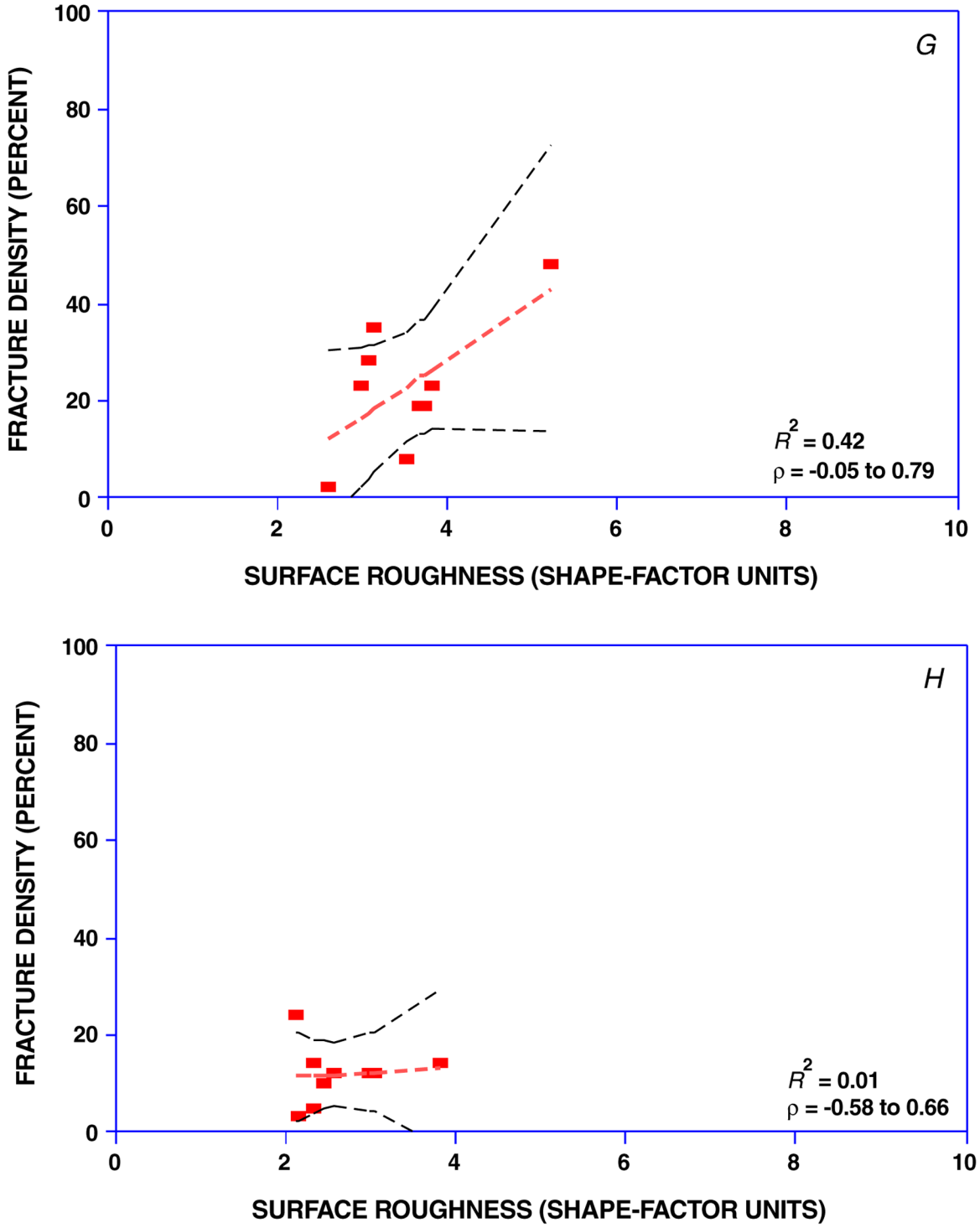

Figure 33 (Cont.)—Fracture density versus surface roughness for uncleaned (*A*, *C*, *E*, *G*, *I*, *K*, *M*) and cleaned (*B*, *D*, *F*, *H*, *J*, *L*, *N*) sides of core samples cleaned by power-wash (*A*, *B*), gommage (*C*, *D*), combination (*E*, *F*), Armax (*G*, *H*), JOS (*I*, *J*), laser (*K*, *L*), and dry-ice (*M*, *N*) techniques. Dashed line, least-squares regression line; opposed dashed curves, confidence intervals for least-squares regression line; R^2 value, square of correlation coefficient; ρ, confidence intervals for parent-population correlation coefficient. All confidence intervals were calculated at 95-percent-confidence level—Continued.

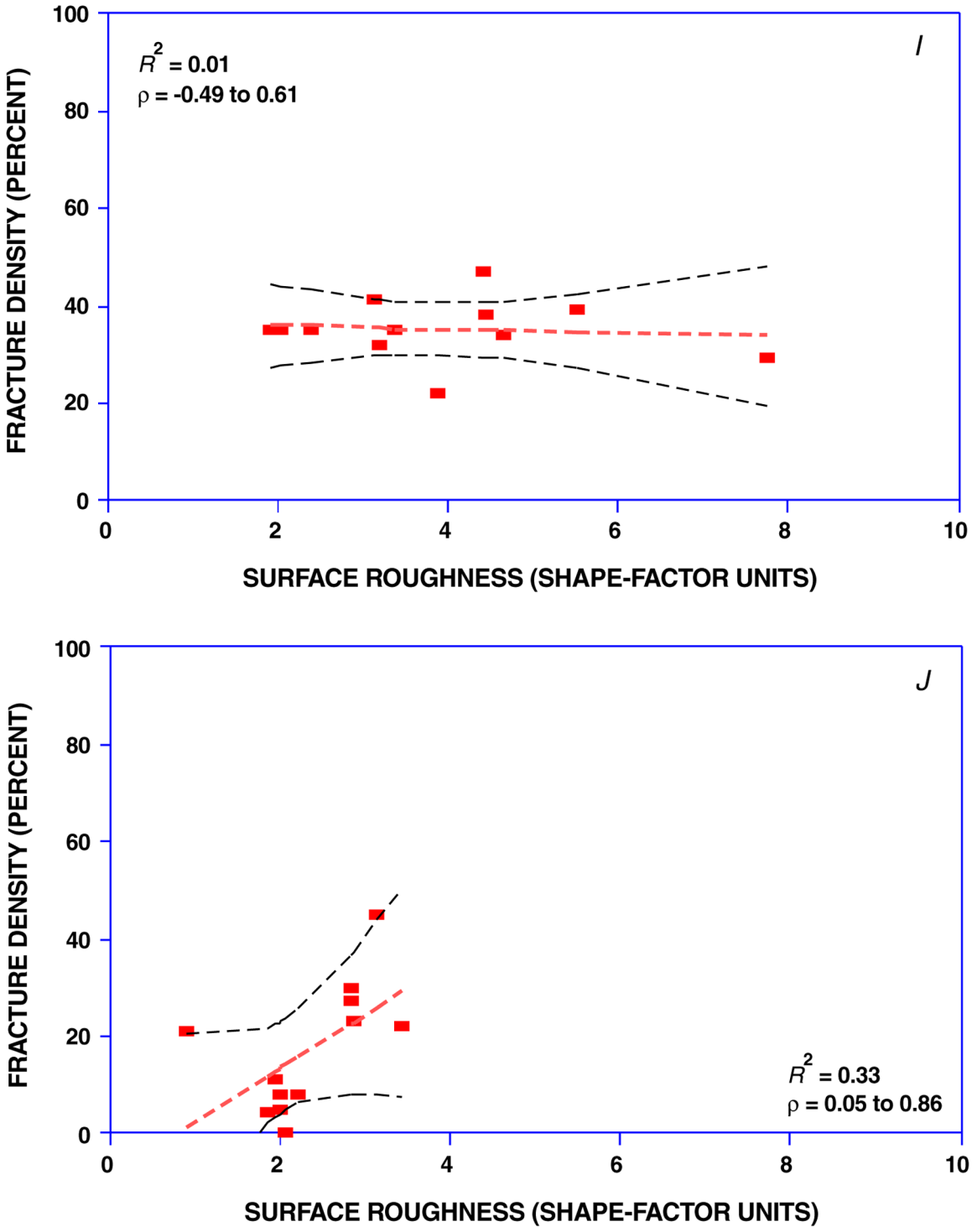

Figure 33 (Cont.)—Fracture density versus surface roughness for uncleaned (*A*, *C*, *E*, *G*, *I*, *K*, *M*) and cleaned (*B*, *D*, *F*, *H*, *J*, *L*, *N*) sides of core samples cleaned by power-wash (*A*, *B*), gommage (*C*, *D*), combination (*E*, *F*), Armax (*G*, *H*), JOS (*I*, *J*), laser (*K*, *L*), and dry-ice (*M*, *N*) techniques. Dashed line, least-squares regression line; opposed dashed curves, confidence intervals for least-squares regression line; R^2 value, square of correlation coefficient; ρ, confidence intervals for parent-population correlation coefficient. All confidence intervals were calculated at 95-percent-confidence level—Continued.

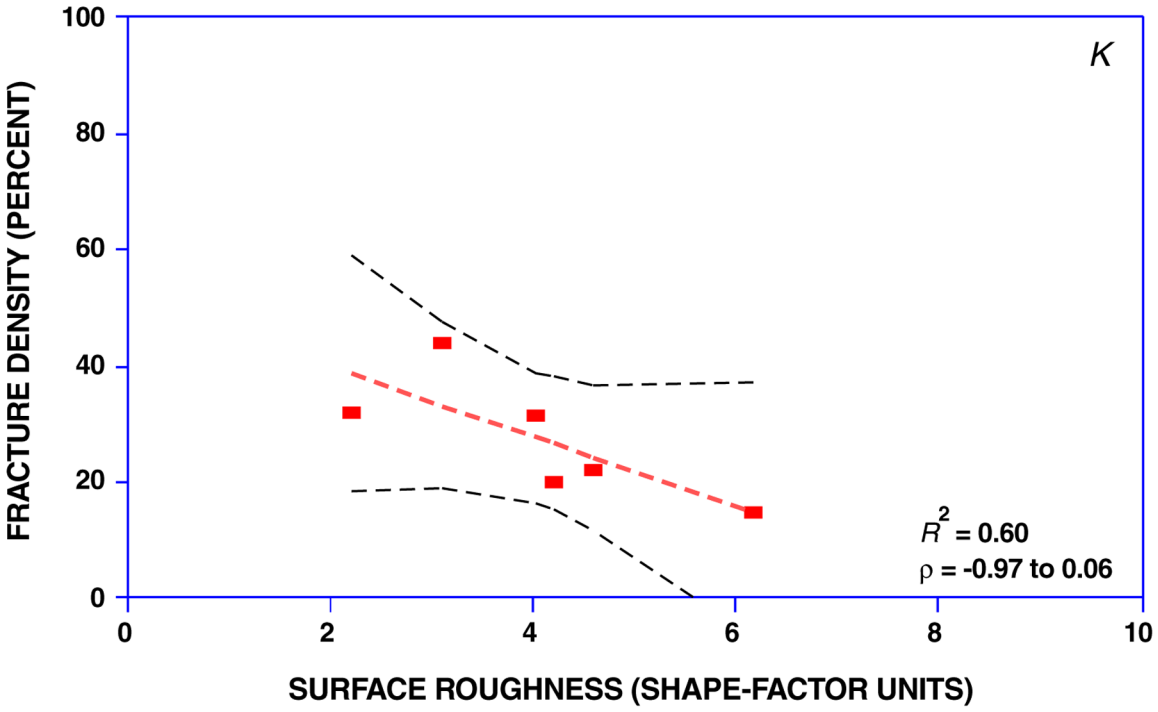

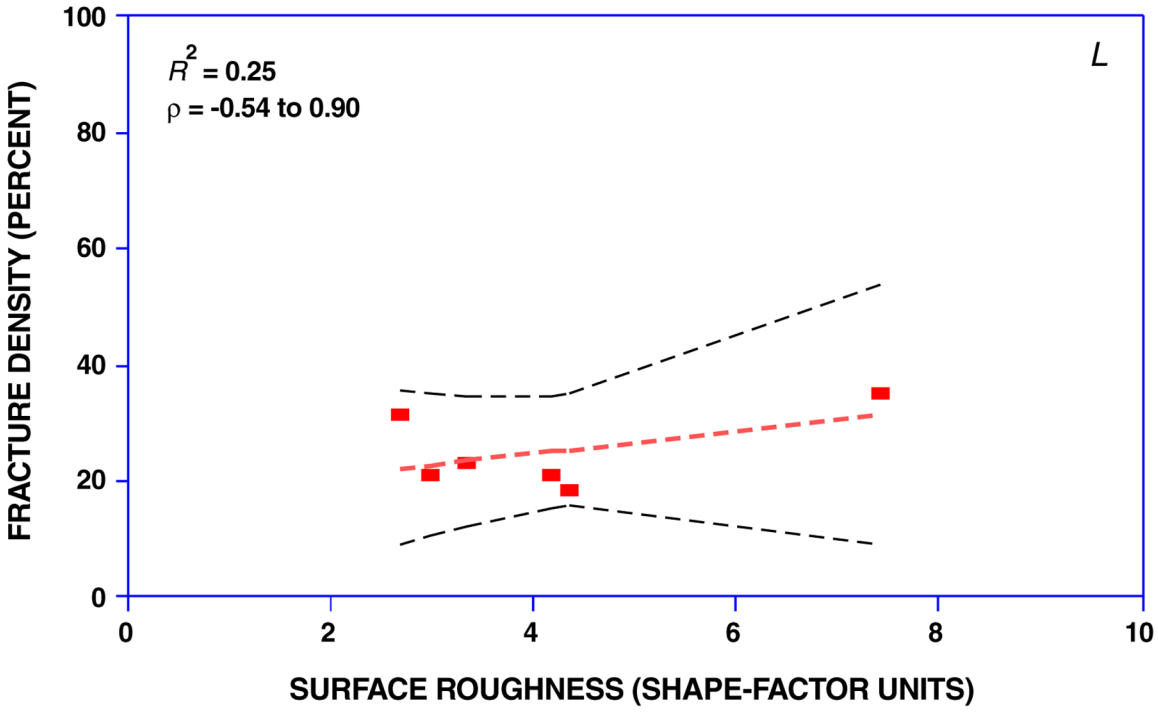

Figure 33 (Cont.)—Fracture density versus surface roughness for uncleaned (*A*, *C*, *E*, *G*, *I*, *K*, *M*) and cleaned (*B*, *D*, *F*, *H*, *J*, *L*, *N*) sides of core samples cleaned by power-wash (*A*, *B*), gommage (*C*, *D*), combination (*E*, *F*), Armax (*G*, *H*), JOS (*I*, *J*), laser (*K*, *L*), and dry-ice (*M*, *N*) techniques. Dashed line, least-squares regression line; opposed dashed curves, confidence intervals for least-squares regression line; R^2 value, square of correlation coefficient; ρ, confidence intervals for parent-population correlation coefficient. All confidence intervals were calculated at 95-percent-confidence level—Continued.

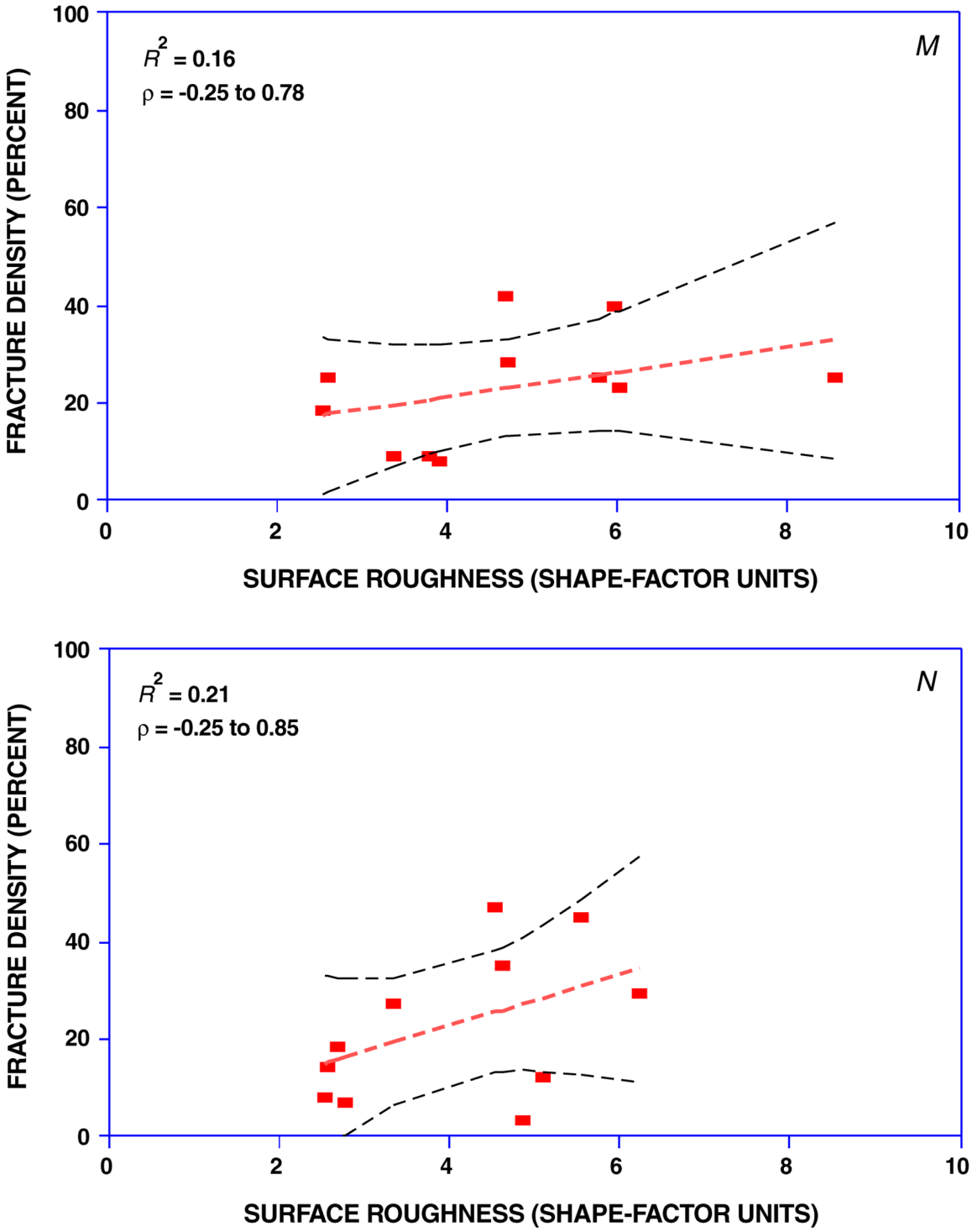

Figure 33 (Cont.)—Fracture density versus surface roughness for uncleaned (*A*, *C*, *E*, *G*, *I*, *K*, *M*) and cleaned (*B*, *D*, *F*, *H*, *J*, *L*, *N*) sides of core samples cleaned by power-wash (*A*, *B*), gommage (*C*, *D*), combination (*E*, *F*), Armax (*G*, *H*), JOS (*I*, *J*), laser (*K*, *L*), and dry-ice (*M*, *N*) techniques. Dashed line, least-squares regression line; opposed dashed curves, confidence intervals for least-squares regression line; R^2 value, square of correlation coefficient; ρ, confidence intervals for parent-population correlation coefficient. All confidence intervals were calculated at 95-percent-confidence level.

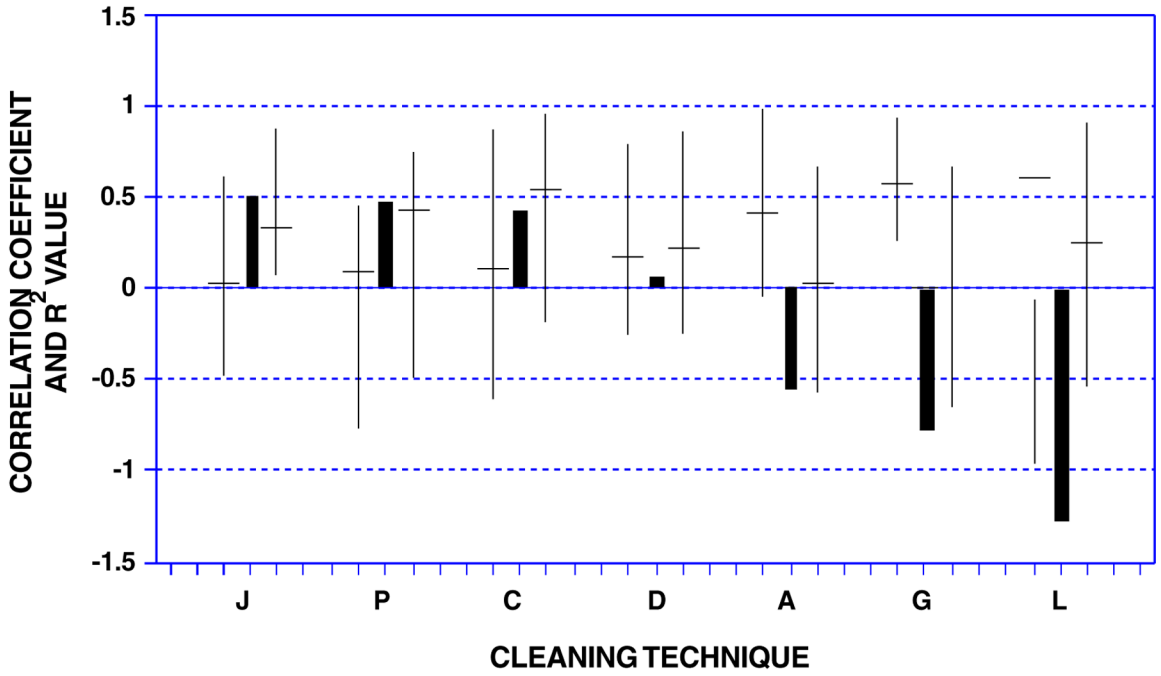

Figure 34.—Summary of statistical data for various cleaning techniques plotted in figure 33. Cleaning techniques: A, Armax; C, combination; D, dry ice; G, gommage; J, JOS; L, laser; P, power wash. Bars, change in sample correlation coefficient; tickmarks, R^2 value for least-squares regression line; vertical lines, 95-percent-confidence interval for parent-population correlation coefficient (soiled stone to left of bar, cleaned stone to right of bar).

A

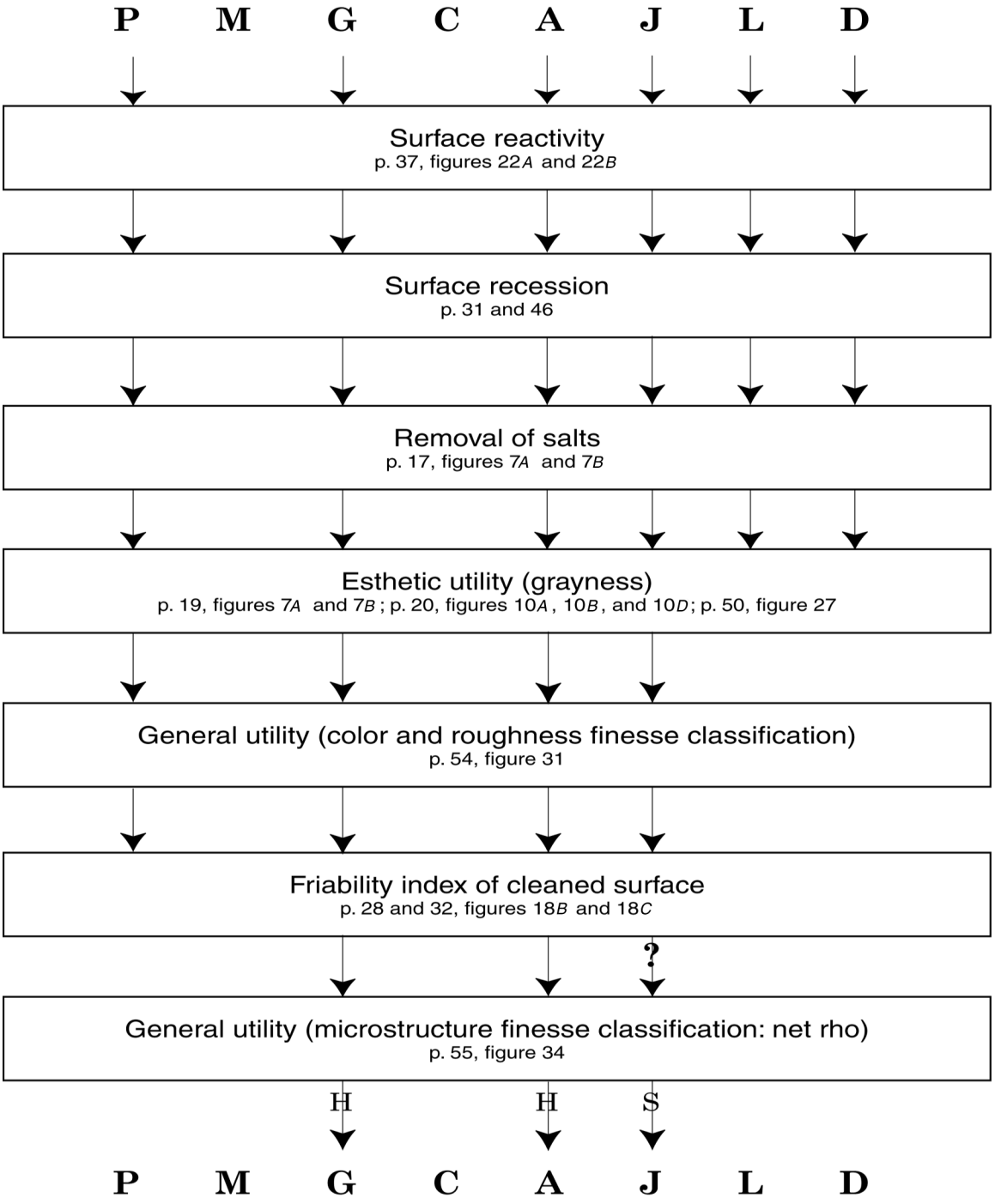

Figure 35.—Summary diagram showing criteria used to filter cleaning techniques applied to lightly soiled, smooth and rough stone (*A*) and gypsum-crusted, smooth and rough stone (*B*). Cleaning techniques: A, Armax; C, combination; D, dry ice; G, gommage; J, JOS; L, laser; P, power wash. Classifications: H, hard; S, soft; ?, indeterminate—Continued.

B

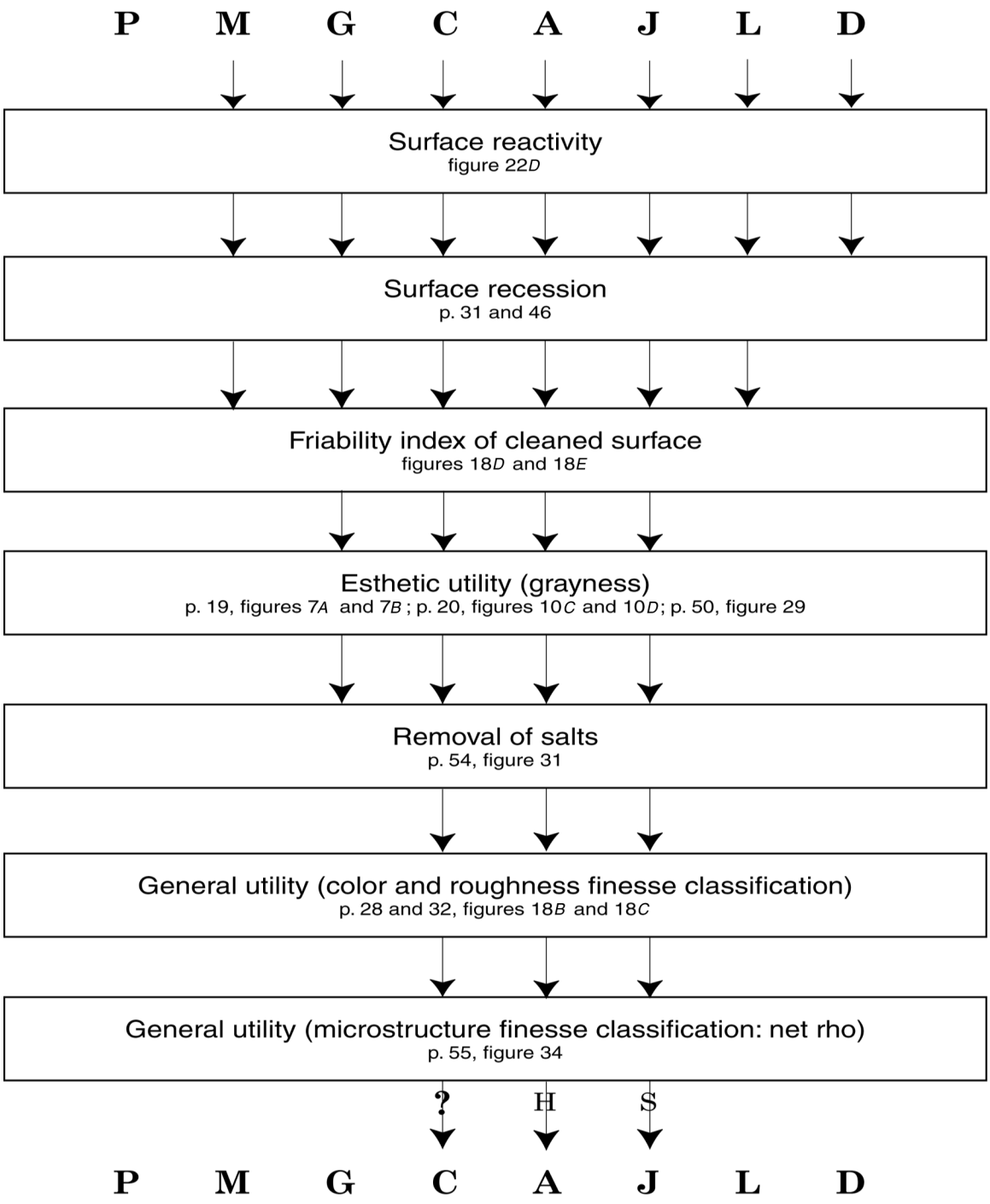

Figure 35 (Cont.)—Summary diagram showing criteria used to filter cleaning techniques applied to lightly soiled, smooth and rough stone (*A*) and gypsum-crusted, smooth and rough stone (*B*). Cleaning techniques: A, Armax; C, combination; D, dry ice; G, gommage; J, JOS; L, laser; P, power wash. Classifications: H, hard; S, soft; ?, indeterminate.

Figure 36.—East façade of building, south of east portal, showing locations of masonry-testing sites.

Figure 37.—Ledge outside Room 428, upper and lower scaffold levels, showing lightly soiled marble on ledge and gypsum-crusted areas on projecting cornice and frieze below ledge.

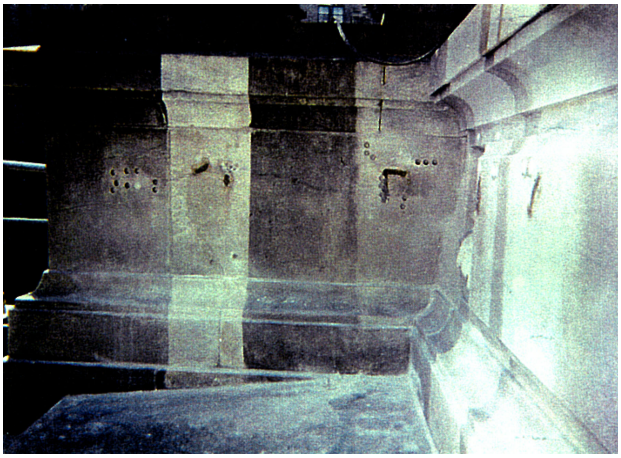

Figure 38.—South wall, upper scaffold level, showing area of lightly soiled, rough stone. Patches, from left to right: soiled, gommage cleaned, soiled, power-wash cleaned.

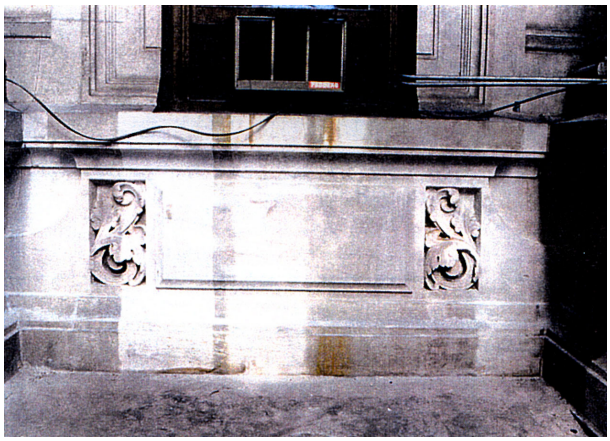

Figure 39.—West wall, upper scaffold level, showing area of lightly soiled, smooth stone. Patches, from left to right: power-wash cleaned, soiled, gommage cleaned, soiled, Armax cleaned, soiled, JOS cleaned.

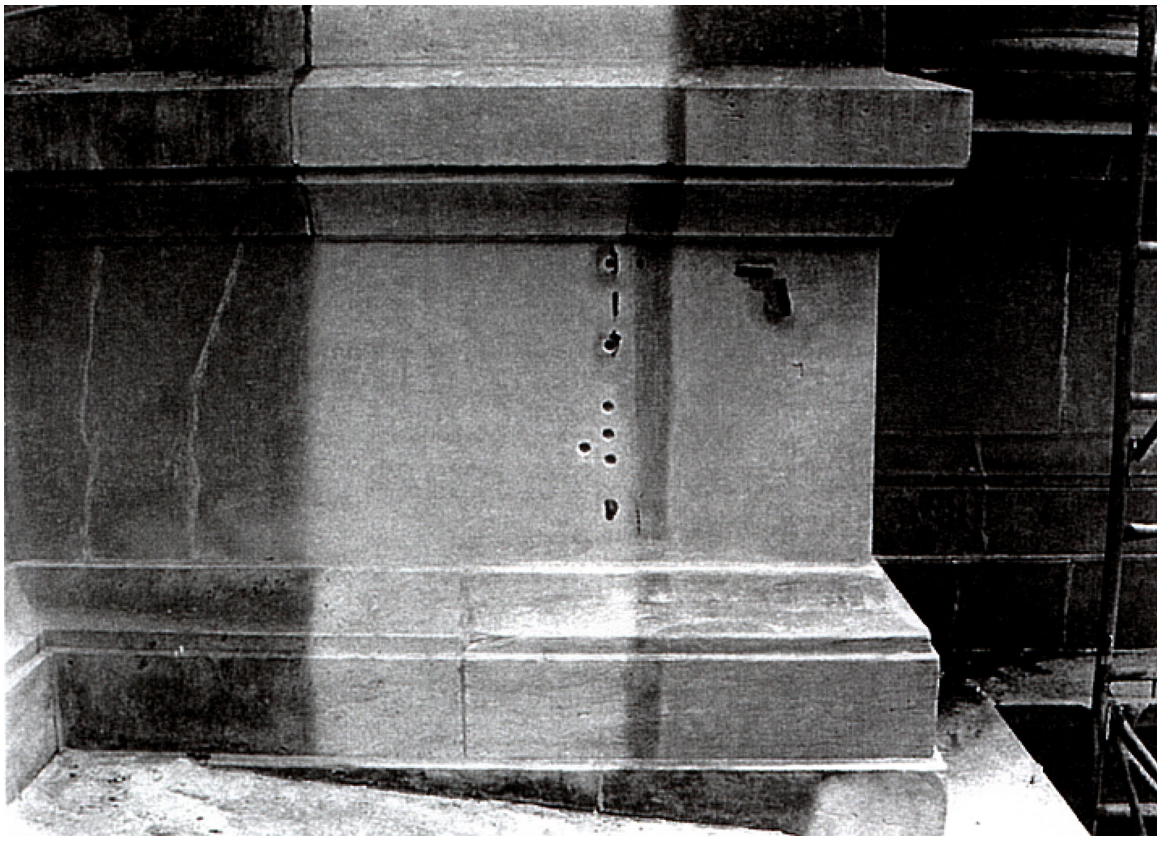

Figure 40.—North wall, upper scaffold level. Patches, from left to right: soiled, JOS cleaned, soiled, power-wash cleaned.

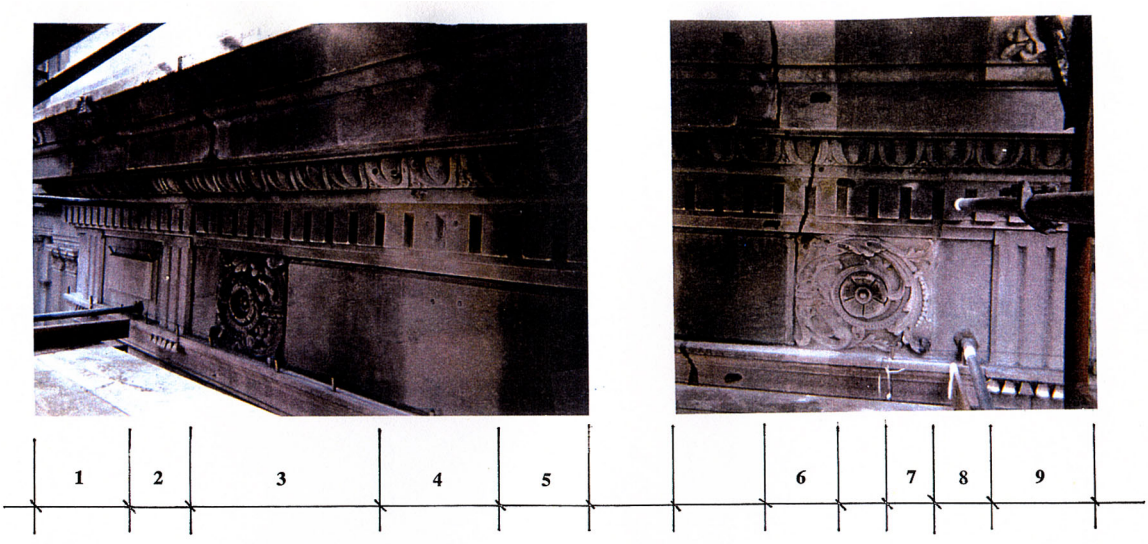

Figure 41.—Lower scaffold level. Patches: 1, soiled; 2, misting cleaned; 3, soiled; 4, Armax cleaned; 5, soiled; 6, gommage cleaned; 7, combination cleaned; 8, soiled; 9, gommage cleaned.

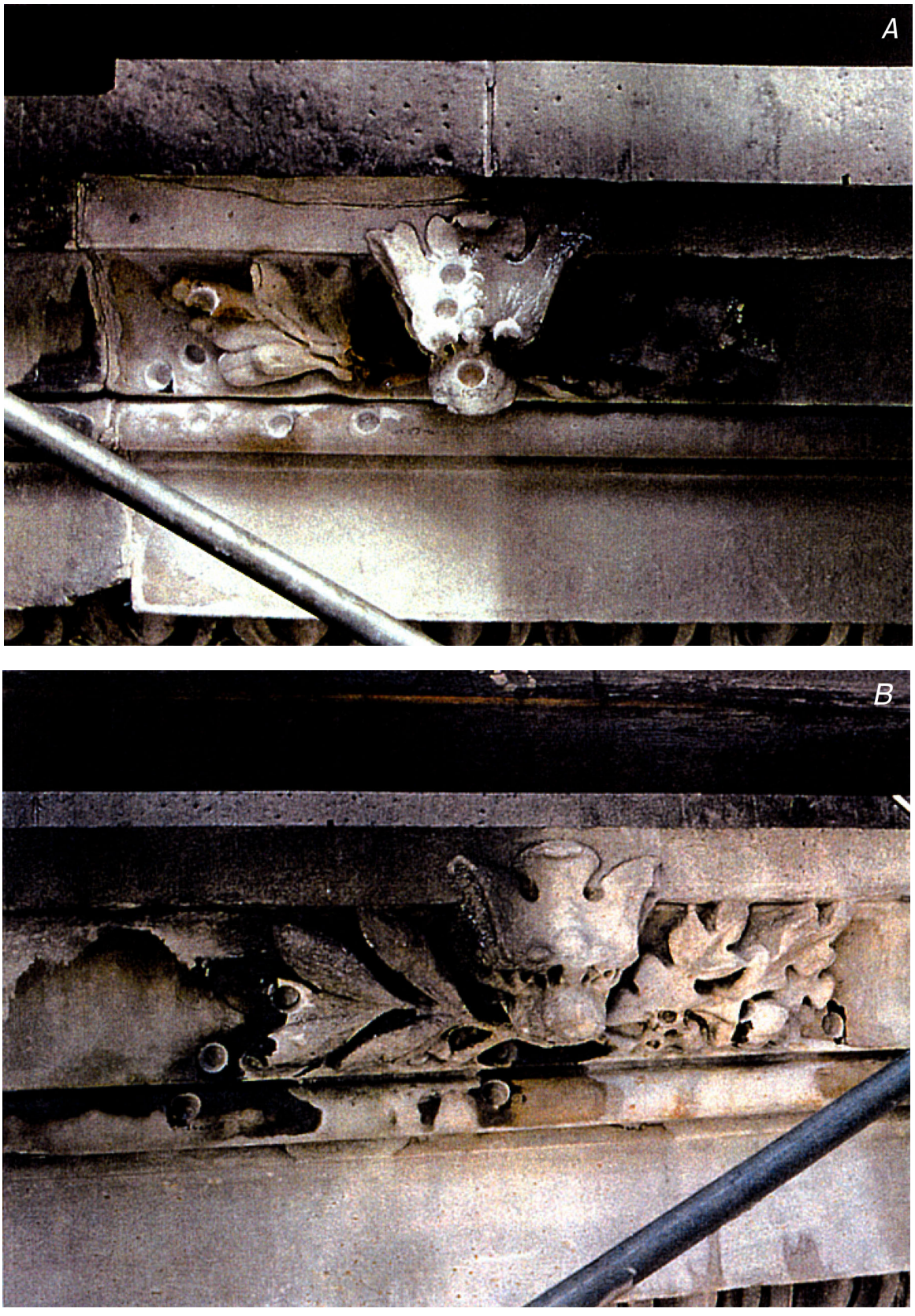

Figure 42.—South side of building. *A*, Animal carving on cornice return. JOS cleaned, standard nozzle. *B*, Animal carving to west of carving shown in figure 42*A*. JOS cleaned, piccolo nozzle.

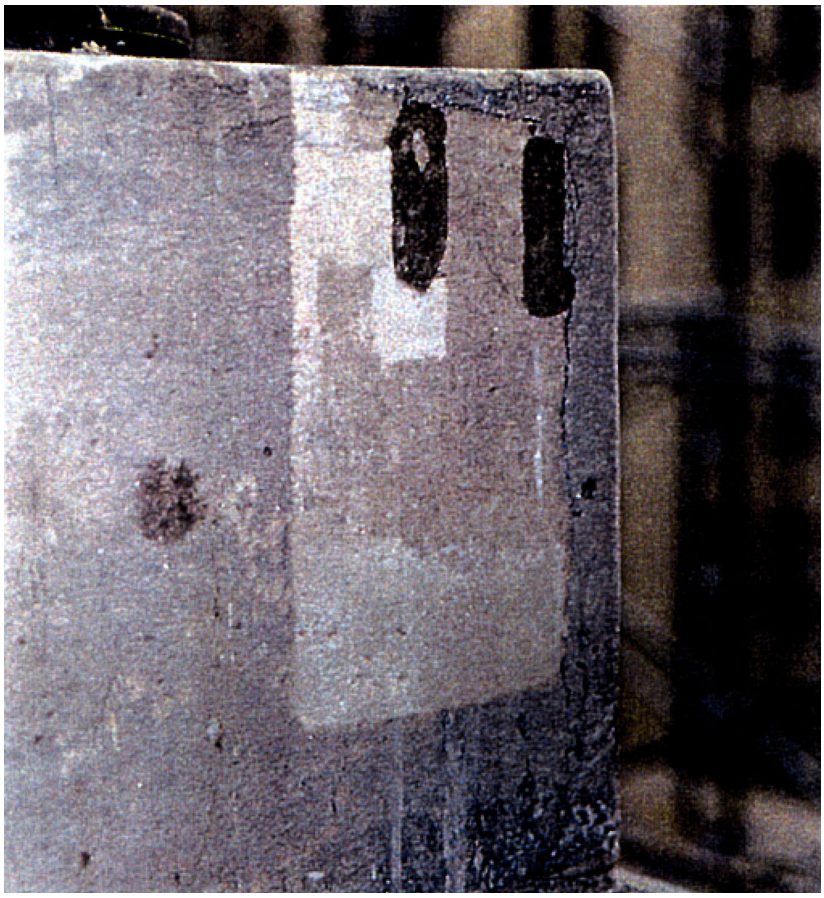

Figure 43.—Ashlar on ledge outside Room 622, showing area of lightly soiled, rough stone cleaned by laser cleaning technique. Within rectangle, different-colored patches demonstrate operator's control over extent of cleaning: dark brown (center and top right), least cleaned, with only superficial gray dirt removed; light brown (bottom), intermediate level of cleaning; white (upper left), soiling completely removed.

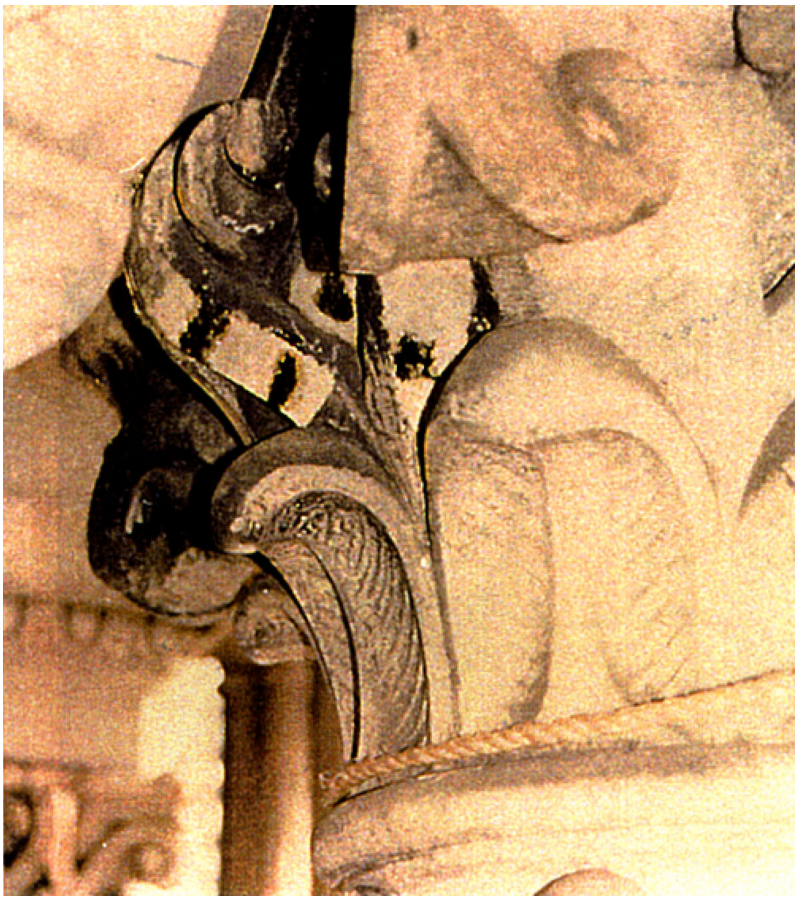

Figure 44.—Ledge outside Room 622, showing back of capital on column. Gypsum crust has been removed to cleanest level on test areas. Dark patches in white fields are epoxy resin, which preserves gypsum-crusted surfaces, permitting laboratory comparison of soiled and cleaned areas under microscope.

Figure 45.—Marble fragment from unknown location on building, showing gypsum-crusted, smooth stone.

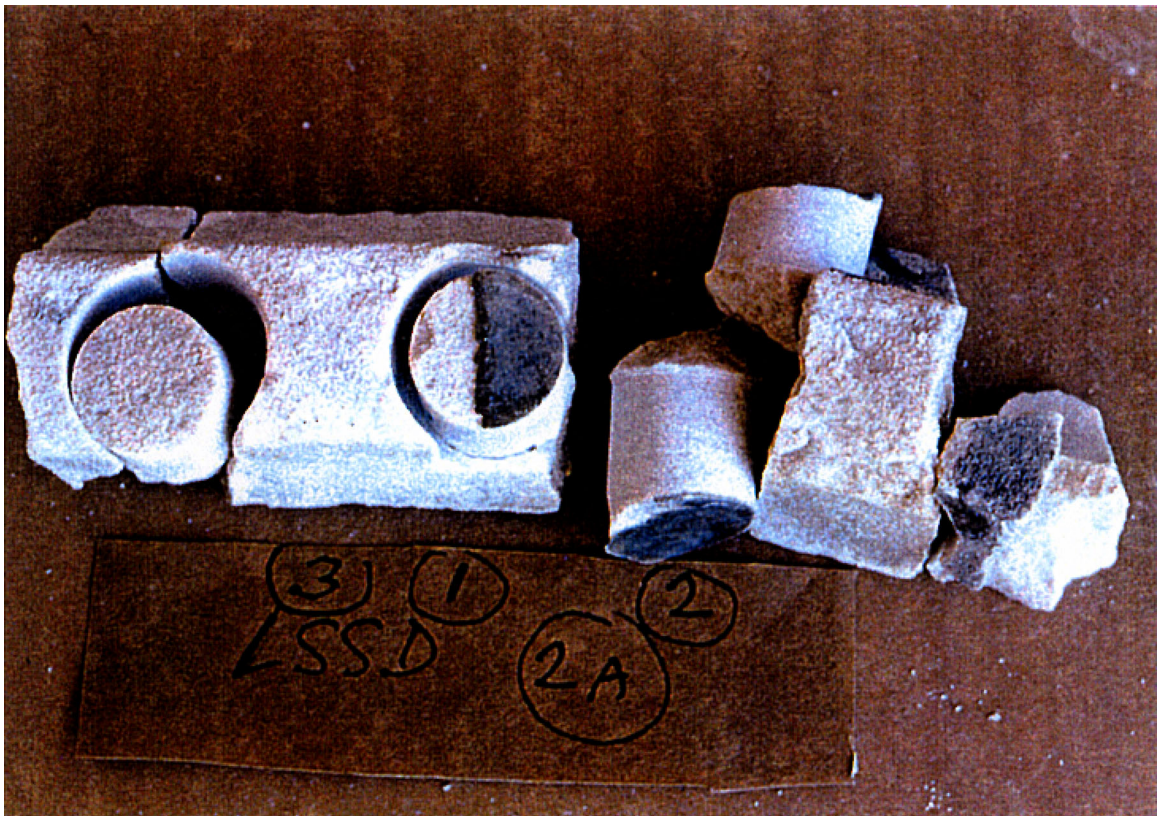

Figure 46.—Marble fragment from unknown location on building, showing lightly soiled, smooth stone after dry-ice cleaning. Numbers denote core samples in series LSSD.

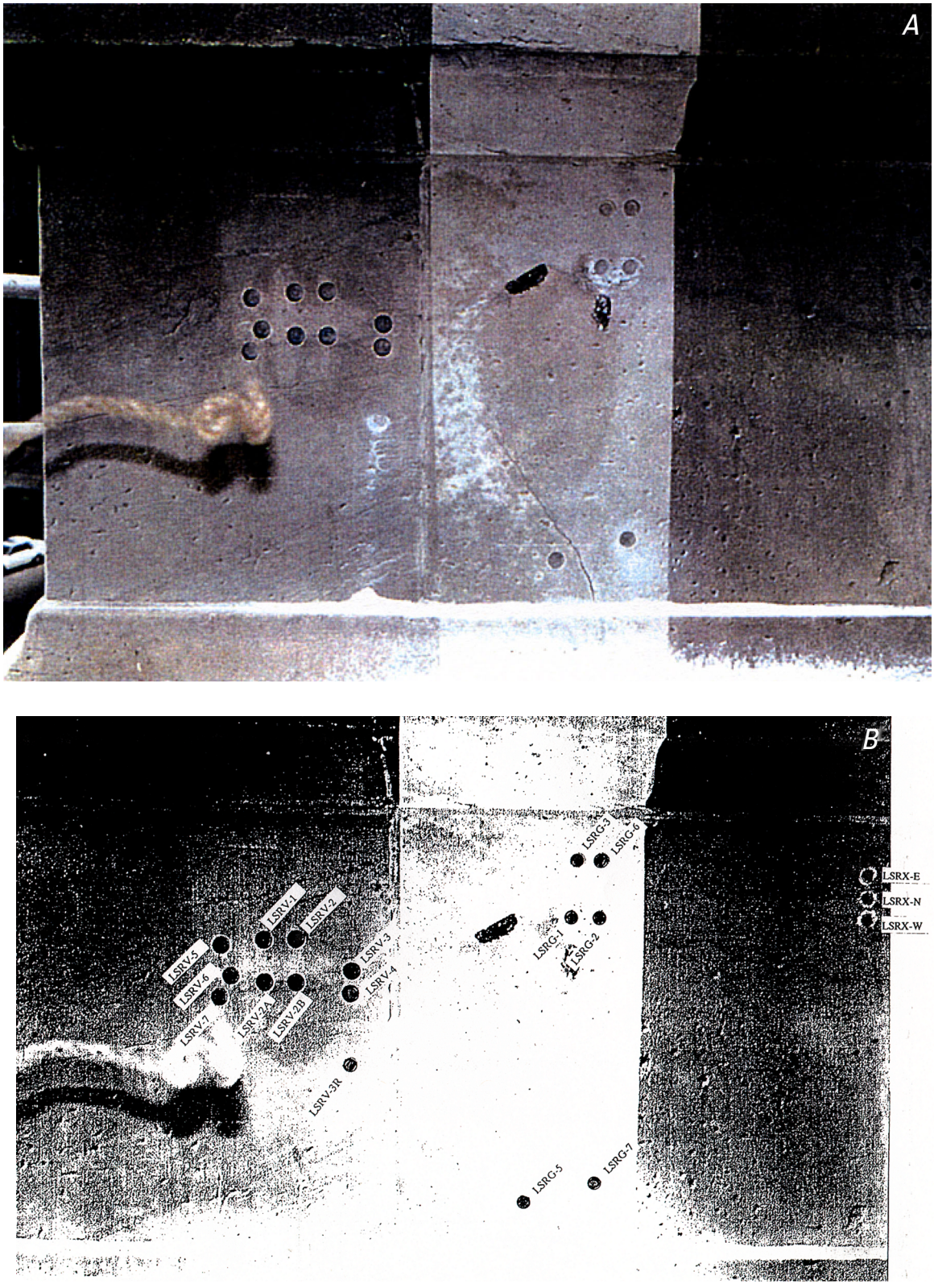

Figure 47.—North wall, upper scaffold level, showing locations of core samples in series LSRG, LSRV, and LSRX.

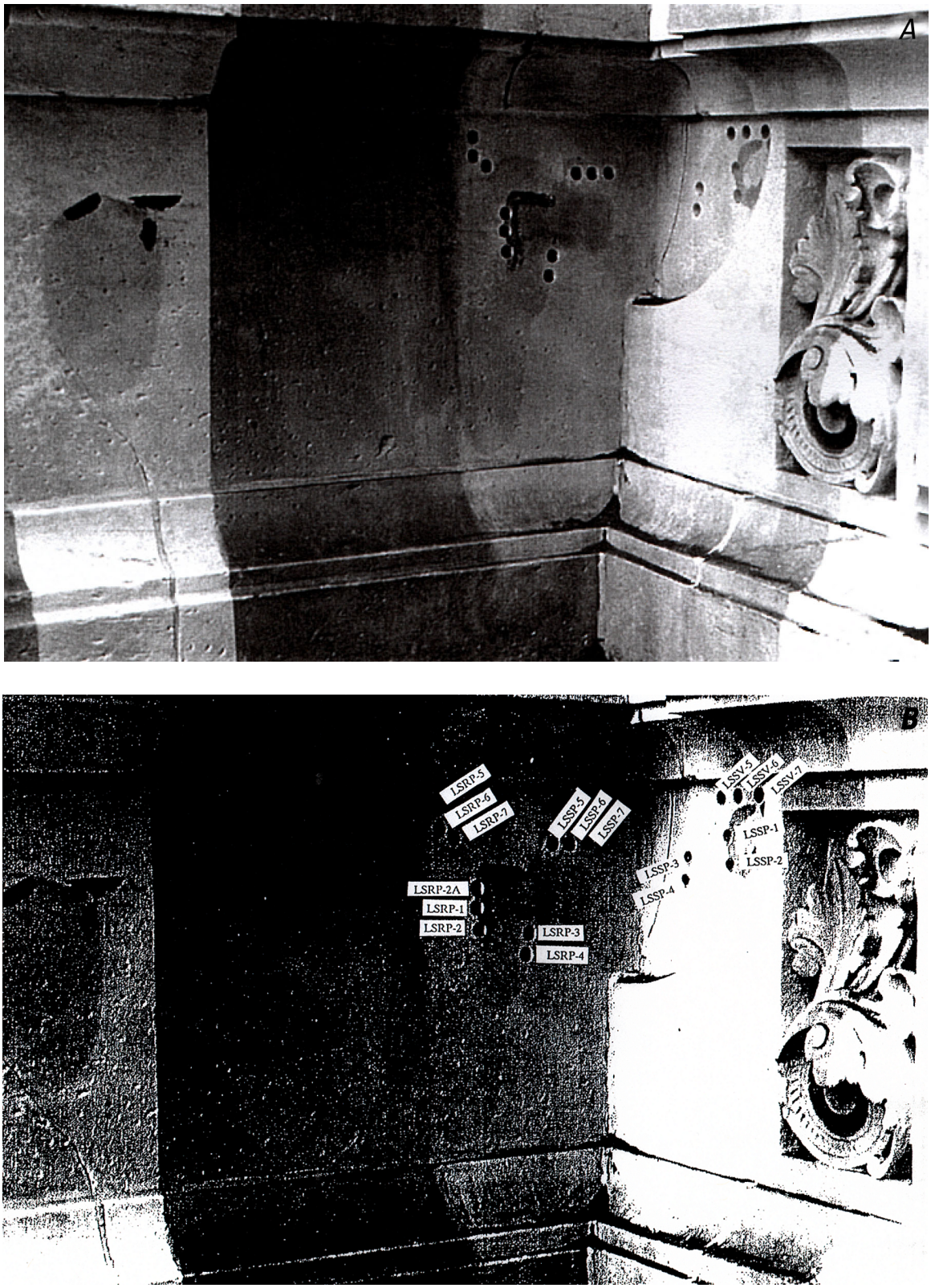

Figure 48.—South wall, upper scaffold level, showing locations of core samples in series LSRP, LSSP, and LSSV.

Figure 49.—West wall, upper scaffold level, showing locations of core samples in series LSSA, LSSG, and LSSV.

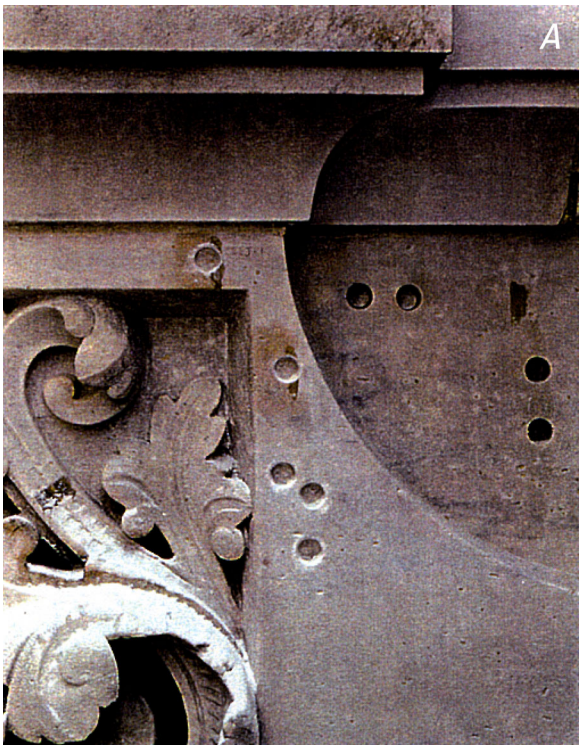

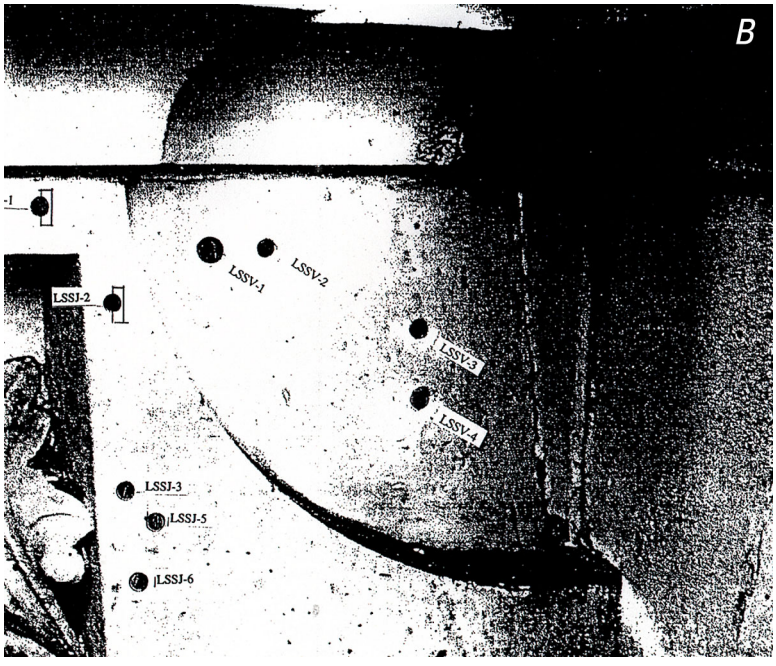

Figure 50.—West wall, upper scaffold level, showing locations of core samples in series LSSJ and LSSV.

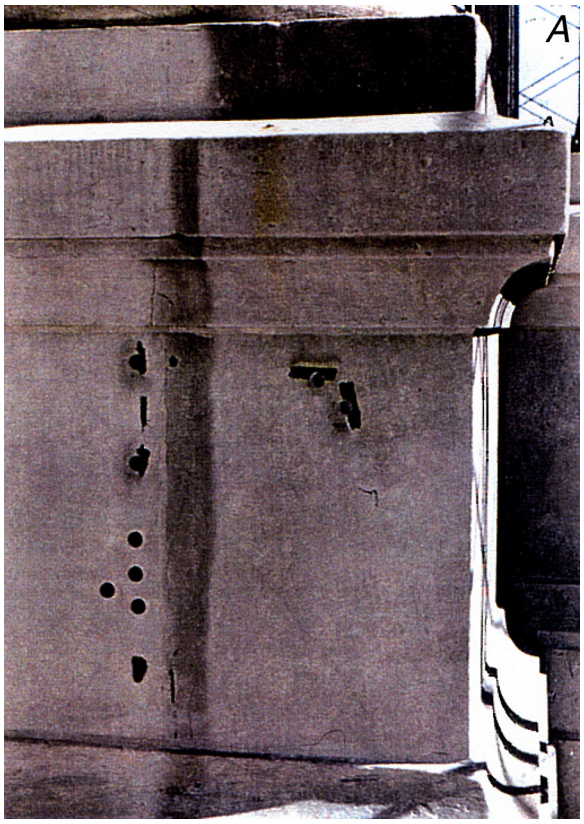

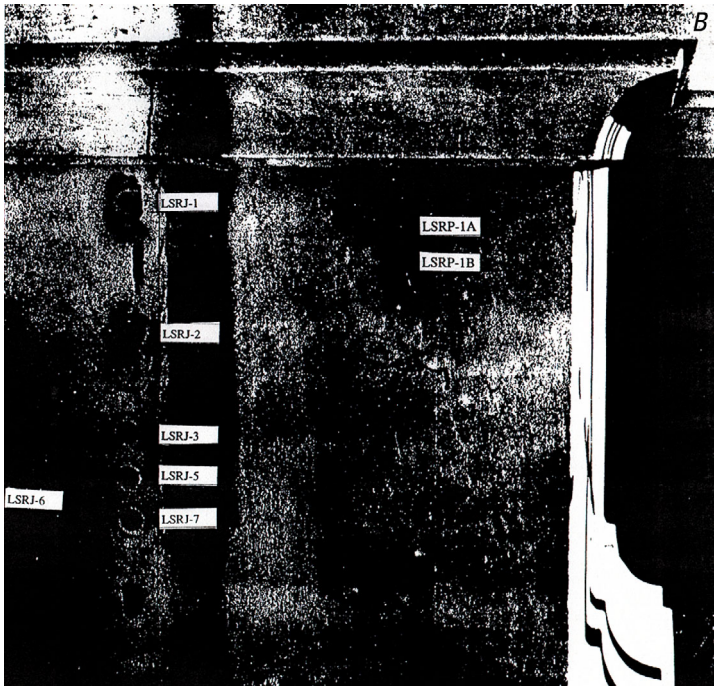

Figure 51.—North wall, upper scaffold level, showing locations of core samples in series LSRJ and LSRP.

Figure 52.—Entablature, lower scaffold level, showing locations of core samples in series GCRM, GCRV, and GCSM.

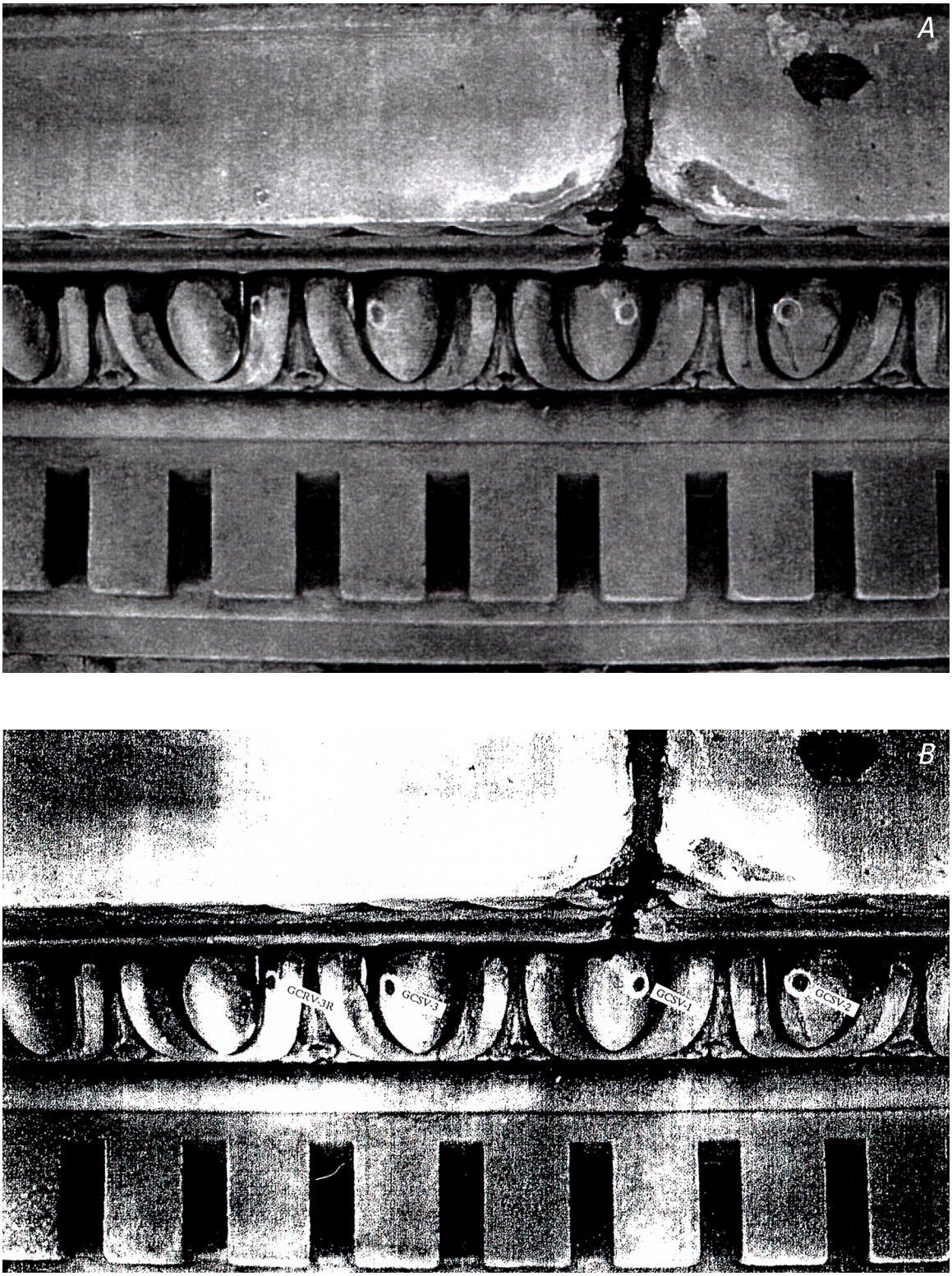

Figure 53.—Entablature, lower scaffold level, showing locations of core samples in series GCRV and GCSV.

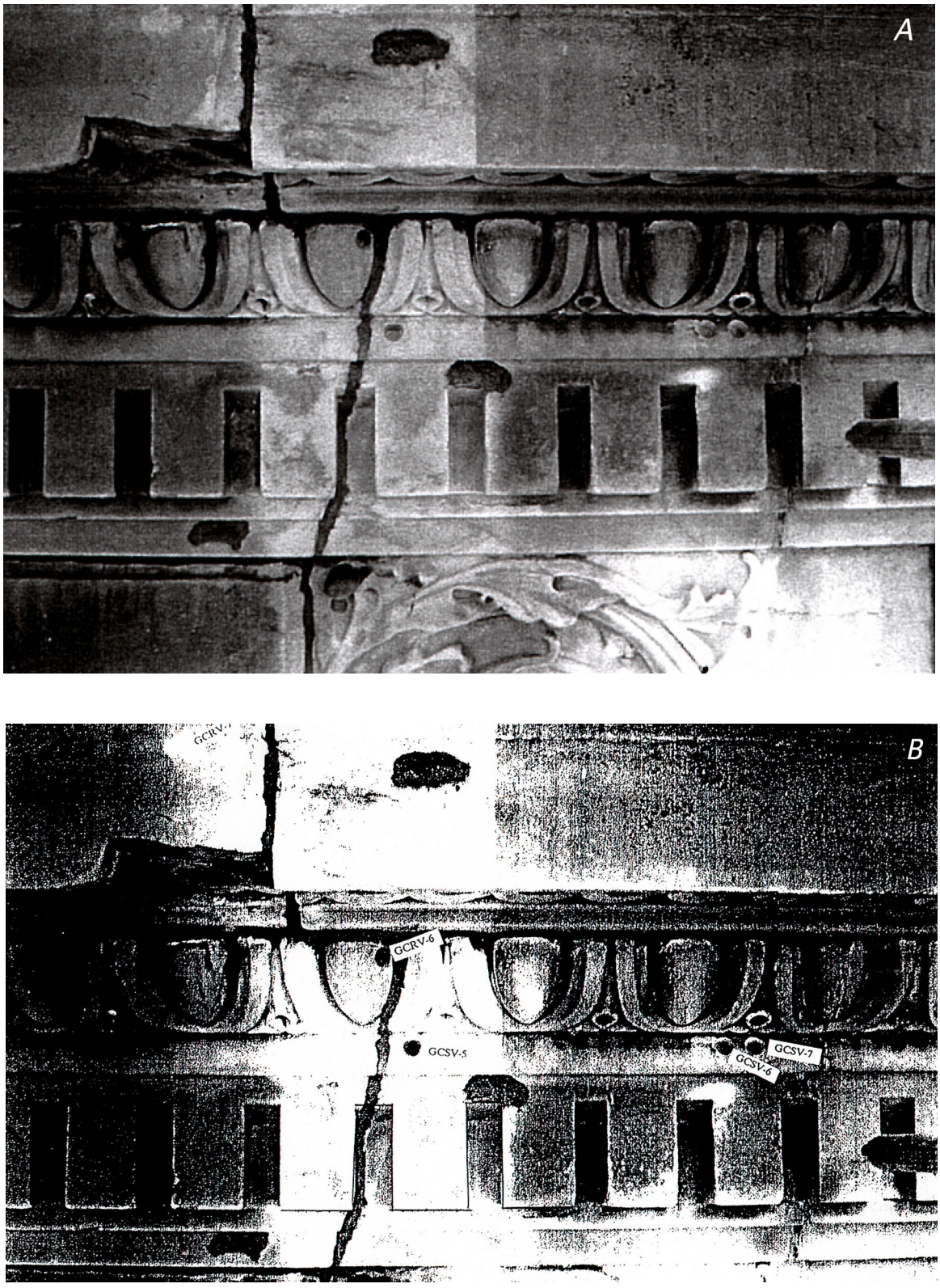

Figure 54.—Entablature, lower scaffold level, showing locations of core samples in series GCRV and GCSV.

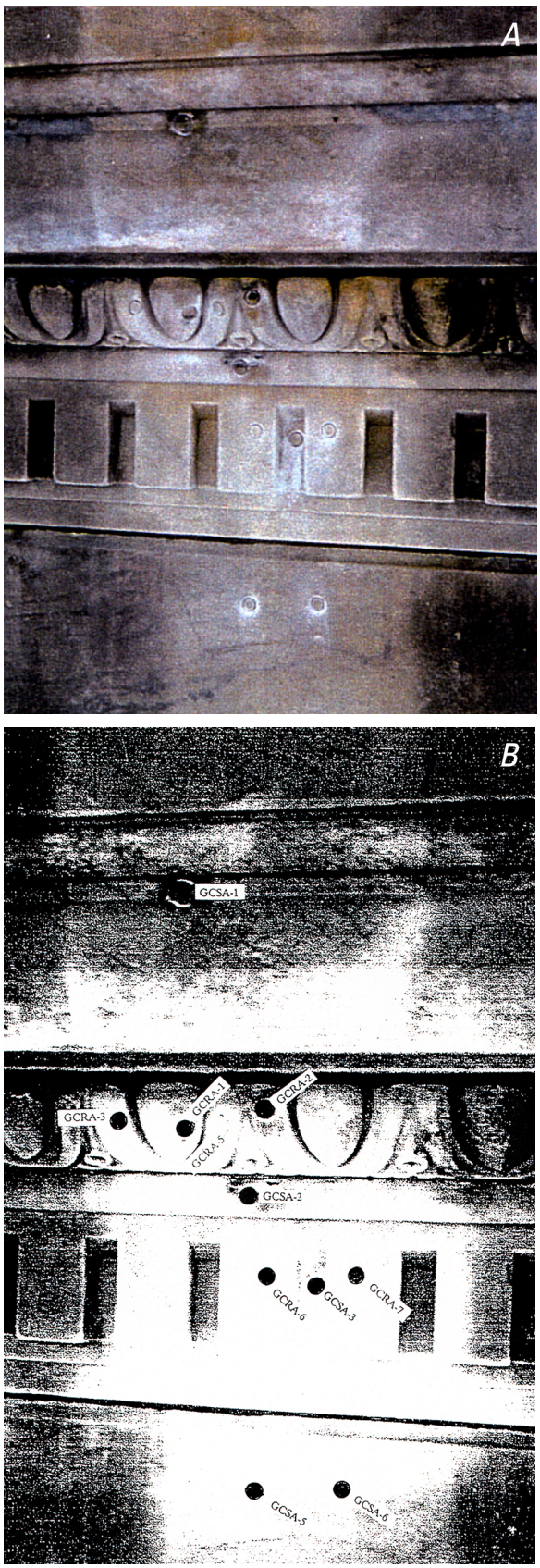

Figure 55.—Entablature, lower scaffold level, showing locations of cores samples in series GCRA and GCSA.

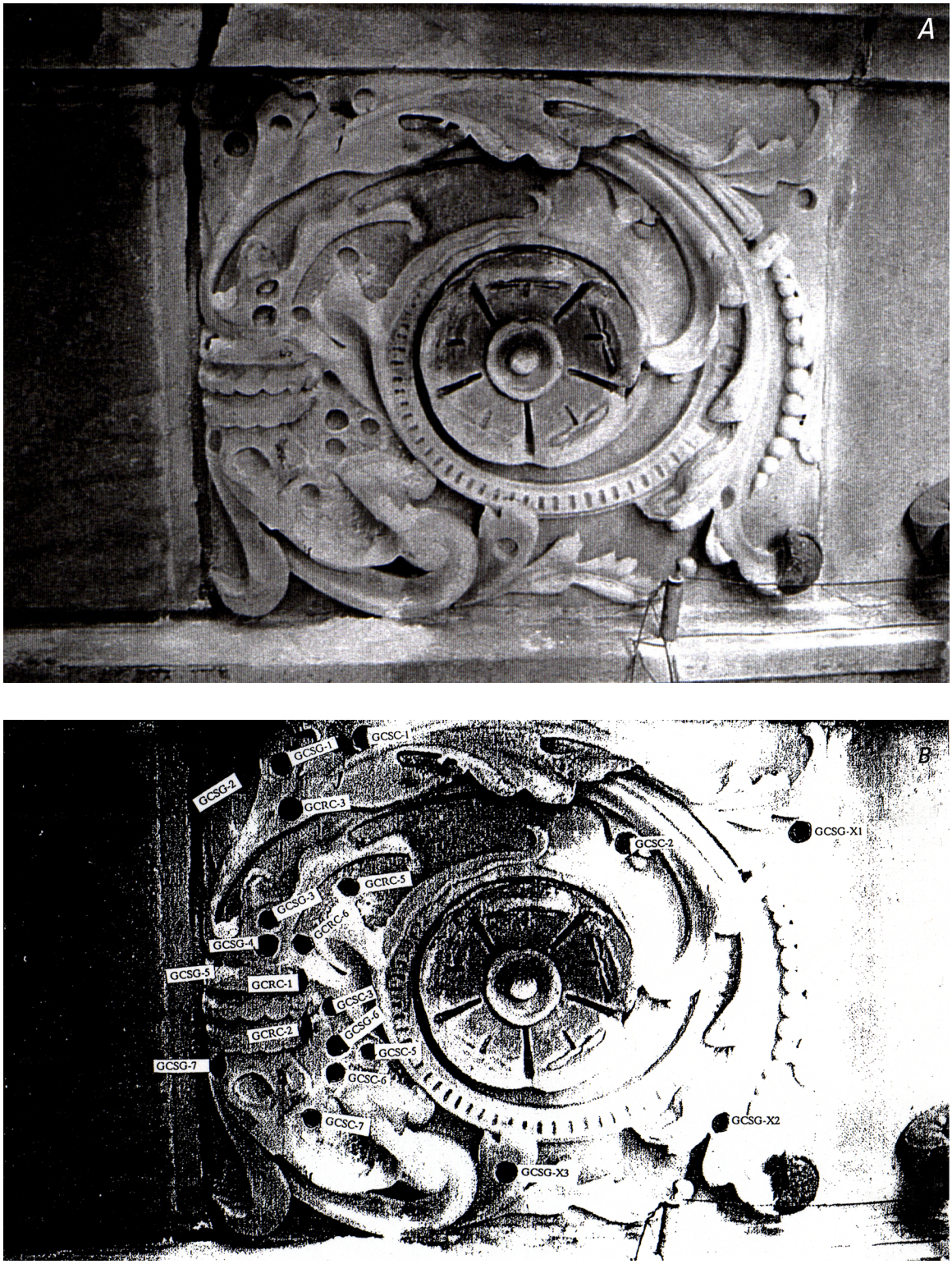

Figure 56.—Entablature, lower scaffold level, showing locations of core samples in series GCRC, GCSC, and GCSG.

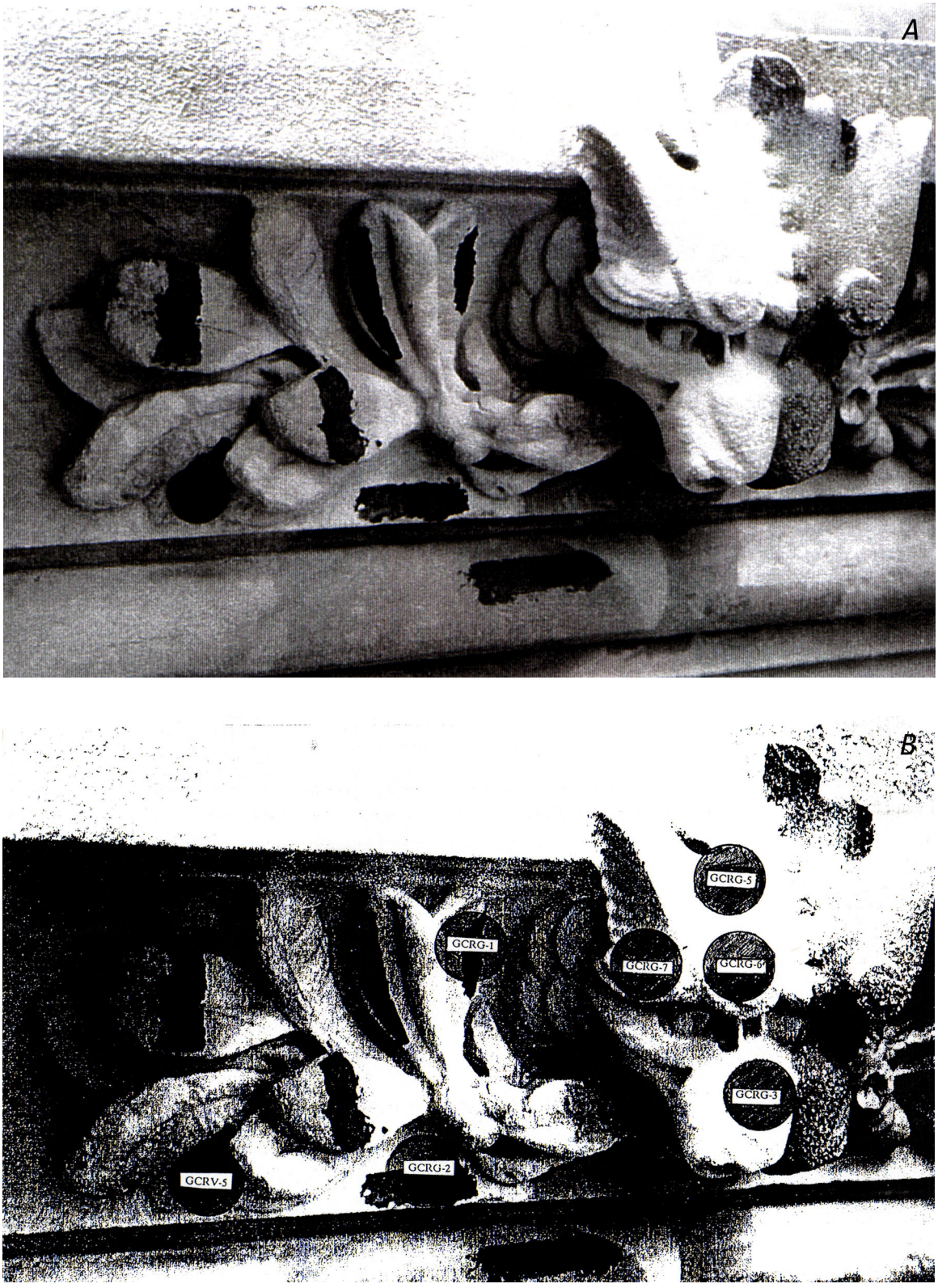

Figure 57.—Entablature, lower scaffold level, showing locations of core samples in series GCRG and GCRV.

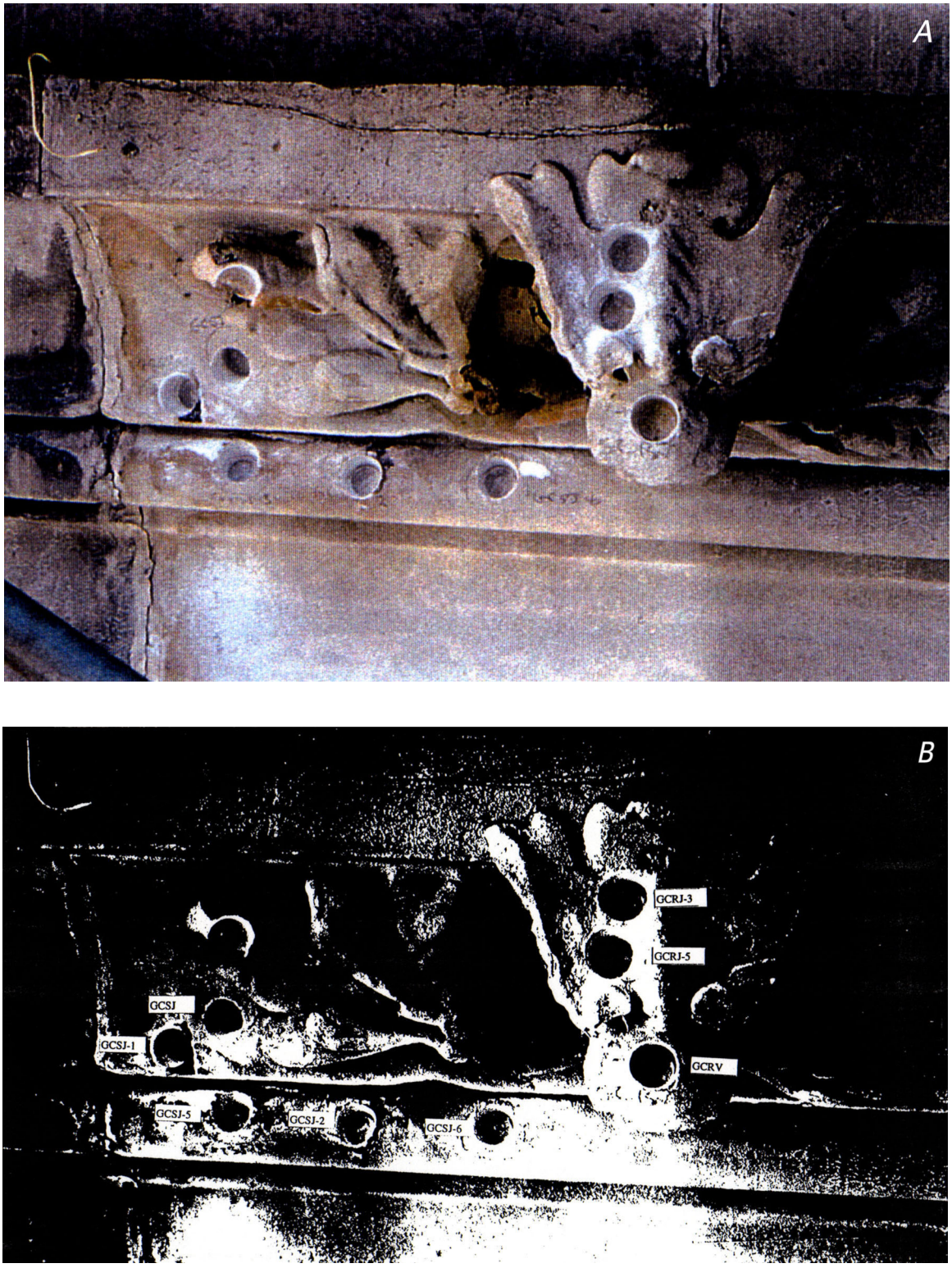

Figure 58.—Entablature on south side, lower scaffold level, showing locations of core samples in series GCRJ, GCRV, and GCSJ.

Figure 59.—Entablature, lower scaffold level, showing locations of core samples in series GCSJ.

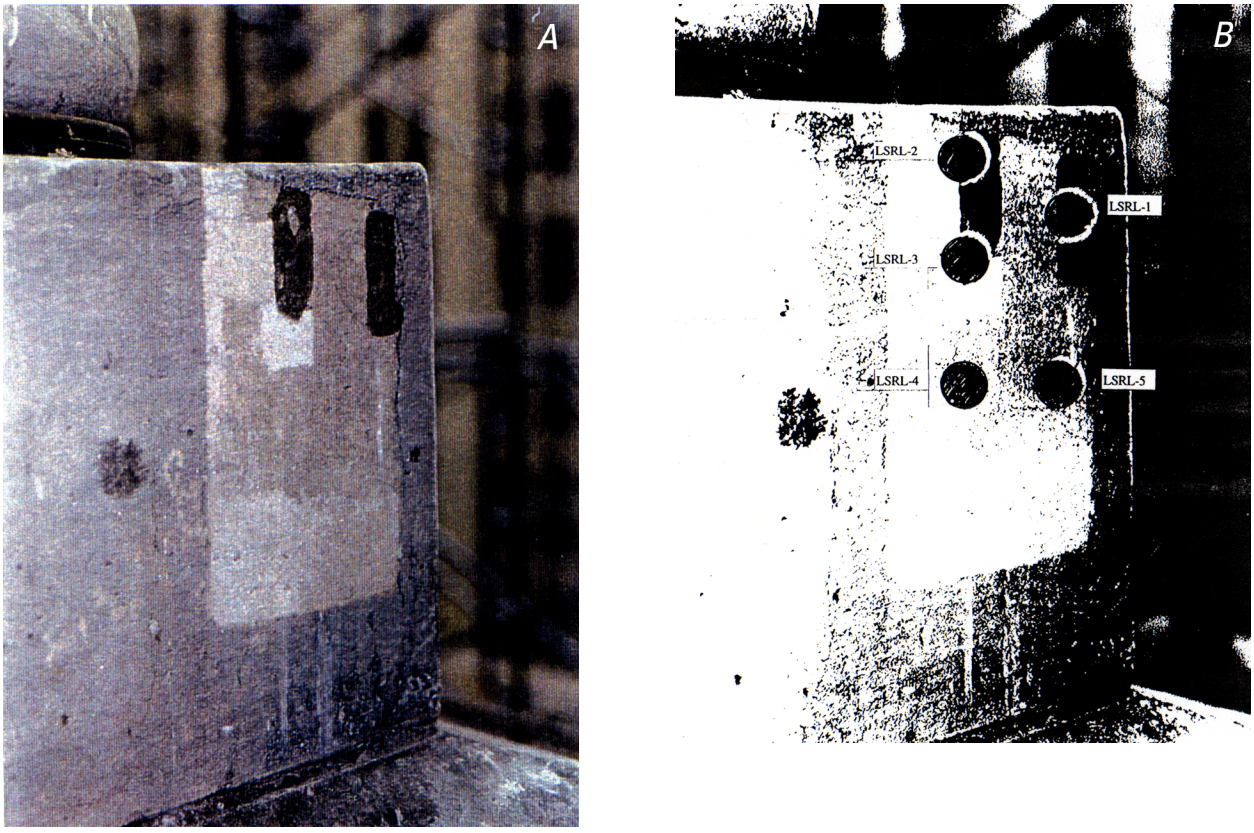

Figure 60.—Column base at 6th-floor level (see fig. 43), showing locations of core samples in series LSRL.

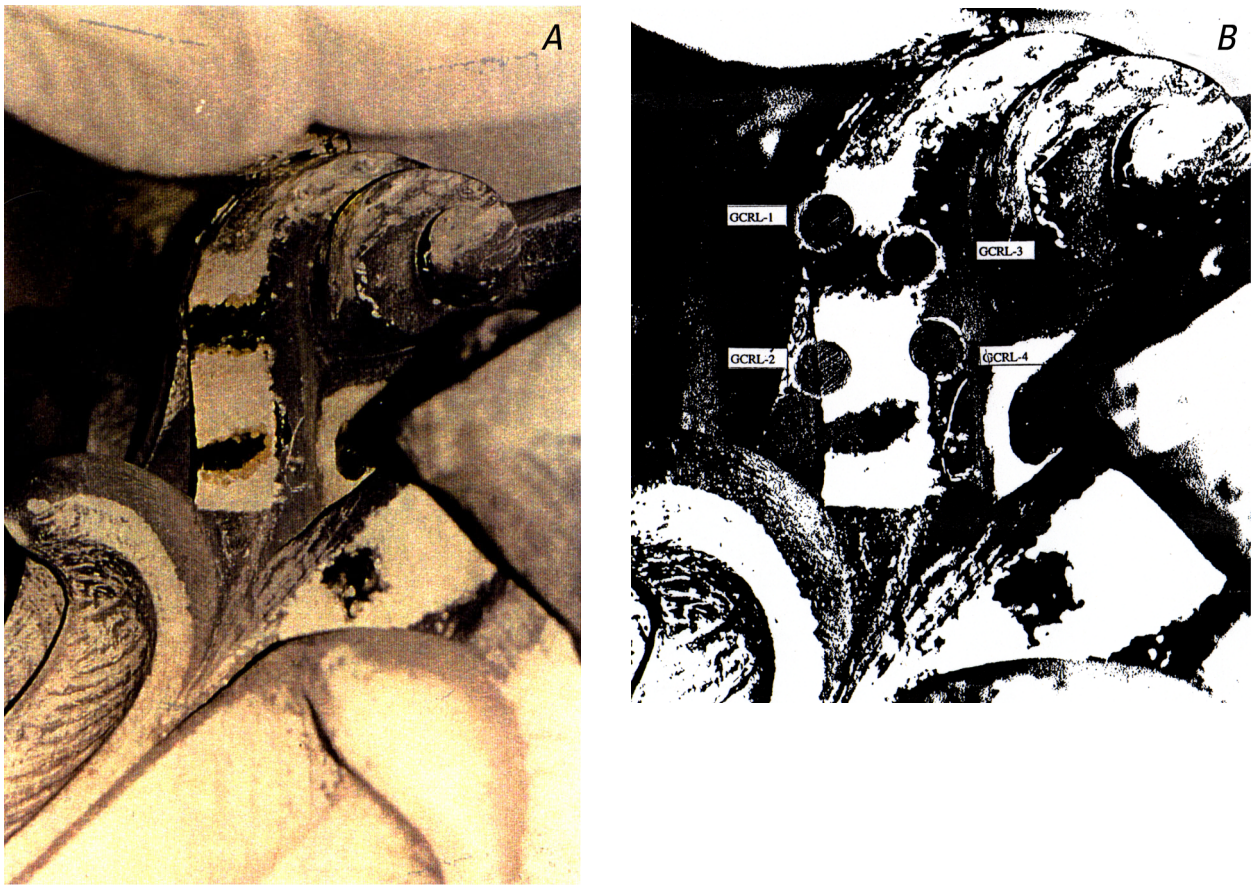

Figure 61.—Detail of column base at 6th-floor level, showing locations of core samples in series GCRL.

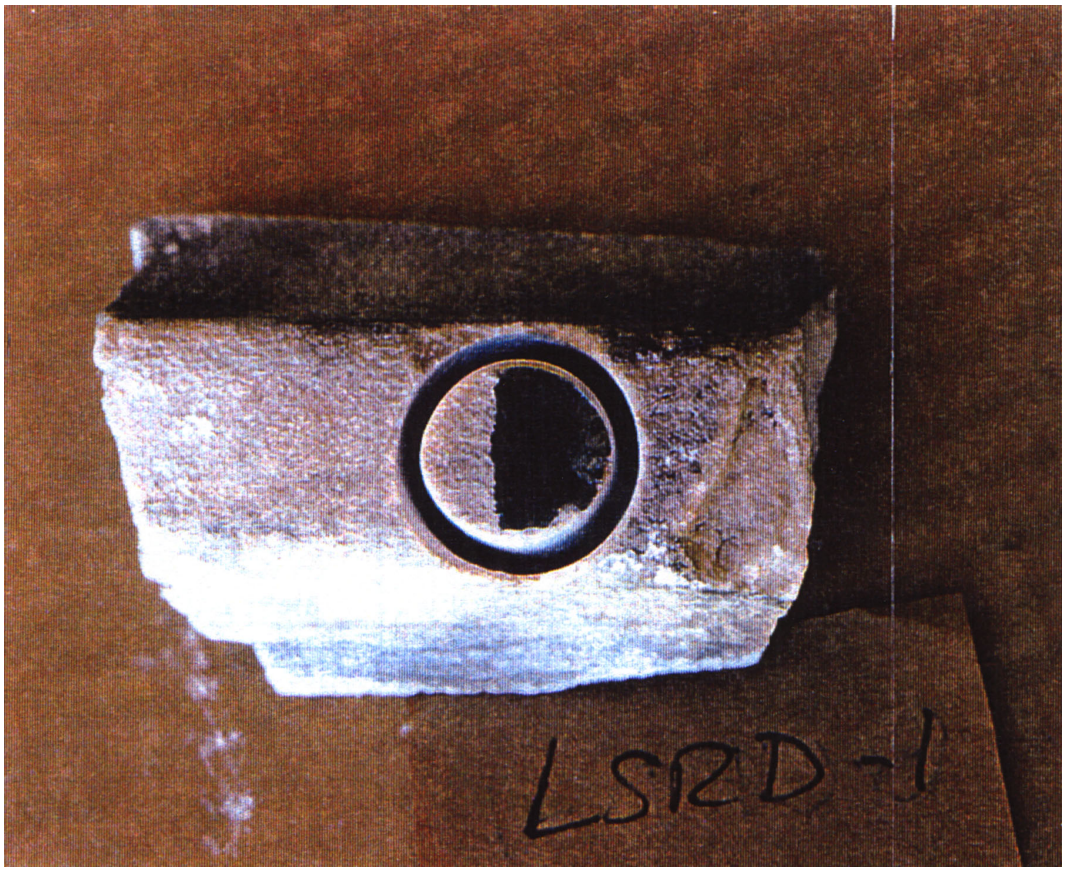

Figure 62.—Marble fragment from unknown location on building, showing location of core samples in series LSRD.

Figure 63.—Marble fragments from unknown locations on building, showing material for core samples in series GCRD.

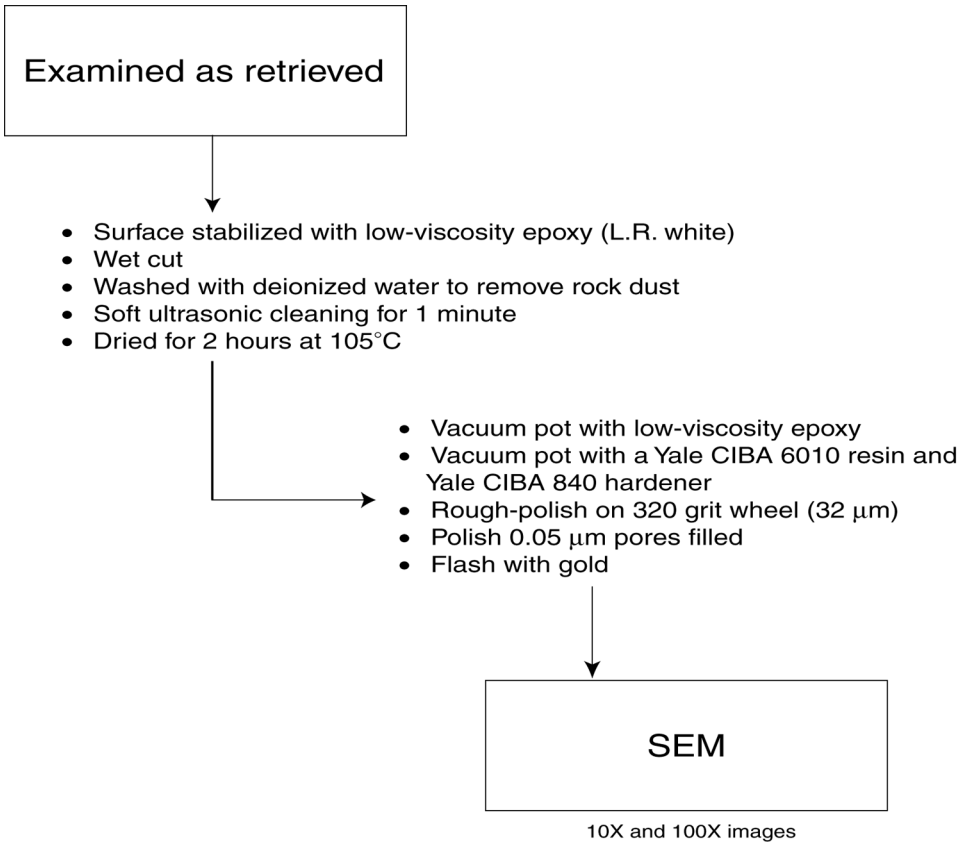

Figure 64.—Sample-preparation protocol for core samples selected for SEM analysis.

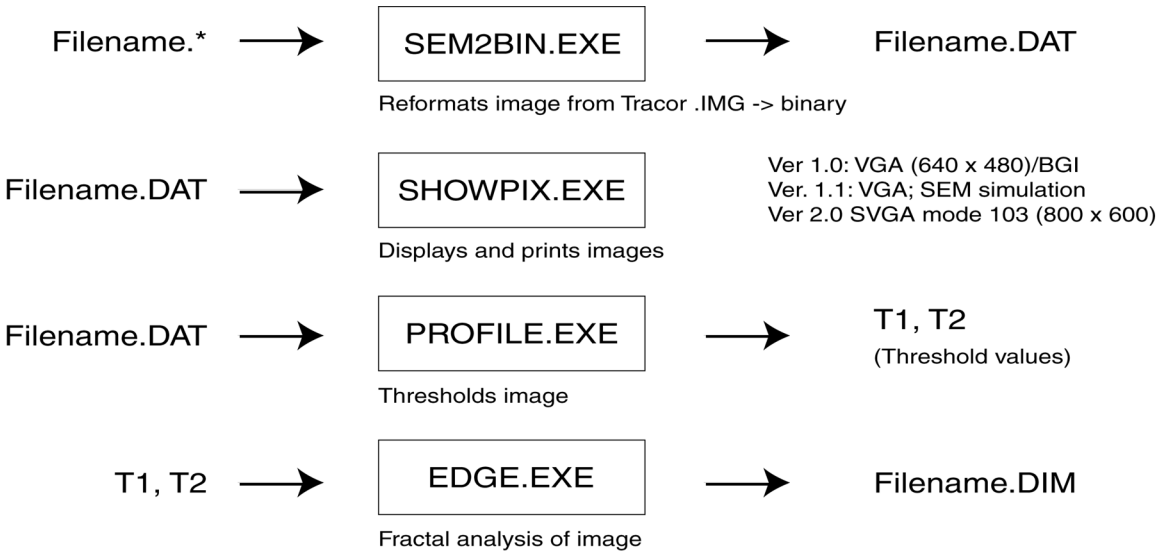

Figure 65.—Summary of SEM image-analysis programs.

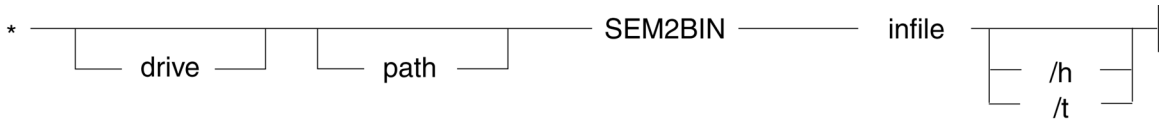

Figure 66.—Syntax for program SEM2BIN as run from DOS command line.

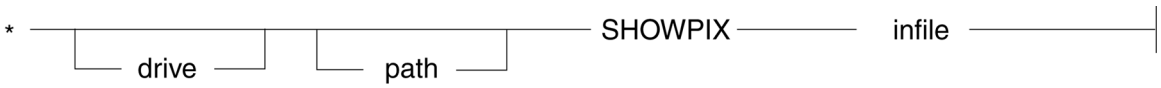

Figure 67.—Syntax for program SHOWPIX as run from DOS command line.

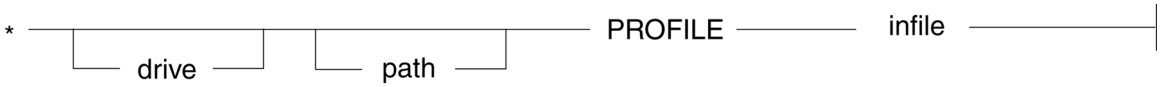

Figure 68.—Syntax for program PROFILE as run from DOS command line.

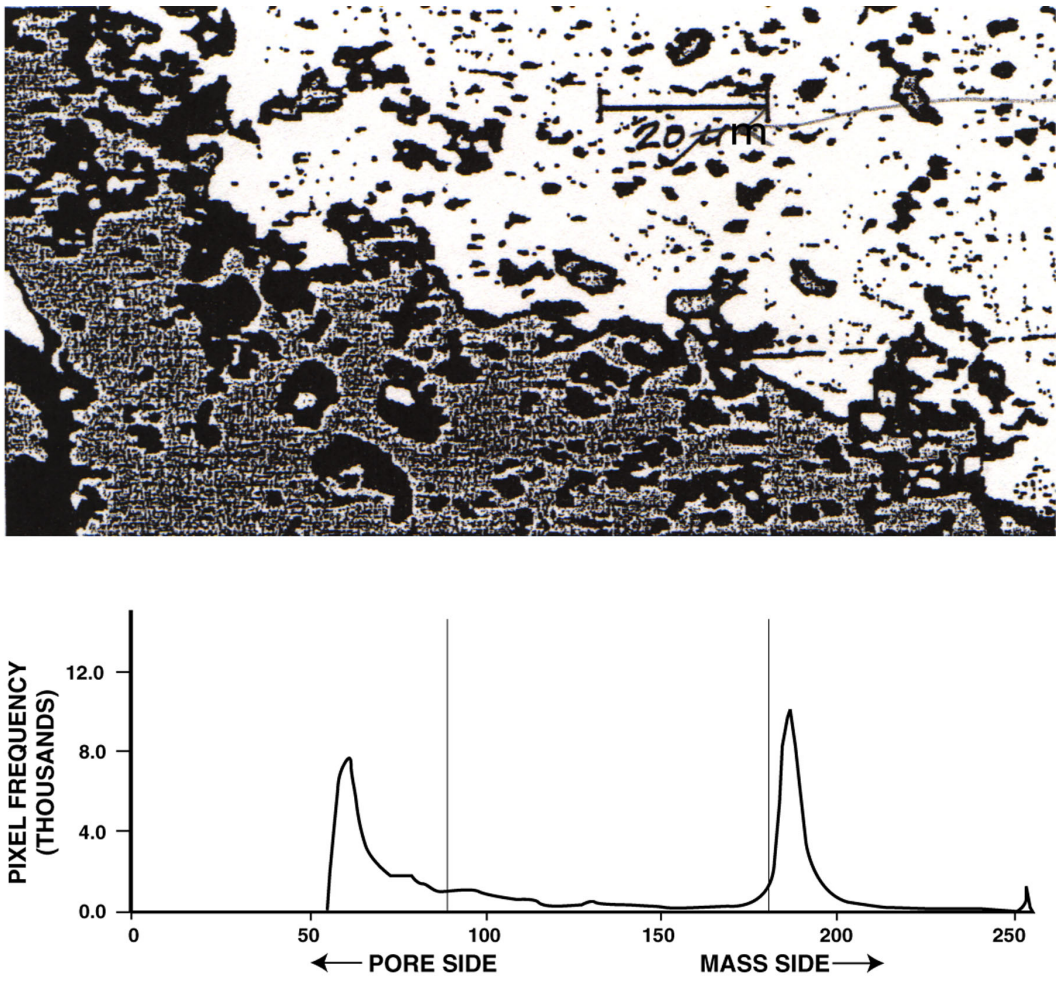

Figure 69.—Typical output image from program PROFILE. Bimodal histogram shows high occurrence frequency of both dark and light pixels. Location of bimodal peaks along gray scale differs from image to image because SEM images are not produced with same average brightness.

Figure 70.—Syntax for program EDGE as run from DOS command line.

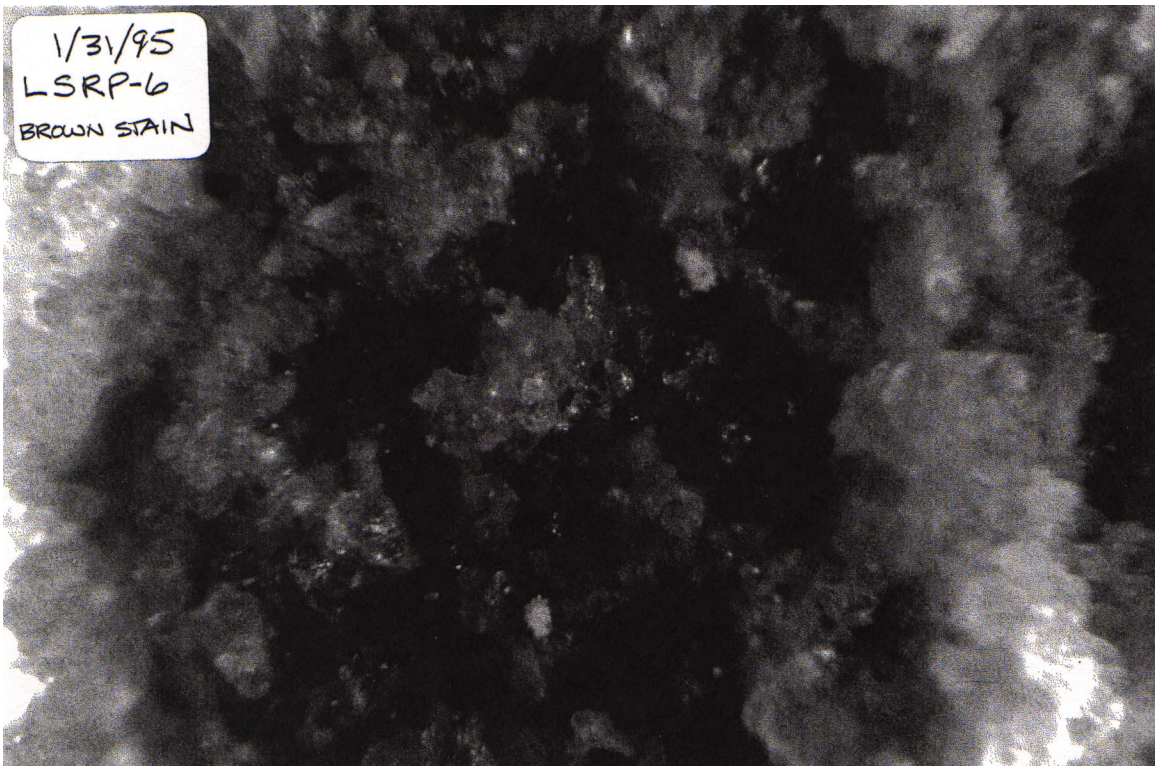

Figure 71.—Brown stain (approximately 2.5 mm across) on sample LSRP–6.

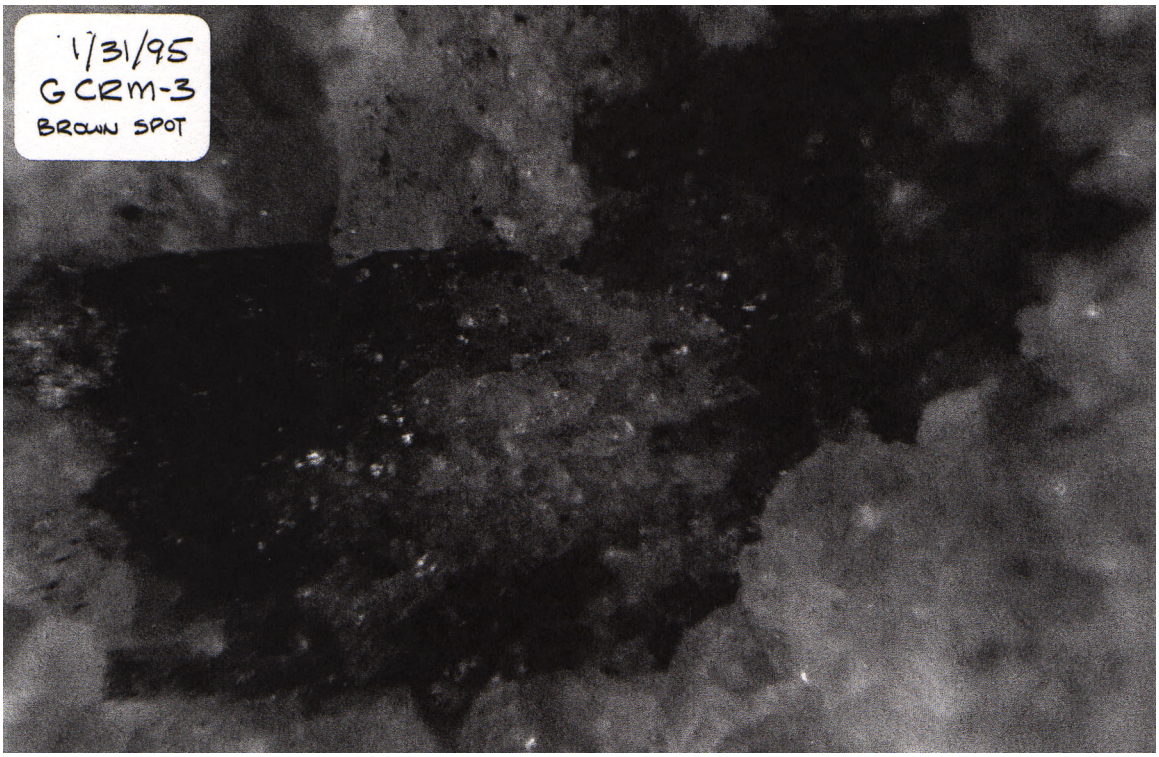

Figure 72.—Brown stain (approximately 1 by 2 mm) on sample GCRM–3.

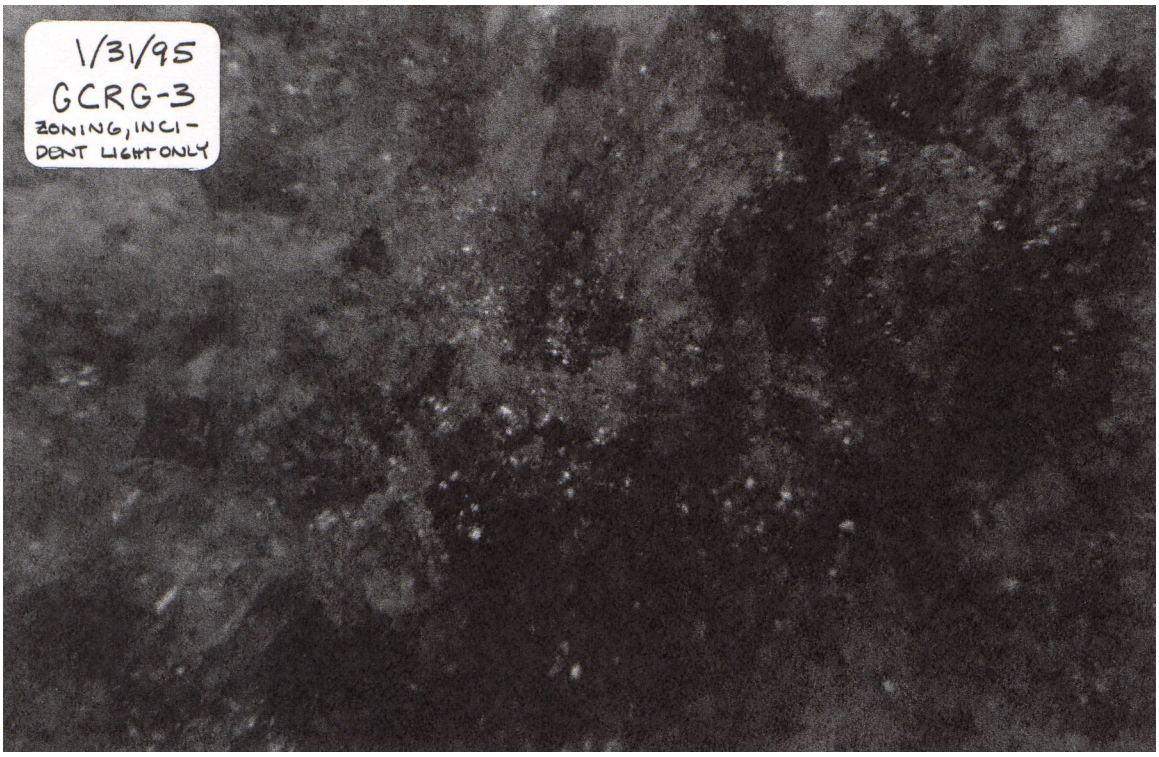

Figure 73.—Zoning on sample GCRG–3.

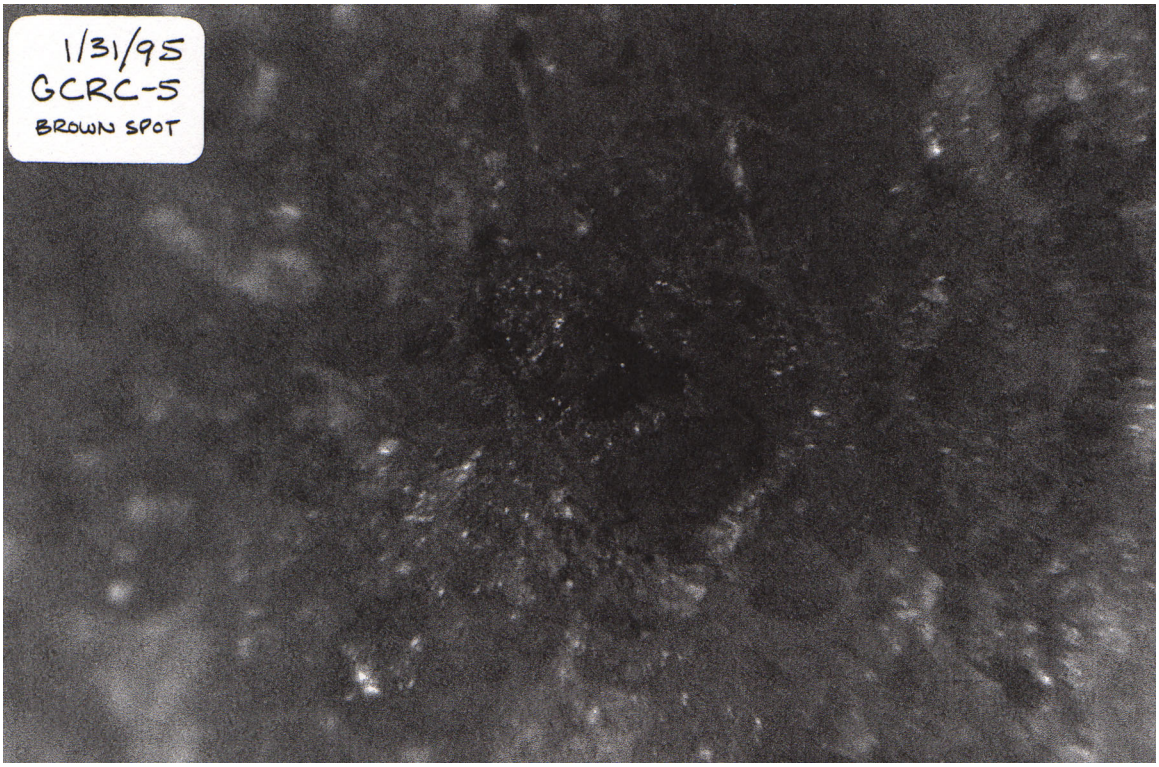

Figure 74.—Typical stained area on sample GCRC–5.

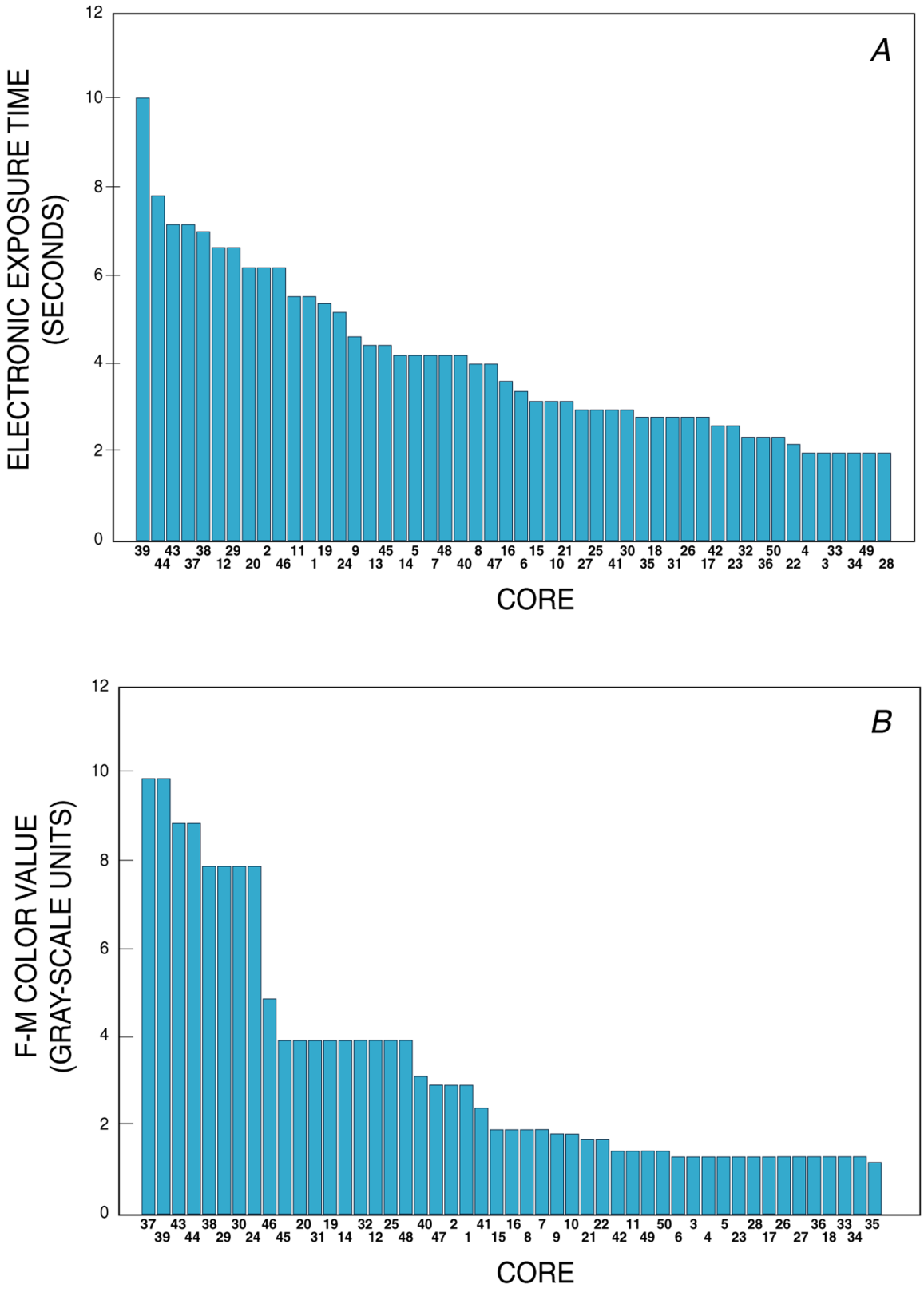

Figure 75.—Measured color values of core samples, in descending order from 10 to 0. *A*, Electronic technique. *B*, Visual method.

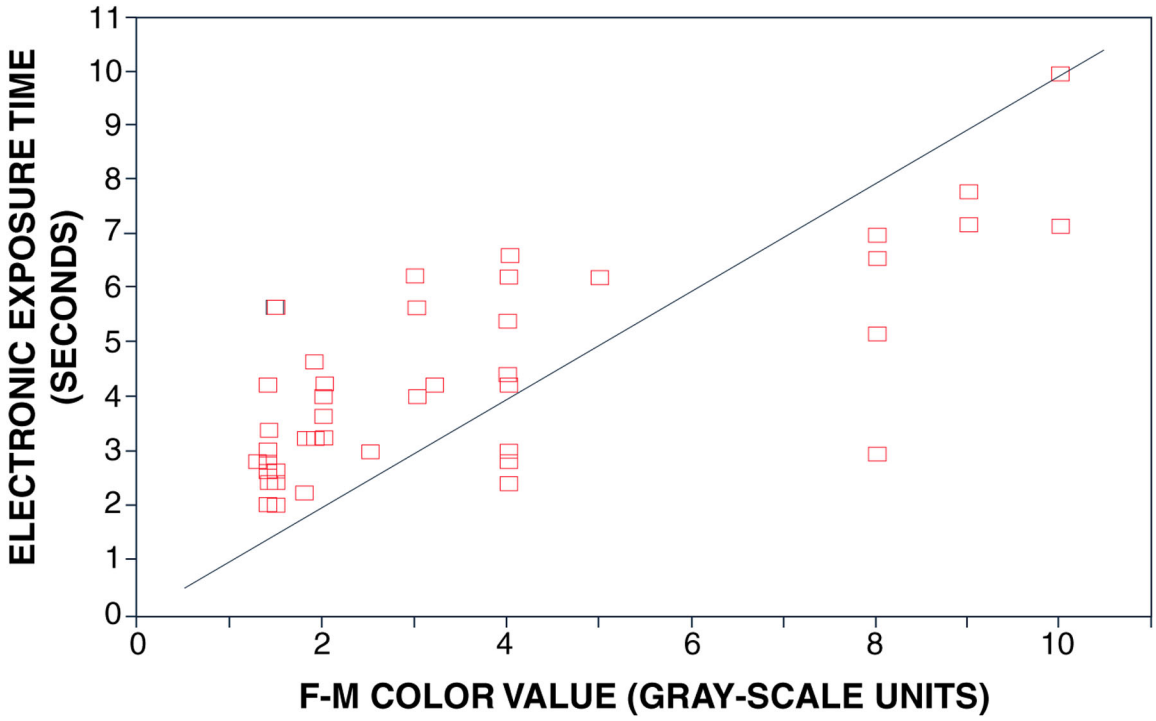

Figure 76.—Electronic exposure time versus F-M color value for grayness measurements on core series. Straight line is a curve with a slope of 1.

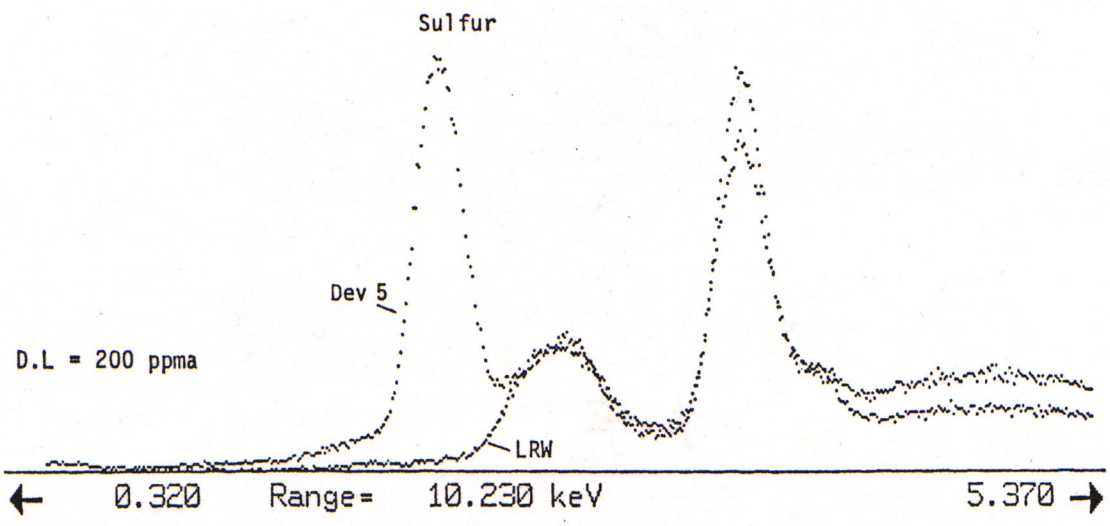

Figure 77.—X-ray-fluorescence spectra of Devcon 5 epoxy resin (Dev 5) and L.R. white acrylic resin (LRW). Leftmost peak is sulfur K_{α} line; rightmost peak is argon in ambient air.

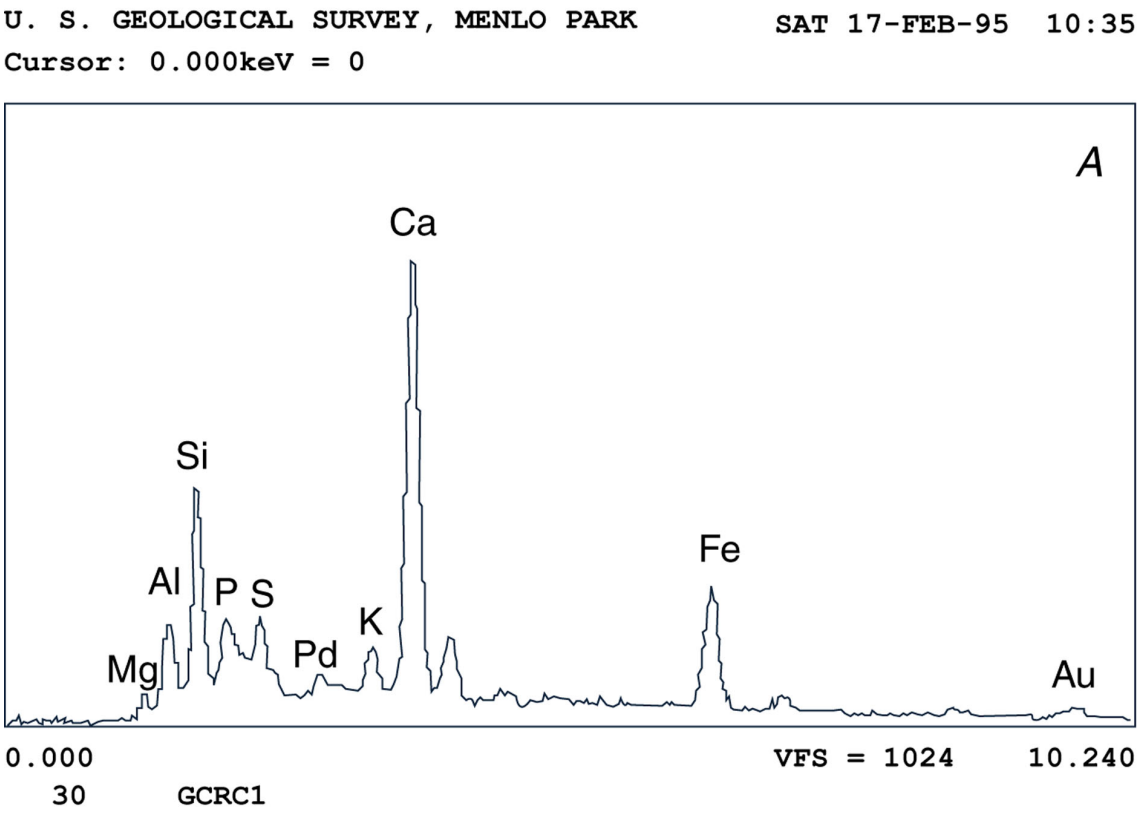

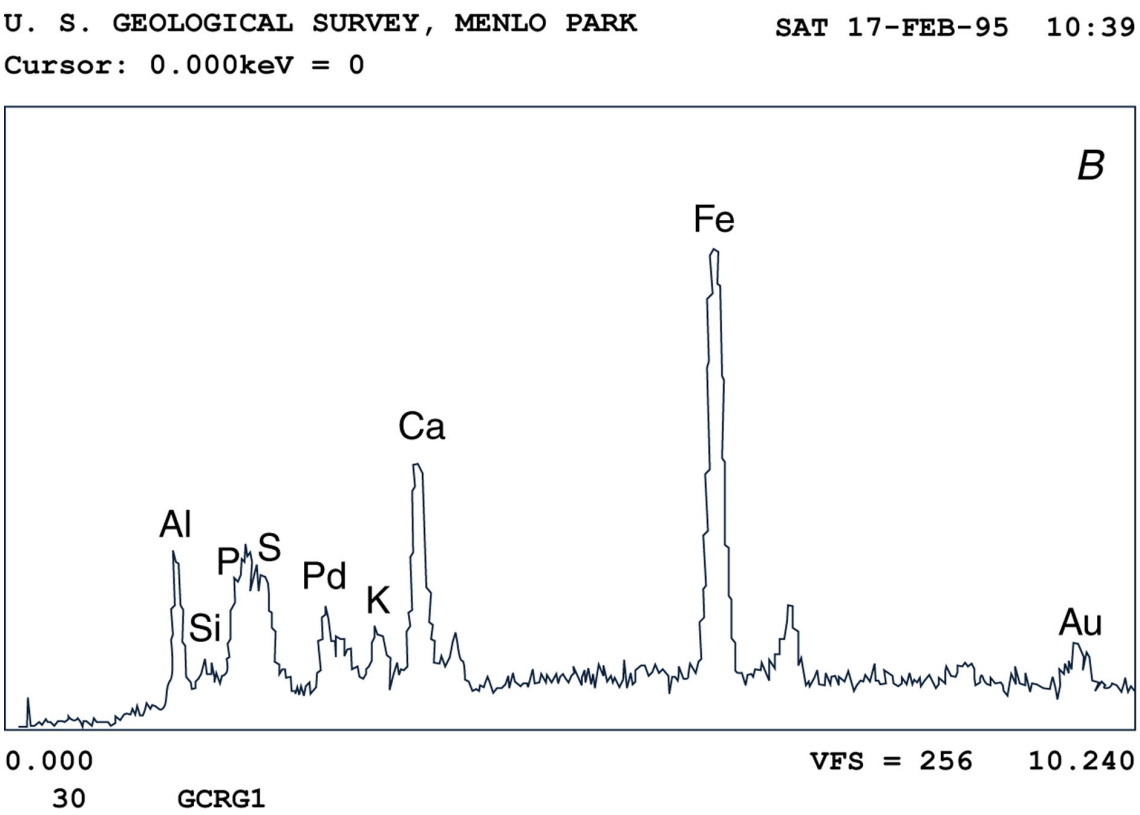

Figure 78.—Typical X-ray-fluorescence spectra of uncleaned samples in core series GCR. *A*, Silicate minerals. *B*, Iron minerals.

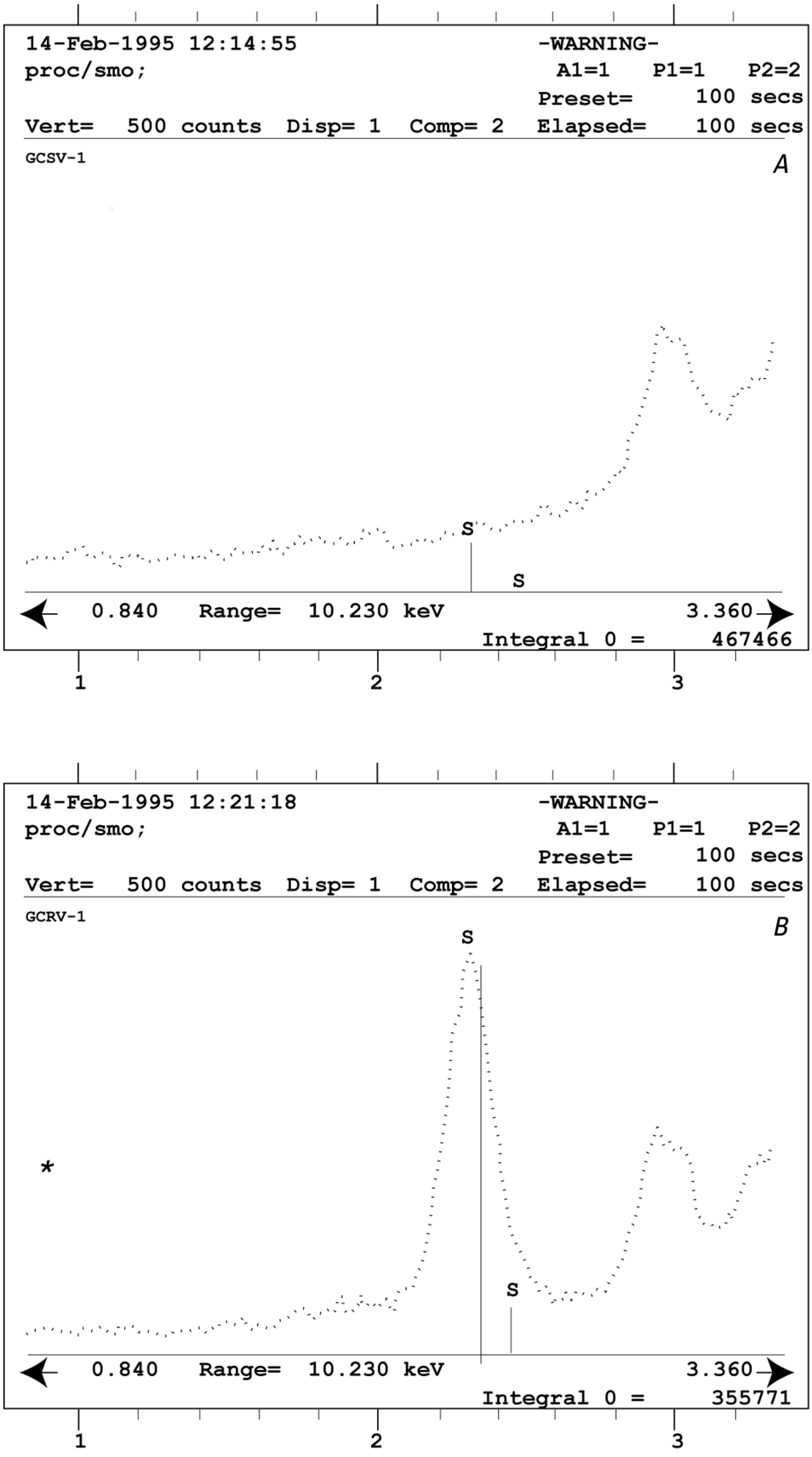

Figure 79.—Typical X-ray-fluorescence spectra of silicate and iron minerals in uncleaned samples in core series GCS (*A*) and GCR (*B*).

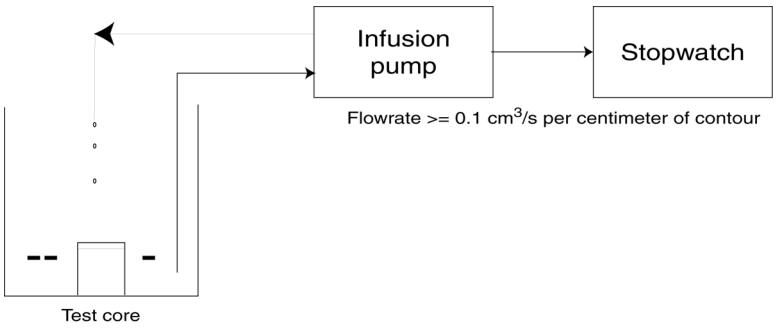

Figure 80.—Schematic diagram of system used for surface-reactivity test.

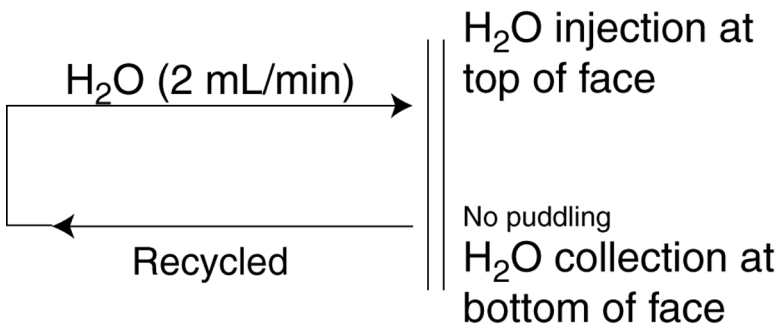

Figure 81.—Configuration of alternative apparatus used for surface-reactivity test.

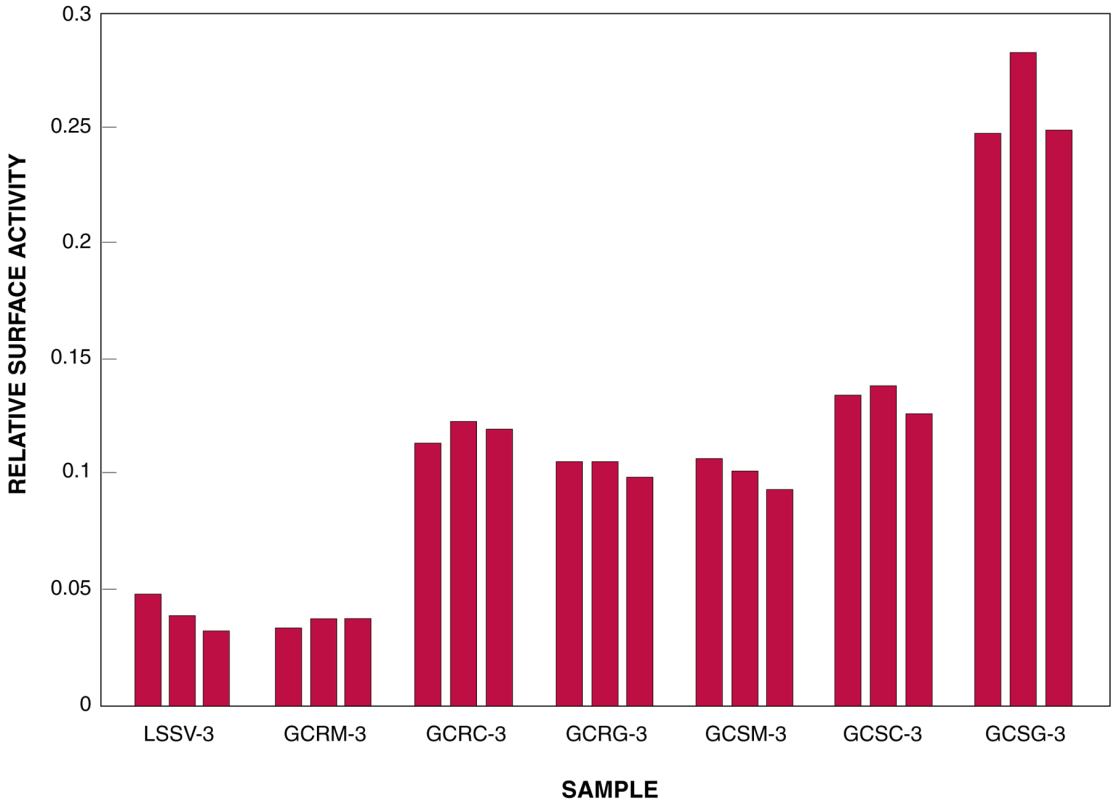

Figure 82.—Relative surface activity (*W* value) of samples in core series 3.

Table 1.—Summary of technical details on four cleaning techniques selected during first phase of this study—Continued.

Symbol	Description	Comments
WW	Water wash	Hose pressure. Not useful as a cleaning or rinsing method.
PW	Power wash	Water delivered at approx 100 to 600 lb/in^2 pressure, depending on standoff distance, tip of wand to stone surface. Effective on protected areas, such as the pilaster to the south of the window at the top-platform level; not effective on exposed areas without aid of detergents. Streaks of clean stone appear when tip is held close to surface. Danger of damage to stone when tip is used in this manner. Effective as a rinse.
ST	Steam	Deliver at 80 °C at approx 150 lb/in^2 pressure. Uneven results. Difficulty experienced in delivering even flow. Streaky. Less effective than PW. Note problems with cold weather on 3/16/95 and problems with equipment.
ADC	Alkali detergent liquid concentrate	pH 10.6. Brush-coat dwell time, 10 minutes. Even cleaning when followed by PW at the top-platform level, but not as effective as ADG. Not effective at the second-level frieze.
ADG	Alkali detergent gel	pH 9.7. Gel left on 10 to 15 minutes. Even cleaning when followed by PW at the top-platform level. Easier to use than detergent in liquid-concentrate form. Not effective at the second-level frieze. G.S. Wheeler thinks ADG/PW is the most practical general cleaning system if a water-based cleaning technique is selected but that approx 20 percent of the surface will have to be recleaned by other techniques.
ACH	Alkali gel with chelating agents	pH 8.5. Potentially more aggressive than detergent solutions, produced a spottier cleaning than detergents on the top-platform level but was as ineffective as the detergents on the second-level frieze.
APW AR	Alkali prewash/acid rinse	A two-step system. The alkali pretreatment sits on the stone for 30 minutes and then is rinsed off. An acid cleaner is then applied for 3 to 5 minutes and rinsed off. When used with PW, this technique produced very clean surfaces. Problems include a rough, etched surface appearance, likely removal of stone, and potential chemical residue in spite of rinse.

Table 1 (Cont.)—Summary of technical details on four cleaning techniques selected during first phase of this study.

Symbol	Description	Comments
Misting	Filtered water	Delivered as a fine spray from a series of nozzles and played over the stone from 4 to 24 hours. This technique works by dissolving gypsum crusts. Problems are that it is time consuming to control so that maximum cleaning is achieved without removal of marble from weakened substrates. Also, more water can enter the building by this technique than as a result of any other water-based cleaning technique tested.
Thomann-Hanry process	---	An abrasive cleaning technique using a proprietary mixture of glass particles (5 to 50 μm) and aluminum silicate crystals, delivered at very low pressure (approx 30 lb/in^2). Gypsum crusts and soiling layers are removed from the surface. The method is fast and produces an even, clean appearance that is less rough than APW/AR and possibly less rough to the touch than detergent-cleaner/PW techniques. Main advantages are control, absence of water, smoothness of finished surface, and effectiveness.

Table 2.—Summary of important operational features of four of the eight cleaning techniques evaluated in this study. Features not discussed, but that should be considered in future studies, include liability and cyclical maintenance—Continued. [Chemical: chemical cleaning techniques tested in 1994.]

Cleaning technique:	LASER	Misting	Power wash	Chemical	Gommage
Criteria					
Cost	High	Moderate	Lowest	Moderate	High.
Sequence	Light delivered from portable source connected to portable power unit. Work area by area in flexible patterns.	Soak 4 hours; scrub with detergent, scrub without detergent. Rinse by more watersoak. Work in vertical strips entire height of building or to drainage points.	Pretreat with water. Scrub with and without detergent. Water-rinse at medium (100 to 500 lb/in^2) pressure. Rinse with vaporized water at low pressure (10 to 30 lb/in^2). Work up area by area.	Pretreat with water. Apply alkali prewash on marble. Apply acid wash. Rinse with low-pressure water. Work up area by area.	Mineral or aluminum silicate crystals, approximately 50 μm, in gentle air-abrasive system at low (5 to 35 lb/in^2) pressure. Apply dry, collect with water for drainage and removal. Work in flexible patterns.
Selectivity	Level of cleaning optional by electronic controls. Adjustment possible for varying thicknesses of soiling or to allow for fragile areas of stone.	Operator has little control over final appearance. Repetition of watersoak cycle if soiling is stubborn.	Operator controls by adjusting pressure, flow, standoff, and duration. Continuous evaluation.	Can control by testing for concentration and dwelltime. Cannot control overcleaning in places. May appear spotty and require retreatment.	Operator can control pressure, flow, standoff, and dwelltime and adjust for varying surface-soiling conditions.
Sensitivity	Removes dirt but not chemical or biological stains. Chemical or mechanical cleaning must follow in problem areas.	Removes surficial water-soluble dirt but not chemical or biological stains. Problem areas may require chemical or abrasive followup cleaning.	Removes superficial soiling and accretions and some entrapped matter because of water pressure. Removes some chemical and biological stains. Spot followup treatments with chemical or abrasives may be needed.	Removed surface and some subsurface soiling. Most stains are removable by adjusting or adding chemical after rinsing cycles.	Removes dirt and pollutant crusts but not chemical stains. Retreatment with power wash may be necessary for green frugal staining.
Protection of adjacent materials	Easily controlled because cleaning power is highly focused and exhaust plume can be directed.	Essential to seal well all cracks and open joints in stone and to seal windows.	Masking of windows, cracks, and open joints required.	Attention needed to assure adequate masking of windows, cracks, and open joints.	Minimal protection required. Controlled delivery and efficient collection system within isolated work cabin.
Duration	Slow process; takes several minutes to clean 6 in^2.	Slow process; 4 to 24 hours.	As fast as number of workstations.	As fast as number of workstations. Each workstation should be relatively small area.	Relatively fast.

Table 2 (Cont.)—Summary of important operational features of four of the eight cleaning techniques evaluated in this study. Features not discussed, but that should be considered in future studies, include liability and cyclical maintenance. [Chemical: chemical cleaning techniques tested in 1994.]

Cleaning technique:	LASER	Misting	Power wash	Chemical	Gommage
Criteria					
Structural	Risk to stone from heat burst appears less severe than force of water or abrasive media.	Some loss of sugary-textured stone must be accepted. Water soaking into building can cause problems.	Powdery and loose stone removed by pressure. Operator must note surface-soiling condition forward of power-wash path.	Method removes surface of stone. Potential chemical residues may cause damage.	Removes some surface stone, but less than chemical techniques or power wash.
Ease of operation	Special training required. Technique is slow enough to allow adjustment of control settings as situation changes on stone surfaces.	Wet, messy, and labor intensive.	Operator likely to be engaged by obvious success and control of cleaning treatment.	Unpleasant but familiar work for operators.	Special training required. Method requires concentration at all times.
Health and safety	Not fully identified at present time.	Minimal	Minimal	Moderate	Moderate.
Protection of pedestrians	Beam source must not be visible to pedestrians or operators.	Runoff channels and equipment on street must be monitored regularly.	Street barriers must be maintained.	Street barriers must include runoff paths and waste-collection areas.	Isolated work cabin on scaffolding protects pedestrians. Street barriers underneath.
Waste removal	Material from plume must be caught by vacuum and collected.	Runoff can be directed into sewer system.	Runoff can be directed into sewer system.	Waste must be collected and arrangements made for required disposal system.	Waste removal required and an integral part of Thomann-Hanry system.
Adaptability to changing technology	Excellent because it causes minimal change at stone surface.	New technology used on another area of building will probably yield better results.	Yes	Residues may react with future cleaning materials.	Yes.
Annoyance factor	Minor	Moderate	Moderate	Considerable	Minor.
Public perception	Developing technololgy unknown in the United States.	Familiar	Familiar	Accepted	Hardly known in the United States and likely to get some negative press.
Availability of independent testing	Prelimary tests available.	Yes	Yes	Yes	Yes, but limited and not available for dolomite.
Proprietary	Yes	No	No	No	Thomann-Hanry has developed a system with nonproprietary cleaning material and technology.

Table 3.—Inventory of core samples from the building—Continued.

	Virgin stone (uncleaned) (V)	Cleaning technique							
		Misting (M)	Power wash (P)	Gommage (G)	Combination (C)	Armax (A)	JOS (J)	Laser (L)	Dry ice (D)
					Lightly soiled, smooth (LSS)				
USGS samples taken for surface-loss, surface-roughness, pore-space, and salt-mapping tests	LSSV-1, LSSV-2	---	LSSP-1, LSSP-2	LSSG-1, LSSG-2	---	LSSA-1, LSSA-2	LSSJ-1, LSSJ-2	---	LSSD-1, LSSD-2, LSSD-2A
Samples taken for accelerated-weathering tests	LSSV-3, LSSV-4	---	LSSP-3, LSSP-4	LSSG-3, LSSG-4	---	LSSA-3	LSSJ-3	---	LSSD-3
Samples taken for deposition-velocity tests	LSSV-5, LSSV-6	---	LSSP-5, LSSP-6	LSSG-5, LSSG-6	---	LSSA-5, LSSA-6	LSSJ-5, LSSJ-6	---	---
Client sample	LSSV-7	---	LSSP-7	LSSG-7	---	LSSA-7	---	---	---
Additional samples	LSSV-3R	---	---	LSSG-1A	---	---	---	---	---

Table 3 (Cont.)—Inventory of core samples from the building—Continued.

	Virgin stone (uncleaned) (V)	Cleaning technique							
		Misting (M)	Power wash (P)	Gommage (G)	Combination (C)	Armax (A)	JOS (J)	Laser (L)	Dry ice (D)
		Lightly soiled, rough (LSR)							
USGS samples taken for surface-loss, surface-roughness, pore-space, and salt-mapping tests.	LSRV-1, LSRV-2	---	LSRP-1, LSRP-2	LSRG-1, LSRG-2	---	---	LSRJ-1, LSRJ-2	LSRL-1, LSRL-2	LSRD-1, LSRD-2
Samples taken for accelerated-weathering tests.	LSRV-3, LSRV-4	---	LSRP-3, LSRP-4	LSRG-3,	---	---	LSRJ-3	LSRL-3	LSRD-3
Samples taken for deposition-velocity tests.	LSRV-5, LSRV-6	---	LSRP-5, LSRP-6	LSRG-5, LSRG-6	---	---	LSRJ-5, LSRJ-6	LSRL-5, LSRL-6	---
Client sample	LSRV-7	---	LSRP-7	LSRG-7	---	---	LSRJ-7	---	---
Additional samples	LSRV-1E, LSRV-2A, LSRV-2B, LSRV-2E, LSRV-3R, LSRV-E, LSRV-N, LSRV-W	---	LSRP-1A, LSRP-1B, LSRP-2A	---	---	---	---	---	---

Table 3 (Cont.)—Inventory of core samples from the building—Continued.

	Virgin stone (uncleaned) (V)	Cleaning technique							
		Misting (M)	Power wash (P)	Gommage (G)	Combination (C)	Armax (A)	JOS (J)	Laser (L)	Dry ice (D)
				Gypsum crusted, smooth (GCS)					
USGS samples taken for surface-loss, surface-roughness, pore-space, and salt-mapping tests.	GCSV-1, GCSV-2	GCSM-1, GCSM-2	---	GCSG-1, GCSG-2	GCSC-1, GCSC-2	GCSA-1, GCSA-2	GCSJ-1, GCSJ-2	---	GCSD-1, GCSD-2
Samples taken for accelerated-weathering tests.	GCSV-3	GCSM-3	---	GCSG-3, GCSG-4	GCSC-3	GCSA-3	GCSJ-3	---	GCSD-3, GCSD-4
Samples taken for deposition-velocity tests.	GCSV-5, GCSV-6	GCSM-5, GCSM-6	---	GCSG-5, GCSG-6	GCSC-5, GCSC-6	GCSA-5, GCSA-6	GCSJ-5, GCSJ-6	---	---
Client sample	GCSV-7	---	---	GCSG-7	GCSC-7	---	---	---	---
Additional samples	---	---	---	GCSG-X1, GCSG-X2, GCSG-X3	---	---	GCSJ-1P, GCSJ-2P, GCSJ-3P, GCSJ-4P, GCSJ-5P, GCSJ-6P	---	---

Table 3 (Cont.)—Inventory of core samples from the building.

	Virgin stone (uncleaned) (V)	Cleaning technique							
		Misting (M)	Power wash (P)	Gommage (G)	Combination (C)	Armax (A)	JOS (J)	Laser (L)	Dry ice (D)
		Gypsum crusted, rough (GCR)							
USGS samples taken for surface-loss, surface-roughness, pore-space, and salt-mapping tests.	GCRV-1, GCRV-2	GCRM-1, GCRM-2	---	GCRG-1, GCRG-2	GCRC-1, GCRC-2	GCRA-1, GCRA-2	GCRJ-1, GCRJ-2	GCRL-1, GCRL-2	GCSD-1
Samples taken for accelerated-weathering tests.	GCRV-3, GCRV-4	GCRM-3	---	GCRG-3,	GCRC-3	GCRA-3	GCRJ-3	GCRL-3, GCRL-4	---
Samples taken for deposition-velocity tests.	GCRV-5, GCRV-6	GCRM-5, GCRM-6	---	GCRG-5, GCRG-6	GCRC-5, GCRC-6	GCRA-5, GCRA-6	GCRJ-5	---	---
Client sample	GCRV-7	GCRM-7	---	GCRG-7	---	GCRA-7	---	---	---
Additional samples	GCRV-3R	---	---	---	---	---	---	---	---

Table 4.—Inventory of SEM images for computer analysis. [Surface-soiling conditions: GCR, gypsum crusted, rough; GCS, gypsum crusted, smooth; LSR, lightly soiled, rough; LSS, lightly soiled, smooth.]

Surface-soiling condition and core series	Virgin stone (uncleaned) (V)	Cleaning technique			
		Power wash (P)	Misting (M)	Gommage (G)	Combination (C)
Sample----------	LSSV	LSSP		LSSG	
	ABCDEFG	ABCDEFG	No	ABCDEFG	No
LSS-1	√√√–––––	–––––––	samples	√√√√√√√	samples
LSS-2	√√–––––	√√√√√√√		√√√√√√√	
Sample----------	LSRV	LSRP		LSRG-	
	ABCDEFG	ABCDEFG	No	ABCDEFG	No
LSR-1	√√√√–––	√√√√√√√	samples	–––––––	samples
LSR-2	√√√√–––	√√√√√√√		√√√√√√√	
Sample----------	GCSV		GCSM	GCSG	GCSC
	ABCDEFG	No	ABCDEFG	ABCDEFG	ABCDEFG
GCS-1	√√√–––––	samples	–––––––	–––––––	–––––––
GCS-2	–––––––		√√√√√√√	√√√√√√√	√√√√√√√
Sample----------	GCRV		GCRM	GCRG	GCRC
	ABCDEFG	No	ABCDEFG	ABCDEFG	ABCDEFG
GCR-1	–––––––	samples	–––––––	√√√√√√√	√√√√√√√
GCR-2	√√√–––––		√√√√√√√	–––––––	–––––––

Table 5.—Summary of visual grayness measurements. [Surface-soiling conditions: GCR, gypsum crusted, rough; GCS, gypsum crusted, smooth; LSR, lightly soiled, rough; LSS, lightly soiled, smooth.]

Surface-soiling condition and core series	Virgin stone (uncleaned) (V)	Cleaning technique			
		Power wash (P)	Misting (M)	Gommage (G)	Combination (C)
Sample----------	LSSV	LSSP		LSSG	
LSS-3	3.0	1.4	No	1.4	No
LSS-4	3.0	1.4	test	1.4	test
LSS-5	2.0	1.9		1.5	
LSS-6	2.0	1.9		--	
Sample----------	LSRV	LSRP		LSRG	
LSR-3	4.0	2.0	No	1.4	No
LSR-4	4.0	2.0	test	1.4	test
LSR-5	4.0	1.8		1.4	
LSR-6	4.0	1.8		--	
Sample----------	GCSV		GCSM	GCSG	GCSC
GCS-3	8.0	No	4.0	1.4	1.4
GCS-4	--	test	--	1.4	--
GCS-5	8.0		4.0	1.4	1.3
GCS-6	8.0		4.0	1.4	1.4
Sample----------	GCRV		GCRM	GCRG	GCRC
GCR-3	10.0	No	--	--	--
GCR-3R	8.0	test	3.2	2.5	1.5
GCR-4	10.0		--	--	--
GCR-5	9.0		4.0	3.0	1.5
GCR-6	9.0		5.0	4.0	1.5

Table 6.—Chemical analyses of rainwater in the Philadelphia area. [Averages of 31 rain events in the 1980's. Data from U.S. Environmental Protection Agency, provided by A. Lins, Conservation Department, Philadelphia Museum of Art.]

Soluble ion	Concentration (μequiv/L)
H^+	143
NH^{4+}	58
Ca^{2+}	73
Mg^{2+}	30
Na^+	31
K^+	11
Zn^{2+}	8
SO_4^{2-}	219
NO_3^-	98
Cl^-	24
pH	3.84

Table 7.—Semiquantitative analyses of silicate inclusions on soiled stone surfaces.

Semi-quantitative analysis: LSRP1

Element	Norm. K-ratio
Mg-K	0.28186+-0.00408
Al-K	0.12470+-0.00225
Si-K	0.37794+-0.00340
K-K	0.20584+-0.00247
Ti-K	0.00966+-0.00060

ZAF correction 20.00 kV 14.14 Degs
No. of iterations: 24

---	K	[Z]	[A]	[F]	[ZAF]	Atom. %	Wt. %	
Mg-K	0.282	0.979	1.481	0.989	1.434	24.49	20.79	*
Al-K	0.125	1.023	2.307	0.987	2.328	15.64	14.93	*
Si-K	0.378	0.990	2.446	0.999	2.418	47.43	46.97	*
K-K	0.206	1.037	1.512	1.000	1.567	12.02	16.59	*
Ti-K	0.010	1.113	1.289	1.000	1.434	0.42	0.71	

* - high absorbance

Table 8.—Estimated surface recession caused by the various cleaning techniques, as measured by two methods. [All values in micrometers. n.d., not determined; n.t., not tested. Asterisk (*), value used in figure 17. σ, standard deviation. Misting technique was not tested on LSS and LSR surfaces, and epoxy resin inadvertently was not applied to GCS and GCR surfaces.]

Surface-soiling condition	Cleaning technique							
	Power wash	Misting	Gommage	Combination	Armax	JOS	Laser	Dry ice
Surface-recession measurements based on change in surface level								
LSS	17*±65	n.t.	n.d. (s=100)	n.t.	122*±65	115*±99	n.t.	n.t.
LSR	131*±75	n.t.	52*±45	n.t.	n.t.	194*±90	n.t.	n.t.
GCS	n.t.	n.t.	n.t.	17*±65	100*±50	n.t.	n.t.	n.d. (s=200)
GCR	n.t.	n.t.	n.d. (s=100)	278*±90	75*±50	200*±99	150*±99	n.d. (s=250)
Surface-recession measurements based on surface smoothing								
LSS	183±33	n.t.	115*±30	n.t.	88±40	77±30	n.t.	n.t.
LSR	-46±33	n.t.	[1]193±90	n.t.	n.t.	105±45	190*±90	250*±90
GCS	n.t.	n.t.	n.t.	[1]136±200	70±35	n.t.	n.t.	65*±35
GCR	n.t.	n.t.	[1]111*±35	146±33	55±35	85±35	100±50	175*±100

[1]Revised value averaged from multiple images.

Table 9.—Results of fracture-density measurements based on SEM-image analysis of core samples obtained in this study—Continued.
[Rcssn, surface recession; sigma, standard deviation. Ecldn Length, Euclidian length of trace of exposed surface, measured along regression line through trace from end to end. D, in (D-1)*100, Richardson dimension (see app. 7). Crossings, number of crossings of trace of exposed surface over regression line through trace. Dev, standard deviation of trace of exposed surface. Pixel count, number of pixels in trace of exposed surface used in computing the shape factor. Grn size, estimated average grain size, using calipers provided by "Loss" option from menu of program EDGE. Note that the distance between calipers as reported on monitor is based on the assumption that the SEM image magnification is 10X; if other than 10X images are used for analysis, values reported by program should by multiplied by the factor 10/actual magnification. For most samples, two values are listed for grain size: the first is the average grain size in the first 50 mm of exposed surface, and the second is the average grain size in the region deeper than 150 mm below the surface. If only one value is listed, no observable difference was noted in the perceived grain size with depth into the sample. FD, fracture density. Two values are listed: the first is the fracture density near the surface, and the second is the fracture density deep into the sample. N/L, pixel count divided by Euclidean length (in pixels). Frgnness, fractal dimension of trace of exposed surface. Rel Hausdorf, for discussion of the Hausdorf measure, see Peitgen and others, 1992. Shape factor, measure of surface roughness derived for this study (see app. 7).]

Image analysis data of core: LSSVn

	A	B	C	D	Avg(BCD)	E	F	G	Avg(EFG)
Rcssn (μm) (D/S) (Dirct//Smooth)									
Rcssn (sigma)									
Ecldn Length (cm)	23.00	20.00	22.50	22.50	22.00				
Ecldn Length (pix)	523	455	512	512	501				
(D-1)*100	8.80	9.30	7.60	3.10	7.20				
Crossings	4	17	5	10	9				
Dev (sigma)	330	78	344	335	272				
Pixel count	856	680	821	682	760				
Grn size (100 μm)	155	140	250	400	236				
Grn size (300 μm)	155	140	250	400	236				
FD (%) at surface (100 μm)	18	16	4	2	10				
FD (%) subsurface (300 μm)	18	8	4	2	8				
N/L	1.64	1.49	1.60	1.33	1.52				
FRghness = $((N/L)^{D-1})*100$	71	55	66	34	57				
Rel Hausdorf	1.01	1.01	1.00	0.98	1.00				
Shape factor	3.03	2.77	2.95	2.39	2.78				
	LSSV1B	**LSSV1C**	**LSSV2A**	**LSSV2B**	**Avg**				**Avg**

Table 9 (Cont.)—Results of fracture-density measurements based on SEM-image analysis of core samples obtained in this study—Continued.
[Rcssn, surface recession; sigma, standard deviation. Ecldn Length, Euclidian length of trace of exposed surface, measured along regression line through trace from end to end. D, in (D-1)*100, Richardson dimension (see app. 7). Crossings, number of crossings of trace of exposed surface over regression line through trace. Dev, standard deviation of trace of exposed surface. Pixel count, number of pixels in trace of exposed surface used in computing the shape factor. Grn size, estimated average grain size, using calipers provided by "Loss" option from menu of program EDGE. Note that the distance between calipers as reported on monitor is based on the assumption that the SEM image magnification is 10X; if other than 10X images are used for analysis, values reported by program should by multiplied by the factor 10/actual magnification. For most samples, two values are listed for grain size: the first is the average grain size in the first 50 mm of exposed surface, and the second is the average grain size in the region deeper than 150 mm below the surface. If only one value is listed, no observable difference was noted in the perceived grain size with depth into the sample. FD, fracture density. Two values are listed: the first is the fracture density near the surface, and the second is the fracture density deep into the sample. N/L, pixel count divided by Euclidean length (in pixels). Frgnness, fractal dimension of trace of exposed surface. Rel Hausdorf, for discussion of the Hausdorf measure, see Peitgen and others, 1992. Shape factor, measure of surface roughness derived for this study (see app. 7).]

Image analysis data of core: LSSA2

	A	B	C	D	Avg(BCD)	E	F	G	Avg(EFG)
Rcssn (μm) (D/S) (Dirct//Smooth)	*122+-65//88+-40								
Rcssn (sigma)									
Ecldn Length (cm)		22.50	22.50	22.50		22.50	22.50	22.50	
Ecldn Length (pix)		0	0	0		0	0	0	
(D-1)*100		9.70	9.30	14.30	11.10	3.10	9.20	3.40	5.23
Crossings		6	5	6	6	7	11	4	7
Dev (sigma)		292	282	333	302	166	270	380	272
Pixel count		842	822	1024	896	608	840	665	704
Grn size (100 μm)		*	*	*	0	*	*	*	0
Grn size (300 μm)		*	*	*	0	*	*	*	0
FD (%) at surface (100 μm)		28	23	23	25	24	12	5	14
FD (%) subsurface (300 μm)		15	5	6	9	12	2	5	6
N/L		1.64	1.61	2.00	1.75	1.19	1.64	1.30	1.38
FRghness = $((N/L)^{D-1})*100$		73	68	121	87	19	72	31	41
Rel Hausdorf		0.99	0.99	1.02	1.00	0.99	0.99	0.98	0.99
Shape factor		3.06	2.98	3.82	3.28	2.13	3.04	2.33	2.50
	LSSA2A	**LSSA2B**	**LSSA2C**	**LSSA2D**	**LSSAo**	**LSSA2E**	**LSSA2F**	**LSSA2G**	**LSSA**

Table 9 (Cont.)—Results of fracture-density measurements based on SEM-image analysis of core samples obtained in this study—Continued.
[Rcssn, surface recession; sigma, standard deviation. Ecldn Length, Euclidian length of trace of exposed surface, measured along regression line through trace from end to end. D, in (D-1)*100, Richardson dimension (see app. 7). Crossings, number of crossings of trace of exposed surface over regression line through trace. Dev, standard deviation of trace of exposed surface. Pixel count, number of pixels in trace of exposed surface used in computing the shape factor. Grn size, estimated average grain size, using calipers provided by "Loss" option from menu of program EDGE. Note that the distance between calipers as reported on monitor is based on the assumption that the SEM image magnification is 10X; if other than 10X images are used for analysis, values reported by program should by multiplied by the factor 10/actual magnification. For most samples, two values are listed for grain size: the first is the average grain size in the first 50 mm of exposed surface, and the second is the average grain size in the region deeper than 150 mm below the surface. If only one value is listed, no observable difference was noted in the perceived grain size with depth into the sample. FD, fracture density. Two values are listed: the first is the fracture density near the surface, and the second is the fracture density deep into the sample. N/L, pixel count divided by Euclidean length (in pixels). Frgnness, fractal dimension of trace of exposed surface. Rel Hausdorf, for discussion of the Hausdorf measure, see Peitgen and others, 1992. Shape factor, measure of surface roughness derived for this study (see app. 7).]

Image analysis data of core: LSSD1

	A	B	C	D	Avg(BCD)	E	F	G	Avg(EFG)
Rcssn (μm) (D/S)									
(Dirct//Smooth)	No test								
Rcssn (sigma)									
Ecldn Length (cm)		22.50	22.50	22.50		22.50	22.50	22.50	
Ecldn Length (pix)		512	512	512		512	512	512	
(D-1)*100		4.70	5.00	14.80	8.17	7.30	6.00	7.30	6.87
Crossings		3	5	11	6	8	10	13	10
Dev (sigma)		454	456	359	423	262	249	252	254
Pixel count		699	716	1049	821	710	726	777	738
Grn size (100 μm)		*	*	*	0	*	*	*	0
Grn size (300 μm)		*	*	*	0	*	*	*	0
FD (%) at surface (100 μm)		*	18	8	49	8	14	7	10
FD (%) subsurface (300 μm)		*	5	8	12	3	7	7	6
N/L		1.37	1.40	2.05	1.60	1.39	1.42	1.52	1.44
FRghness = $((N/L)^{D-1})*100$		39	42	128	70	42	45	56	48
Rel Hausdorf		0.98	0.98	1.03	1.00	0.99	0.98	0.98	0.98
Shape factor		2.47	2.53	3.92	2.97	2.54	2.58	2.78	2.64
	LSSD1A	**LSSD1B**	**LSSD1C**	**LSSD1D**	**LSSDo**	**LSSD1E**	**LSSD1F**	**LSSD1G**	**LSSD**

Table 9 (Cont.)—Results of fracture-density measurements based on SEM-image analysis of core samples obtained in this study—Continued.
[Rcssn, surface recession; sigma, standard deviation. Ecldn Length, Euclidian length of trace of exposed surface, measured along regression line through trace from end to end. D, in (D-1)*100, Richardson dimension (see app. 7). Crossings, number of crossings of trace of exposed surface over regression line through trace. Dev, standard deviation of trace of exposed surface. Pixel count, number of pixels in trace of exposed surface used in computing the shape factor. Grn size, estimated average grain size, using calipers provided by "Loss" option from menu of program EDGE. Note that the distance between calipers as reported on monitor is based on the assumption that the SEM image magnification is 10X; if other than 10X images are used for analysis, values reported by program should by multiplied by the factor 10/actual magnification. For most samples, two values are listed for grain size: the first is the average grain size in the first 50 mm of exposed surface, and the second is the average grain size in the region deeper than 150 mm below the surface. If only one value is listed, no observable difference was noted in the perceived grain size with depth into the sample. FD, fracture density. Two values are listed: the first is the fracture density near the surface, and the second is the fracture density deep into the sample. N/L, pixel count divided by Euclidean length (in pixels). Frgnness, fractal dimension of trace of exposed surface. Rel Hausdorf, for discussion of the Hausdorf measure, see Peitgen and others, 1992. Shape factor, measure of surface roughness derived for this study (see app. 7).]

Image analysis data of core: LSSG2

	A	B	C	D	Avg(BCD)	E	F	G	Avg(EFG)
Rcssn (μm) (D/S)									
(Dirct//Smooth)	u.d.//*115+-30								
Rcssn (sigma)									
Ecldn Length (cm)		19.50	22.50	20.00	20.67	22.50	19.50	22.50	21.50
Ecldn Length (pix)		444	512	455	470	512	444	512	489
(D-1)*100		19.00	11.10	14.50	14.87	6.40	9.60	6.00	7.00
Crossings		18	8	15	14	9	7	8	8
Dev (sigma)		387	238	232	286	322	280	197	266
Pixel count		1192	888	939	1006	777	737	661	725
Grn size (100 μm)		50	50	50	50	300	300	30	210
Grn size (300 μm)		100	100	200	133	300	300	250	283
FD (%) at surface (100 μm)		17	14	14	15	6	6	15	9
FD (%) subsurface (300 μm)		10	7	7	8	5	5	4	5
N/L		2.69	1.73	2.06	2.16	1.52	1.66	1.29	1.49
FRghness = $((N/L)^{D-1})*100$		224	84	129	146	56	74	31	54
Rel Hausdorf		1.14	1.03	1.07	1.08	1.00	1.02	1.00	1.00
Shape factor		5.26	3.25	3.94	4.15	2.77	3.09	2.35	2.74
	LSSG2A	**LSSG2B**	**LSSG2C**	**LSSG2D**	**Avg**	**LSSG2E**	**LSSG2F**	**LSSG2G**	**Avg**

Table 9 (Cont.)—Results of fracture-density measurements based on SEM-image analysis of core samples obtained in this study—Continued.
[Rcssn, surface recession; sigma, standard deviation. Ecldn Length, Euclidian length of trace of exposed surface, measured along regression line through trace from end to end. D, in (D-1)*100, Richardson dimension (see app. 7). Crossings, number of crossings of trace of exposed surface over regression line through trace. Dev, standard deviation of trace of exposed surface. Pixel count, number of pixels in trace of exposed surface used in computing the shape factor. Grn size, estimated average grain size, using calipers provided by "Loss" option from menu of program EDGE. Note that the distance between calipers as reported on monitor is based on the assumption that the SEM image magnification is 10X; if other than 10X images are used for analysis, values reported by program should by multiplied by the factor 10/actual magnification. For most samples, two values are listed for grain size: the first is the average grain size in the first 50 mm of exposed surface, and the second is the average grain size in the region deeper than 150 mm below the surface. If only one value is listed, no observable difference was noted in the perceived grain size with depth into the sample. FD, fracture density. Two values are listed: the first is the fracture density near the surface, and the second is the fracture density deep into the sample. N/L, pixel count divided by Euclidean length (in pixels). Frgnness, fractal dimension of trace of exposed surface. Rel Hausdorf, for discussion of the Hausdorf measure, see Peitgen and others, 1992. Shape factor, measure of surface roughness derived for this study (see app. 7).]

Image analysis data of core: **LSSJ2**

	A	B	C	D	Avg(BCD)	E	F	G	Avg(EFG)
Rcssn (μm) (D/S)									
(Dirct//Smooth)	*115+-100//77+-30								
Rcssn (sigma)									
Ecldn Length (cm)		22.50	22.50	22.50		22.50	22.50	22.50	
Ecldn Length (pix)		512	512	512		512	512	512	
(D-1)*100		12.30	17.00	24.20	17.83	7.90	12.00	14.30	11.40
Crossings		18	14	10	14	15	8	11	11
Dev (sigma)		195	278	354	276	251	249	311	270
Pixel count		919	1021	1400	1113	789	250	843	627
Grn size (100 μm)		*	*	*	0	*	*	*	0
Grn size (300 μm)		*	*	*	0	*	*	*	0
FD (%) at surface (100 μm)		35	22	39	32	27	21	45	31
FD (%) subsurface (300 μm)		17	4	14	12	12	11	16	13
N/L		1.79	1.99	2.73	2.17	1.54	0.49	1.65	1.23
FRghness = $((N/L)^{D-1})*100$		93	124	249	155	59	-55	77	27
Rel Hausdorf		1.01	1.04	1.14	1.06	0.99	0.99	1.02	1.00
Shape factor		3.39	3.86	5.52	4.26	2.84	0.92	3.14	2.30
	LSSJ2A	**LSSJ2B**	**LSSJ2C**	**LSSJ2D**	**LSSJo**	**LSSJ2E**	**LSSJ2F**	**LSSJ2G**	**LSSJ**

Table 9 (Cont.)—Results of fracture-density measurements based on SEM-image analysis of core samples obtained in this study—Continued.
[Rcssn, surface recession; sigma, standard deviation. Ecldn Length, Euclidian length of trace of exposed surface, measured along regression line through trace from end to end. D, in (D-1)*100, Richardson dimension (see app. 7). Crossings, number of crossings of trace of exposed surface over regression line through trace. Dev, standard deviation of trace of exposed surface. Pixel count, number of pixels in trace of exposed surface used in computing the shape factor. Grn size, estimated average grain size, using calipers provided by "Loss" option from menu of program EDGE. Note that the distance between calipers as reported on monitor is based on the assumption that the SEM image magnification is 10X; if other than 10X images are used for analysis, values reported by program should by multiplied by the factor 10/actual magnification. For most samples, two values are listed for grain size: the first is the average grain size in the first 50 mm of exposed surface, and the second is the average grain size in the region deeper than 150 mm below the surface. If only one value is listed, no observable difference was noted in the perceived grain size with depth into the sample. FD, fracture density. Two values are listed: the first is the fracture density near the surface, and the second is the fracture density deep into the sample. N/L, pixel count divided by Euclidean length (in pixels). Frgnness, fractal dimension of trace of exposed surface. Rel Hausdorf, for discussion of the Hausdorf measure, see Peitgen and others, 1992. Shape factor, measure of surface roughness derived for this study (see app. 7).]

Image analysis data of core: **LSSP2**

	A	B	C	D	Avg(BCD)	E	F	G	Avg(EFG)
Rcssn (µm) (D/S) (Dirct//Smooth)	*17+-65//183+-33								
Rcssn (sigma)									
Ecldn Length (cm)		22.50	23.00	22.50	22.67	22.00	22.00	22.50	22.17
Ecldn Length (pix)		512	523	512	516	501	501	512	504
(D-1)*100		8.40	15.50	6.50	10.13	10.70	8.60	7.00	9.00
Crossings		13	16	2	10	14	12	6	11
Dev (sigma)		369	327	532	409	283	381	15	226
Pixel count		813	1014	849	892	873	679	800	784
Grn size (100 µm)		190	220	191	200	75	250	150	158
Grn size (300 µm)		250	220	191	220	200	250	150	200
FD (%) at surface (100 µm)		26	10	10	15	35	17	14	22
FD (%) subsurface (300 µm)		5	2	6	4.33	7	9	3	6
N/L		1.59	1.94	1.66	1.73	1.74	1.36	1.56	1.55
FRghness = $((N/L)^{D-1})*100$		65	115	71	84	85	39	61	62
Rel Hausdorf		1.01	1.07	1.00	1.02	1.02	1.01	1.00	1.00
Shape factor		2.93	3.72	3.03	3.23	3.26	2.51	2.86	2.88
		LSSP2A	**LSSP2B**	**LSSP2C**	**Avg**	**LSSP2E**	**LSSP2F**	**LSSP2G**	**Avg**

Table 9 (Cont.)—Results of fracture-density measurements based on SEM-image analysis of core samples obtained in this study—Continued.
[Rcssn, surface recession; sigma, standard deviation. Ecldn Length, Euclidian length of trace of exposed surface, measured along regression line through trace from end to end. D, in (D-1)*100, Richardson dimension (see app. 7). Crossings, number of crossings of trace of exposed surface over regression line through trace. Dev, standard deviation of trace of exposed surface. Pixel count, number of pixels in trace of exposed surface used in computing the shape factor. Grn size, estimated average grain size, using calipers provided by "Loss" option from menu of program EDGE. Note that the distance between calipers as reported on monitor is based on the assumption that the SEM image magnification is 10X; if other than 10X images are used for analysis, values reported by program should by multiplied by the factor 10/actual magnification. For most samples, two values are listed for grain size: the first is the average grain size in the first 50 mm of exposed surface, and the second is the average grain size in the region deeper than 150 mm below the surface. If only one value is listed, no observable difference was noted in the perceived grain size with depth into the sample. FD, fracture density. Two values are listed: the first is the fracture density near the surface, and the second is the fracture density deep into the sample. N/L, pixel count divided by Euclidean length (in pixels). Frgnness, fractal dimension of trace of exposed surface. Rel Hausdorf, for discussion of the Hausdorf measure, see Peitgen and others, 1992. Shape factor, measure of surface roughness derived for this study (see app. 7).]

Image analysis data of core: LSRV1

	A	B	C	D	Avg(BCD)	E	F	G	Avg(EFG)
Rcssn (μm) (D/S) (Dirct//Smooth)									
Rcssn (sigma)									
Ecldn Length (cm)		22.50	22.50						
Ecldn Length (pix)		512	512			0	0	0	
(D-1)*100		2.30	9.50						
Crossings		5	3						
Dev (sigma)		380	729						
Pixel count		673	951						
Grn size (100 μm)		172	165						
Grn size (300 μm)		172	165						
FD (%) at surface (100 μm)		12	12						
FD (%) subsurface (300 μm)		12	5						
N/L		1.31	1.86						
FRghness = $((N/L)^{D-1})*100$		32	97						
Rel Hausdorf		0.98	1.02						
Shape factor		2.34	3.45						
					Avg				**Avg**

Table 9 (Cont.)—Results of fracture-density measurements based on SEM-image analysis of core samples obtained in this study—Continued.
[Rcssn, surface recession; sigma, standard deviation. Ecldn Length, Euclidian length of trace of exposed surface, measured along regression line through trace from end to end. D, in (D-1)*100, Richardson dimension (see app. 7). Crossings, number of crossings of trace of exposed surface over regression line through trace. Dev, standard deviation of trace of exposed surface. Pixel count, number of pixels in trace of exposed surface used in computing the shape factor. Grn size, estimated average grain size, using calipers provided by "Loss" option from menu of program EDGE. Note that the distance between calipers as reported on monitor is based on the assumption that the SEM image magnification is 10X; if other than 10X images are used for analysis, values reported by program should by multiplied by the factor 10/actual magnification. For most samples, two values are listed for grain size: the first is the average grain size in the first 50 mm of exposed surface, and the second is the average grain size in the region deeper than 150 mm below the surface. If only one value is listed, no observable difference was noted in the perceived grain size with depth into the sample. FD, fracture density. Two values are listed: the first is the fracture density near the surface, and the second is the fracture density deep into the sample. N/L, pixel count divided by Euclidean length (in pixels). Frgnness, fractal dimension of trace of exposed surface. Rel Hausdorf, for discussion of the Hausdorf measure, see Peitgen and others, 1992. Shape factor, measure of surface roughness derived for this study (see app. 7).]

Image analysis data of core: LSRV2

	A	B	C	D	Avg(BCD)	E	F	G	Avg(EFG)
Rcssn (μm) (D/S) (Dirct//Smooth)									
Rcssn (sigma)									
Ecldn Length (cm)		22.50	22.50	22.50					
Ecldn Length (pix)		512	512	512	512				
(D-1)*100		13.00	12.70	6.80					
Crossings		8	8	3					
Dev (sigma)		482	363	343					
Pixel count		1318	972	754					
Grn size (100 μm)		94	350	266					
Grn size (300 μm)		229	350	266					
FD (%) at surface (100 μm)		20	20	20					
FD (%) subsurface (300 μm)		6	6	9					
N/L		2.57	1.90	1.47	2.00				
FRghness = $((N/L)^{D-1})*100$		191	106	51	116				
Rel Hausdorf		1.07	1.04	1.00	1.00				
Shape factor		4.88	3.59	2.69	3.72				
					Avg				**Avg**

Table 9 (Cont.)—Results of fracture-density measurements based on SEM-image analysis of core samples obtained in this study—Continued.
[Rcssn, surface recession; sigma, standard deviation. Ecldn Length, Euclidian length of trace of exposed surface, measured along regression line through trace from end to end. D, in (D-1)*100, Richardson dimension (see app. 7). Crossings, number of crossings of trace of exposed surface over regression line through trace. Dev, standard deviation of trace of exposed surface. Pixel count, number of pixels in trace of exposed surface used in computing the shape factor. Grn size, estimated average grain size, using calipers provided by "Loss" option from menu of program EDGE. Note that the distance between calipers as reported on monitor is based on the assumption that the SEM image magnification is 10X; if other than 10X images are used for analysis, values reported by program should by multiplied by the factor 10/actual magnification. For most samples, two values are listed for grain size: the first is the average grain size in the first 50 mm of exposed surface, and the second is the average grain size in the region deeper than 150 mm below the surface. If only one value is listed, no observable difference was noted in the perceived grain size with depth into the sample. FD, fracture density. Two values are listed: the first is the fracture density near the surface, and the second is the fracture density deep into the sample. N/L, pixel count divided by Euclidean length (in pixels). Frgnness, fractal dimension of trace of exposed surface. Rel Hausdorf, for discussion of the Hausdorf measure, see Peitgen and others, 1992. Shape factor, measure of surface roughness derived for this study (see app. 7).]

Image analysis data of core:	LSRAn									
	A	B	C	D	Avg(BCD)	E	F	G	Avg(EFG)	Difference P-Po
Rcssn (μm) (D/S) (Dirct//Smooth)	No test									
Rcssn (sigma)										
Ecldn Length (cm)		22.50	22.50	22.50		22.50	22.50	22.50		
Ecldn Length (pix)		512	512	512		512	512	512		
(D-1)*100		*	*	*	0.00	*	*	*	0.00	0.00
Crossings		*	*	*	0	*	*	*	0	
Dev (sigma)		*	*	*	0	*	*	*	0	0.00
Pixel count		*	*	*	0	*	*	*	0	0.00
Grn size (100 μm)		*	*	*	0	*	*	*	0	0.00
Grn size (300 μm)		*	*	*	0	*	*	*	0	0.00
FD (%) at surface (100 μm)		*	*	*	0	*	*	*	0	0.00
FD (%) subsurface (300 μm)		*	*	*	0	*	*	*	0	0.00
N/L										
FRghness = $((N/L)^{D-1})*100$										
Rel Hausdorf										
Shape factor										
	LSRAn	LSRAn	LSRAn	LSRAn	LSRAn	LSRAn	LSRAn	LSRAn	LSRAn	

Table 9 (Cont.)—Results of fracture-density measurements based on SEM-image analysis of core samples obtained in this study—Continued.
[Rcssn, surface recession; sigma, standard deviation. Ecldn Length, Euclidian length of trace of exposed surface, measured along regression line through trace from end to end. D, in (D-1)*100, Richardson dimension (see app. 7). Crossings, number of crossings of trace of exposed surface over regression line through trace. Dev, standard deviation of trace of exposed surface. Pixel count, number of pixels in trace of exposed surface used in computing the shape factor. Grn size, estimated average grain size, using calipers provided by "Loss" option from menu of program EDGE. Note that the distance between calipers as reported on monitor is based on the assumption that the SEM image magnification is 10X; if other than 10X images are used for analysis, values reported by program should by multiplied by the factor 10/actual magnification. For most samples, two values are listed for grain size: the first is the average grain size in the first 50 mm of exposed surface, and the second is the average grain size in the region deeper than 150 mm below the surface. If only one value is listed, no observable difference was noted in the perceived grain size with depth into the sample. FD, fracture density. Two values are listed: the first is the fracture density near the surface, and the second is the fracture density deep into the sample. N/L, pixel count divided by Euclidean length (in pixels). Frgnness, fractal dimension of trace of exposed surface. Rel Hausdorf, for discussion of the Hausdorf measure, see Peitgen and others, 1992. Shape factor, measure of surface roughness derived for this study (see app. 7).]

Image analysis data of core: **LSRD2**

	A	B	C	D	Avg(BCD)	E	F	G	Avg(EFG)
Rcssn (µm) (D/S)									
(Dirct//Smooth)	u.d.+-100//*250+-90								
Rcssn (sigma)									
Ecldn Length (cm)		13.50	13.50	13.50		13.50	13.50	13.50	
Ecldn Length (pix)		307	307	307		307	307	307	
(D-1)*100		22.90	17.80	7.60		9.50	10.30	10.10	9.97
Crossings		16	8	2	9	8	8	2	6
Dev (sigma)		408	309	540	419	314	314	798	475
Pixel count		1312	951	790	1018	841	800	1024	888
Grn size (100 µm)		*	*	*	0	*	*	*	0
Grn size (300 µm)		*	*	*	0	*	*	*	0
FD (%) at surface (100 µm)		25	23	28	25	12	3	29	15
FD (%) subsurface (300 µm)		25	7	3	12	1	1	1	1
N/L		4.27	3.10	2.57	3.31	2.74	2.60	3.33	2.89
FRghness = $((N/L)^{D-1})*100$		496	279	176	317	201	187	276	222
Rel Hausdorf		1.19	1.08	0.97	1.08	0.98	0.99	0.99	0.99
Shape factor		8.56	6.03	4.72	6.44	5.08	4.86	6.21	5.38
	LSRD2A	**LSRD2B**	**LSRD2C**	**LSRD2D**	**LSRDo**	**LSRD2E**	**LSRD2F**	**LSRD2G**	**LSRD**

Table 9 (Cont.)—Results of fracture-density measurements based on SEM-image analysis of core samples obtained in this study—Continued.
[Rcssn, surface recession; sigma, standard deviation. Ecldn Length, Euclidian length of trace of exposed surface, measured along regression line through trace from end to end. D, in (D-1)*100, Richardson dimension (see app. 7). Crossings, number of crossings of trace of exposed surface over regression line through trace. Dev, standard deviation of trace of exposed surface. Pixel count, number of pixels in trace of exposed surface used in computing the shape factor. Grn size, estimated average grain size, using calipers provided by "Loss" option from menu of program EDGE. Note that the distance between calipers as reported on monitor is based on the assumption that the SEM image magnification is 10X; if other than 10X images are used for analysis, values reported by program should by multiplied by the factor 10/actual magnification. For most samples, two values are listed for grain size: the first is the average grain size in the first 50 mm of exposed surface, and the second is the average grain size in the region deeper than 150 mm below the surface. If only one value is listed, no observable difference was noted in the perceived grain size with depth into the sample. FD, fracture density. Two values are listed: the first is the fracture density near the surface, and the second is the fracture density deep into the sample. N/L, pixel count divided by Euclidean length (in pixels). Frgnness, fractal dimension of trace of exposed surface. Rel Hausdorf, for discussion of the Hausdorf measure, see Peitgen and others, 1992. Shape factor, measure of surface roughness derived for this study (see app. 7).]

Image analysis data of core: LSRG2

	A	B	C	D	Avg(BCD)	E	F	G	Avg(EFG)
Rcssn (µm) (D/S) (Dirct//Smooth)	*52+-45//193+-150								
Rcssn (sigma)									
Ecldn Length (cm)		21.00	21.00	21.00	21.00	21.00	22.00	22.00	21.67
Ecldn Length (pix)		478	478	478	478	478	501	501	493
(D-1)*100		18.40	19.10	14.00	17.17	5.20	7.80	1.00	5
Crossings		22	6	10	13	4	8	3	5
Dev (sigma)		640	537	264	480	335	230	298	288
Pixel count		1700	971	919	1197	641	709	594	648
Grn size (100 µm)		198	191	167	185	40	50	212	101
Grn size (300 µm)		198	191	167	185	170	200	212	194
FD (%) at surface (100 µm)		28	21	28	26	33	22	11	22
FD (%) subsurface (300 µm)		11	9	6	9	9	5	11	8
N/L		3.56	2.03	1.92	2.50	1.34	1.42	1.19	1.31
FRghness = $((N/L)^{D-1})*100$		349	133	111	198	36	46	19	34
Rel Hausdorf		1.17	1.11	1.06	1.11	0.99	1.00	0.98	0.99
Shape factor		6.95	3.98	3.66	4.86	2.43	2.60	2.10	2.38
	LSRG2A	**LSRG2B**	**LSRG2C**	**LSRG2D**	**Avg**	**LSRG2E**	**LSRG2F**	**LSRG2G**	**Avg**

Table 9 (Cont.)—Results of fracture-density measurements based on SEM-image analysis of core samples obtained in this study—Continued.
[Rcssn, surface recession; sigma, standard deviation. Ecldn Length, Euclidian length of trace of exposed surface, measured along regression line through trace from end to end. D, in (D-1)*100, Richardson dimension (see app. 7). Crossings, number of crossings of trace of exposed surface over regression line through trace. Dev, standard deviation of trace of exposed surface. Pixel count, number of pixels in trace of exposed surface used in computing the shape factor. Grn size, estimated average grain size, using calipers provided by "Loss" option from menu of program EDGE. Note that the distance between calipers as reported on monitor is based on the assumption that the SEM image magnification is 10X; if other than 10X images are used for analysis, values reported by program should by multiplied by the factor 10/actual magnification. For most samples, two values are listed for grain size: the first is the average grain size in the first 50 mm of exposed surface, and the second is the average grain size in the region deeper than 150 mm below the surface. If only one value is listed, no observable difference was noted in the perceived grain size with depth into the sample. FD, fracture density. Two values are listed: the first is the fracture density near the surface, and the second is the fracture density deep into the sample. N/L, pixel count divided by Euclidean length (in pixels). Frgnness, fractal dimension of trace of exposed surface. Rel Hausdorf, for discussion of the Hausdorf measure, see Peitgen and others, 1992. Shape factor, measure of surface roughness derived for this study (see app. 7).]

Image analysis data of core: **LSRJ1**

	A	B	C	D	Avg(BCD)	E	F	G	Avg(EFG)
Rcssn (μm) (D/S)									
(Dirct//Smooth)	*194+-90//105+-45								
Rcssn (sigma)									
Ecldn Length (cm)		22.50	22.50	22.50		22.50	22.50	22.50	
Ecldn Length (pix)		512	512	512		512	512	512	
(D-1)*100		15.80	10.30	14.60	13.57	9.80	7.70	10.00	9.17
Crossings		8	6	7	7	8	10	3	7
Dev (sigma)		701	401	672	591	284	244	769	432
Pixel count		1186	871	1242	1100	786	786	943	838
Grn size (100 μm)		*	*	*	0	*	*	*	0
Grn size (300 μm)		*	*	*	0	*	*	*	0
FD (%) at surface (100 μm)		38	32	34	35	23	30	22	25
FD (%) subsurface (300 μm)		18	14	11	14	11	14	15	13
N/L		2.32	1.70	2.43	2.15	1.54	1.54	1.84	1.64
FRghness = $((N/L)^{D-1})*100$		165	80	176	140	60	59	96	72
Rel Hausdorf		1.04	1.00	1.03	1.02	0.99	0.99	0.99	0.99
Shape factor		4.46	3.17	4.64	4.09	2.86	2.82	3.43	3.04
	LSRJ1A	**LSRJ1B**	**LSRJ1C**	**LSRJ1D**	**LSRJo**	**LSRJ1E**	**LSRJ1F**	**LSRJ1G**	**LSRJ**

Table 9 (Cont.)—Results of fracture-density measurements based on SEM-image analysis of core samples obtained in this study—Continued.
[Rcssn, surface recession; sigma, standard deviation. Ecldn Length, Euclidian length of trace of exposed surface, measured along regression line through trace from end to end. D, in (D-1)*100, Richardson dimension (see app. 7). Crossings, number of crossings of trace of exposed surface over regression line through trace. Dev, standard deviation of trace of exposed surface. Pixel count, number of pixels in trace of exposed surface used in computing the shape factor. Grn size, estimated average grain size, using calipers provided by "Loss" option from menu of program EDGE. Note that the distance between calipers as reported on monitor is based on the assumption that the SEM image magnification is 10X; if other than 10X images are used for analysis, values reported by program should by multiplied by the factor 10/actual magnification. For most samples, two values are listed for grain size: the first is the average grain size in the first 50 mm of exposed surface, and the second is the average grain size in the region deeper than 150 mm below the surface. If only one value is listed, no observable difference was noted in the perceived grain size with depth into the sample. FD, fracture density. Two values are listed: the first is the fracture density near the surface, and the second is the fracture density deep into the sample. N/L, pixel count divided by Euclidean length (in pixels). Frgnness, fractal dimension of trace of exposed surface. Rel Hausdorf, for discussion of the Hausdorf measure, see Peitgen and others, 1992. Shape factor, measure of surface roughness derived for this study (see app. 7).]

Image analysis data of core: **LSRL1**

	A	B	C	D	Avg(BCD)	E	F	G	Avg(EFG)
Rcssn (μm) (D/S)									
(Dirct//Smooth)	u.d.+-100//*190+-90								
Rcssn (sigma)									
Ecldn Length (cm)		22.50	22.50	22.50		22.50	22.50	22.50	
Ecldn Length (pix)		512	512	512		512	512	512	
(D-1)*100		20.70	20.00	14.40	18.37	11.60	16.50	8.70	12.27
Crossings		8	21	11	13	10	7	8	8
Dev (sigma)		506	245	253	335	280	422	369	357
Pixel count		1602	1049	833	1161	909	1103	824	945
Grn size (100 μm)		*	*	*	0	*	*	*	0
Grn size (300 μm)		*	*	*	0	*	*	*	0
FD (%) at surface (100 μm)		15	31	44	30	23	21	21	22
FD (%) subsurface (300 μm)		10	24	20	18	14	14	12	13
N/L		3.13	2.05	1.63	2.27	1.78	2.15	1.61	1.85
FRghness = $((N/L)^{D-1})*100$		296	136	75	169	90	145	68	101
Rel Hausdorf		1.12	1.07	1.02	1.07	1.00	1.04	0.99	1.01
Shape factor		6.19	4.04	3.11	4.44	3.34	4.16	2.98	3.49
	LSRL1A	**LSRL1B**	**LSRL1C**	**LSRL1D**	**LSRLo**	**LSRL1E**	**LSRL1F**	**LSRL1G**	**LSRL**

Table 9 (Cont.)—Results of fracture-density measurements based on SEM-image analysis of core samples obtained in this study—Continued.
[Rcssn, surface recession; sigma, standard deviation. Ecldn Length, Euclidian length of trace of exposed surface, measured along regression line through trace from end to end. D, in (D-1)*100, Richardson dimension (see app. 7). Crossings, number of crossings of trace of exposed surface over regression line through trace. Dev, standard deviation of trace of exposed surface. Pixel count, number of pixels in trace of exposed surface used in computing the shape factor. Grn size, estimated average grain size, using calipers provided by "Loss" option from menu of program EDGE. Note that the distance between calipers as reported on monitor is based on the assumption that the SEM image magnification is 10X; if other than 10X images are used for analysis, values reported by program should by multiplied by the factor 10/actual magnification. For most samples, two values are listed for grain size: the first is the average grain size in the first 50 mm of exposed surface, and the second is the average grain size in the region deeper than 150 mm below the surface. If only one value is listed, no observable difference was noted in the perceived grain size with depth into the sample. FD, fracture density. Two values are listed: the first is the fracture density near the surface, and the second is the fracture density deep into the sample. N/L, pixel count divided by Euclidean length (in pixels). Frgnness, fractal dimension of trace of exposed surface. Rel Hausdorf, for discussion of the Hausdorf measure, see Peitgen and others, 1992. Shape factor, measure of surface roughness derived for this study (see app. 7).]

Image analysis data of core: **LSRP1**

	A	B	C	D	Avg(BCD)	E	F	G	Avg(EFG)
Rcssn (μm) (D/S) (Dirct//Smooth)	*122+-75//65+-25								
Rcssn (sigma)									
Ecldn Length (cm)		22.50	22.50	22.50	22.50	22.50	22.50	22.50	22.50
Ecldn Length (pix)		512	512	512	512	512	512	512	512
(D-1)*100		1.2	0.4	6.6	2.7	8.5	9.8	10.7	9.7
Crossings		12	4	6	7	3	11	27	14
Dev (sigma)		298	370	538	402	775	308	161	415
Pixel count		605	594	811	670	971	871	798	880
Grn size (100 μm)		150	150	87	129	215	40	62	106
Grn size (300 μm)		150	150	120	140	215	130	170	172
FD (%) at surface (100 μm)		40	9	26	25	9	21	11	14
FD (%) subsurface (300 μm)		2	5	15	7	13	5	1	6
N/L		1.18	1.16	1.58	1.00	1.90	1.70	1.56	1.72
FRghness = $((N/L)^{D-1})*100$		18	16	63	33	100	79	63	81
Rel Hausdorf		0.98	0.98	1.00	0.99	1.01	1.02	1.02	1.02
Shape factor		2.09	2.05	2.89	2.34	3.50	3.16	2.19	3.19
		LSRP1A	**LSRP1B**	**LSRP1C**	**Avg**	**LSRP1E**	**LSRP1F**	**LSRP1G**	**Avg**

Table 9 (Cont.)—Results of fracture-density measurements based on SEM-image analysis of core samples obtained in this study—Continued.
[Rcssn, surface recession; sigma, standard deviation. Ecldn Length, Euclidian length of trace of exposed surface, measured along regression line through trace from end to end. D, in (D-1)*100, Richardson dimension (see app. 7). Crossings, number of crossings of trace of exposed surface over regression line through trace. Dev, standard deviation of trace of exposed surface. Pixel count, number of pixels in trace of exposed surface used in computing the shape factor. Grn size, estimated average grain size, using calipers provided by "Loss" option from menu of program EDGE. Note that the distance between calipers as reported on monitor is based on the assumption that the SEM image magnification is 10X; if other than 10X images are used for analysis, values reported by program should by multiplied by the factor 10/actual magnification. For most samples, two values are listed for grain size: the first is the average grain size in the first 50 mm of exposed surface, and the second is the average grain size in the region deeper than 150 mm below the surface. If only one value is listed, no observable difference was noted in the perceived grain size with depth into the sample. FD, fracture density. Two values are listed: the first is the fracture density near the surface, and the second is the fracture density deep into the sample. N/L, pixel count divided by Euclidean length (in pixels). Frgnness, fractal dimension of trace of exposed surface. Rel Hausdorf, for discussion of the Hausdorf measure, see Peitgen and others, 1992. Shape factor, measure of surface roughness derived for this study (see app. 7).]

Image analysis data of core: **LSRP2**

	A	B	C	D	Avg(BCD)	E	F	G	Avg(EFG)
Rcssn (μm) (D/S) (Dirct//Smooth)	*139+-75//27+-25								
Rcssn (sigma)									
Ecldn Length (cm)	22.00	22.00	22.00		22.00	22.00	22.50	22.50	22.33
Ecldn Length (pix)	501	501	501		501	501	512	512	508
(D-1)*100	6.70	4.00	7.40		6.03	7.20	10.00	13.10	10.10
Crossings	6	8	5		6	3	6	15	8
Dev (sigma)	512	376	451		446	718	436	419	524
Pixel count	770	672	819		754	839	907	1025	924
Grn size (100 μm)	100	121	118		113	100	160	90	117
Grn size (300 μm)	100	121	118		113	100	160	180	147
FD (%) at surface (100 μm)	7	14	26		16	18	19	21	19
FD (%) subsurface (300 μm)	3	14	4		7	10	19	9	13
N/L	1.54	1.34	1.64		1.51	1.68	1.77	2.00	1.82
FRghness = $((N/L)^{D-1})*100$	58	36	70		55	74	88	119	94
Rel Hausdorf	1.00	0.99	1.00		0.99	1.00	1.02	1.05	1.02
Shape factor	2.81	2.42	3.00		2.74	3.07	3.30	3.79	3.39
	LSRP2A	**LSRP2B**	**LSRP2C**		**Avg**	**LSRP2E**	**LSRP2F**	**LSRP2G**	**Avg**

Table 9 (Cont.)—Results of fracture-density measurements based on SEM-image analysis of core samples obtained in this study—Continued.
[Rcssn, surface recession; sigma, standard deviation. Ecldn Length, Euclidian length of trace of exposed surface, measured along regression line through trace from end to end. D, in (D-1)*100, Richardson dimension (see app. 7). Crossings, number of crossings of trace of exposed surface over regression line through trace. Dev, standard deviation of trace of exposed surface. Pixel count, number of pixels in trace of exposed surface used in computing the shape factor. Grn size, estimated average grain size, using calipers provided by "Loss" option from menu of program EDGE. Note that the distance between calipers as reported on monitor is based on the assumption that the SEM image magnification is 10X; if other than 10X images are used for analysis, values reported by program should by multiplied by the factor 10/actual magnification. For most samples, two values are listed for grain size: the first is the average grain size in the first 50 mm of exposed surface, and the second is the average grain size in the region deeper than 150 mm below the surface. If only one value is listed, no observable difference was noted in the perceived grain size with depth into the sample. FD, fracture density. Two values are listed: the first is the fracture density near the surface, and the second is the fracture density deep into the sample. N/L, pixel count divided by Euclidean length (in pixels). Frgnness, fractal dimension of trace of exposed surface. Rel Hausdorf, for discussion of the Hausdorf measure, see Peitgen and others, 1992. Shape factor, measure of surface roughness derived for this study (see app. 7).]

Image analysis data of core: GCSV1

	A	B	C	D	Avg(BCD)	E	F	G	Avg(EFG)
Rcssn (μm) (D/S) (Dirct//Smooth)									
Rcssn (sigma)									
Ecldn Length (cm)		19.00	17.00	19.00	18.33				
Ecldn Length (pix)		432	387	432	417				
(D-1)*100		11.50	18.10	4.00	11.20				
Crossings		6	15	10	10				
Dev (sigma)		415	226	128	256				
Pixel count		767	914	552	744				
Grn size (100 μm)		73	14	148	78				
Grn size (300 μm)		73	14	148	78				
FD (%) at surface (100 μm)		41	33	27	34				
FD (%) subsurface (300 μm)		12	30	9	17				
N/L		1.77	2.36	1.28	1.80				
FRghness = $((N/L)^{D-1})*100$		89	176	29	98				
Rel Hausdorf		1.03	1.12	0.99	1.05				
Shape factor		3.33	4.61	2.30	3.41				
	GCSV1A	**GCSV1B**	**GCSV1C**	**GCSV1D**	**Avg**				**Avg**

Table 9 (Cont.)—Results of fracture-density measurements based on SEM-image analysis of core samples obtained in this study—Continued.
[Rcssn, surface recession; sigma, standard deviation. Ecldn Length, Euclidian length of trace of exposed surface, measured along regression line through trace from end to end. D, in (D-1)*100, Richardson dimension (see app. 7). Crossings, number of crossings of trace of exposed surface over regression line through trace. Dev, standard deviation of trace of exposed surface. Pixel count, number of pixels in trace of exposed surface used in computing the shape factor. Grn size, estimated average grain size, using calipers provided by "Loss" option from menu of program EDGE. Note that the distance between calipers as reported on monitor is based on the assumption that the SEM image magnification is 10X; if other than 10X images are used for analysis, values reported by program should by multiplied by the factor 10/actual magnification. For most samples, two values are listed for grain size: the first is the average grain size in the first 50 mm of exposed surface, and the second is the average grain size in the region deeper than 150 mm below the surface. If only one value is listed, no observable difference was noted in the perceived grain size with depth into the sample. FD, fracture density. Two values are listed: the first is the fracture density near the surface, and the second is the fracture density deep into the sample. N/L, pixel count divided by Euclidean length (in pixels). Frgnness, fractal dimension of trace of exposed surface. Rel Hausdorf, for discussion of the Hausdorf measure, see Peitgen and others, 1992. Shape factor, measure of surface roughness derived for this study (see app. 7).]

Image analysis data of core: **GCSA1**

	A	B	C	D	Avg(BCD)	E	F	G	Avg(EFG)
Rcssn (μm) (D/S)									
(Dirct//Smooth)	*100+-50//70+-35								
Rcssn (sigma)									
Ecldn Length (cm)		22.50	16.20	22.50		22.50	19.80	22.50	
Ecldn Length (pix)		512	369	512		512	451	512	
(D-1)*100		11.70	9.60	13.10	11.47	6.10	15.50	5.90	9.17
Crossings		13	5	11	10	12	19	12	14
Dev (sigma)		228	572	310	370	227	193	164	195
Pixel count		853	696	1002	850	655	897	721	758
Grn size (100 μm)		*	*	*	0	*	*	*	0
Grn size (300 μm)		*	*	*	0	*	*	*	0
FD (%) at surface (100 μm)		35	8	19	21	14	14	12	13
FD (%) subsurface (300 μm)		8	8	3	6	0	2	4	2
N/L		1.67	1.89	1.96	1.84	1.28	1.99	1.41	1.56
FRghness = $((N/L)^{D-1})*100$		77	101	114	97	30	122	44	65
Rel Hausdorf		1.00	0.99	1.01	1.00	0.99	1.03	0.98	1.00
Shape factor		3.13	3.51	3.71	3.45	2.33	3.82	2.56	2.91
	GCSA1A	**GCSA1B**	**GCSA1C**	**GCSA1D**	**GCSAo**	**GCSA1E**	**GCSA1F**	**GCSA1G**	**GCSA**

Table 9 (Cont.)—Results of fracture-density measurements based on SEM-image analysis of core samples obtained in this study—Continued.
[Rcssn, surface recession; sigma, standard deviation. Ecldn Length, Euclidian length of trace of exposed surface, measured along regression line through trace from end to end. D, in (D-1)*100, Richardson dimension (see app. 7). Crossings, number of crossings of trace of exposed surface over regression line through trace. Dev, standard deviation of trace of exposed surface. Pixel count, number of pixels in trace of exposed surface used in computing the shape factor. Grn size, estimated average grain size, using calipers provided by "Loss" option from menu of program EDGE. Note that the distance between calipers as reported on monitor is based on the assumption that the SEM image magnification is 10X; if other than 10X images are used for analysis, values reported by program should by multiplied by the factor 10/actual magnification. For most samples, two values are listed for grain size: the first is the average grain size in the first 50 mm of exposed surface, and the second is the average grain size in the region deeper than 150 mm below the surface. If only one value is listed, no observable difference was noted in the perceived grain size with depth into the sample. FD, fracture density. Two values are listed: the first is the fracture density near the surface, and the second is the fracture density deep into the sample. N/L, pixel count divided by Euclidean length (in pixels). Frgnness, fractal dimension of trace of exposed surface. Rel Hausdorf, for discussion of the Hausdorf measure, see Peitgen and others, 1992. Shape factor, measure of surface roughness derived for this study (see app. 7).]

Image analysis data of core: **GCSC2**

	A	B	C	D	Avg(BCD)	E	F	G	Avg(EFG)
Rcssn (μm) (D/S)									
(Dirct//Smooth)	*17+-50//136+-200								
Rcssn (sigma)									
Ecldn Length (cm)		22.00	20.00	22.00	21.33	22.00	22.00	22.00	22.00
Ecldn Length (pix)		501	455	501	485	501	501	501	501
(D-1)*100		5.40	5.60	7.40	6.13	3.00	4.20	1.60	2.93
Crossings		5	9	7	7	10	12	14	12
Dev (sigma)		368	241	303	304	287	122	94	168
Pixel count		704	609	716	676	645	613	550	603
Grn size (100 μm)		121	160	68	116	196	81		139
Grn size (300 μm)		121	160	68	116	196	81		139
FD (%) at surface (100 μm)		8	7	24	13	0	4	0	1
FD (%) subsurface (300 μm)		2	1	4	2	3	4	1	3
N/L		1.41	1.34	1.43	1.39	1.29	1.22	1.10	1.20
FRghness = $((N/L)^{D-1})*100$		43	36	47	42	30	23	10	21
Rel Hausdorf		0.99	0.99	1.00	1.00	0.98	0.99	0.99	0.99
Shape factor		2.55	2.43	2.62	2.54	2.31	2.21	1.95	2.15
	GCSC2A	**GCSC2B**	**GCSC2C**	**GCSC2D**	**Avg**	**GCSC2E**	**GCSC2F**	**GCSC2G**	**Avg**

Table 9 (Cont.)—Results of fracture-density measurements based on SEM-image analysis of core samples obtained in this study—Continued.
[Rcssn, surface recession; sigma, standard deviation. Ecldn Length, Euclidian length of trace of exposed surface, measured along regression line through trace from end to end. D, in (D-1)*100, Richardson dimension (see app. 7). Crossings, number of crossings of trace of exposed surface over regression line through trace. Dev, standard deviation of trace of exposed surface. Pixel count, number of pixels in trace of exposed surface used in computing the shape factor. Grn size, estimated average grain size, using calipers provided by "Loss" option from menu of program EDGE. Note that the distance between calipers as reported on monitor is based on the assumption that the SEM image magnification is 10X; if other than 10X images are used for analysis, values reported by program should by multiplied by the factor 10/actual magnification. For most samples, two values are listed for grain size: the first is the average grain size in the first 50 mm of exposed surface, and the second is the average grain size in the region deeper than 150 mm below the surface. If only one value is listed, no observable difference was noted in the perceived grain size with depth into the sample. FD, fracture density. Two values are listed: the first is the fracture density near the surface, and the second is the fracture density deep into the sample. N/L, pixel count divided by Euclidean length (in pixels). Frgnness, fractal dimension of trace of exposed surface. Rel Hausdorf, for discussion of the Hausdorf measure, see Peitgen and others, 1992. Shape factor, measure of surface roughness derived for this study (see app. 7).]

Image analysis data of core: **GCSD1**

	A	B	C	D	Avg(BCD)	E	F	G	Avg(EFG)
Rcssn (μm) (D/S)									
(Dirct//Smooth)	u.d.+-200//*65+-35								
Rcssn (sigma)									
Ecldn Length (cm)		22.50	17.00	22.50		20.50	17.50	22.50	
Ecldn Length (pix)		512	387	512		466	398	512	
(D-1)*100		13.90	21.80	8.00	14.57	22.60	22.80	17.10	20.83
Crossings		15	9	3	9	15	19	12	15
Dev (sigma)		160	377	251	263	339	147	449	312
Pixel count		904	1124	721	916	1292	904	1221	1139
Grn size (100 μm)		*	*	*	0	*	*	*	0
Grn size (300 μm)		*	*	*	0	*	*	*	0
FD (%) at surface (100 μm)		9	25	25	20	45	47	35	42
FD (%) subsurface (300 μm)		9	12	9	10	13	9	12	11
N/L		1.77	2.91	1.41	2.03	2.77	2.27	2.38	2.47
FRghness = $((N/L)^{D-1})*100$		91	267	45	134	249	174	177	200
Rel Hausdorf		1.02	1.12	0.99	1.04	1.13	1.10	1.05	1.09
Shape factor		3.36	5.78	2.59	3.91	5.54	4.54	4.62	4.90
	GCSD1A	**GCSD1B**	**GCSD1C**	**GCSD1D**	**GCSDo**	**GCSD1E**	**GCSD1F**	**GCSD1G**	**GCSD**

Table 9 (Cont.)—Results of fracture-density measurements based on SEM-image analysis of core samples obtained in this study—Continued.
[Rcssn, surface recession; sigma, standard deviation. Ecldn Length, Euclidian length of trace of exposed surface, measured along regression line through trace from end to end. D, in (D-1)*100, Richardson dimension (see app. 7). Crossings, number of crossings of trace of exposed surface over regression line through trace. Dev, standard deviation of trace of exposed surface. Pixel count, number of pixels in trace of exposed surface used in computing the shape factor. Grn size, estimated average grain size, using calipers provided by "Loss" option from menu of program EDGE. Note that the distance between calipers as reported on monitor is based on the assumption that the SEM image magnification is 10X; if other than 10X images are used for analysis, values reported by program should by multiplied by the factor 10/actual magnification. For most samples, two values are listed for grain size: the first is the average grain size in the first 50 mm of exposed surface, and the second is the average grain size in the region deeper than 150 mm below the surface. If only one value is listed, no observable difference was noted in the perceived grain size with depth into the sample. FD, fracture density. Two values are listed: the first is the fracture density near the surface, and the second is the fracture density deep into the sample. N/L, pixel count divided by Euclidean length (in pixels). Frgnness, fractal dimension of trace of exposed surface. Rel Hausdorf, for discussion of the Hausdorf measure, see Peitgen and others, 1992. Shape factor, measure of surface roughness derived for this study (see app. 7).]

Image analysis data of core: GCSG2

	A	B	C	D	Avg(BCD)	E	F	G	Avg(EFG)
Rcssn (μm) (D/S) (Dirct//Smooth)	No test								
Rcssn (sigma)									
Ecldn Length (cm)						22.25	22.25	22.25	22.25
Ecldn Length (pix)						506	506	506	506
(D-1)*100						5.00	9.60	2.60	6
Crossings						6	6	3	5
Dev (sigma)						518	567	387	491
Pixel count						751	949	633	778
Grn size (100 μm)						212	118		165
Grn size (300 μm)						212	118	174	168
FD (%) at surface (100 μm)						15	15	15	15
FD (%) subsurface (300 μm)						5	5	8	6
N/L						1.48	1.87	1.25	1.54
FRghness = $((N/L)^{D-1})*100$						51	99	26	59
Rel Hausdorf						0.99	1.02	0.98	1
Shape factor						2.69	3.48	2.23	2.80
	GCSG2A	**GCSG2B**	**GCSG2C**	**GCSG2D**	**Avg**	**GCSG2E**	**GCSG2F**	**GCSG2G**	**Avg**

Table 9 (Cont.)—Results of fracture-density measurements based on SEM-image analysis of core samples obtained in this study—Continued.
[Rcssn, surface recession; sigma, standard deviation. Ecldn Length, Euclidian length of trace of exposed surface, measured along regression line through trace from end to end. D, in (D-1)*100, Richardson dimension (see app. 7). Crossings, number of crossings of trace of exposed surface over regression line through trace. Dev, standard deviation of trace of exposed surface. Pixel count, number of pixels in trace of exposed surface used in computing the shape factor. Grn size, estimated average grain size, using calipers provided by "Loss" option from menu of program EDGE. Note that the distance between calipers as reported on monitor is based on the assumption that the SEM image magnification is 10X; if other than 10X images are used for analysis, values reported by program should by multiplied by the factor 10/actual magnification. For most samples, two values are listed for grain size: the first is the average grain size in the first 50 mm of exposed surface, and the second is the average grain size in the region deeper than 150 mm below the surface. If only one value is listed, no observable difference was noted in the perceived grain size with depth into the sample. FD, fracture density. Two values are listed: the first is the fracture density near the surface, and the second is the fracture density deep into the sample. N/L, pixel count divided by Euclidean length (in pixels). Frgnness, fractal dimension of trace of exposed surface. Rel Hausdorf, for discussion of the Hausdorf measure, see Peitgen and others, 1992. Shape factor, measure of surface roughness derived for this study (see app. 7).]

Image analysis data of core: GCSJ1

	A	B	C	D	Avg(BCD)	E	F	G	Avg(EFG)
Rcssn (μm) (D/S)									
(Dirct//Smooth)	No test								
Rcssn (sigma)									
Ecldn Length (cm)		12.15	22.50	22.50		22.50	22.50	22.50	
Ecldn Length (pix)		276	512	512		512	512	512	
(D-1)*100		1.20	2.90	6.40	3.50	2.80	1.40	2.60	2.27
Crossings		18	13	9	13	18	11	8	12
Dev (sigma)		71	135	177	128	101	94	109	101
Pixel count		300	578	669	516	573	537	569	560
Grn size (100 μm)		*	*	*	0	*	*	*	0
Grn size (300 μm)		*	*	*	0	*	*	*	0
FD (%) at surface (100 μm)		0	0	0	0	8	4	5	6
FD (%) subsurface (300 μm)		0	0	0	0	2	0	0	1
N/L		1.09	1.13	1.31	1.17	1.12	1.05	1.11	1.09
FRghness = $((N/L)^{D-1})*100$		9	13	33	18	12	5	11	10
Rel Hausdorf		0.99	0.99	0.99	0.99	0.99	0.99	0.99	0.99
Shape factor		1.92	2.02	2.38	2.11	2.00	1.86	1.98	1.95
	GCSJ1A	**GCSJ1B**	**GCSJ1C**	**GCSJ1D**	**GCSJo**	**GCSJ1E**	**GCSJ1F**	**GCSJ1G**	**GCSJ**

Table 9 (Cont.)—Results of fracture-density measurements based on SEM-image analysis of core samples obtained in this study—Continued.
[Rcssn, surface recession; sigma, standard deviation. Ecldn Length, Euclidian length of trace of exposed surface, measured along regression line through trace from end to end. D, in (D-1)*100, Richardson dimension (see app. 7). Crossings, number of crossings of trace of exposed surface over regression line through trace. Dev, standard deviation of trace of exposed surface. Pixel count, number of pixels in trace of exposed surface used in computing the shape factor. Grn size, estimated average grain size, using calipers provided by "Loss" option from menu of program EDGE. Note that the distance between calipers as reported on monitor is based on the assumption that the SEM image magnification is 10X; if other than 10X images are used for analysis, values reported by program should by multiplied by the factor 10/actual magnification. For most samples, two values are listed for grain size: the first is the average grain size in the first 50 mm of exposed surface, and the second is the average grain size in the region deeper than 150 mm below the surface. If only one value is listed, no observable difference was noted in the perceived grain size with depth into the sample. FD, fracture density. Two values are listed: the first is the fracture density near the surface, and the second is the fracture density deep into the sample. N/L, pixel count divided by Euclidean length (in pixels). Frgnness, fractal dimension of trace of exposed surface. Rel Hausdorf, for discussion of the Hausdorf measure, see Peitgen and others, 1992. Shape factor, measure of surface roughness derived for this study (see app. 7).]

Image analysis data of core: GCSL

	A	B	C	D	Avg(BCD)	E	F	G	Avg(EFG)
Rcssn (μm) (D/S)									
(Dirct//Smooth)	No test								
Rcssn (sigma)									
Ecldn Length (cm)		22.50	22.50	22.50	22.50	22.50	22.50	22.50	22.50
Ecldn Length (pix)		512	512	512	512	512	512	512	512
(D-1)*100		*	*	*		*	*	*	
Crossings		*	*	*		*	*	*	
Dev (sigma)		*	*	*		*	*	*	
Pixel count		*	*	*		*	*	*	
Grn size (100 μm)		*	*	*		*	*	*	
Grn size (300 μm)		*	*	*		*	*	*	
FD (%) at surface (100 μm)		*	*	*		*	*	*	
FD (%) subsurface (300 μm)		*	*	*		*	*	*	
N/L									
FRghness = $((N/L)^{D-1})*100$									
Rel Hausdorf									
Shape factor									

Table 9 (Cont.)—Results of fracture-density measurements based on SEM-image analysis of core samples obtained in this study—Continued.
[Rcssn, surface recession; sigma, standard deviation. Ecldn Length, Euclidian length of trace of exposed surface, measured along regression line through trace from end to end. D, in (D-1)*100, Richardson dimension (see app. 7). Crossings, number of crossings of trace of exposed surface over regression line through trace. Dev, standard deviation of trace of exposed surface. Pixel count, number of pixels in trace of exposed surface used in computing the shape factor. Grn size, estimated average grain size, using calipers provided by "Loss" option from menu of program EDGE. Note that the distance between calipers as reported on monitor is based on the assumption that the SEM image magnification is 10X; if other than 10X images are used for analysis, values reported by program should by multiplied by the factor 10/actual magnification. For most samples, two values are listed for grain size: the first is the average grain size in the first 50 mm of exposed surface, and the second is the average grain size in the region deeper than 150 mm below the surface. If only one value is listed, no observable difference was noted in the perceived grain size with depth into the sample. FD, fracture density. Two values are listed: the first is the fracture density near the surface, and the second is the fracture density deep into the sample. N/L, pixel count divided by Euclidean length (in pixels). Frgnness, fractal dimension of trace of exposed surface. Rel Hausdorf, for discussion of the Hausdorf measure, see Peitgen and others, 1992. Shape factor, measure of surface roughness derived for this study (see app. 7).]

Image analysis data of core: GCSM2

	A	B	C	D	Avg(BCD)	E	F	G	Avg(EFG)
Rcssn (μm) (D/S) (Dirct//Smooth)	No test								
Rcssn (sigma)									
Ecldn Length (cm)							22.50		22.50
Ecldn Length (pix)							512		512
(D-1)*100							13.60		14
Crossings							10		10
Dev (sigma)							173		173
Pixel count							892		892
Grn size (100 μm)							40		40
Grn size (300 μm)							116		116
FD (%) at surface (100 μm)							28		28
FD (%) subsurface (300 μm)							12		12
N/L							1.74		1.74
FRghness = $((N/L)^{D-1})*100$							88		88
Rel Hausdorf							1.05		1.05
Shape factor		3.41	3.41	3.41			3.31		3.31
	GCSM2A	**GCSM2B**	**GCSM2C**	**GCSM2D**	**Avg**	**GCSM2E**	**GCSM2F**	**GCSM2G**	**Avg**

Table 9 (Cont.)—Results of fracture-density measurements based on SEM-image analysis of core samples obtained in this study—Continued.
[Rcssn, surface recession; sigma, standard deviation. Ecldn Length, Euclidian length of trace of exposed surface, measured along regression line through trace from end to end. D, in (D-1)*100, Richardson dimension (see app. 7). Crossings, number of crossings of trace of exposed surface over regression line through trace. Dev, standard deviation of trace of exposed surface. Pixel count, number of pixels in trace of exposed surface used in computing the shape factor. Grn size, estimated average grain size, using calipers provided by "Loss" option from menu of program EDGE. Note that the distance between calipers as reported on monitor is based on the assumption that the SEM image magnification is 10X; if other than 10X images are used for analysis, values reported by program should by multiplied by the factor 10/actual magnification. For most samples, two values are listed for grain size: the first is the average grain size in the first 50 mm of exposed surface, and the second is the average grain size in the region deeper than 150 mm below the surface. If only one value is listed, no observable difference was noted in the perceived grain size with depth into the sample. FD, fracture density. Two values are listed: the first is the fracture density near the surface, and the second is the fracture density deep into the sample. N/L, pixel count divided by Euclidean length (in pixels). Frgnness, fractal dimension of trace of exposed surface. Rel Hausdorf, for discussion of the Hausdorf measure, see Peitgen and others, 1992. Shape factor, measure of surface roughness derived for this study (see app. 7).]

Image analysis data of core: GCRV2

	A	B	C	D	Avg(BCD)	E	F	G	Avg(EFG)
Rcssn (μm) (D/S) (Dirct//Smooth)									
Rcssn (sigma)									
Ecldn Length (cm)		22.50	22.00	22.50	22.33				
Ecldn Length (pix)		512	501	512	508				
(D-1)*100		4.20	7.40	7.70	6.43				
Crossings		26	6	4	12				
Dev (sigma)		97	160	267	175				
Pixel count		602	667	509	593				
Grn size (100 μm)		76	132		104				
Grn size (300 μm)		76	132		104				
FD (%) at surface (100 μm)		15	7	18	13				
FD (%) subsurface (300 μm)		5	7	7	6				
N/L		1.18	1.33	0.99	1.17				
FRghness = $((N/L)^{D-1})*100$		18	36	-1	18				
Rel Hausdorf		0.99	1.00	1.00	1.00				
Shape factor		2.12	2.45	1.83	2.13				
	GCRV2A	**GCRV2B**	**GCRV2C**	**GCRV2D**	**Avg**	**GCRV2E**	**GCRV2F**	**GCRV2G**	**Avg**

Table 9 (Cont.)—Results of fracture-density measurements based on SEM-image analysis of core samples obtained in this study—Continued.
[Rcssn, surface recession; sigma, standard deviation. Ecldn Length, Euclidian length of trace of exposed surface, measured along regression line through trace from end to end. D, in (D-1)*100, Richardson dimension (see app. 7). Crossings, number of crossings of trace of exposed surface over regression line through trace. Dev, standard deviation of trace of exposed surface. Pixel count, number of pixels in trace of exposed surface used in computing the shape factor. Grn size, estimated average grain size, using calipers provided by "Loss" option from menu of program EDGE. Note that the distance between calipers as reported on monitor is based on the assumption that the SEM image magnification is 10X; if other than 10X images are used for analysis, values reported by program should by multiplied by the factor 10/actual magnification. For most samples, two values are listed for grain size: the first is the average grain size in the first 50 mm of exposed surface, and the second is the average grain size in the region deeper than 150 mm below the surface. If only one value is listed, no observable difference was noted in the perceived grain size with depth into the sample. FD, fracture density. Two values are listed: the first is the fracture density near the surface, and the second is the fracture density deep into the sample. N/L, pixel count divided by Euclidean length (in pixels). Frgnness, fractal dimension of trace of exposed surface. Rel Hausdorf, for discussion of the Hausdorf measure, see Peitgen and others, 1992. Shape factor, measure of surface roughness derived for this study (see app. 7).]

Image analysis data of core: **GCRA1**

	A	B	C	D	Avg(BCD)	E	F	G	Avg(EFG)
Rcssn (μm) (D/S)									
(Dirct//Smooth)	*75+-50//55+-35								
Rcssn (sigma)									
Ecldn Length (cm)		22.50	22.50	22.50		22.50	22.50	22.50	
Ecldn Length (pix)		512	512	512		512	512	512	
(D-1)*100		5.90	3.80	17.90	9.20	8.00	4.70	2.40	5.03
Crossings		4	6	15	8	6	9	2	
Dev (sigma)		608	428	549	528	532	464	325	440
Pixel count		733	1050	1372	1052	834	696	620	717
Grn size (100 μm)		*	*	*	0	*	*	*	0
Grn size (300 μm)		*	*	*	0	*	*	*	0
FD (%) at surface (100 μm)		2	19	48	23	12	10	3	8
FD (%) subsurface (300 μm)		2	10	38	17	12	4	3	6
N/L		1.43	2.05	2.68	2.05	1.63	1.36	1.21	1.40
FRghness = $((N/L)^{D-1})*100$		46	111	220	126	69	38	22	43
Rel Hausdorf		0.98	0.95	1.07	1.00	0.98	0.98	0.98	0.98
Shape factor		2.61	3.69	5.22	3.84	3.00	2.46	2.16	2.54
	GCRA1A	**GCRA1B**	**GCRA1C**	**GCRA1D**	**GCRAo**	**GCRA1E**	**GCRA1F**	**GCRA1G**	**GCRA**

Table 9 (Cont.)—Results of fracture-density measurements based on SEM-image analysis of core samples obtained in this study—Continued.
[Rcssn, surface recession; sigma, standard deviation. Ecldn Length, Euclidian length of trace of exposed surface, measured along regression line through trace from end to end. D, in (D-1)*100, Richardson dimension (see app. 7). Crossings, number of crossings of trace of exposed surface over regression line through trace. Dev, standard deviation of trace of exposed surface. Pixel count, number of pixels in trace of exposed surface used in computing the shape factor. Grn size, estimated average grain size, using calipers provided by "Loss" option from menu of program EDGE. Note that the distance between calipers as reported on monitor is based on the assumption that the SEM image magnification is 10X; if other than 10X images are used for analysis, values reported by program should by multiplied by the factor 10/actual magnification. For most samples, two values are listed for grain size: the first is the average grain size in the first 50 mm of exposed surface, and the second is the average grain size in the region deeper than 150 mm below the surface. If only one value is listed, no observable difference was noted in the perceived grain size with depth into the sample. FD, fracture density. Two values are listed: the first is the fracture density near the surface, and the second is the fracture density deep into the sample. N/L, pixel count divided by Euclidean length (in pixels). Frgnness, fractal dimension of trace of exposed surface. Rel Hausdorf, for discussion of the Hausdorf measure, see Peitgen and others, 1992. Shape factor, measure of surface roughness derived for this study (see app. 7).]

Image analysis data of core: **GCRC1**

	A	B	C	D	Avg(BCD)	E	F	G	Avg(EFG)
Rcssn (μm) (D/S)									
(Dirct//Smooth)	*278+-90//146+-33								
Rcssn (sigma)									
Ecldn Length (cm)		22.00	22.00	22.00	22.00	22.50	22.00	22.00	22.17
Ecldn Length (pix)		501	501	501	501	512	501	501	504
(D-1)*100		7.30	4.60	4.90	5.60	8.50	5.10	0.90	5
Crossings		9	5	4	6	16	7	4	9
Dev (sigma)		488	401	456	448	243	330	335	303
Pixel count		854	763	637	751	802	719	632	718
Grn size (100 μm)		2000	0	1900	1300	240	1800	661	900
Grn size (300 μm)		2000	0	1900	1300	240	1800	661	900
FD (%) at surface (100 μm)		14	12	10	12	6	10	3	6
FD (%) subsurface (300 μm)		14	12	10	12	5	10	3	6
N/L		1.71	1.52	1.27	1.5	1.57	1.44	1.26	1.42
FRghness = $((N/L)^{D-1})*100$		77	55	29	54	63	46	27	45
Rel Hausdorf		1.00	0.99	0.99	0.99	1.01	0.99	0.98	0.99
Shape factor		3.13	2.75	2.30	2.73	2.89	2.60	2.23	2.58
	GCRC1A	**GCRC1B**	**GCRC1C**	**GCRC1D**	**Avg**	**GCRC1E**	**GCRC1F**	**GCRC1G**	**Avg**

Table 9 (Cont.)—Results of fracture-density measurements based on SEM-image analysis of core samples obtained in this study—Continued.
[Rcssn, surface recession; sigma, standard deviation. Ecldn Length, Euclidian length of trace of exposed surface, measured along regression line through trace from end to end. D, in (D-1)*100, Richardson dimension (see app. 7). Crossings, number of crossings of trace of exposed surface over regression line through trace. Dev, standard deviation of trace of exposed surface. Pixel count, number of pixels in trace of exposed surface used in computing the shape factor. Grn size, estimated average grain size, using calipers provided by "Loss" option from menu of program EDGE. Note that the distance between calipers as reported on monitor is based on the assumption that the SEM image magnification is 10X; if other than 10X images are used for analysis, values reported by program should by multiplied by the factor 10/actual magnification. For most samples, two values are listed for grain size: the first is the average grain size in the first 50 mm of exposed surface, and the second is the average grain size in the region deeper than 150 mm below the surface. If only one value is listed, no observable difference was noted in the perceived grain size with depth into the sample. FD, fracture density. Two values are listed: the first is the fracture density near the surface, and the second is the fracture density deep into the sample. N/L, pixel count divided by Euclidean length (in pixels). Frgnness, fractal dimension of trace of exposed surface. Rel Hausdorf, for discussion of the Hausdorf measure, see Peitgen and others, 1992. Shape factor, measure of surface roughness derived for this study (see app. 7).]

Image analysis data of core: **GCRD1**

	A	B	C	D	Avg(BCD)	E	F	G	Avg(EFG)
Rcssn (μm) (D/S) (Dirct//Smooth)	n.d.+-250//*175+-100								
Rcssn (sigma)									
Ecldn Length (cm)		22.50	22.50	22.50		22.50	22.50	22.50	
Ecldn Length (pix)		512	512	512		512	512	512	
(D-1)*100		17.10	13.70	22.10	17.63	11.90	6.90	11.90	10.23
Crossings		2	4	17	8	14	9	14	12
Dev (sigma)		1173	606	200	660	203	418	203	275
Pixel count		1577	1022	1205	1268	912	752	912	859
Grn size (100 μm)		*	*	*	0	*	*	*	0
Grn size (300 μm)		*	*	*	0	*	*	*	0
FD (%) at surface (100 μm)		40	9	42	30	27	18	27	24
FD (%) subsurface (300 μm)		40	28	37	35	22	18	22	21
N/L		3.08	2.00	2.35	2.48	1.78	1.47	1.78	1.68
FRghness = $((N/L)^{D-1})*100$		273	119	184	192	91	51	91	77
Rel Hausdorf		1.07	1.02	1.10	1.06	1.00	0.98	1.00	1.00
Shape factor		5.97	3.80	4.69	4.82	3.35	2.69	3.35	3.13
	GCRD1A	**GCRD1B**	**GCRD1C**	**GCRD1D**	**GCRDo**	**GCRD1E**	**GCRD1F**	**GCRD1G**	**GCRD**

Table 9 (Cont.)—Results of fracture-density measurements based on SEM-image analysis of core samples obtained in this study—Continued.
[Rcssn, surface recession; sigma, standard deviation. Ecldn Length, Euclidian length of trace of exposed surface, measured along regression line through trace from end to end. D, in (D-1)*100, Richardson dimension (see app. 7). Crossings, number of crossings of trace of exposed surface over regression line through trace. Dev, standard deviation of trace of exposed surface. Pixel count, number of pixels in trace of exposed surface used in computing the shape factor. Grn size, estimated average grain size, using calipers provided by "Loss" option from menu of program EDGE. Note that the distance between calipers as reported on monitor is based on the assumption that the SEM image magnification is 10X; if other than 10X images are used for analysis, values reported by program should by multiplied by the factor 10/actual magnification. For most samples, two values are listed for grain size: the first is the average grain size in the first 50 mm of exposed surface, and the second is the average grain size in the region deeper than 150 mm below the surface. If only one value is listed, no observable difference was noted in the perceived grain size with depth into the sample. FD, fracture density. Two values are listed: the first is the fracture density near the surface, and the second is the fracture density deep into the sample. N/L, pixel count divided by Euclidean length (in pixels). Frgnness, fractal dimension of trace of exposed surface. Rel Hausdorf, for discussion of the Hausdorf measure, see Peitgen and others, 1992. Shape factor, measure of surface roughness derived for this study (see app. 7).]

Image analysis data of core: **GCRG1**

	A	B	C	D	Avg(BCD)	E	F	G	Avg(EFG)
Rcssn (μm) (D/S)									
(Dirct//Smooth)	u.d.+-100//*11+-35								
Rcssn (sigma)									
Ecldn Length (cm)		16.00	22.00	21.00	19.67	22.00	22.00	21.00	21.67
Ecldn Length (pix)		364	501	478	448	501	501	478	493
(D-1)*100		21.50	29.70	30.70	27.30	4.70	2.40	4.10	4
Crossings		11	6	12	10	2	4	4	3
Dev (sigma)		477	574	532	528	519	329	578	475
Pixel count		1288	2308	1147	1581	629	642	695	655
Grn size (100 μm)		44	24	24	31	150	150	85	128
Grn size (300 μm)		128	94	134	119	150	150	150	150
FD (%) at surface (100 μm)		46	62	54	54	7	3	18	9
FD (%) subsurface (300 μm)		8	7	12	9	7	3	7	6
N/L		3.54	4.61	2.40	3.52	1.26	1.28	1.45	1.33
FRghness = $((N/L)^{D-1})*100$		364	626	214	401	27	29	48	35
Rel Hausdorf		1.22	1.46	1.27	1.32	0.99	0.98	0.98	0.98
Shape factor		7.03	9.60	5.03	7.22	2.27	2.29	2.62	2.39
	GCRG1A	**GCRG1B**	**GCRG1C**	**GCRG1D**	**Avg**	**GCRG1E**	**GCRG1F**	**GCRG1G**	**Avg**

Table 9 (Cont.)—Results of fracture-density measurements based on SEM-image analysis of core samples obtained in this study—Continued.
[Rcssn, surface recession; sigma, standard deviation. Ecldn Length, Euclidian length of trace of exposed surface, measured along regression line through trace from end to end. D, in (D-1)*100, Richardson dimension (see app. 7). Crossings, number of crossings of trace of exposed surface over regression line through trace. Dev, standard deviation of trace of exposed surface. Pixel count, number of pixels in trace of exposed surface used in computing the shape factor. Grn size, estimated average grain size, using calipers provided by "Loss" option from menu of program EDGE. Note that the distance between calipers as reported on monitor is based on the assumption that the SEM image magnification is 10X; if other than 10X images are used for analysis, values reported by program should by multiplied by the factor 10/actual magnification. For most samples, two values are listed for grain size: the first is the average grain size in the first 50 mm of exposed surface, and the second is the average grain size in the region deeper than 150 mm below the surface. If only one value is listed, no observable difference was noted in the perceived grain size with depth into the sample. FD, fracture density. Two values are listed: the first is the fracture density near the surface, and the second is the fracture density deep into the sample. N/L, pixel count divided by Euclidean length (in pixels). Frgnness, fractal dimension of trace of exposed surface. Rel Hausdorf, for discussion of the Hausdorf measure, see Peitgen and others, 1992. Shape factor, measure of surface roughness derived for this study (see app. 7).]

Image analysis data of core: **GCRJ2**

	A	B	C	D	Avg(BCD)	E	F	G	Avg(EFG)
Rcssn (μm) (D/S)									
(Dirct//Smooth)	*200+-100//85+-35								
Rcssn (sigma)									
Ecldn Length (cm)		22.50	22.50	22.50		22.50	22.50	22.50	
Ecldn Length (pix)		512	512	512		512	512	512	
(D-1)*100		11.40	29.00	12.30	17.57	5.30	0.00	3.60	2.97
Crossings		22	26	10	19	8	4	10	7
Dev (sigma)		142	344	418	301	183	311	157	217
Pixel count		860	1916	1202	1326	629	571	586	595
Grn size (100 μm)		*	*	*	0	*	*	*	0
Grn size (300 μm)		*	*	*	0	*	*	*	0
FD (%) at surface (100 μm)		41	29	47	39	8	11	0	6
FD (%) subsurface (300 μm)		25	20	47	31	5	8	0	4
N/L		1.68	3.74	2.35	2.59	1.23	1.12	1.14	1.16
FRghness = $((N/L)^{D-1})*100$		78	449	161	229	24	12	15	17
Rel Hausdorf		1.00	1.27	1.01	1.09	0.99	0.99	0.99	0.99
Shape factor		3.15	7.76	4.43	5.11	2.23	1.96	2.06	2.08
	GCRJ2A	**GCRJ2B**	**GCRJ2C**	**GCRJ2D**	**GCRJo**	**GCRJ2E**	**GCRJ2F**	**GCRJ2G**	**GCRJ**

Table 9 (Cont.)—Results of fracture-density measurements based on SEM-image analysis of core samples obtained in this study—Continued.
[Rcssn, surface recession; sigma, standard deviation. Ecldn Length, Euclidian length of trace of exposed surface, measured along regression line through trace from end to end. D, in (D-1)*100, Richardson dimension (see app. 7). Crossings, number of crossings of trace of exposed surface over regression line through trace. Dev, standard deviation of trace of exposed surface. Pixel count, number of pixels in trace of exposed surface used in computing the shape factor. Grn size, estimated average grain size, using calipers provided by "Loss" option from menu of program EDGE. Note that the distance between calipers as reported on monitor is based on the assumption that the SEM image magnification is 10X; if other than 10X images are used for analysis, values reported by program should by multiplied by the factor 10/actual magnification. For most samples, two values are listed for grain size: the first is the average grain size in the first 50 mm of exposed surface, and the second is the average grain size in the region deeper than 150 mm below the surface. If only one value is listed, no observable difference was noted in the perceived grain size with depth into the sample. FD, fracture density. Two values are listed: the first is the fracture density near the surface, and the second is the fracture density deep into the sample. N/L, pixel count divided by Euclidean length (in pixels). Frgnness, fractal dimension of trace of exposed surface. Rel Hausdorf, for discussion of the Hausdorf measure, see Peitgen and others, 1992. Shape factor, measure of surface roughness derived for this study (see app. 7).]

Image analysis data of core: **GCRL1**

	A	B	C	D	Avg(BCD)	E	F	G	Avg(EFG)
Rcssn (μm) (D/S)									
(Dirct//Smooth)	*150+-90//100+-50								
Rcssn (sigma)									
Ecldn Length (cm)		22.50	22.50	22.50	22.50	18.41	22.50	22.50	21.14
Ecldn Length (pix)		512	512	512	512	419	512	512	481
(D-1)*100		3.80	17.00	14.70	11.83	27.70	15.30	8.80	17.27
Crossings		6	7	9	7	16	18	7	14
Dev (sigma)		289	523	440	417	367	230	228	275
Pixel count		628	1219	1123	990	1506	1164	747	1139
Grn size (100 μm)		*	*	*	0	*	*	*	0
Grn size (300 μm)		*	*	*	0	*	*	*	0
FD (%) at surface (100 μm)		32	22	20	25	35	18	31	28
FD (%) subsurface (300 μm)		17	18	5	13	10	4	8	7
N/L		1.23	2.38	2.19	1.93	3.60	2.27	1.46	2.44
FRghness = $((N/L)^{D-1})*100$		24	176	146	115	412	158	51	207
Rel Hausdorf		0.98	1.05	1.03	1.02	1.24	1.04	0.99	1.09
Shape factor		2.21	4.61	4.19	3.67	7.40	4.36	2.70	4.82
	GCRL1A	**GCRL1B**	**GCRL1C**	**GCRL1D**	**GCRLo**	**GCRL1E**	**GCRL1F**	**GCRL1G**	**GCRL**

Table 9 (Cont.)—Results of fracture-density measurements based on SEM-image analysis of core samples obtained in this study.
[Rcssn, surface recession; sigma, standard deviation. Ecldn Length, Euclidian length of trace of exposed surface, measured along regression line through trace from end to end. D, in (D-1)*100, Richardson dimension (see app. 7). Crossings, number of crossings of trace of exposed surface over regression line through trace. Dev, standard deviation of trace of exposed surface. Pixel count, number of pixels in trace of exposed surface used in computing the shape factor. Grn size, estimated average grain size, using calipers provided by "Loss" option from menu of program EDGE. Note that the distance between calipers as reported on monitor is based on the assumption that the SEM image magnification is 10X; if other than 10X images are used for analysis, values reported by program should by multiplied by the factor 10/actual magnification. For most samples, two values are listed for grain size: the first is the average grain size in the first 50 mm of exposed surface, and the second is the average grain size in the region deeper than 150 mm below the surface. If only one value is listed, no observable difference was noted in the perceived grain size with depth into the sample. FD, fracture density. Two values are listed: the first is the fracture density near the surface, and the second is the fracture density deep into the sample. N/L, pixel count divided by Euclidean length (in pixels). Frgnness, fractal dimension of trace of exposed surface. Rel Hausdorf, for discussion of the Hausdorf measure, see Peitgen and others, 1992. Shape factor, measure of surface roughness derived for this study (see app. 7).]

Image analysis data of core: GCRM2

	A	B	C	D	Avg(BCD)	E	F	G	Avg(EFG)
Rcssn (μm) (D/S)									
(Dirct//Smooth)	No test								
Rcssn (sigma)									
Ecldn Length (cm)						22.00	22.00	22.50	22.17
Ecldn Length (pix)						501	501	512	504
(D-1)*100						6.50	9.80	3.40	7
Crossings						2	6	4	4
Dev (sigma)						675	699	568	647
Pixel count						822	979	738	846
Grn size (100 μm)						135	230	66	144
Grn size (300 μm)						135	230	66	144
FD (%) at surface (100 μm)						14	49	13	25
FD (%) subsurface (300 μm)						5	20	4	10
N/L						1.64	1.96	1.44	1.68
FRghness = $((N/L)^{D-1})*100$						70	109	46	75
Rel Hausdorf						1.00	1.02	0.98	1.00
Shape factor						3.00	3.64	2.59	3.07
	GCRM2A	**GCRM2B**	**GCRM2C**	**GCRM2D**	**Avg**	**GCRM2E**	**GCRM2F**	**GCRM2G**	**Avg**